UNIVERSITÄTSKLINIKUM HAMBURG EPPENDORF

Zentrum für Molekulare Neurobiologie Hamburg

Institute for Synaptic Physiology

Prof. Dr. Thomas G. Oertner

The role of cFOS and ΔFOSB in episodic-like memory

Dissertation

With the aim of achieving a doctoral degree (Dr. rer. nat.) at the Faculty of Mathematics, Informatics and Natural Sciences of the University of Hamburg

Submitted by

Andreas Franzelin

Hamburg, Germany

February 21, 2024

The following evaluators recommend the admission of the dissertation:

Oral defense: 15.05.24

Prof. Dr. Thomas Oertner

Institut für Synaptische Physiologie

Zentrum für molekulare Neurowissenschaft Hamburg

Prof. Dr. Dietmar Kuhl

Institut für Molekulare und Zelluläre Kognition

Zentrum für molekulare Neurowissenschaft Hamburg

Prof. Dr. Matthias Kneussel

Institut für Molekulare Neurogenetik

Zentrum für molekulare Neurowissenschaft Hamburg

Thesis:

Prof. Dr. Thomas Oertner

Institut für Synaptische Physiologie

Zentrum für molekulare Neurowissenschaft Hamburg

Prof. Dr. Thomas Eschenhagen

Institute of Experimental Pharmacology and Toxicology

Universitätsklinikum Hamburg Eppendorf

Table of content

Table of content....3
Table of figures....5
Introduction....5
Publication #1:....5
Publication #2:....6
Publication #3:....6
Publication #4:....6
General Discussion....7
Summary....8
Zusammenfassung....8
List of Abbreviations....10
Introduction....13
Cellular and molecular mechanism of memory....13
The engram theory, hippocampus and episodic memory....13
Hippocampal connectivity- the trisynaptic pathway....15
Hippocampus – spatial memory and navigation....17
The Immediate early genes....18
Induction of cFOS (Ca^{2+} influx)....19
FOS as a marker for neuronal activity....22
ΔFOSB related to addiction (Striatum, Nucleus accumbens)....23
ΔFOSB related to memory (Hippocampus)....26
Regulating Chromatin accessibility via histone modification....27
The role of histone acetylation in memory formation....28
Publications....31
Publication #1: ΔFOSB accumulation in hippocampal granule cells drives cFOS pattern separation during spatial learning....31
Publication (preprint) #2: Neuronal FOS reports synchronized activity of presynaptic neurons....64
Publication (preprint) #3: Epigenetic repression of cFOS supports sequential formation of distinct spatial memories....95
General Discussion....133
cFOS labels engram neurons during first memory encounter but cannot be predicted by Ca^{2+}....133
ΔFOS repressive action is an epigenetic feedback mechanism important for memory formation....142

References....148
Appendix....166
Publication #4: Tool development Freeze-frame imaging of dendritic Ca^{2+} signals with TubuTag....166
Acknowledgements....178

Table of figures

Introduction

Figure I1: Schematic overview of the hippocampal formation and para hippocampal structures 16
Figure I2: Dimerization of cFOS and cJUN forming leucine zipper 19
Figure I3: Schematic representation of cFOS induction 22
Figure I4: Schematic representation of cFOS and ΔFOSB expression levels over time 23
Figure I5: Activin and Dopamine signaling enhance ΔFOSB slicing 25

Publication #1:

Figure 1 Behavioral performance in a spatial memory task is not reflected by cFOS ensemble overlap in the DG 35
Figure 2 Effects of task and environment on cFOS ensemble overlap 36
Figure 3 Optogenetic silencing of cFOS-tagged granule cells impairs spatial memory recall 37
Figure 4 cFOS-tagged dentate granule cells are reactivated during water maze training 38
Figure 5 Temporal dynamics of cFOS overlap in dentate gyrus 39
Figure 6 Mechanism of cFOS suppression in WM-trained mice 41
Figure 7 Repeated chemogenetic induction of cFOS expression in slice culture 42
Figure 8 Water maze training leads to accumulation of ΔFOSB and cFOS repression in DG 43

Supplementary Figure 1 Characterization of cFOS reporter expression in TetTag mice 49
Supplementary Figure 2 Size of cFOS ensembles in TetTag mice 50
Supplementary Figure 3 Optimization of cFOS tagging in TetTag mice 51
Supplementary Figure 4 BiPOLES characterization in granule cells (GCs) 51
Supplementary Figure 5 Effect of optogenetic reactivation of cFOS-tagged GCs on spatial memory recall 52
Supplementary Figure 6 Chemogenetic silencing of dentate gyrus affects spatial memory recall 53
Supplementary Figure 7 Estimating the radius of photoconversion by coexpression of CaMPARI and channelrhodopsin 54
Supplementary Figure 8 Expression analysis in DG in individual mice 55
Supplementary Figure 9 Chemogenetic activation of cFOS and pan FOSB 56
Supplementary Figure 10 Subtraction method to estimate ΔFOSB expression 57
Supplementary Figure 11 Kernel density estimates in DG, more examples 58
Supplementary Figure 12 Kernel density estimates from CA1 pyramidal cells 59

Supplementary Table 1 Statistics 60
Supplementary Table 2 Primary and secondary antibodies 63

Publication #2:

Figure 1 Optogenetic spike threshold is independent of cell size 69
Figure 2 Activity-induced FOS expression depends on cell type 70
Figure 3 FOS is induced at high and low, not intermediate frequencies 72
Figure 4 Low and high frequency-induced FOS use different pathways and depend on mGluRs 74
Figure 5 Presynaptic stimulation induces postsynaptic FOS 76
Figure 6 Activation of mGluRs rather than electrically-driven spiking drives FOS in cultured hippocampal neurons 78

Table 1 Primary and secondary antibodies 85

Supplementary Figure 1 Action potential generation by current injection and light intensity threshold for action potential generation in CheRiff expressing hippocampal neurons 92
Supplementary Figure 2 Time course of FOS expression after high K+ 92
Supplementary Figure 3 Bimodal relationship between firing frequency and FOS expression 93
Supplementary Figure 4 No effect of pharmacological agents tested on non-stimulated slice cultures 94
Supplementary Figure 5 Inhibitors of fast synaptic transmission (NBQX, CPPene, picrotoxin) have no effect on high K+ induced FOS 94

Publication #3:

Figure 1 Correlations between nuclear calcium levels and cFos expression 99
Figure 2 Bicuculline-induced activity increases ΔFosB expression in all hippocampal subregions 101
Figure 3 ΔFosB electroporation decreases bicuculline-induced cFos expression in CA1. 103
Figure 4 History of activity affects cFos expression 105
Figure 5 Expression of cFos and ΔFosB in the hippocampus after water maze training. 107
Figure 6 HDAC inhibitor increases cFos re-expression in dentate gyrus 108
Figure 7 Spatial memory formation under HDAC inhibition 110
Figure 8 Spatial memory retrieval 112

Table 1 Plasmid list 116
Table 2 Slice culture experiments 116
Table 3 Primary and secondary antibody combinations 117
Table 4 Imaris spot selection methods 119

Publication #4:

Figure 1 Design and performance of TubuTag 169
Figure 2 Design and performance of the Rapid3D microscope 170

Figure 3 Photoconversion of TubuTag by extracellular stimulation paired with violet light 171
Figure 4 TubuTag immunodetection 172

General Discussion:

Figure D1 Correlation of Ca2+ and cFOS in the CA1 and DG 134
Figure D2 Effects of opto- or chemogenetic stimulation on pre- and postsynaptic neurons 139
Figure D3 Possible pathways of cFOS induction after high and chronic stimulation 141
Figure D4 Schematic illustration of cFOS and ΔFOSB expression in the hippocampus of pathological, healthy, and HDACi-treated mice 145

Summary

In the quest to understand how memory works, a lot of effort has been invested in identifying the physiological substrate of memory in the brain. In recent decades, several studies have used the immediate early gene cFOS as a marker to identify active neurons during memory formation and recall. This approach assumes that neuronal activity always results in cFOS expression, and expression is consistent between neurons and throughout the brain. Investigating in detail the relationship between cFOS and neuronal activity during learning and memory recall is the subject of my thesis. Using a nuclear Ca^{2+} indicator (CaMPARI2) and optogenetic tools (ChrimsonR), I find that the relationship between learning, neuronal activity, Ca^{2+} and cFOS is more complex than was previously thought.

I found that in the hippocampus, cFOS expression does not correlate with Ca^{2+} or action potentials. Despite high Ca^{2+} levels, in some neurons (CA2 region) cFOS expression is absent. Strikingly, cFOS induction is highest at low frequencies and depends on glutamate and mGluR receptor signaling. Hippocampal cFOS is strongly induced during water maze training and optogenetic inhibition of dentate granule cFOS ensembles labeled during learning impairs memory recall on subsequent days. After analyzing cFOS in mice visiting the water maze, we made an intriguing observation: cFOS labeled ensembles of neurons in the dentate gyrus segregate over time and rarely re-express cFOS twice, despite elevated calcium levels. The same results were observed in the home cage environment, suggesting that once cFOS is expressed, a repressive mechanism is activated to suppress cFOS expression when these neurons are reactivated.

I found that this suppression of cFOS is mediated by ΔFOSB and depends on histone deacetylase enzymes, which make epigenetic modifications to DNA. This epigenetic repression of cFOS occurs specifically in the dentate gyrus. Interfering with histone deacetylation over days of learning caused memory problems, particularly during recall. My results challenge the traditional link between neuronal activity/Ca^{2+} and cFOS and suggest that cFOS expression is a more complex regulated process. Further, we conclude that ΔFOSB-mediated cFOS repression represents a critical mechanism for a flexible memory system.

Zusammenfassung

Um die Funktionsweise des Gedächtnisses zu verstehen, ist es notwendig, das physiologische Substrat des Gedächtnisses zu identifizieren, das sogenannte Engram. In den letzten Jahrzehnten haben mehrere Studien den Transkriptionsfaktor cFOS als Marker verwendet, um Neuronen zu identifizieren, die während der Gedächtnisbildung und des Gedächtnisabrufs

aktiv sind. Dieser Ansatz geht davon aus, dass neuronale Aktivität immer zur Expression von cFOS führt und dass dies für alle Neuronen im gesamten Gehirn gilt. Das Ziel meiner Doktorarbeit war, die Beziehung zwischen neuronaler Aktivität und cFOS während desLernens und des Gedächtnisabrufs im Detail zu untersuchen. Mit Hilfe eines im Zellkern lokalisierten Ca^{2+}-Indikators (CaMPARI2) und lichtgesteuerter Ionenkanäle (ChrimsonR) habe ich herausgefunden, dass die Beziehung zwischen Lernen, neuronaler Aktivität, Ca^{2+} und cFOS komplexer ist als bisher angenommen.

Ich konnte zeigen, dass die cFOS-Expression im Hippocampus nicht mit der Ca^{2+}-Konzentration im Nukleus oder mit Aktionspotentialen korreliert. Trotz hoher Ca^{2+}-Spiegel wird cFOS in einigen Neuronen, z.B. in CA2 Pyramidenzellen, nicht exprimiert. Interessant ist, dass die cFOS-Induktion nach synchroner optogenetischer Stimulation mit sehr niedriger Frequenz (0.1 Hz) am höchsten ist und von Glutamat-Freisetzung und metabotropen Glutamatrezeptoren abhängt, also nicht zellautonom ausgelöst wird. Im Hippocampus wird cFOS während des Trainings im Wasserlabyrinth induziert. Die optogenetische Inhibition von cFOS-Ensembles im Gyrus dentatus, die während des Lernens markiert wurden, beeinträchtigt den Gedächtnisabruf an den folgenden Tagen. Bei der Analyse der cFOS Expression in Mäusen, die das Wasserlabyrinth besuchten, machten wir eine überraschende Beobachtung: Das Muster cFOS-markierter Neurone im Gyrus dentatus ändert sich von Tag zu Tag. Dies deutet darauf hin, dass nach der Expression von cFOS ein repressiver Mechanismus aktiviert wird, der die erneute cFOS-Expression unterdrückt, wenn diese Neuronen reaktiviert werden. Ich konnte an Schnittkulturen zeigen, dass der repressive Mechanismus auf der Expression und Anreicherung von ΔFOSB beruht und über epigenetische Veränderungen (Acetylierung von Histonen) vermittelt wird. Wir vermuten, dass dieser Mechanismus, der im intakten Tier auf den Gyrus dentatus beschränkt ist, für die Speicherung von episodischen (d.h. zeitlich gruppierten) Gedächtnisinhalten besonders wichtig ist.

Ich fand heraus, dass diese cFOS-Suppression durch ΔFOSB vermittelt wird und von Histondeacetylase-Enzymen abhängt, die epigenetische Modifikationen an der DNA vornehmen. Diese epigenetische Suppression von cFOS findet spezifisch im Gyrus dentatus statt. Die repetitive Inhibition der Histondeacetylierung während des Lernens führte zu Gedächtnisproblemen, insbesondere beim Abruf. Unsere Ergebnisse stellen den traditionellen Zusammenhang zwischen neuronaler Aktivität/Ca^{2+} und cFOS in Frage und deuten darauf hin, dass die cFOS-Expression ein komplexer regulierter Prozess ist. Darüber hinaus kommen wir zu dem Schluss, dass die ΔFOSB-vermittelte cFOS-Unterdrückung ein entscheidender Mechanismus für ein flexibles Gedächtnissystem ist.

List of Abbreviations

A.U.:	Arbitrary Unit
AAV:	Adeno-Associated Virus
AC:	Adenylyl Cyclase
AD:	Alzheimer's Disease
Amigo2:	Amphoterin Induced Gene and ORF
AMPA:	α-Amino-3-Hydroxy-5-Methyl-4-Isoxazolepropionic Acid
AMPA(R):	α-Amino-3-Hydroxy-5-Methyl-4-Isoxazolepropionic Acid (Receptor)
AP-1:	Activator Protein-1
APP:	Amyloid Precursor Protein
Arg1/Arc:	Arg3.1/Activity-Regulated Cytoskeleton-Associated Protein
CA1:	Cornu Ammonis Area 1
CA2:	Cornu Ammonis Area 2
CA3:	Cornu Ammonis Area 3
CaMKII:	Ca^{2+}/Calmodulin-Dependent Kinase II
CaMKs:	Ca^{2+}/Calmodulin-Dependent Protein Kinases
CaMPARI2:	Calcium Modulating Photoactivatable Ratiometric Integrator 2
cAMP:	Cyclic Adenosine Monophosphate
CDK5:	Cyclin-Dependent Kinase 5
CKII:	Casein Kinase II
CLOCK:	Circadian Locomotor Output Cycles Kaput
CNS:	Central Nervous System
CRE:	cAMP Response Element
CREB:	Cyclic AMP Response Element Binding Protein
Ctx:	Cortex
D1-MSNs:	D1 Dopamine Receptor Medium Spiny Neurons
D2-MSNs:	D2 Dopamine Receptor Medium Spiny Neurons
DAG:	Diacylglycerin
DARPP-32:	Dopamine- and cAMP-Regulated Phosphoprotein, 32 kDa
DBD:	DNA Binding Domain
DG:	Dentate Gyrus
DMSO:	Dimethyl Sulfoxide
EAAT3:	Excitatory Amino Acid Transporter 3
EC:	Entorhinal Cortex
Elk-1:	ETS-Like Gene 1

ER:	Endoplasmic Reticulum
ERK:	Extracellular Signal-Regulated Kinases
ERK/MAPK:	Extracellular Signal-Regulated Kinase/Mitogen-Activated Protein Kinase
FOSB:	FOSB
Fra-1:	FOS-Related Antigen 1
Fra-2:	FOS-Related Antigen 2
GABAA:	Gamma-Aminobutyric Acid Type A
Gi-DREADD:	Gi-Coupled Designer Receptors Exclusively Activated by Designer Drugs
GFP:	Green Fluorescent Protein
GPCR:	G Protein-Coupled Receptor
Gq-DREADD:	Gq-Coupled Designer Receptors Exclusively Activated by Designer Drugs
GTP:	Guanosine-5'-Triphosphate
HDAC1:	Histone Deacetylase 1
HDACi:	Histone Deacetylase Inhibitors
HATs:	Histone Acetyltransferases
IEG:	Immediate Early Genes
IP3:	Inositol 1,4,5-Trisphosphate
ITF:	Inducible Transcription Factor
K+:	Potassium Ion
Kir2.1:	Inward Rectifier Potassium Channel 2.1
LEC:	Lateral Entorhinal Cortex
LTD:	Long-Term Depression
LTP:	Long-Term Potentiation
L-VSCC:	L-Type Voltage-Sensitive Ca^{2+} Channel
LZ:	Leucine Zipper
MAPK:	Mitogen-Activated Protein Kinase
MEC:	Medial Entorhinal Cortex
MPEP:	2-Methyl-6-(Phenylethynyl)-Pyridine
mGluRs:	Metabotropic Glutamate Receptors
MSNs:	Medium Spiny Neurons
NAc:	Nucleus Accumbens
NGF:	Nerve Growth Factor
NMDA:	N-Methyl-D-Aspartate
NMDAR:	N-Methyl-D-Aspartate Receptor

NPAS4:	Neuronal PAS Domain Protein 4
PBS:	Phosphate Buffered Saline
PCP4:	Purkinje Cell Protein 4
PER2:	Period Circadian Regulator 2
PFA:	Paraformaldehyde
PIP2:	Phosphatidylinositol-4,5-Bisphosphate
PKA:	Protein Kinase A
PKC:	Protein Kinase C
PLC:	Phospholipase C
ParaSb:	Parasubiculum
PreSb:	Presubiculum
RGS14:	Regulator of G protein Signaling 14
ROI:	Region of Interest
S-27:	Phosphorylated form of ΔFOSB
S27A:	Non-phosphorylatable form of ΔFOSB
SCN:	Suprachiasmatic Nuclei
SD:	Standard Deviation
SEM:	Standard Error of the Mean
SPW-R:	Sharp Wave Ripples
SRE:	Serum Response Element
SRF:	Serum Response Factor
Sub:	Subiculum
TTX:	Tetrodotoxin
VGCC:	Voltage-Gated Calcium Channel
VSCC:	Voltage-Sensitive Ca^{2+} Channel
WM:	Water Maze
WT:	Wild Type
cAMP:	Cyclic AMP; 3',5'-cyclic adenosine monophosphate
cFOS:	Cellular FOS
mRNA:	Messenger Ribonucleic Acid
mV:	Millivolt
ΔFOSB:	Delta FOSB

Introduction

Cellular and molecular mechanism of memory

Contemporary neuroscience focuses on how the brain encodes environmental stimuli, including spatial, temporal, and valence information, to construct a conscious representation of the self. The brain is composed of neuronal networks made up of synaptically connected neurons. In the resting state, a neuron maintains a membrane potential of approximately -65 mV. Neurotransmitters released from the presynapse dock onto the corresponding receptors of the postsynaptic neuron, inducing a change in the electrical gradient through the influx of ions. Consequently, the membrane potential decreases, causing an action potential that leads to the subsequent release of transmitter and stimulation of the next postsynaptic cell where the cycle repeats. In the simplest abstraction, neurons are individual units with an on (spiking)or off (silent) state, akin to the 0s and 1s of binary code. The property believed to convey the capability to store information is synaptic plasticity, which changes the weight of connections i.e. how likely a piece of information will propagate to the next element in the circuit. Not only does the amount of synaptic depolarization exhibit plastic changes but also long-lasting structural changes may occur. The explored mechanism of neuroplasticity, rooted in Donald Hebb's theory (Hebb, 1949), indicates that neurons firing together in specific patterns lead to the strengthening or long-term potentiation of causally-connected synapses whereas synapses between neurons with non-causal firing connections undergo long-term depression as postulated by Stent (Stent, 1973). Long-term plasticity and particularly structural plasticity require the production of new proteins. A requirement for new protein production is that the chromatin needs to be accessible for mRNA transcription. The epigenetic modulation of the chromatin in the nucleus may also be regulated by plasticity-inducing activity and play a key role in effecting how a stimulus is translated into long-term structural changes.

The engram theory, hippocampus and episodic memory

The German zoologist Richard Semon was among the first who tried to conceptualize the physical basis of memory storage. In 1904, Semon coined the term "engram" which refers to

the physical or biochemical substrate of memories in the neural system (“Die Mneme als erhaltendes Prinzip im Wechsel des organischen Geschehens,” 1906). Semon also introduced “ecphory”, whereby an external cue activates the engram so that the memory is recalled (Semon & Semon, 1909). Once established, an engram may remain inactive but can be reactivated by the presentation of parts of the original event. Notably, the stimulus that reawakens the engram does not have to match the original engram-forming stimulus perfectly. This concept is in line with the contemporary concept of pattern completion where a retrieval cue provides sufficient information to trigger memory retrieval (Neunuebel; Knierim, 2014). Despite Semon's anticipation of contemporary memory concepts, researchers in his time largely ignored his theories. In the 1920s, Karl Lashley attempted to confirm to locate a memory engram within the rat's cortex. Lashley trained rats to find food in a maze before selectively ablating different cortical regions, hypothesizing that the ablated area would contain the corresponding engram (Lashley, 1925). Surprisingly, Lashley's results showed that the size of the lesion correlated with the extent of memory impairment, but not its location (Lashley, 1950). Despite his best efforts, Lashley was unable to locate the engram in a specific brain region, which led him to conclude that the engram supporting this form of memory is not localized in a specific cortical area. Later it was found that bilateral lesions of the hippocampus profoundly disrupt the ability to form new declarative memories. Around 1955, Brenda Milner and Wilder Graves Penfield investigated patients experiencing profound memory loss after unilateral temporal lobectomy to reduce epileptic seizures (Penfield & Milner, 1958). This impact on memory was unusual, since the lobectomy was unilateral and in the other similarly operated patients, there was no retrograde memory loss. Further studies confirmed unexpected pre-existing functional lesions in the contralateral temporal lobe. Therefore, they strongly warned against complete temporal lobectomy if there were any indications that abnormalities might exist in both lobes. Around the same time, the American surgeon William Scoville performed a bilateral temporal lobe resection on the famous patient Henry Molaison (patient HM). Milner met Scoville at the American Neurological Association conference and began to study HM, concluding that the hippocampal region, including the hippocampus proper and adjacent

temporal lobe structures, was crucial for episodic memory formation but not for recall of remote memories or the formation of non-declarative memory (Scoville & Milner, 1957). Milner and Scoville's findings provided compelling evidence for memory localization, pioneering a dedicated field focused on understanding the hippocampus role in memory.

Episodic memory pertains to our conscious capacity to explicitly recall personally experienced events (Tulving et al., 1983). In humans, the hippocampus plays a crucial role in encoding and retrieving the order of events in memories. While memory content for events is largely unaffected, remembering the temporal order of events is greatly impaired by damage to the hippocampus (Dede et al., 2016). Similarly, studies in rats with selective hippocampal lesions show impairments in remembering the order of a sequence, even when memory for the stimuli themselves was unaffected. (Fortin et al., 2002; Kesner et al., 2002). Recording studies in animals further support the hippocampus's involvement in mapping temporal events, independent of spatial coding (Kraus et al., 2013; Naya & Suzuki, 2011; Pastalkova et al., 2008; Paz et al., 2010; Spiers et al., 2001). This indicates that the hippocampus is specifically implicated in the temporal organization of memories, highlighting its role in formation of episodic memory.

Hippocampal connectivity- the trisynaptic pathway

In the early 20th century, Lorente de Nó was among the first pioneering scientists to describe parts of the hippocampal cytoarchitecture, specifically the cornu ammonis fields: CA1, CA2, and CA3 (Lorente, 1932). In the mid-20th century, the identification of extrinsic and intrinsic pathways in the medial temporal lobe provided evidence that the hippocampus is part of a broader highly conserved circuitry known as the hippocampal formation (Blackstad, 1956; Zimmer, 1971). The hippocampal formation includes the medial and lateral entorhinal cortex (MEC, LEC), the dentate gyrus (DG), the cornu ammonis fields CA1, CA2, CA3, and parahippocampal structures such as the presubiculum (PreSb) and parasubiculum (ParaSb) (Hartley et al., 2013; van Strien et al., 2009) (Fig. 1). The predominantly unidirectional

information flow (EC-DG-CA3-CA1-Sub) along the hippocampal structure, is unique across brain regions and offers an optimal model to study connectivity (Hartley et al., 2013; Squire et al., 2004; van Strien et al., 2009). Para-hippocampal structures, such as the perirhinal and

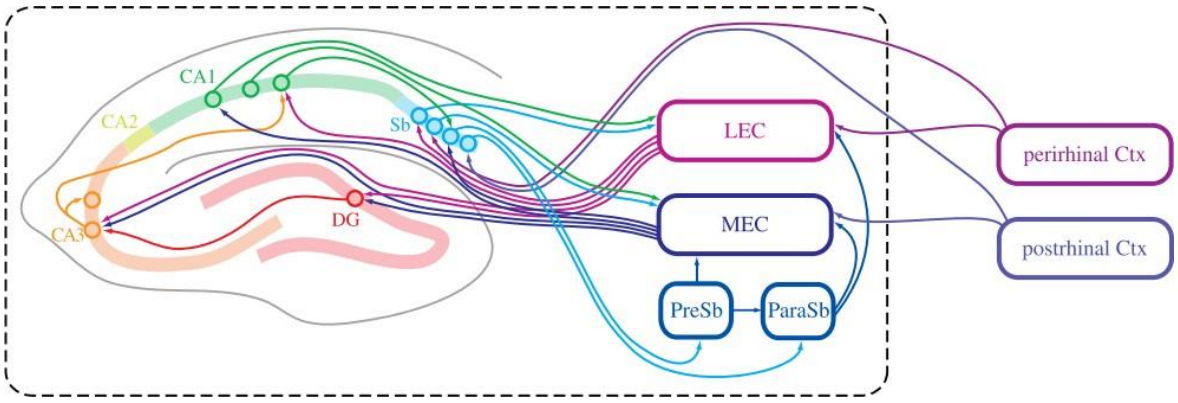

Figure I1: Schematic overview of the hippocampal formation and parahippocampal structures(Hartley et al., 2013).

postrhinal cortex, enable the hippocampal formation to exchange information with cortical areas (van Strien et al., 2009). There are two primary routes targeting the parahippocampal structures: the first leads from the perirhinal cortex (Ctx) to the lateral entorhinal cortex (LEC), while the second connects the postrhinal cortex with the medial entorhinal cortex (MEC) (Witter et al., 2013). The MEC projections forming the perforant pathway terminate on the dendrites of dentate granule cells within the molecular layer of the dentate gyrus (DG) (Amaral et al., 2007). Additionally, both regions of the entorhinal cortex establish monosynaptic connections with both CA1 and CA3 and subiculum (Sub) (Witter et al., 2013). The axons of dentate granule cells extend through so-called mossy fibers, reaching the pyramidal cells located in the CA3 region. Notably, CA3 pyramidal cells form intrinsic connections with other CA3 cells, known as recurrent collaterals, and project through Schaffer collaterals to the CA1 region (Hartley et al., 2013). The CA1 region serves as the primary output of the trisynaptic circuit, targeting back to the MEC and LEC and the subiculum (Amaral et al., 2007; Wible, 2013). Additional pathways include connections from the subiculum to both the presubiculum (PreSb) and parasubiculum (ParaSb) along with connections from the presubiculum to the medial entorhinal cortex and from the parasubiculum to both the lateral and medial entorhinal cortex (Hartley et al., 2013).

Hippocampus – spatial memory and navigation

As mentioned above, the hippocampus is localized in the medial temporal lobe and plays a critical function in memory formation. Damage to the hippocampus or the medial temporal lobe in pathological conditions such as Alzheimer's disease (Scheff et al., 2006; Zhu et al., 2017) or temporal lobe epilepsy (Butler & Zeman, 2008; Giovagnoli & Avanzini, 1999), impairs memory acquisition and recall. Studies in humans and rodents show that the hippocampus is crucial for processing spatial information in both virtual and real navigation (Ekstrom & Ranganath, 2017; Hartley et al., 2013). Spatial navigation involves different strategies, ranging from simple to more strategic approaches (Eichenbaum, 2017). The most basic navigation strategy is “search," where individuals explore the environment without a defined goal. In this sense, "to remember that rewards can be found by random searching" is a critical feature for successful performance (Eichenbaum, 2017). Beyond simple search, individuals use more complex navigation strategies. This can range from simple “route following”, where known paths are retraced, to more elaborate “wayfinding” and “survey navigation” techniques (Eichenbaum, 2017; Lisman et al., 2017). The latter methods involve the formation and use of mental representation of an area for navigation, explained by the cognitive map theory.

The cognitive map theory, indicates that spatial orientation is governed by memory representations that are organized as cognitive maps (Tolman, 1948). Spatial orientation is perceived through two different frameworks: allocentric and egocentric. "Allocentricframework" involves the ability to represent and see the environment from an externalperspective (Lisman et al., 2017). This involves forming cognitive maps that include the spatialrelationships between different landmarks. On the other hand, "egocentric framework" involves the capability to perceive the environment through a self-centered perspective. In this case, individuals rely on the personal cues and their position within the environment. The cognitive map theory was supported by the discovery of "place cells" in the hippocampus, which refer toneurons that fire in a specific place in the environment (O’Keefe & Dostrovsky, 1971). Additional modalities are also encoded in neuronal firing. These include grid cells in the

entorhinal cortex, head-direction cells signaling orientation, speed-coding cells indicating movement speed, and time-coding cells contributing to temporal aspects of spatial representation (Hafting et al., 2005; Sargolini et al., 2006; Taube et al., 1990; Whitlock et al., 2008). The hippocampus's involvement in both spatial and temporal processing suggests an intertwined representation where the spatial context provides a framework for organizing events along a temporal axis. By separating elements from the current time and place, the hippocampus offers a type of representation useful for retrospective (specific episodic memory recall) and prospective (prediction or simulation) cognition (Lisman et al., 2017). The question remains whether the hippocampus creates a temporal framework similar to spatial representation, or whether the sense of time is merely a consequence of moving through places in a particular order.

The Immediate early genes

Stimulation of neurons can elicit two separate mechanisms for processing and transmitting information: immediate electrophysiological activity, swiftly conveying information about the stimulus, and more delayed second-messenger signaling pathways, which lead to the induction of the nuclear transcription machinery via constitutively expressed transcription factors (Herdegen & Leah, 1998). The first genes that undergo rapid expression after cellular stimulation are termed immediate early genes (IEGs). The induction of IEGs takes place within minutes and does not need de novo protein synthesis prior to their induction (Herdegen & Leah, 1998). Most IEGs are inducible transcription factors (ITF) (Cruz-Mendoza et al., 2022; Saha & Dudek, 2013). Well studied ITFs are proteins from the FOS family (cFOS, FOSB, ΔFOSB, FRA-1, FRA-2) and the JUN family (cJUN, JUNB, JUND), (Herdegen & Leah, 1998). Following translation in the cytoplasm, ITFs are translocated to the nucleus, where they orchestrate the transcription of intermediate or late-expressing genes (Angel & Karin, 1991; Silver, 1991; Wisdom, 1999), which may be relevant for the induction of long-term structural changes in neurons and synapses (Davis & Squire, 1984; Matthies, 1989). ITFs initiate

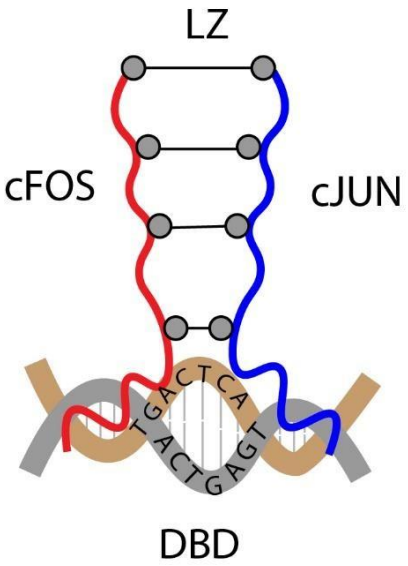

	cJUN	JUNB	JUND	cFOS	FOSB
cJUN	+ ↑				
JUNB	+ ↑	+ ↑			
JUND	+ ↑	+ ↑	+ ↑		
cFOS	+ ↑	+ ↑	+ ↑	-	-
FOSB	+ ↑	+ ↑	+ ↑	-	-
ΔFOSB	+ ↑			-	-

Figure I2: Dimerization of cFOS and cJUN forming leucine zipper (LZ) and DNA binding domain (DBD) (left). Table of observed dimerization of inducible transcription factors (right) (Herdegen & Leah, 1998).

transcription by binding to pre-existing initiation complexes, forming homo- or heterodimers with the activating protein 1 (AP-1) transcription factor complex at the appropriate promoter binding site (Angel & Karin, 1991; Silver, 1991; Wisdom, 1999). AP-1, cJUN and cFOS heterodimers assemble via the C-terminal leucine zipper (LZ) and bind to DNA via the N-terminal DNA binding domains (DBD) (Figure 2, left). They are highly stable and bind efficiently to both AP-1 and CRE sites (Hirai et al., 1990; Ryseck & Bravo, 1991). On the other hand, cJUN homodimers exhibit a strong affinity for CRE binding sites (Halazonetis et al., 1988). Examples of observed dimerization between the FOS and JUN family members resulting in up or down regulation of gene expression are shown in (Figure 2, right) (Herdegen & Leah, 1998).

Induction of cFOS (Ca^{2+} influx)

Among the first IEGs identified is cFOS (cellular-FOS) (Curran et al., 1984; Curran & Teich, 1982). One of the first observations of cFOS induction was noted in fibroblasts following stimulation with growth factors (Greenberg & Ziff, 1984), which suggested that cFOS plays an active role in the transcriptional control of cell division (Stiles, 1985). Subsequently, cFOS was also identified in neuroendocrine cells upon stimulation with nerve growth factor (NGF), which,

like cFOS, regulates cell differentiation (Curran & Morgan, 1985). In the rat nervous system, cFOS was identified via immunohistological staining in response to noxious stimulation (Bullitt, 1990) and cFOS mRNA is detected in neurons of the cortex, hippocampus, and limbic system within 5-20 minutes after seizures (Morgan et al., 1987; Morgan & Curran, 1986). cFOS consists of 380 amino acids with a molecular weight of 56–62 kDa (Herdegen et al., 1995). The basal level of cFOS mRNA is very low because of its instability and auto-repression by the cFOS protein itself (Lucibello et al., 1989; Morgan & Curran, 1991). In most regions of thebrain cFOS expression is transient (60 - 90 min.) and has a half-life of 2 hours (Del-Bel et al.,2000; Morgan & Curran, 1991; Onodera et al., 1989; Saha & Dudek, 2013; Yokoyama et al., 2013).

Various stimuli like growth factors, cytokines, electric or neurochemical-induced seizures, nociceptive stimulation, stress, learning, sexual behavior, or exposure to light can trigger neuronal activity and expression of cFOS (Gustems et al., 2014; Hsu et al., 2007; Hudson, 2018; Jackson et al., 2002; Pang et al., 1993; Xu et al., 2006). In order to translate synaptic activity into nuclear gene expression, intracellular Ca^{2+} is thought to play a crucial role (Deisseroth et al., 2003; Ghosh et al., 1994). Neurons actively maintain low intracellular Ca^{2+} levels by extruding Ca^{2+} to the extracellular space and storing it within intracellular Ca^{2+} stores like the endoplasmic reticulum (Cohen & Greenberg, 2008). Upon neuronal activation, the increase in intracellular Ca^{2+} concentration mainly results from Ca^{2+} influx through two main sources: the glutamate-activated NMDA receptor (NMDAR), and the L-type voltage-sensitive Ca^{2+} channel (VSCC) (Chaudhuri et al., 2000) (Figure 3). NMDARs are highly permeable to Ca^{2+} (Lau & Zukin, 2007) and are activated by glutamate plus glycine/D-serine/taurine binding and simultaneous depolarization through fast-acting glutamatergic AMPA receptors (Derkach et al., 2007). Upon depolarization, more Ca^{2+} can flow into the neuron through voltage-sensitive Ca^{2+} channels (VSCC) (Rajadhyaksha et al., 1999). In contrast to P/Q-, N-, and R-type Ca^{2+} channels, which are responsible to evoke synaptic transmission (Catterall, 2011; Olivera et al., 1994), several studies indicate that IEG expression is predominantly driven by Ca^{2+} entry

through L-type voltage-sensitive Ca^{2+} channels (L-VSCCs). This preference is attributed to their Ca^{2+} conductance, gating properties (Simms & Zamponi, 2014; Wheeler et al., 2012), and localization in cell bodies and proximal dendritic regions (Westenbroek et al., 1990), which brings them in closer proximity to the nucleus. Activation of metabotropic glutamate receptors (mGluRs) also induces cFOS (J. Q. Wang et al., 2007). Synaptically released glutamate activates mGluRs releasing the associated GTP-binding proteins. From the group I mGluRs, Gq proteins activate downstream phospholipase C (PLC). Once activated, PLC cleaves the membrane-bound phosphatidylinositol-4,5-bisphosphate (PIP2), producing diacylglycerol (DAG) and soluble inositol 1,4,5-trisphosphate (IP3), which can subsequently diffuse and activate IP3 receptors on the ER membrane (Bodzęta et al., 2021; Hagenston & Bading, 2011). IP3 receptor activation induces the release of Ca^{2+} from the ER. The increase in cytoplasmic Ca^{2+} stimulates a cascade of signaling events, including the activation of the Ras-mitogen-associated protein kinase (MAPK), Ca^{2+}/ calmodulin-dependent protein kinases (CaMKs), and calcineurin-mediated signaling pathways (Bito et al., 1996; Hardingham et al., 1997; Xing et al., 1996). Activation of the MAPK pathway leads to the phosphorylation of ETS-like gene 1 (Elk-1). Elk1 binds in collaboration with the serum response factor (SRF) to the serum response element (SRE) on the c-fos promoter (Cruz et al., 2015). The activation of calmodulin and subsequently CaMKII/IV activates nuclear CREB (cyclic AMP response element binding protein), which undergoes phosphorylation by ribosomal S6 kinase (Chung, 2015). The phosphorylated CREB then binds in association with the CREB binding protein (CBP) to the Ca^{2+} response element (CRE) in the c-fos promoter, inducing activation of the polymerase II transcription machinery (Chung, 2015). Following translation in the cytoplasm, cFOS protein translocates back into the nucleus serving as a transcription factor for "late" genes. Despite all the studies that have linked Ca^{2+} to cFOS induction, I find that there is very little correlation between the two. In the following work, I will present evidence demonstrating a poor correlation between intracellular Ca^{2+} and cFOS in individual neurons. I also found that it is spiking of the presynaptic neurons and not spiking per se that is critical for cFOS induction in an mGluR- and Gq-dependent manner.

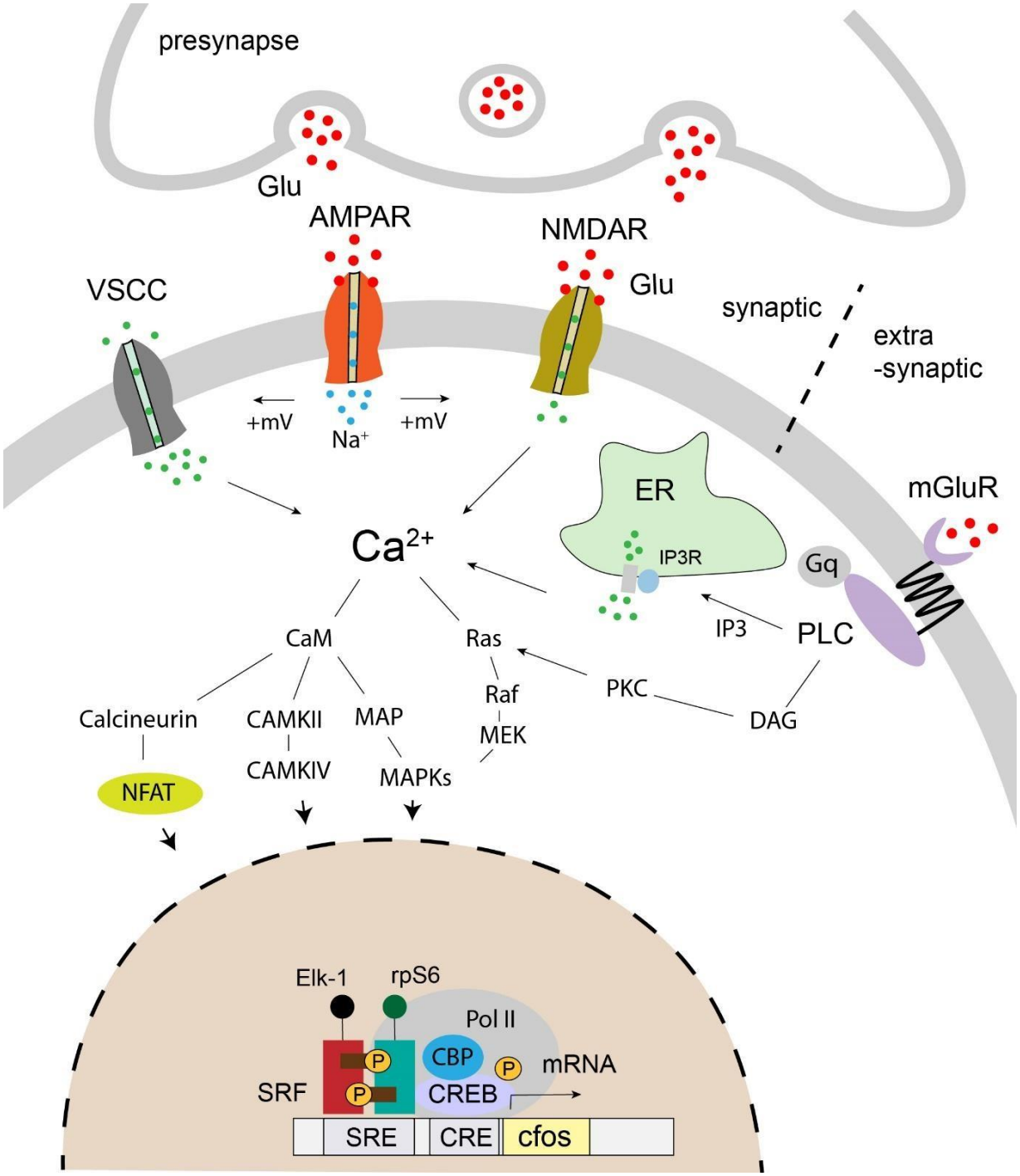

Figure I3: Schematic representation of cFOS induction

FOS as a marker for neuronal activity

Neuronal cFOS increases in rodents during learning and in novel environments, with the novelty of presented stimuli and their associations being significant factors (Bernstein et al., 2019; Bourgeois et al., 2012; Day et al., 2001; Handa et al., 1993; Monfil et al., 2018). The

highest expression of cFOS occurs during the early phases of training when learning is at its peak. Mice lacking cFOS in the CNS display normal general and emotional behavior but have specific impairments in hippocampus-dependent spatial and associative learning tasks, accompanied by a decrease in long-term potentiation (LTP) between CA3 to CA1 synapses (Fleischmann et al., 2003). These findings, coupled with the ease of using immunohistological techniques for detecting cFOS in individual neurons, sparked the use of cFOS as a proxy for active neurons and attempts to identify engrams formed during learning paradigms. A better understanding of how cFOS expression is controlled is also a subject investigated in this thesis

ΔFOSB related to addiction (Striatum, Nucleus accumbens)

During the course of my studies, I found that in the dentate gyrus an important factor predicting cFOS expression was the absence of ΔFOSB. ΔFOSB is a member of the FOS family and an alternative splicing product of fosB mRNA (Nestler et al., 2001). The feature that distinguishes ΔFOSB from other FOS family transcription factors is its persistence. The 33kD isoform peaks at around 6 hours and has an in vitro half-life of around 10 hours (Ulery et al., 2006) with some

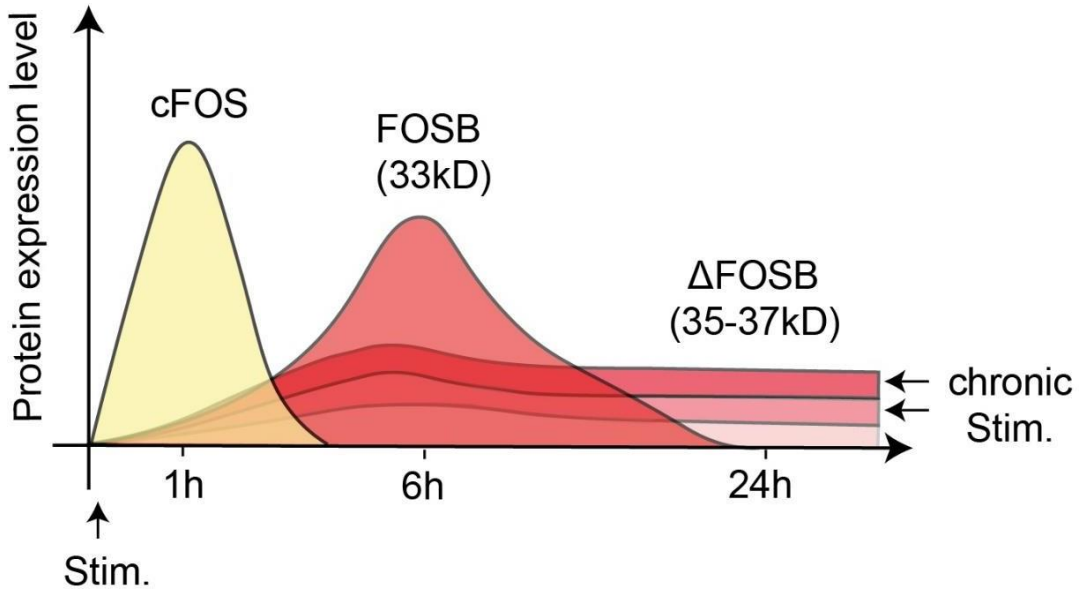

Figure I4: Schematic representation of cFOS and ΔFOSB expression levels over time (Nestler et al., 2001)

isoforms persisting for up to several weeks in vivo (Fig 4.) (Carle et al., 2007; Ulery-Reynolds et al., 2009). ΔFOSB gradually accumulates following chronic exposure to various

psychoactive stimuli, such as stress, specific lesions, drugs of abuse, and natural rewards in various regions of the brain. (Andersson et al., 2003; Bing et al., 1997; Colby et al., 2003; Hiroi & Graybiel, 1996; M. B. Kelz et al., 1999; Mandelzys et al., 1997; Moratalla, Vallejo, et al., 1996; Peakman et al., 2003; Linda I. Perrotti et al., 2004; Werme et al., 2002; Zachariou et al., 2006). Accumulation of ΔFOSB in the nucleus accumbens has been documented in response to substances such as cocaine, morphine, amphetamine, alcohol, nicotine, and phencyclidine (Hope, Nye, et al., 1994; Max B. Kelz & Nestler, 2000; Moratalla, Elibol, et al., 1996; Nye et al., 1995; Nye & Nestler, 1996; Pich et al., 1997). The longevity of ΔFOSB is not attributed toa consistent mRNA production but rather to the posttranslational phosphorylation of the proteinby casein kinase II (CKII) at a highly conserved serine residue (Ser27), which prevents its proteasomal degradation (Ulery et al., 2006). ΔFOSB accumulation is dependent on several other factors. In the absence of the dopamine- and cAMP-regulated phosphoprotein (DARPP-32), a protein that regulates the catalytic activity of protein phosphatase-1 and protein kinase A, ΔFOSB accumulation is attenuated (Bibb et al., 1999; Greengard et al., 1999). DARPP-32is enriched in multiple brain regions, with highest enrichment in the dopaminoceptive neuronsof the striatum (Fienberg et al., 1998; Hiroi et al., 1999), in neurons of the amygdala, the neocortex including layers II, III, VI, the granule cell layer of the dentate gyrus (Barbas et al., 1993), choroid plexus, hypothalamus and cerebellum (Ouimet et al., 1984). Furthermore, dopamine D1 receptor signaling interacts with the activin receptor-like kinase 4/Smad3 pathway in medium spiny neurons of the nucleus accumbens resulting in the translocation of PCBP1 and Smad3 to the nucleus (Krapacher et al., 2022). The PCBP1 RNA-binding protein-SMAD3 complex increases FOSB mRNA splicing and is essential for ΔFOSB accumulation and behavioral sensitization to cocaine in adult mice (Fig. 5). Key regions related to ΔFOSB accumulation are the nucleus accumbens and dorsal striatum. Both are important mediators of the behavioral responses to drugs, in particular for the effects of reward and locomotor activity. Overexpression of ΔFOSB in D1-MSNs in the nucleus accumbens (NAc) and dorsal striatum in mice leads to increased addiction-related behaviour. For example, heightened locomotor responsiveness for cocaine (Grueter et al., 2013; M. B. Kelz et al., 1999), increased

conditioned place preference for both cocaine and morphine (Grueter et al., 2013; M. B. Kelz et al., 1999; Zachariou et al., 2006), and increased self-administration of cocaine with an elevated risk of relapse (Colby et al., 2003). Despite lacking parts of the C-terminal transactivation domain, ΔFOSB can function as a potent activator and repressor (Dobrazanski et al., 1991; McClung & Nestler, 2003; Nakabeppu & Nathans, 1991) through dimerization with JUN proteins (predominantly with ΔJUND) facilitated by its leucine zipper domain (Rylski & Kaczmarek, 2004). Within the nucleus accumbens, ΔFOSB exerts its inhibitory effect on cFOS

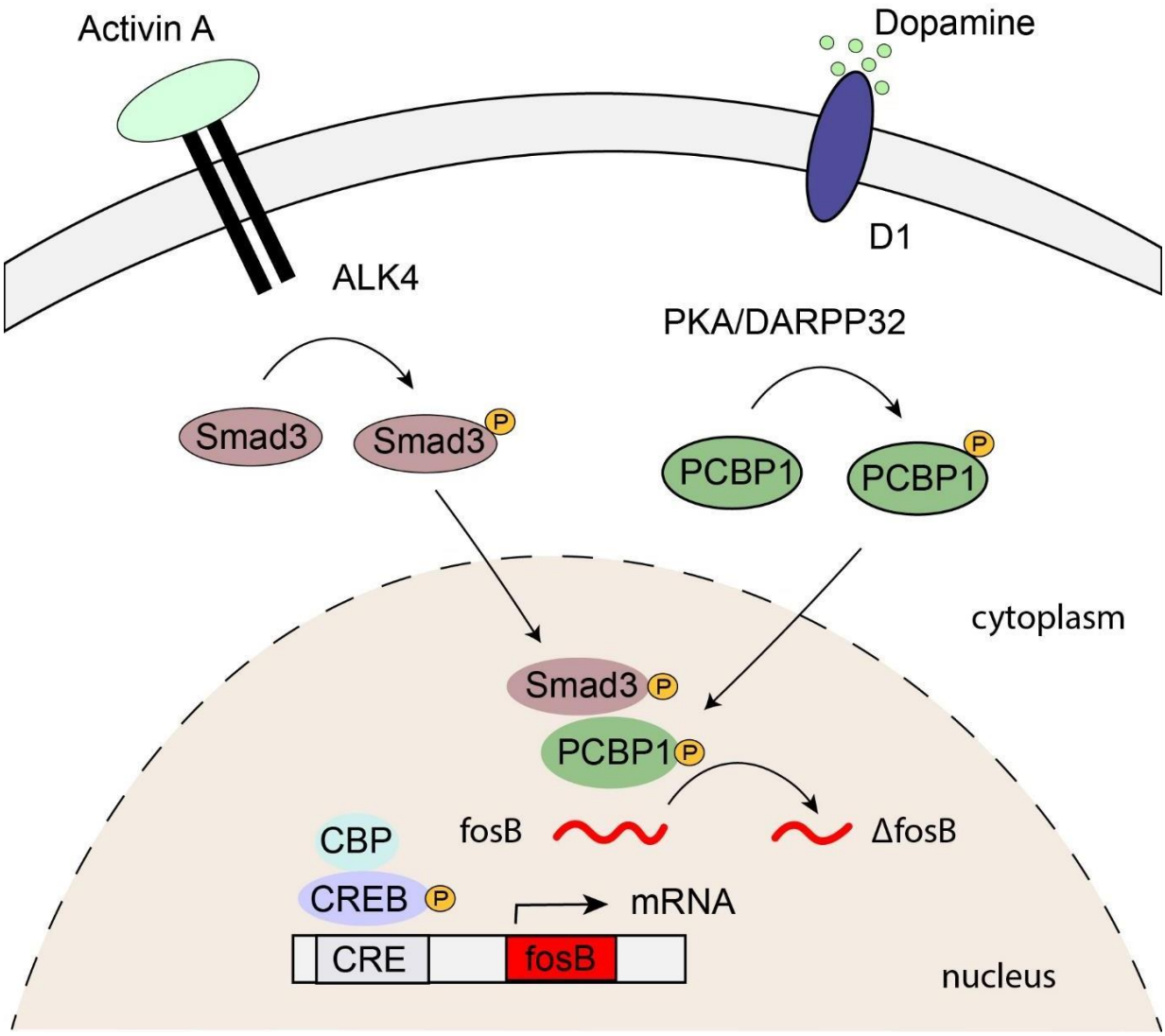

Figure I5: Activin and Dopamine signaling enhance ΔFOSB slicing

by binding directly to its promoter and recruiting histone deacetylase class I (HDAC1) (Renthal et al., 2008). This recruitment results in the deacetylation of nearby histones, leading to a reduction in gene activity. This mechanism is supported by findings showing that the local knockout of HDAC1 in the striatum eliminates amphetamine-induced desensitization of the c-

fos gene (Renthal et al., 2008). Further, ΔFOSB regulates genes for glutamatergic synaptic strength, for example AMPA receptor subunits (M. B. Kelz et al., 1999; Vialou et al., 2010), CaMKIIa (Robison et al., 2013), and cyclin-dependent kinase 5 (CDK5) (Chen et al., 2000). In the nucleus accumbens, ΔFOSB exhibits distinct effects on D1 and D2 medium spiny neurons (MSNs) in response to chronic social defeat stress. Resilient mice accumulate ΔFOSB in D1-MSNs in chronic social defeat, while susceptible mice show ΔFOSB accumulation in D2-MSNs (Lobo et al., 2013). These data align with the outcome observed in optogenetic activation experiments of MSN subtypes during chronic social defeat (Francis et al., 2015). Altogether, the ΔFOSB gene is an important gene expression mediator for repetitive, addictive behavior.

ΔFOSB related to memory (Hippocampus)

Epilepsy is a neurological disorder characterized by repetitive, unprovoked seizures. Seizures are episodes of high electrical activity in the brain, leading to various symptoms such as convulsions, loss of consciousness, unusual behaviors, sensations, or emotions (Shneker & Fountain, 2003). Epilepsy in humans and mice is associated with cognitive decline (Chin & Scharfman, 2013; Minkeviciene et al., 2009; Palop & Mucke, 2009). There is a growing body of evidence suggesting that seizures and epileptiform activity occur also in patients with Alzheimer's disease (AD). A recent study indicates that 42 % of AD patients without a clinical history of seizures displayed subclinical epileptiform activity (Vossel et al., 2016). Furthermore, AD is associated with a significantly elevated risk, up to 10 times higher, of experiencing seizures (Amatniek et al., 2006; Larner, 2010; Lozsadi & Larner, 2006). Similar to the nucleus accumbens, chronic activity leads to accumulation of ΔFOSB in the hippocampus. In the hippocampus, ΔFOSB increases after externally induced electroconvulsive seizures in rats (Chen et al., 2000; Hope, Kelz, et al., 1994) and in several genetic mouse models prone to seizures (Biagini et al., 2005; T.-S. Lee et al., 2021; You et al., 2017). In the dentate gyrus, ΔFOSB levels increase due to spontaneous seizures in a mouse model of Alzheimer’s disease (APP mice) (Corbett et al., 2017). In the dentate gyrus, ΔFOSB recruits HDAC1 to the cFOS

promoter, resulting in the suppression of genes, including cFOS (Corbett et al., 2017) and calbindin (You et al., 2017). The repression of both proteins leads to cognitive deficits and can be restored blocking ΔFOSB signaling via ΔJUND overexpression or treatment with HDAC inhibitors (Corbett et al., 2017; You et al., 2017). Further, ΔFOSB is highly induced in the DG (dentate gyrus) and to a lesser extent in the CA1 region during physiological induced activities like spatial learning and exposure to a novel environment (Eagle et al., 2015). There is evidence that ΔFOSB plays a crucial role in hippocampal-dependent memory by modulating the excitability of pyramidal neurons in both the dorsal and ventral hippocampus (Eagle et al., 2018). A total knockout of the fosb gene increases excitability, increases the risk of seizures, and impairs in spatial memory (Eagle et al., 2020; Yutsudo et al., 2013). Similarly, overexpression of ΔJUND, an inhibitory modulator of the transcriptional action of ΔFOSB, impaired learning and memory in hippocampal-dependent tasks (Eagle et al., 2015). On the neuronal level, the overexpression of ΔFOSB decreases excitability of CA1 pyramidal neurons, while the overexpression of its dominant negative form increases excitability (Eagle et al., 2018). Overexpression of ΔFOSB also increases the number of immature dendritic spines on CA1 pyramidal cells. Conversely, ΔJUND overexpression reduces both immature and mature spine types, indicating an attempt to compensate for the changes in excitability (Eagle et al., 2015). These findings suggest that ΔFOSB expression in response to high or chronic neuronal activity serves as an essential negative feedback mechanism and may be important for homeostatic scaling (Turrigiano et al., 1998).

Regulating Chromatin accessibility via histone modification

Long-term memory formation is based on the interplay between synaptic communication and nuclear signaling (Hagenston & Bading, 2011). Activity-induced signaling cascades, such as those initiated by Ca^{2+} influx, can activate CAMKII, triggering signals that lead to gene transcription (S.-J. R. Lee et al., 2009). The initiation of gene transcription depends on the chromatin state (Klemm et al., 2019). Chromatin accessibility refers to the ease with which

nuclear macromolecules, such as transcription factors and regulatory proteins, can physically interact with DNA, such as promoter or enhancer regions. Closed states involve tightly wound chromatin that allows limited access to the encoded genes although pioneer transcription factors may still access and bind to the DNA. Permissive or primed states are characterized by pre-bound transcription factors and histone modifications, facilitating the relaxation of the chromatin. Finally, open states allow fast access to the transcriptional complex. (Klemm et al., 2019). The histone modification machinery regulates the epigenetic state of a cell by modulating the state of the chromatin in response to stimulus- and time-specific factors. (Klemm et al., 2019). It involves 'writing' enzymes known as histone acetyltransferases (HATs). These enzymes transfer acetyl groups to lysine residues on histones Histone acetyltransferases (HATs) will facilitate the opening of DNA by the addition of acetyl groups to histone proteins. Acetylation neutralizes the positive charge of histones. This reduces their affinity for negatively charged DNA. This modification relaxes the chromatin structure, making the DNA more accessible to the transcriptional machinery. In contrast, 'erasing' enzymes referred to as histone deacetylases (HDACs) remove acetyl residues and cause chromatin condensation. Eleven histone deacetylase (HDAC) proteins have been identified, with distribution in different cellular compartments (X.-J. Yang & Seto, 2008). HDACs found in the nucleus are HDAC1, HDAC2, HDAC3, and HDAC8. Those located in the cytosol are HDAC6 and HDAC10. HDACs distributed in both the nucleus and cytosol are HDAC4, HDAC5, HDAC7, HDAC9, and HDAC11. Additionally, 'reading' enzymes are equipped with bromodomains and responsible for the localization and identification of acetylated lysine residues. This enzymatic machinery contributes to the maintenance of the chromatin state, and can be seen as a regulator of gene transcription (Peixoto & Abel, 2013).

The role of histone acetylation in memory formation

The combination of HDAC inhibitors with different learning paradigms has been shown to increase histone acetylation. Increased hippocampal histone acetylation was observed after

contextual fear conditioning, novel object recognition, and spatial memory tasks (Bousiges et al., 2010; Levenson et al., 2004; Takuma et al., 2014; Villain et al., 2016). In the CA1 region, the acetylation of histone H3 is increased after contextual fear conditioning. (Levenson et al., 2004). In the dentate gyrus, histone acetylation is increased during the phase of consolidation following water maze training. (Bousiges et al., 2010). The exposure to a new environment, significantly increases the level of acetylated histones H3 in the in the dentate gyrus of rats (Chandramohan et al., 2007). On the other hand, reduced histone acetylation was observed in hippocampi associated with pathological conditions with reduced cognitive abilities, such as Alzheimer's disease (AD) (Janczura et al., 2018; Panikker et al., 2018). It was shown, that HDAC inhibitors rescue memory impairment in neurodegenerative diseases (Agís-Balboa et al., 2017; Bowers et al., 2015; Whittle et al., 2016; Wilson et al., 2014). Interestingly, the inhibition of HDACs after learning enhances memory recall (Fischer et al., 2007; Gräff et al., 2014; Kwapis et al., 2017; Levenson et al., 2004; Valiati et al., 2017; Yuan et al., 2015). How HDAC inhibitors improve memory is not fully understood, but it is noteworthy that some HDAC inhibitors can cause unfavorable symptoms such as increased aggression and restlessness. (Herrmann et al., 2007).

Publications

Publication #1: ΔFOSB accumulation in hippocampal granule cells drives cFOS pattern separation during spatial learning

Lamothe-Molina, Paul J.*, **Andreas Franzelin***, Lennart Beck, Dong Li, Lea Auksutat, Tim Fieblinger, Laura Laprell, et al. 2022. “ΔFOSB Accumulation in Hippocampal Granule Cells Drives CFOS Pattern Separation during Spatial Learning.” ***Nature Communications*** 13 (1): 6376.

* these authors contributed equally

This study uses optogenetic inhibition during memory recall in the water maze to investigate the expression of immediate early genes in dentate gyrus. We describe a novel epigenetic mechanism that leads to sparse and changing patterns of cFOS expression during a multi-day learning paradigm.

In order to manipulate active neurons during memory recall we were investigating under which conditions dentate granule cells once cFOS positive, re-express cFOS again. I conducted all the ex-vivo analysis on brain tissue samples obtained from mice that underwent training under various conditions in the water maze. (Fig. 1j, k; Fig. 2f, g; Fig. 3e, j; Fig. S2; Fig. S3; Fig. S5b, c; Fig. S7b; Fig. S8; Fig. S10, Fig. S11, Fig. S12). We observed that dentate granule cells rarely re-expressed cFOS on two consecutive days during water maze training, which was an unexpected result. With the help of the photo-convertible Ca^{2+} indicator CaMPARI2, we could prove that cFOS positive neurons are indeed reactivated during the water maze training on day 2 but do not re-express cFOS. For this experiment I tested antibodies against CaMPAIR2 and analyzed tissue samples from trained and untrained mice (Fig. 4c - e). Based on my suggestion we designed an experiment to investigate the temporal characteristics of cFOS positive ensembles while mice are in their home cage. This experiment was important to show that the inability to re-express cFOS is an intrinsic feature of dentate granule cells and not unique to neurons that expressed cFOS in the water maze. I was responsible for the design and the analysis of the experiment. (Fig. 5b – g, also Fig. S1d-h). We therefore learned that cFOS is not consistently expressed in response to neural activity. I identified ΔFOSB as a potential candidate for the underlying mechanism of cFOS repression after an extensive literature search. I then helped design, and performed all ex-vivo analysis using anti- ΔFOSB antibodies (Fig. 6). I also designed and performed the experiments in Fig. 7, where I learned that DG neurons are particularly resistant to FOS re-expression. I also helped design the water

maze experiments in Fig. 8 and performed the analysis (Fig. 8a - c). I also helped write the manuscript, and created the figures showing the data I collected and analyzed.

nature communications

Article

https://doi.org/10.1038/s41467-022-33947-w

ΔFosB accumulation in hippocampal granule cells drives cFos pattern separation during spatial learning

Received: 9 September 2020

Accepted: 7 October 2022

Published online: 26 October 2022

Check for updates

Paul J. Lamothe-Molina[1,6], Andreas Franzelin[1,6], Lennart Beck[1], Dong Li[2], Lea Auksutat[3], Tim Fieblinger[1], Laura Laprell[1], Joachim Alhbeck[4], Christine E. Gee[1], Matthias Kneussel[5], Andreas K. Engel[4], Claus C. Hilgetag[2], Fabio Morellini[3,7] & Thomas G. Oertner[1,7]

Mice display signs of fear when neurons that express cFos during fear conditioning are artificially reactivated. This finding gave rise to the notion that cFos marks neurons that encode specific memories. Here we show that cFos expression patterns in the mouse dentate gyrus (DG) change dramatically from day to day in a water maze spatial learning paradigm, regardless of training level. Optogenetic inhibition of neurons that expressed cFos on the first training day affected performance days later, suggesting that these neurons continue to be important for spatial memory recall. The mechanism preventing repeated cFos expression in DG granule cells involves accumulation of ΔFosB, a long-lived splice variant of FosB. CA1 neurons, in contrast, repeatedly expressed cFos. Thus, cFos-expressing granule cells may encode new features being added to the internal representation during the last training session. This form of timestamping is thought to be required for the formation of episodic memories.

Adaptive decision making requires an accurate memory of past events. For instance, a mouse should revisit locations where it has found food before and avoid dangerous places. The hippocampus is well-known for processing spatial information[1,2] but it also processes other types of sensory input and organizes sequential elements of experience into episodic memories[3–5]. Our understanding of how time is represented in the hippocampus is incomplete. The expression of many genes affecting synaptic plasticity undergoes pronounced circadian oscillations, changing the rules of synaptic plasticity depending on the time of day[6]. Theoretical and empirical work suggests that the dentate gyrus (DG) actively reduces the overlap between activity patterns from the entorhinal cortex, a process dubbed pattern separation[7–9]. In vivo electrophysiology and calcium imaging experiments revealed that the majority of the granule cells (GCs) in the DG are silent, and of the active cells, just a small fraction show spatial tuning (place cells)[10–12]. Spatially tuned GCs provide a stable, albeit coarse representation of the global environment across time[10,13–15]. These findings highlight an apparent design conflict: while a perfect 'episode encoder' should avoid using the same neurons on consecutive days, accurate place coding is thought to require stable place cells that signal the animal's position in a given environment. In view of this conundrum, we set out to study the impact of time and space on GCs in the dorsal DG.

[1]Institute for Synaptic Physiology, Center for Molecular Neurobiology (ZMNH), University Medical Center Hamburg-Eppendorf, Hamburg, Germany. [2]Institute of Computational Neuroscience, University Medical Center Hamburg-Eppendorf, Hamburg, Germany. [3]Research Group Behavioral Biology, Center for Molecular Neurobiology (ZMNH), University Medical Center Hamburg-Eppendorf, Hamburg, Germany. [4]Department of Neurophysiology and Pathophysiology, Center for Experimental Medicine (ZEM), University Medical Center Hamburg-Eppendorf, Hamburg, Germany. [5]Institute for Molecular Neurogenetics, Center for Molecular Neurobiology (ZMNH), University Medical Center Hamburg-Eppendorf, Hamburg, Germany. [6]These authors contributed equally: Paul J. Lamothe-Molina, Andreas Franzelin. [7]These authors jointly supervised this work: Fabio Morellini, Thomas G. Oertner. e-mail: paul@lamothe.de; thomas.oertner@zmnh.uni-hamburg.de

To monitor and manipulate neuronal activity in freely behaving animals, reporter mice have been developed that use the immediate-early gene cFos[16] to drive the expression of fluorescent proteins and optogenetic actuators[17]. Fear conditioning experiments with an activity-dependent expression of optogenetic silencing tools suggest that recall of a fearful episode requires reactivation of the original encoding ensemble[18–20]. Vice versa, artificial reactivation of the encoding ensemble has been shown to reinstate a fearful state[19,21,22], suggesting that memories can be activated by specific subsets of hippocampal neurons. When freezing is used as a proxy to assess the emotional state of the animal, it is difficult to determine whether, during the optogenetic reactivation, the animal recalls the fear-inducing episode (engram) or simply feels fear. The reactivated ensemble may form an internal representation of the external world (cognitive map theory[23,24]) or trigger the pattern of cortical activity that was active in the previous experience (indexing theory[25]).

We investigated the temporal stability of DG cFos ensembles and their relation to spatial learning and the formation of cognitive maps. We used cFos-dependent tagging to assess how cFos ensemble overlap changes over training days in the Morris water maze (WM). Even in expert mice, cFos expression patterns in DG changed from day to day. In spite of these changing expression patterns, optogenetic inhibition of cFos-tagged GCs impaired navigation 5 days after tagging, suggesting that the absence of cFos expression in these GCs did not imply the absence of activity. We show in vivo and in vitro that cFos$^+$ GCs accumulate ΔFosB, a long-lived splice variant of FosB. As this splice variant inhibits cFos expression[26], it provides a potential mechanism for the daily shift of cFos ensembles that occurs even when mice are exposed to the same environment. The changing pattern of cFos expression in DG could be the basis of an episodic memory system that write-protects synapses on the most recently used subset of GCs during the following days.

Results

Spatial learning and cFos ensemble overlap in the DG: novice vs expert mice

Although cFos expression is considered a proxy of neuronal activity[27–29], the relationships between action potential firing, immediate-early gene expression, and synaptic long-term plasticity are not obvious[30]. We chose a spatial learning paradigm, the Morris WM, to investigate cFos expression patterns in DG during learning. TetTag mice were trained to find a hidden platform in the WM (Fig. 1a–c). We labeled cFos ensembles from two consecutive days (Fig. 1d). The window for labeling the first cFos ensemble was opened by taking the mouse off doxycycline (Dox), allowing for long-term expression of the fluorescent protein mKate2 fused to an opsin for membrane labeling (cFos-tagged, Fig. 1d). A short half-life version of the green fluorescent protein (shEGFP) works as an in-built cFos reporter in the TetTag mouse to label the second cFos$^+$ ensemble. In calibration experiments, we observed slightly faster temporal dynamics of the native cFos protein than of the shEGFP reporter, yet nearly all shEGFP-expressing neurons also expressed cFos (Supplementary Fig. 1). The highest correlation between native cFos and shEGFP was obtained 2–4 h after stimulation. We, therefore, chose 3 h after the last training trial as the time point to sacrifice mice and fix the brains. The first cFos-tagged ensemble was revealed by immunofluorescence (IF) staining against mKate2 and the second cFos-expressing ensemble was revealed by staining against the shEGFP (cFos$^+$). The ensemble sizes (proportion of GCs cFos-tagged and cFos$^+$, Supplementary Fig. 2) were used to calculate the amount of overlap (GCs that are both cFos-tagged and cFos$^+$) expected due to chance for each sample and compared to the actual overlap (number of cFos-tagged cFos$^+$ GCs).

During probe trials, mice early in training (ET, Fig. 1b, c, e, f) were less precise and accurate while searching for the target but within 5 days became experts (overtrained group, OT, Fig. 1b, c, g, h). Not only the time spent searching in an annulus around the hidden platform increased (Fig. 1f, h) but also the distance to the platform was significantly lower in the expert mice (Fig. 1i). Our expectation was that, if cFos expression is linked to the activity of the neurons that are important for solving the WM task, there would be a high degree of overlap between the cFos$^+$ and the cFos-tagged neurons, which were labeled 1 day earlier. We also expected overlap to increase with increasing search accuracy in the probe trials. Instead, we observed that very few GCs expressed both mKate2 (cFos-tagged) and shEGFP (cFos$^+$) and that both overlap (ET 9% and OT 7% Fig. 1e, g, j) and ensemble sizes were similar in novices and expert mice (Supplementary Fig. 2). In both ET and OT mice the observed overlap was, however, significantly higher than expected due to chance (Fig. 1j, k, Supplementary Fig. 2). Surprisingly, there was no difference between the novices and experts and, assuming that cFos indicates the active GCs, less than 90% of the neurons that expressed cFos the first day were reactivated the following day. Thus, in the DG cFos overlap in GCs on consecutive days of WM training is low and independent of spatial search accuracy.

Effect of novelty on cFos ensembles: reversal training vs novel environment

We next tested whether changing the position of the escape platform (reversal training) would decrease cFos ensemble overlap. The first cFos ensemble was labeled in expert mice on day 5 of WM training (OFF Dox Fig. 2a). The following day, these mice were trained (ON-Dox) with the platform on the opposite side of the tank (reversal training, RT). Reversal training with the new platform position had no effect on cFos overlap (9%, Fig. 2a; compare with ET and OT groups, Fig. 1e, g), although it dramatically decreased search accuracy during the day 6 probe trials (Fig. 2b). The mice now searched equally in both E and W annuli, further suggesting that cFos overlap in DG GCs is a poor indicator of performance.

Given that after reversal training, the overlap was still higher than expected (Fig. 2f), we tested whether overlap of cFos ensembles is specific to the WM. The overlap was reduced to 4% and no longer above chance when cFos-tagged ensemble on day 1 of WM training was compared with the cFos+ ensemble generated while mice explored an open field for 20 min (Fig. 2c, d, f, novel environment NE). Likewise, cFos overlap was only 2% if mice were kept in their home cages (Fig. 2e, f home cage HC) for the 24 h OFF Dox, as in the other groups, and mice were sacrificed the following day. The cFos overlap of all groups trained in the WM (the ET, OT, and RT mice) were not significantly different from each other but significantly higher than expected due to chance whereas in both NE and HC groups, cFos overlap was at chance level and significantly lower than the WM groups (Fig. 2f, Supplementary Fig. 2). Despite ensemble sizes being the same in all conditions except the home cage, the intensity of shEGFP was higher in all groups WM trained on the second day (Fig. 2g, Supplementary Fig. 2). Thus, DG cFos expression and overlap are strongly driven in the WM regardless of training level (ET vs OT) or difficulty of the task (OT vs RT), consistent with the concept that the hippocampus is highly engaged in spatial navigation tasks and that very different environments activate non-overlapping ensembles.

cFos$^+$ neurons in DG participate in spatial memory recall days later

Lesion[31,32] and optogenetic manipulation[33–36] experiments indicate that the DG plays a role in spatial memory acquisition and recall. However, those experiments did not address if particular memories are encoded by a specific subset or ensemble of neurons in the DG (engram cells). We speculated that cFos$^+$ cells in the DG may encode relevant information needed to solve the WM task. To test their importance during platform search, we employed a bidirectional optogenetic tool that can be used to inhibit or excite neurons with 473 and 594 nm light,

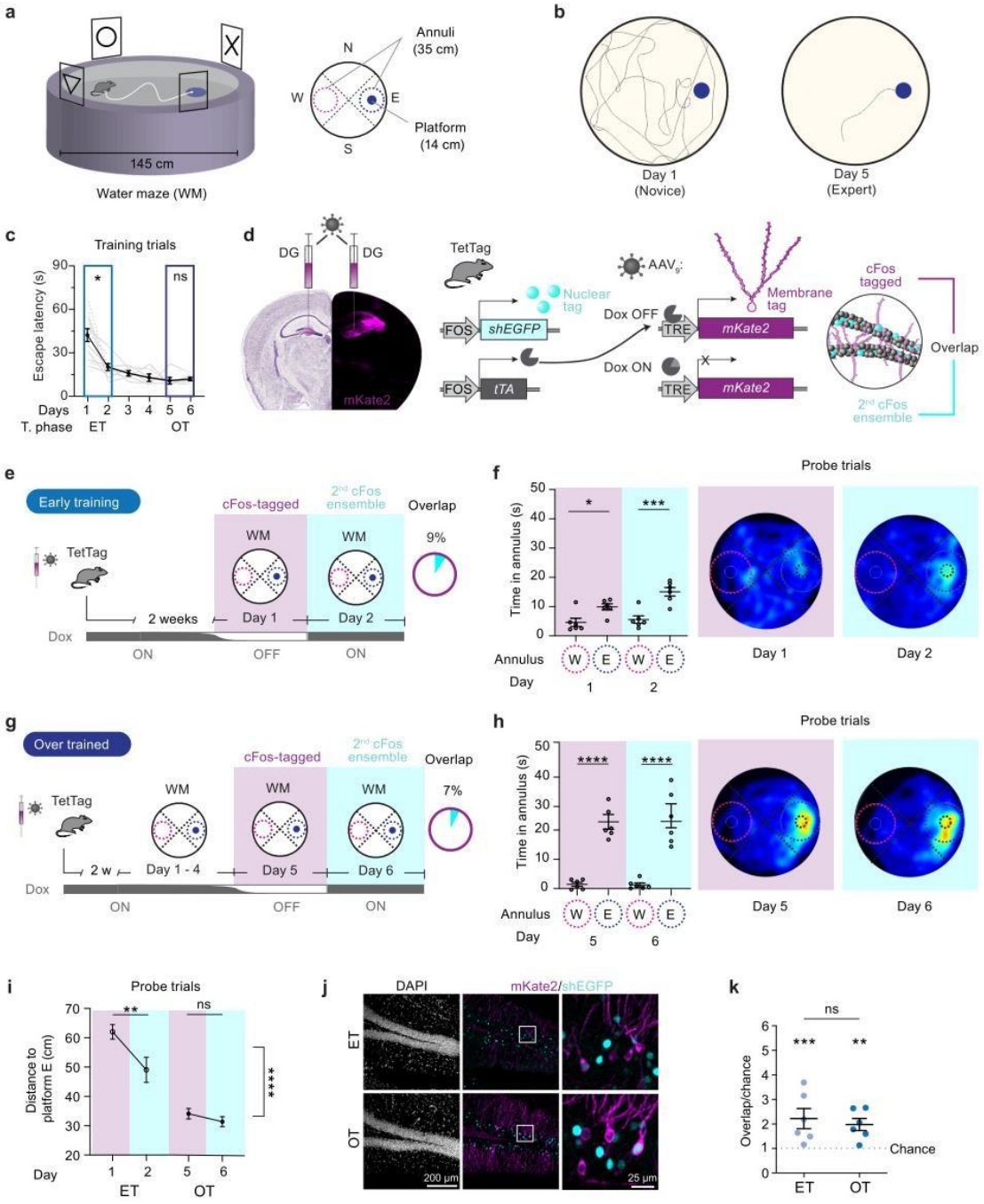

respectively (BiPOLES[37]). We expressed BiPOLES under the control of the non-leaky TRE3G promoter (Supplementary Fig. 3) and confirmed that 473 nm light prevented action potentials in BIPOLES-expressing GCs while 594 nm light pulses repeated at 20 Hz reliably elicited single action potentials (Supplementary Fig. 4). For in vivo experiments, mice were bilaterally injected in DG with $AAV_{PHP.eB}$-TRE3G-*BiPOLES-mKate2* and implanted with a custom-made tapered fiber implant[38] (Fig. 3a). To perform optogenetic experiments in the WM, we had to ensure that the weight of the optical fibers was compensated when mice were tethered to them via their implants. We achieved this by attaching a helium balloon to the optical fibers (Fig. 3a). Implanted mice were trained without being tethered and successfully learned the WM task (Fig. 3b). Tethering to the weight-balanced optical fibers did not affect swimming speed (Fig. 3c), nor did 473 or 594 nm light (Fig. 3d).

To investigate the importance of day 1 cFos-tagged neurons on memory recall, we silenced BiPOLES-expressing neurons during

Fig. 1 | Behavioral performance in a spatial memory task is not reflected by cFos ensemble overlap in the DG. a Water maze (WM) with the platform in east quadrant (E). Virtual 35 cm diameter annuli for spatial accuracy analysis (E vs W). **b** Exemplary mouse swim paths during training trials. **c** WM learning (escape latency) over 6 training days (black line: average of all mice. days 1–2, $n = 12$; days 3–6, $n = 6$). Note the rapid learning during early training (ET, $n = 6$ mice, $^{*}p = 0.02$) and lack of improvement when overtrained (OT, $n = 6$ mice, $n = 0.98$). Mixed effects model with Šídák's multiple comparisons test. **d** Tagging method. In TetTag mice injected with AAV-TRE-*mKate2*, cFos+ granule cells (GC) express mKate2 in the absence of Doxycycline (Dox), resulting in permanent fluorescence (cFos-tagged, magenta). Left hemisphere: Nissl from the Allen Reference Atlas[70]. Nuclear fluorescence identifies recent cFos expression (2nd ensemble, shEGFP, cyan). Overlap is the fraction of mKate2^{+} neurons expressing shEGFP. **e** Experimental timeline for ET mice and cFos overlap. **f** Time spent in annuli in probe trials on day 1 and 2 (ET mice). Heatmaps show average swim paths during probe trials ($n = 6$ mice, $^{*}p = 0.03$, $^{***}p = 0.001$). **g** Experimental timeline for OT mice and cFos overlap. **h** Time spent in annuli in probe trials on day 5 and 6. Heatmaps show average swim paths during probe trials ($n = 6$ mice, $^{****}p < 0.0001$). **i** Spatial search accuracy (distance to platform E) was significantly higher in the OT than in the ET group ($^{****}p < 0.0001$). Only ET mice improved their spatial accuracy between tagging days (ET group: $^{**}p = 0.004$; OT group: ns $p = 0.65$). **f**, **h**, **i** Symbols represent individual mice, lines represent mean ±SEM. Matched two-way-ANOVA with Šídák's multiple comparisons test. **j** Immunofluorescence images for cFos overlap analysis. **k** cFos overlap significantly higher than chance: ET: $^{***}p = 0.0008$, OT: $^{**}p = 0.003$, see Supplementary Fig. 2) but similar in both groups ($p = 0.99$, ordinary one-way-ANOVA with Šídák's multiple comparisons test). Data are presented as mean ±SEM. Complete statistical information in Supplementary Table 1. Source data are provided as a Source Data file.

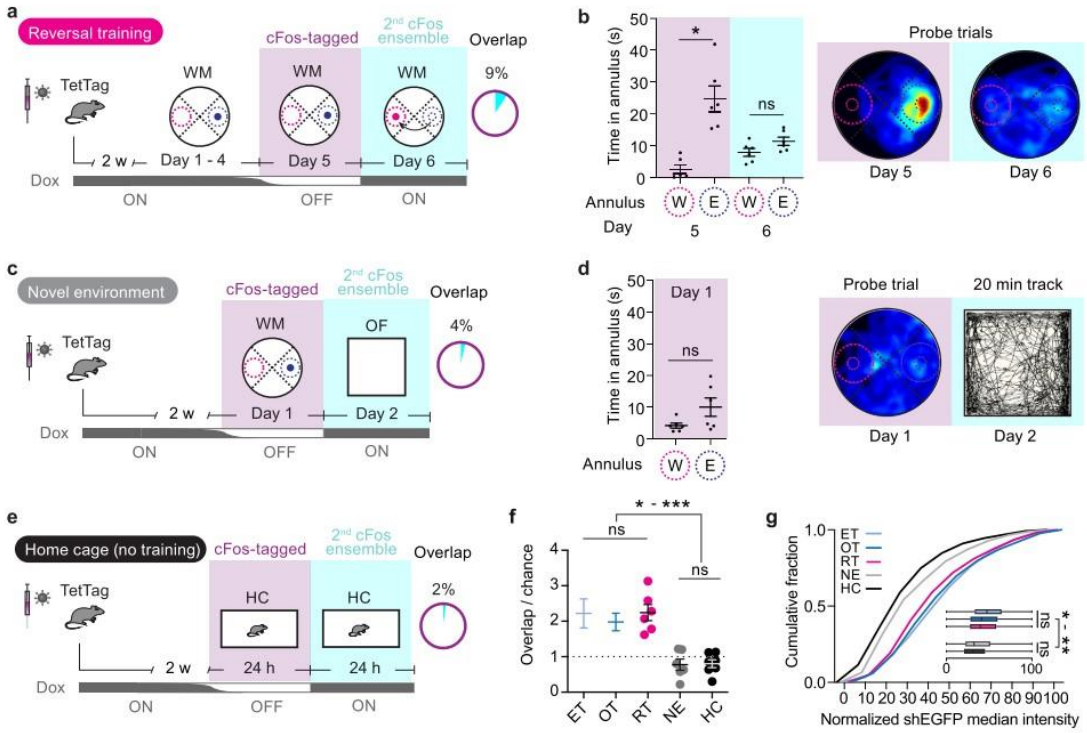

Fig. 2 | Effects of task and environment on cFos ensemble overlap. **a** Experimental timeline for reversal training (RT) group ($n = 6$ mice) and cFos overlap. Note that the platform position was changed to the opposite quadrant (W) on day 6. **b** Time spent in annuli in probe trials on day 5 and 6 of RT mice. Heatmap showing average swim paths during probe trials. Note that despite the strong preference for E annulus on day 5 ($n = 6$ mice, $^{*}p = 0.01$), after only 1 reversal training session, mice searched equally around the new and the old platform position during a probe trial on day 6 (ns, $p = 0.72$). Matched two-way-ANOVA with Šídák's multiple comparisons test. **c** Experimental timeline for novel environment (NE) group and cFos overlap. Note that mice visit an unfamiliar open field (OF) arena on day 2. **d** Time NE mice spent in annuli during day 1 probe trial shows no significant preference for E annulus ($n = 6$ mice, $p = 0.16$, two-sided, paired t test). Heatmap shows average swim paths during probe trial on day 1. Exemplary track of one mouse during OF exploration on day 2. **b**, **d** Symbols represent individual mice, lines represent mean ±SEM. **e** Experimental timeline for home-caged (HC) control mice and cFos overlap. **f** cFos ensemble overlap/chance in the different experimental groups (ET early training from Fig. 1i; OT, overtrained from Fig. 1i; RT reversal training, NE novel environment, HC home cage). cFos overlap in the RT group is higher than expected by chance ($n = 6$ mice, $^{***}p = 0.0006$, matched two-way-ANOVA with Šídák's multiple comparisons test, see Supplementary Fig. 2). All WM-trained groups showed higher cFos overlap than the NE and HC groups (p values in supplementary table 1), but no difference between each other. Symbols represent individual mice, lines represent mean ±SEM. **g** cFos expression (normalized shEGFP median intensity) was significantly higher in mice that visited the WM than mice that visited an OF arena (NE group) or control mice (HC group) (p values in Supplementary table 1). Source data are provided as a Source Data file.

probe trials on days 2, 3, and 5 (Fig. 3f). Mice were placed on an elevated Atlantis platform that submerged after 30 s, forcing the mice to swim[39]. After 60 s, a second Atlantis platform (in quadrant E) was elevated, and mice were directed towards it if they did not find it themselves. We assessed memory performance in the first half of the probe trials (30 s). Optogenetic inhibition did not affect time spent in the target quadrant on days 2 and 3 when mice were novices and their spatial accuracy was still poor (Fig. 3g). On day 5, when mice were experts and spatial accuracy was high, optogenetic inhibition significantly decreased time spent in the target

https://doi.org/10.1038/s41467-022-33947-w

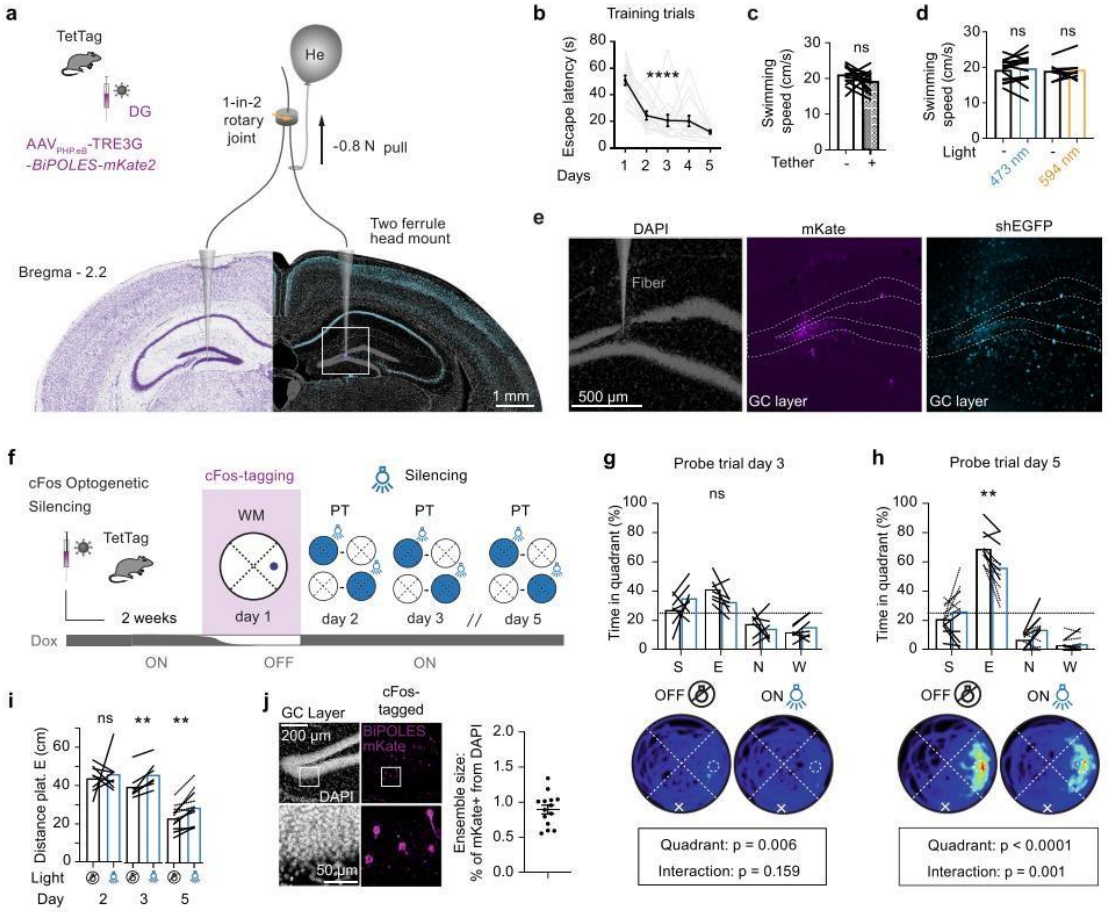

Fig. 3 | Optogenetic silencing of cFos-tagged granule cells impairs spatial memory recall. a TetTag mice were injected with AAV for cFos-dependent expression of BiPOLES and fluorescent label (mKate2, magenta). Mice were bilaterally tethered with ultra-thin light fibers targeting the granule cell (GC) layer of the dentate gyrus[70]. **b** Fibers and implant did not affect learning (gray lines: $n = 15$ mice; black: mean ±SEM; $^{****}p < 0.0001$, ordinary one-way-ANOVA for repeated measures). **c** Swimming speed of tethered mice with balloons was not different from the same animals in untethered trials ($n = 15$ mice, $p = 0.12$, two-sided paired t test). **d** Optogenetic inhibition (473 nm) or excitation (596 nm) did not affect swimming speed (473 nm light, $n = 15$ mice, $p = 0.53$, two-sided paired t test) (594 nm light, $n = 8$ mice, $p = 0.74$, paired t test). **e** Tapered fiber caused minimal damage in DG. **f** On days 2, 3, and 5 of water maze training, the cFos-tagged ensemble from day 1 was inhibited (blue shading) in one of two tethered probe trials. **g** On day 3, probe trial optogenetic inhibition had no significant effect on the time spent in the target quadrant ($p = 0.35$, matched two-way-ANOVA with Šídák's multiple comparisons test). Heatmaps show average swim paths during probe trials. White 'x' indicates starting Atlantis platform location, dashed circle indicates the location of target Atlantis platform. **h** On day 5, probe trial optogenetic inhibition significantly decreased the time spent in the target quadrant (Light x Quadrant interaction $^{***}p = 0.001$; light effect $^{**}p = 0.0025$). Similar results were obtained in two batches of mice (solid/dotted lines). **i** Optogenetic inhibition increased the average distance from the target platform location on days 3 and 5, but not on day 2 (two-sided, paired t test: day 3 $^{**}p = 0.004$, Day 5 $^{**}p = 0.002$). **j** After the behavioral experiments, the expression of BiPOLES was verified in 14 of 15 animals ($n = 14$ mice, mean ±SEM). **c**, **d**, **g**–**i** Lines show individual mice, bars show mean. Complete statistical information in Supplementary Table 1. Source data are provided as a Source Data file.

quadrant (Fig. 3h, Supplementary Video 1). The mean distance to the target platform confirmed the results of the quadrant analysis, detecting significant effects of optogenetic inhibition on days 3 and 5 (Fig. 3i). We confirmed that GCs still expressed BiPOLES even 9 days after tagging (Fig. 3j). These results suggest that activity in the small ensemble of cFos-tagged neurons from the first training day (~2% of GCs) is important for successful memory recall on subsequent days. BiPOLES can also be used to increase the activity of tagged neurons (Supplementary Fig. 4). However, artificial firing (20 Hz optogenetic stimulation) during day 6 probe trials had no significant effect on WM performance in expert mice (Supplementary Fig. 5).

To address whether the activity of cFos-tagged cells is of particular importance for WM navigation or if inhibition of a random group of GCs would suffice to decrease performance, we used a chemogenetic inhibition strategy that is not dependent on cFos (Supplementary Fig. 6). The proportion of hM4Di-mCherry expressing neurons in the DG determined whether chemogenetic silencing disrupted memory recall ($R^2 = 0.67$, $p = 0.003$, Supplementary Fig. 6). Silencing of ~30% of GCs was required to decrease WM performance, a much higher fraction compared to cFos-dependent optogenetic silencing, suggesting that GCs expressing cFos on training day 1 remain important for successful spatial navigation in the WM many days later. If cFos-tagged cells from day 1 are indeed highly active on consecutive WM days, this

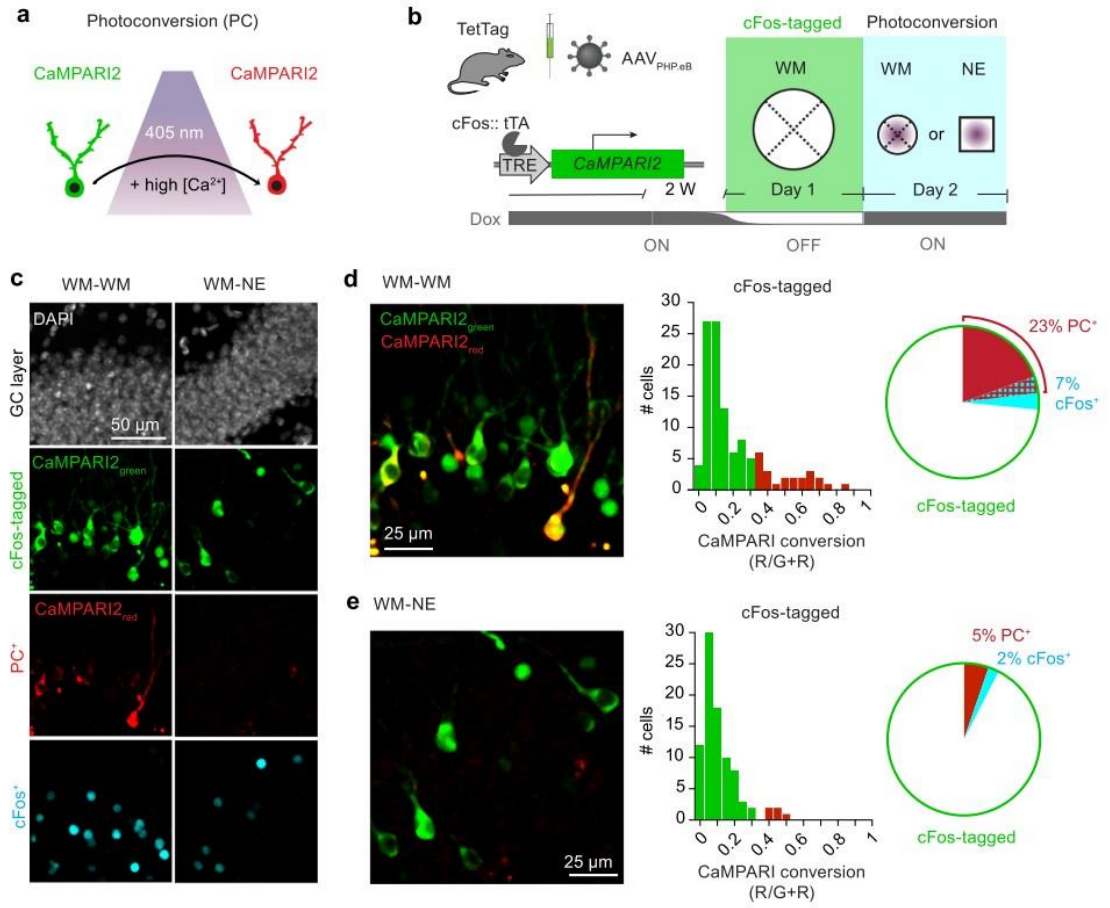

Fig. 4 | cFos-tagged dentate granule cells are reactivated during water maze training. a The calcium integrator CaMPARI2 is photoconverted by 405 nm light (violet shading) only in neurons with high intracellular Ca^{2+}. **b** Experimental timeline: TetTag mice were injected with $AAV_{PHP.eB}$-TRE-*CaMPARI2* and trained in the WM OFF Dox (day 1, cFos tagging, green shading). On day 2, photoconversion light was applied to the DG during WM training or in a novel environment (NE, open field). **c** Confocal images of DG. Gray is DAPI staining, green is cFos-dependent CaMPARI2 expression, red is immunostaining against photoconverted CaMPARI2 (PC^+), cyan is shEGFP immunostaining ($cFos^+$) performed 90 min after the last trial. Note: CaMPARI2 is expressed throughout the cytosol, green nuclear signal is the native shEGFP cFos reporter protein from the TetTag mice. **d**, **e** Analysis of CaMPARI2 conversion. Left: Merged images of CaMPARI2 (green) and photoconverted CaMPARI2 (red). Histogram: red bars indicate photoconverted neurons (ratio >0.3). Pie charts indicate % of cFos-tagged (CaMPARI2 expressing) neurons that were photoconverted (red, PC^+), $cFos^+$ (cyan), or both (red hatched). **d** Day 1 and day 2 in water maze (WM-WM, $n = 113$ cells, 2 mice). **e** Day 1 WM day 2 novel environment (WM-NE $n = 100$ cells, 2 mice). Source data are provided as a Source Data file.

activity should generate intracellular calcium transients. To generate a lasting record of calcium concentrations during behavior, we tagged $cFos^+$ GCs with calcium-dependent photoconvertible CaMPARI2[40] on training day 1 and applied photoconversion light via implanted optical fibers either during all WM training trials on day 2 (WM–WM) or during the same amount of time in a novel environment (WM–NE, Fig. 4a, b). In order to estimate the volume of tissue that can be photoconverted by 405 nm light, we tagged cFos+ GCs with CaMPARI2 together with an opsin that is activated by PC light, resulting in strong photoconversion of cells up to 300 µm from the tapered fiber tip (Supplementary Fig. 7). Based on these tests, we restricted our analysis to GCs within 200 µm of the fiber tip to assess calcium levels during behavior. During WM training on day 2, photoconversion occurred in 23% of the cFos-tagged GCs, indicating a high degree of functional reactivation (Fig. 4d). This reactivation was context-specific, as only 5% cFos-tagged GCs were photoconverted during exploration of a novel environment (Fig. 4e)[41]. We also analyzed cFos expression on day 2 in the cFos-tagged cells. As expected from our previous experiments (Figs. 1 and 2), cFos overlap was higher in the WM-WM group (7%, Fig. 4d) than in the WM-NE group (2%, Fig. 4e). Interestingly, even in the WM-WM group, 85% of photoconverted (and thus reactivated) GCs did not express cFos again, confirming our suspicion that cFos expression is not a good proxy for GC activity.

Temporal dynamics of cFos ensembles

An engram cell, by definition, is a cell that is active during both the encoding event and during memory retrieval[17]. Many studies used cFos expression as a surrogate marker of neuronal activity, but our WM experiments suggest that the underlying assumption may be wrong. In our experiments, cFos overlap was about 9% when mice revisited the WM arena on consecutive days ($\Delta t = 1$ days). Would these GCs continue to activate cFos on the following days of WM training? To evaluate longer time intervals, we trained the mice exactly as the RT group (highest overlap) but tagged GCs on day 1 and sacrificed the mice on

https://doi.org/10.1038/s41467-022-33947-w

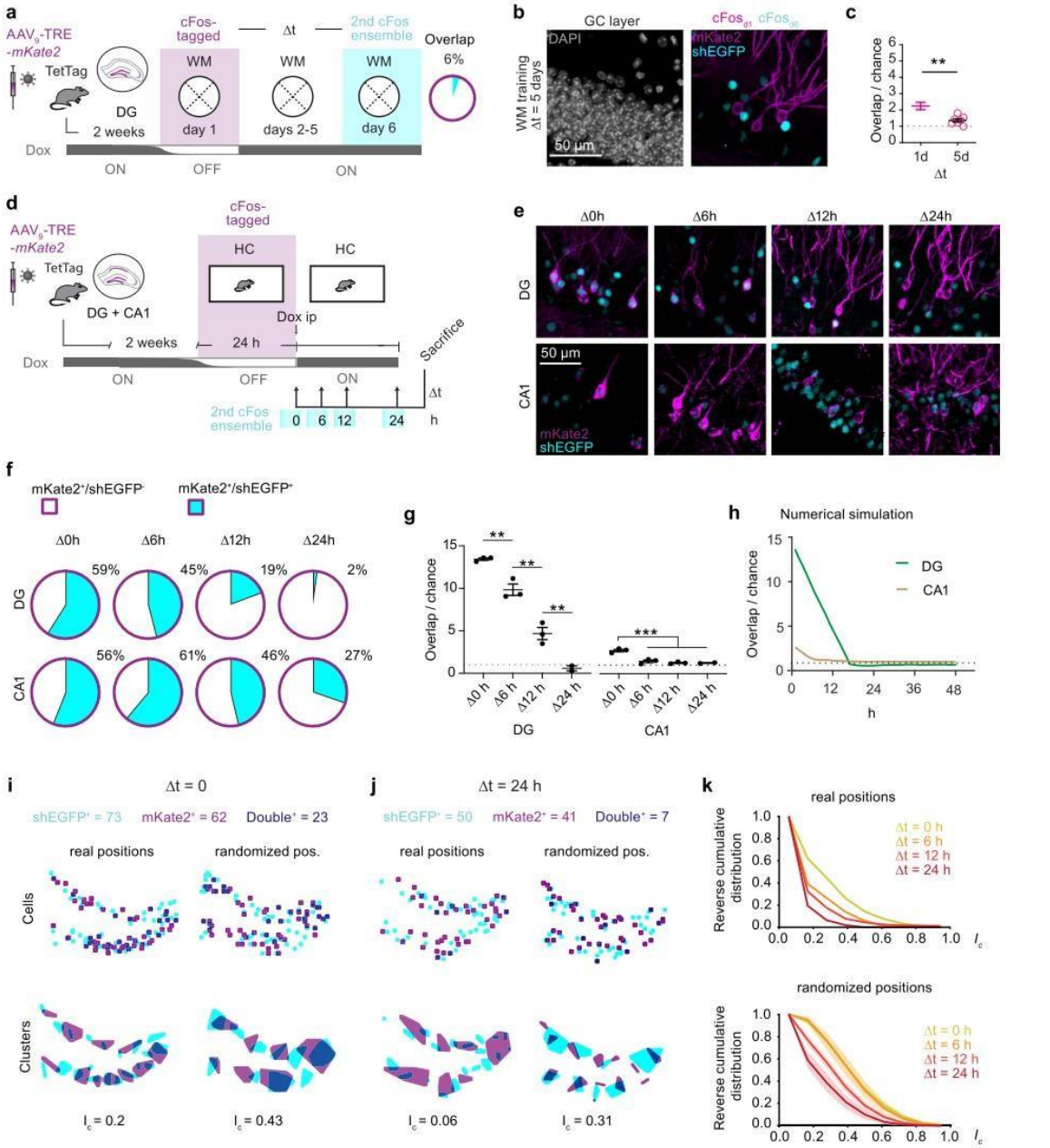

Fig. 5 | Temporal dynamics of cFos overlap in dentate gyrus. a Experimental timeline and cFos overlap. TetTag mice were injected with AAV_9-TRE-*mKate2* in dentate gyrus (DG) to tag cFos$^+$ neurons on training day 1 (magenta shading, $cFos_{d1}$). They were trained for 6 days and sacrificed for shEGFP immunostaining (cyan shading, $cFos_{d6}$). **b** Immunofluorescence example images from the granule cell (GC) layer showing low overlap between $cFos_{d1}$ (magenta) and $cFos_{d6}$ (cyan). **c** After 5 days of WM training, cFos overlap was not significantly different from chance ($n = 7$ mice, two-way-ANOVA, $p = 0.11$, see Supplementary Figure 2) and significantly lower (**$p = 0.003$, two-sided, unpaired t test) than after 1 day of WM training (RT group, data from Fig. 2d). **d** Home cage experiment. TetTag mice were injected AAV injected with AAV_9-TRE-*mKate2* in DG and CA1 regions. Dox was removed to tag cFos neurons while mice were in their home cage (HC). Mice were sacrificed at different time points after Dox injection. **e** IF staining of cFos-tagged and shEGFP (cFos$^+$) neurons in DG and CA1. **f** Fractions of cFos-tagged cells that remained cFos-positive for different time intervals Δt (mean values, three mice per group). **g** Detected cFos overlap normalized to the expected overlap for random expression (dotted line: chance level) in DG and CA1 ($n = 3$ mice per group, mean ± SEM, ordinary one-way-ANOVA with Šídák's multiple comparisons test). See Supplementary Table 1 for full statistical information. **h** Numerical simulation of cFos expression with negative feedback (green curve) reproduces linear drop in cFos pattern similarity found in DG. CA1 simulation without negative feedback (brown curve) does not drop below 1 (chance level). **i** Clusters of cFos$^+$ cells have less overlap (I_c) than expected by chance (randomized cell positions) at $\Delta t = 0$. **j** At $\Delta t = 24$ h, cluster overlap has further decreased. **k** Cluster overlap (I_c) drops with increasing Δt. Clusters of real cellular positions (top panel) overlap less than expected by chance (randomized cell positions, bottom panel). Source data are provided as a Source Data file.

day 6 ($\Delta t = 5$ days, Fig. 2a). In contrast to the $RT_{\Delta t=1}$, cFos overlap in the $RT_{\Delta t=5}$ was significantly lower and not different from overlap expected by chance (Fig. 5a–c, Supplementary Fig. 2). Thus, the cFos ensemble tagged in DG on the first day of WM training is not stable over multiple training days, but the neurons remain relevant for spatial memory retrieval (Figs. 3g–i, 4e).

We next explored the dynamics of cFos patterns in untrained mice, tagging cFos$^+$ neurons in DG and CA1 in the home cage. Two weeks after injecting both regions of TetTag mice with AAV_9-TRE-*mKate2*, mice were taken OFF Dox for a 24 h period and either immediately sacrificed, or given an i.p. Dox injection to rapidly close the tagging window and sacrificed after 6, 12, or 24 h (Fig. 5d). Overlap between cFos-tagged (mKate2$^+$) and cFos$^+$ (shEGFP$^+$) neurons was highest at the end of the OFF Dox window in both DG (59%) and CA1 (56%, Fig. 5e, f). During the next 24 h, the overlap dropped to 2% in DG but only to 27% in CA1, indicating different temporal dynamics of cFos expression in the two areas (Fig. 5e, f). In the DG the overlap at Δ0h was 12-fold higher than expected due to chance and fell below-chance level within 24 h (Fig. 4g). CA1 cFos ensembles were larger (Supplementary Fig. 2), increasing the expected overlap due to chance. At Δ0h overlap in CA1 was significantly higher than expected by chance but within 6 h was at chance levels (Fig. 4g). The very linear drop of ensemble similarity in DG was initially surprising (Fig. 4g), but could be readily reproduced in a numerical simulation of a negative feedback loop, including the below-chance overlap at $\Delta t = 24$ h (Fig. 4h). As the shEGFP reporter is more stable than cFos itself, endogenous cFos expression might change somewhat faster. These results indicate that in a stable environment and without training (i.e., home cage), the default mechanism is for DG GCs to shift cFos expression to a completely new ensemble every day.

cFos-expressing GCs form spatial clusters that segregate over time

The sparse activity of GCs is controlled by robust inhibitory inputs from hilar interneurons[42]. We were interested in the spatial patterns of cFos-expressing GCs, which may not be randomly distributed, but could instead reflect the sphere of influence of individual interneurons. We used the maps generated in the home cage experiments (Fig. 5d) to analyze clusters of cFos$^+$ neurons at the different time points (Fig. 5i, j). As a measure of cluster overlap I_c, we divided the overlapping area by the union of both areas (see methods). While at $\Delta t = 0$, clusters were partially overlapping (high I_c), cluster overlap gradually decreased with time to very low values at $\Delta t = 24$ h (Fig. 5k). This result was not simply a consequence of the decreasing number of double-positive neurons because randomizing the positions of single- and double-positive neurons within the GC layer yielded clusters with higher overlap and less segregation over time. We conclude that the process of temporal segregation we describe here not only plays out in individual GCs, but also prevents the re-use of DG regions that were highly active 24 h ago.

GCs possess an intrinsic cFos blocking mechanism

The decorrelation of cFos ensembles in DG could reflect changes in synaptic input (i.e. network-level effects), membrane excitability[43], or a cFos shut-off mechanism in individual GCs, e.g. by transcriptional or translational repression of cFos. A candidate suppressor of cFos transcription is ΔFosB, a long-lived splice variant of FosB that accumulates in active neurons[26,44–46]. To find out whether ΔFosB accumulates during WM training, we analyzed the DG of mice that were trained for 7 days in the WM, using a pan-FosB antibody that recognizes both FosB and ΔFosB (pan-FosB, Fig. 6a). GCs had either high cFos expression or high pan-FosB, but rarely both, resulting in an inverse correlation that was highly significant in data pooled from 3 mice and in individual mice (Fig. 6b, Supplementary Fig. 8). When considering only GCs that were cFos-tagged on day 1 of WM training (magenta) we observed high levels of pan-FosB on day 7 but low cFos (Fig. 6c, d). Using the same overlap analysis as in previous experiments, cFos overlap was significantly below chance in this Δ6-day cohort (Fig. 6e) whereas overlap between day 1 cFos-tagged and day 7 pan-FosB$^+$ cells was 8-fold higher than expected by chance (Fig. 6f). Thus, cFos expression in GCs that previously expressed cFos in the WM appears to be inhibited, possibly by the FosB variant ΔFosB. The high levels of pan-FosB staining suggest that indeed the cFos-tagged neurons were repeatedly activated during the subsequent WM training, giving ample time for ΔFosB to accumulate in this specific population.

To test whether cFos suppression is a cell-autonomous process or whether it reflects a lack of synaptic input, we used a chemogenetic approach. We expressed the Gq-DREADD to directly activate neurons and trigger cFos expression in rat hippocampal slice cultures[47,48]. In DG, the first clozapine-N-oxide (CNO) application induced cFos in 59% of the DREADD-expressing GCs (Fig. 7a, Supplementary Fig. 9). A second CNO application 24 h later induced cFos in a much smaller fraction (17%). In CA1 pyramidal cells, conversely, the first and the second CNO application were equally effective in inducing cFos (Fig. 7b). To our surprise, we detected high levels of pan-FosB in CA1 neurons on the second day, which apparently did not interfere with their ability to express cFos. The pan-FosB AB detects both FosB and ΔFosB, but only the latter splice variant is thought to suppress cFos[44]. Thus, while we could recapitulate GC-specific cFos inhibition in these slice experiments, we failed to specifically label the inhibiting agent.

To visualize ΔFosB protein levels in individual neurons, we subtracted from the pan-FosB fluorescence the fluorescence signal from a second antibody that recognizes the C-terminus of FosB, which is absent in ΔFosB (Supplementary Figure 10). In hippocampal slice cultures, we detected significantly more ΔFosB in DG neurons than in CA1 neurons, in both stimulated and non-stimulated cultures. This area difference was even more pronounced in mice after 7 days of WM training, where ΔFosB accumulated in many GCs, but not in CA1 pyramidal cells (Supplementary Figure 10).

Spatial learning increases the number of GCs in a cFos-repressed state

If accumulated ΔFosB inhibits cFos in GCs, concentrations of the two transcription factors should be inversely correlated. To test this, we compared home-caged mice with mice that were WM trained on two (spaced training) or on seven days (daily training). As anticipated, WM training increased the number of ΔFosB$^+$ GC (Fig. 8a) as well as the average intensity of ΔFosB$^+$ expression (Fig. 8b). In individual GCs, cFos expression was inversely correlated with ΔFosB, and the strength of the correlation in individual mice increased with WM training (Fig. 8c). We generated kernel density estimates (KDE) of the actual data (Fig. 8d) and 100 KDEs of scrambled data to simulate the null hypothesis (no interaction between ΔFosB and cFos). Compared to the expectation of the null hypothesis, GCs were overrepresented in two regions: Low cFos with high ΔFosB intensity, which we termed the repressed state (Fig. 8e, upper left quadrant), and high cFos with low ΔFosB, which we denote the permissive state (lower right quadrant). In home-cage mice, only 20% of analyzed GC were in the repressed state (Fig. 8f). The repressed fraction increased to 32% after spaced WM training and to 44% after daily training. Thus, training increased the number of cFos-repressed GCs, which was consistent across animals (see Supplementary Fig. 11 for more examples). Importantly, only GCs that expressed cFos or ΔFosB were included in this analysis. GCs that expressed neither marker were presumably not very active in the WM. In the CA1 region of the same animals we rarely detected neurons with ΔFosB signal, even after daily WM training (Supplementary Fig. 12). This suggests that regardless of training level, almost all CA1 pyramidal cells remained in the permissive state.

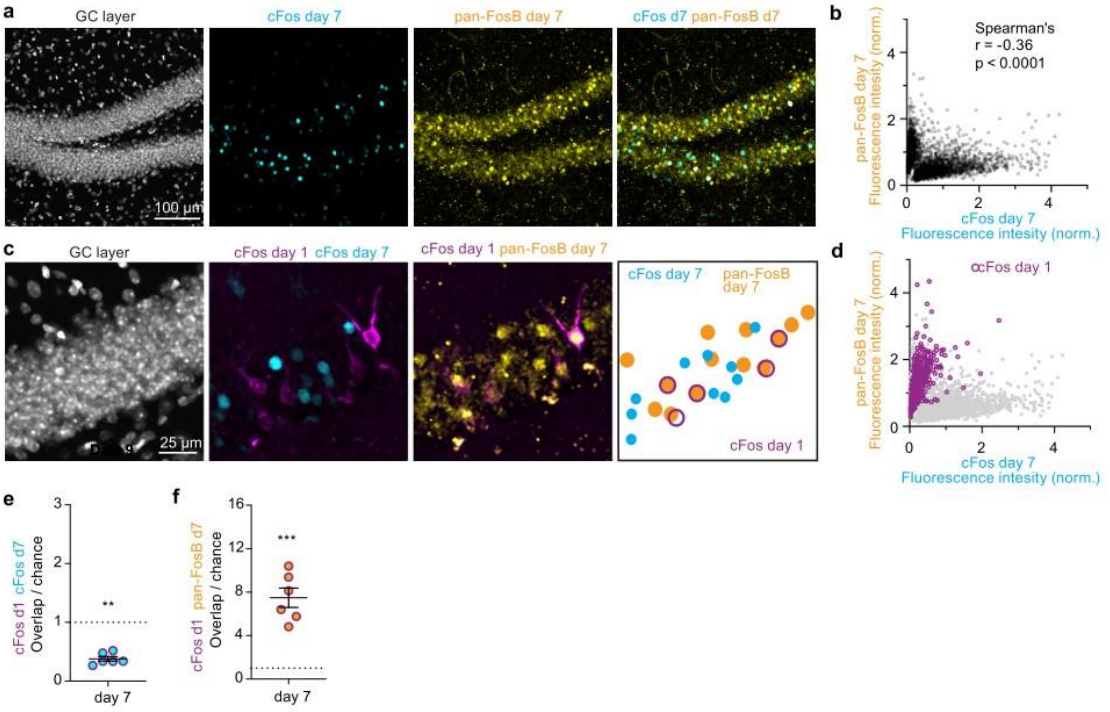

Fig. 6 | Mechanism of cFos suppression in WM-trained mice. a Immunostained hippocampal slice from the DG region against shEGFP (cFos, cyan) and pan-FosB mice (yellow) from mice that received daily training in the water maze for 7 days (from optogenetic experiments, Fig. 3). **b** Quantification of cFos and FosB/pan-FosB expression levels in individual granule cells (GC). GCs appear to be segregated in two clusters, resulting in a significant inverse correlation (****$p < 0.0001$, $n = 4111$ GCs from three mice, Spearman's $r = 0.36$). **c** Same tissue section as **a**, showing $cFos_{day1}$ (magenta), $cFos_{day7}$ (cyan), and pan-$FosB_{day7}$ (yellow) immunoreactive cells. Drawing illustrates co-expression. **d** Day 1 cFos-tagged cells (magenta, pooled from three mice) frequently express pan-FosB. Gray points are replotted from **b**. **e** Overlap between cFos-tagged (magenta, day 1) and cFos (cyan, day 7) is significantly below-chance level (**$p = 0.002$, two-sided paired t test, $n = 6$ mice, mean ± SEM). **f** Overlap between day 1 $cFos^+$ ensembles and FosB/ΔFosB on day 7 is significantly higher than chance (***$p = 0.0004$, two-sided paired t test, $n = 6$ mice, mean ± SEM). Complete statistical information in Supplementary Table 1. Source data are provided as a Source Data file.

Discussion

How time is represented in the brain is still a matter of debate. Using a multi-day training paradigm, we discovered a time-dependent shift in cFos expression patterns that seems to be specific to GCs of the DG. We observed that in individual GCs, accumulation of ΔFosB during water maze training was negatively correlated with cFos expression. Suppression of cFos transcription by ΔFosB has previously been described under pathological conditions (AD models, seizures)[44], and interfering with ΔFosB in hippocampal neurons is known to affect learning and memory[26]. Here we show that even in the home cage, ΔFosB suppression of cFos ensures that the $cFos^+$ ensemble of GCs changes from day to day. Given the extremely high stability of place cells in DG[10], we expected to find stable $cFos^+$ ensembles during multi-day training in a consistent environment, which was not the case. Two questions arise: What does cFos expression tell us about neuronal activity, and second, are $cFos^+$ GCs place cells?

While cFos is known to be driven by high-frequency spiking[27,49,50], the reverse is not true in the DG: The absence of cFos is not evidence for the absence of activity. This became clear when we inhibited the activity of the original (day 1) cFos-tagged ensemble on consecutive days: WM performance was compromised in trials with optogenetic inhibition, even though a very small fraction of GCs in dorsal DG (~1%) was silenced (Fig. 3). The inhibition of cFos-tagged neurons was specific, as inhibition of random GCs was much less effective: we observed behavioral effects only in animals where >30% of GCs were inhibited. Thus, GCs that expressed cFos on the first training day remained particularly relevant for successful navigation in that environment, even though they rarely re-expressed cFos on the successive training days. We confirmed this by showing that cFos-tagged GCs are functionally reactivated when mice revisited the WM, but were not reactivated in a novel environment (Fig. 4). Therefore, low cFos overlap in DG is not in contradiction with the very high stability of place cells in DG[10]. Our findings do, however, indicate a problem when using cFos to identify engram cells. A defining criterion of engram cells stipulates that reactivation—presumably electric—in the same context must occur[17,19,51]. As cFos-tagged neurons in DG remain $cFos^-$ when electrically reactivated on subsequent days (Figs. 4 and 5), using cFos as a proxy for electrical activity is problematic. Defining only a few GCs that express cFos twice as the engram cells would strongly underestimate the number of neurons relevant for memory recall. The DG $cFos^+$ map produced on a given day will mostly contain GCs that have been activated for the first time in the WM. These $cFos^+$ GCs may encode new features being added to the internal representation, possibly acting as a timestamp on the most recently acquired memory. Our optogenetic inhibition experiments suggest that the full set of GCs required to recall the platform position includes many cFos-negative cells.

Why does electrical reactivation of GCs in a behavioral task rarely trigger renewed cFos expression? In slice cultures, we could reproduce this cFos refractory period by repeated chemogenetic stimulation of GCs. CA1 pyramidal cells, in contrast, readily express cFos on successive days. In search of the repressive mechanism, we turned to the FosB splice variant ΔFosB, which is known to be expressed in GCs and to

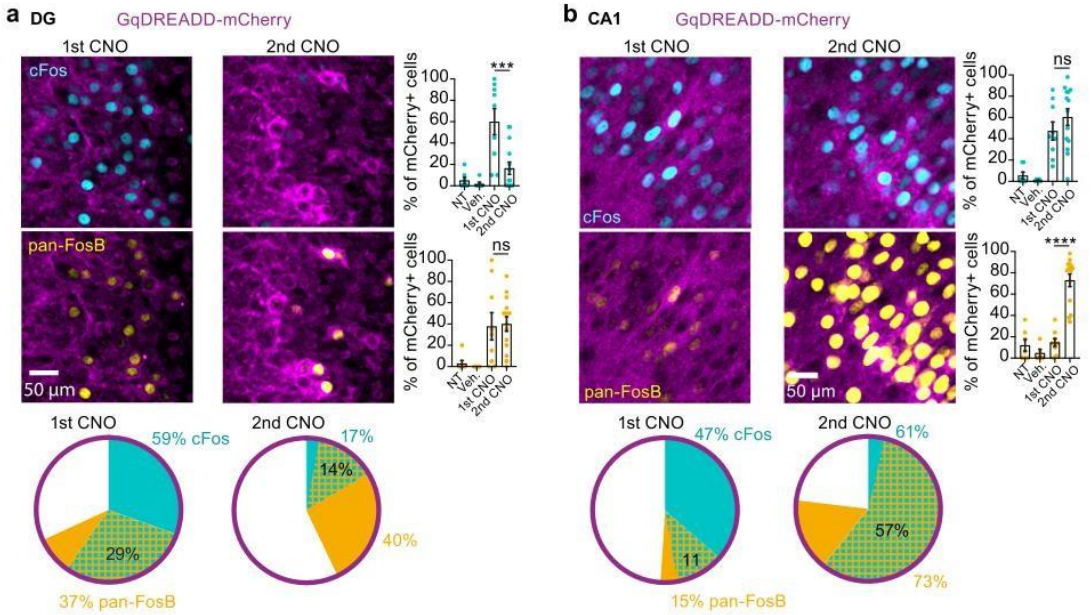

Fig. 7 | Repeated chemogenetic induction of cFos expression in slice culture. **a** AAV transduction of hippocampal slice culture with CaMKaII-*hM3Dq-mCherry* (magenta). Application of CNO activates DREADD and induces strong cFos (cyan) expression in DG (1st CNO, $n = 9$ slices). A second application 24 h later triggered significantly less cFos expression (***$p = 0.0003$, 2nd CNO, $n = 14$ slices, one-way-ANOVA with Šídák's multiple comparisons test). No cFos was detected in cultures with no treatment (NT, $n = 7$ slices) or treated with vehicle (Veh., $n = 5$ slices). On both days, there was also pan-FosB immunoreactivity (yellow) which partially overlapped with cFos (pie charts). **b** CA1 pyramidal cells respond to the second CNO stimulation with renewed cFos expression in spite of high levels of pan-FosB. Bars show mean of all slices ±SEM. Results were replicated at least three times. Complete statistical information in Supplementary Table 1. Source data are provided as a Source Data file.

inhibit the expression of cFos in these neurons[26,44]. We quantified the amount of ΔFosB in individual neurons, revealing the effect of WM training on the GC population: With repeated training, more and more GCs shifted from a low ΔFosB state that is permissive for cFos expression to a high ΔFosB state, in which cFos is repressed. Behavioral training did not have the same effect on CA1 neurons, the large majority of which remained in the permissive state even after 7 days of daily training. Interestingly, the few ΔFosB-positive CA1 neurons we found were all cFos-negative, suggesting that the suppressive mechanism is functional in pyramidal cells, but little ΔFosB is produced during behavior. In vivo imaging experiments have indeed shown that in 60% of the cFos-expressing pyramidal neurons in CA1[47] and 80% in barrel cortex[30], cFos expression is not transient, but sustained for several days. We likewise observed that CA1 neurons express cFos rather persistently, with 27% of homcage-tagged neurons continuing to express cFos 24 h after the mice were back on doxycycline, compared to just 2% of GCs. Active suppression also explains the perfectly linear drop in cFos levels over time we observed in GCs (Fig. 5g) which could not be fitted by simple (exponential) decay functions.

A new picture of time-controlled cFos regulation in the DG begins to emerge. Only 19% of cFos-tagged GCs in the DG expressed cFos 12 h later, and after 24 h, the overlap dropped below-chance level. When neurons express cFos they are hyperexcitable[39,52,53], whereas overexpression of ΔFosB reduces excitability[54]. Hyperexcitability increases the likelihood of burst firing, creating ideal conditions for the potentiation of incoming synapses[55]. Burst firing also maximizes the impact of GCs on postsynaptic CA3 neurons, as the GC-CA3 mossy fiber synapses display extremely strong short-term facilitation[56,57]. During the high cFos period, the probability of long-term potentiation may therefore be increased at both GC input and output synapses, i.e., onto CA3 pyramidal cells and interneurons targeted by the current set of cFos$^+$ GCs[58]. In contrast, synaptic plasticity may be reduced during the refractory period when ΔFosB is high, cFos expression is inhibited and excitability is reduced, possibly write-protecting synapses on high ΔFosB neurons from further modification. In nucleus accumbens, this regulatory mechanism has been proposed to underlie the switch from casual drug use to cocaine addiction[59]. In the amygdala, oscillations of CREB/ICER have been suggested as a mechanism to group memories in time[60].

The assumption that cFos is an indicator of highly active (engram) neurons may hold for naive mice housed under standardized (deprived) conditions and exposed to fear conditioning or other forms of one-trial learning[61,62]. Multi-day training, which may be slightly closer to the daily challenges faced by mice in the wild, leads to the accumulation of ΔFosB in many GCs and potentially other brain areas[63]. Our results suggest that under these conditions, cFos patterns in DG depend not only on input from the entorhinal cortex, but are also gated by the activity history of each GC. Investigation of memory systems "under load" during complex behaviors[64] may thus change our view of hippocampal processing and engram formation.

Methods

Experimental animals

B6.Cg-Tg$^{(Fos\text{-}tTA,Fos\text{-}EGFP^*)1Mmay/J}$ (TetTag) mice were obtained from the Jackson Laboratory (Strain #018306) and bred to wildtype (noncarrier) C57BL6/J mice from our colony. Mice were group-housed with littermates until 2 weeks before rAAV injections, then were single-caged. Mice had access to food and water *ad libitum* and were kept in an animal facility next to the behavioral rooms on a reversed light-dark cycle (dark 7 am–7 pm) at 20–23 °C with 45–65% humidity. All behavioral experiments were done during the dark phase of the cycle. Due to the requirement to swim with optical fibers, only male mice between 20–40 weeks (>28 g by the time of surgery) were used for optogenetic

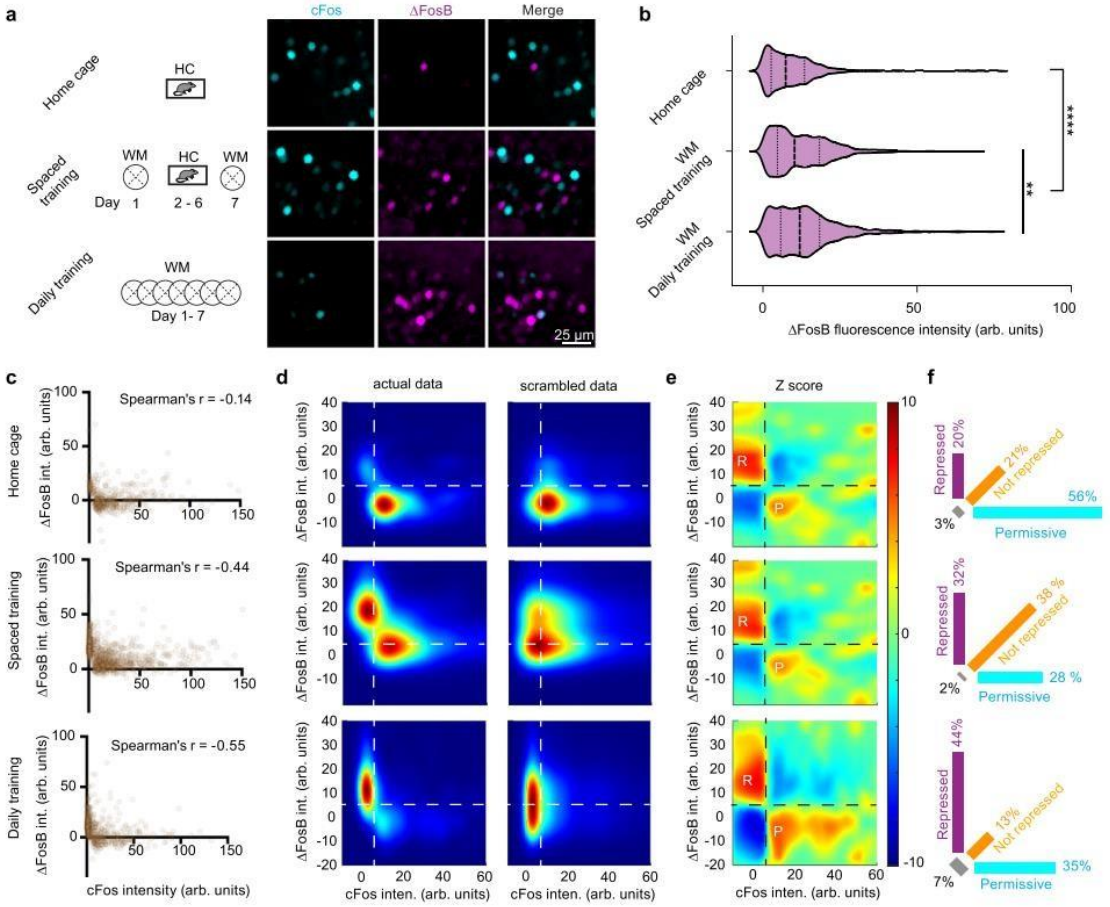

Fig. 8 | Water maze training leads to accumulation of ΔFosB and cFos repression in DG. a ΔFosB (magenta) and cFos expression (cyan) in DG was analyzed after 3 different training regimes: Home-caged (HC) mice, spaced training (ST) and daily training (DT). ΔFosB images show the difference in fluorescence between antibodies against the N-terminal and the C-terminal region of FosB (see Supplementary Figure 10). **b** Water maze training significantly increased ΔFosB in granule cells (GC) from DG (fluorescence intensity from 4 images per mouse. HC: 2 mice, $n = 514$ GCs; ST: 2 mice, $n = 1535$ GCs; DT: 3 mice, $n = 1344$ GCs). Violin plots showing a range of data distribution, median (dashed line), and quartiles (dotted lines). ΔFosB expression increases significantly with spatial learning (****$p < 0.0001$ HC vs ST/DT) ΔFosB expression is significantly higher in DT vs ST mice (**$p = 0.009$) Kruskal–Wallis with multiple comparisons Dunn test. **c** Single-cell analysis of shEGFP (cFos) and ΔFosB expression in DG after the different training regimes (1 mouse each, see also Supplemental Fig. 11). WM training increased the strength of the inverse correlation between cFos and ΔFosB expression (Spearman's *r*). **d** Peak-scaled kernel density estimates of the data shown in **c**. Scrambled data is the average of 100 randomized combinations of the actual data. **e** Z-scores computed from **d**. Dashed lines are drawn between two regions of overrepresented cells (positive *Z* scores, red): Low cFos - high ΔFosB (R, repressed) and high cFos - low ΔFosB (P, permissive) and two underrepresented regions (blue). **f** Percentage of cells in the quadrants indicated in **d** and **e**. Magenta represents cells in the repressed state, orange in the not-repressed state, and cyan in the permissive state. Note that unlabeled GCs were not analyzed. Source data are provided as a Source Data file.

WM experiments (Figs. 3–5). Both male and female mice were included in the cFos ensemble overlap experiments (Figs. 1, 2 and 5). All experiments were conducted in accordance with German law and European Union directives on the protection of animals used for scientific purposes and were approved by the local authorities of the City of Hamburg (Behörde für Justiz und Verbraucherschutz, Lebensmittelsicherheit und Veterinärwesen, N 100/15 and N 046/2021).

Viral constructs

To label the membrane of cFos$^+$ neurons, we used a red fluorescent protein fused to an opsin[65] (iChloC-linker-mKate2). This construct was inserted into a pAAV-TREtight backbone using MluI and EcoRI restriction enzymes to produce pAAV-TREtight-*iChloC-mKate2*. To drive spiking in cFos neurons, iChloC was replaced with CheRiff[66] to create pAAV-TREtight-*CheRiff-mKate2*. To inhibit cFos$^+$ neurons, we used pAAV-TRE3G-*BiPOLES-mKate2* (Addgene # 192579). Constructs were packaged into AAV_9 (iChloC-mKate2) or into $AAV_{PHP.eB}$ (BiPOLES, CheRiff) by the UKE Vector Facility. To photoconvert cFos$^+$ cells with high calcium levels, iChloC-mKate was replaced with CaMPARI2[40]. AAVs for the DREADD experiments were obtained from Addgene (AAV_{AAV}-CaMKIIa-*h4MD(Gi)-mCherry*, Addgene # 50476-AAV_9; AAV_9-CaMKIIa-*hM3Dq-mCherry*, Addgene # 50477-AAV_9).

Stereotactic injection and fiber implant

TetTag mice were virus-injected under analgesia and anesthesia using a stereotaxic drill and injection robot (Neurostar). Mice were fixed to the frame under isoflurane anesthesia (1.5% mixed in O_2), skin and connective tissue was removed, and two craniotomies were performed

using an automated drill on the desired coordinates. AAVs were injected at 10^{12} vg/ml concentration, except for iChloC-mKate2 experiments where it was 10^{13} vg/ml. AAVs were delivered bilaterally into the dorsal hippocampus using a glass micropipette attached to a 5 µl syringe (Hamilton). A single injection per site was performed using stereotaxic coordinates for DG (−2.2 AP, ±1.37 ML, −1.9 DV) with a volume of 500 nl on each side (injection speed: 100 nl/min). CA1 was also injected in a set of experiments (Fig. 5) by moving to −1.4 DV and injecting 400 nl after the DG injection. After the last injection, the pipette was retracted 200 µm and left for at least 5 min to minimize efflux of virus during withdrawal. After the injections, the bone surface was cleaned with 0.9% NaCl solution and the skin was stitched. To avoid hypothermia, a heated pad was placed under the animal during surgery and under its cage for 1 h until full recovery. We provided post-surgery analgesia with Meloxicam mixed with softened Dox-food (see below) for 3 days after surgery. Animals recovered at least 2 weeks before behavioral experiments. Mice for optogenetic experiments were implanted with a custom-made bilateral tapered tip optic fiber implant (Doric) targeting the DG sulcus (−2.2 AP, ±1.37 ML, −1.7 DV) right after AAV injection. Implants were attached to the skull using dental cement (C&B Metabond). A protective cap made of an Eppendorf tube was secured by applying acrylic resin (Pattern Resin LS, GC America) to the exposed skull around the implant.

Doxycycline treatment

Animals were given doxycycline-containing food (Altromin-Dox, 50 mg per kg of body weight, red pellets). To tag the first cFos ensemble, animals were changed to doxycycline-free food (Altromin, light-brown pellets) 24 h before exposure to the task. To ensure that the animals did not eat any Dox-food crumbles that had fallen into their cages, they were moved into new cages with fresh bedding. The old nesting material was transferred to the new cage to decrease novelty. Dox food was resupplied exactly 24 h after removal, right before the behavioral task. For cFos ensemble temporal shift experiments (Fig. 4), doxycycline (50 µg/g body weight) was injected I.P. after the end of the 24 h OFF Dox period.

Behavioral experiments

For ensemble overlap experiments, mice were injected in batches and randomly assigned to an experimental group. Optogenetic experiments had a crossover design where all mice had probe trials with and without light, to minimize sampling errors and reduce the number of animals required to reach statistical power (paired statistics). Mice that did not have adequate viral transduction (see image analysis section), had off-target implants, or performed poorly (floaters or implant intolerance) were excluded from the analysis. All experiments were recorded on digital video. Ethovision XT 11.5 was used for automated tracking.

Water Maze. Animals were handled for 1 week before the start of the pre-training sessions to reduce stress during behavioral tasks. **Pre-training:** Mice were pre-trained for 2 days before their first exposure to the WM arena. Sessions (3-4 trials of max. 60 s each on two days) were done in a small rectangular water tank in the dark, in the same room where the WM task was performed. Water level was 1 cm above the 14 cm diameter escape platform. The position of the platform was alternated between the left and right side of the tank between trials, keeping a distance of 5 cm from the walls to avoid thigmotaxis. Once the animals found the platform, a grid was presented until the animals climbed onto it and were returned to their home cages in the waiting area of the behavioral room. **Training:** The WM consisted of a circular tank (1.45 m diameter) with visual asymmetrical landmarks, filled with water with (non-toxic) white paint. A platform (submerged by 1 cm) was placed in the center of the east quadrant during regular training and switched to the opposite (west) quadrant for reversal training (max. swim time: 90 s). To test spatial reference memory, a probe trial (PT) without a platform was performed on each day. Mice underwent six trials every day (4 training trials (TTs, 90 s) + 1 PT (60 s) + 1 TT), inter-trial interval (ITI) was 8–10 s. For the TTs, mice were lowered into the tank facing the wall in different, pseudo-randomized positions (avoiding the target quadrant). In PTs, mice were lowered in the center of the tank. An opaque cup-sized chamber attached to a pole was used to transfer the mice from their home cage to the drop position and a plastic grid attached to a pole was used to pick up the mice. Mice were picked up 10 s after they found the platform and were returned to their home cage. Mice that did not find the platform during the TT were guided to it using the grid and were picked up after a 10 s on-platform waiting period. For both pre-training and WM, water temperature was 19–21 °C and a heat lamp was placed over the waiting area to prevent hypothermia.

Home cage and open field control experiments. To evaluate the temporal stability of cFos ensembles, mice were left unperturbed in their home cage (HC) during the OFF Dox period and sacrificed after 0, 6, 12, or 24 h ON-Dox. For all the cFos overlap experiments, both $cFos^+$ tagging events were designed to have the same amount of trials and training length. For the open field experiments, mice were placed inside a square arena (50 × 50 cm, 50 lux) for 20 min and stayed in the behavioral room at the same time as their WM counterparts.

Optogenetic silencing in the water maze. Mice were connected to two thin optic fibers (200 µm core diameter, 2 m, Doric Lenses, Canada) using ceramic ferrules (Doric) and put back in their home cage for at least 5 min before any behavioral task. In pre-training trials (2 days, three trials per day), mice were connected and disconnected before every trial to habituate them to the tether. To avoid stress-related cFos tagging, mice were never tethered during the Dox-OFF period. In all trials with tether, the weight of the fibers was compensated with a white helium balloon (0.08 N pull force), attached to a light fiber ~30 cm above the mouse with a transparent thin plastic tubing, long enough to keep the balloon out of the field of view of the video camera. Optogenetic silencing occurred only during memory recall (PTs, no target platform). Blue (473 nm) or yellow (594 nm) light was delivered using a laser combiner (LightHUB, Omicron) connected to a commutator (FRJ_1x2i_FC-2FC_0.22 Doric Lenses, Canada) to split the output into two fibers. The commutator was placed close to the ceiling, at the same height as the camera. Blue light delivery was started when mice were still in their HC (473 nm light pulsed at 33 Hz, 10 ms pulses, 8–10 mW). Immediately after light *on*, mice were placed on a starting platform facing the wall on the south quadrant. The starting platform was submerged with a hydraulic mechanism (Atlantis platform) after 30 s. After 60 s of swim time, the target platform (east quadrant) was raised to just below the water level. Mice that found the target platform was transferred to their HC 10 s later. In cases where mice did not find the platform they were guided to it and then transferred to their HC. Blue light was *on* for a total of 2 min, covering the entire WM trial. "No light" probe trials were done exactly the same, but with the blue laser *off*.

Training protocol. Two batches of mice were used for optogenetic manipulation in the water maze (Fig. 3). On training day 1, the protocol consisted of six trials: four TTs of max. 90 s with the platform in quadrant E, followed by a PT (60 s, without platform) and one more TT. On day 2, mice were placed in the starting Atlantis position for 90 s (visual recall trial). Afterwards, they performed two PTs while blue light was being delivered in the same crossover design, followed by three TTs. Day 3 started with two TTs, followed by two PTs (crossover design, blue light pulses), and two more TTs. On day 4 mice underwent the standard protocol (four TTs, one PT without light, one TT). Day 5 training, mice had two TTs followed by two PTs (blue light, crossover

design). We repeated this protocol on day 6 with yellow light pulses during PTs. This batch was perfused for immunohistochemistry on day 9. The second batch was trained similarly. After tagging (training day 1) mice went through the same training protocol from day 2 to day 4, adding a yellow light trial before the first TT. However, we found that yellow light had no effect on behavior, cFos expression, or cFos overlap. Consequently, we pooled data from "yellow light" and "no yellow light" animals to increase statistical power (Fig. 3h–j). On day 5, mice had two TTs, followed by two PTs, where half of the mice received blue light for the duration of the trial. On day 6, mice had two more TTs and a PT. This batch of mice was perfused for immunohistochemistry on day 7, 90 min after the last PT.

Chemogenetic silencing in the WM. Wild-type mice were bilaterally injected in DG with AAV9-*h4MD(Gi)-mCherry*. After at least 2 weeks of recovery, mice were handled and pre-trained like the previous groups. On day 1, mice were trained for 6 trials. On day 2, mice had two PTs. 40 min before the 1st PT, they received an intraperitoneal (I.P.) injection of 0.9% NaCl solution (vehicle). Mice were then injected with clozapine-N-oxide (CNO, 5 mg kg^{-1}) in 0.9% NaCl solution. After 40 min, their performance was tested again (2nd PT). From days 3–7, mice were trained every day with 4–6 TTs and 1 PT. On day 8, mice were injected again with CNO 40 min before the PT.

CaMPARI2 conversion experiments. TetTag mice were injected bilaterally with $AAV_{PHP.eB}$-TRE-*CaMPARI2* in DG (1.2×10^{12}). Tapered fiber stubs were implanted bilaterally like in the optogenetic experiments. All mice were trained Off-Dox in the WM for 1 day. The following day (On-Dox), one group of mice were again trained in the WM. Photocoverting (PC) light (405 nm) was delivered throughout each WM trial in the ET group and the total illumination time was measured. For each WM-WM animal, we prepared a yoked control animal which, on the second day, received the same dose of PC light (same intensity, same duration) while exploring a novel environment (open field). 90 min after the last trial, mice were sacrificed for immunostaining (cFos-GFP, red CaMPARI2).

Ex vivo brain processing and IF staining

For cFos overlap analysis, mice were perfused 3 h after the last trial. In optogenetic silencing experiments, mice were perfused 1.5 h after the last trial. Mice were injected with ketamine/xylazine (100/10 mg kg^{-1}) intraperitoneal and intracardially perfused with 1x phosphate-buffered saline (PBS, Sigma) followed by 4% paraformaldehyde (PFA, Roth). Brains were extracted and stored in 4% PFA for at least 24 h at 4 °C. Before sectioning, brains were washed with 1× PBS for 20 min at room temperature (RT). The dorsal hippocampal region (−1.2 to −2.3 AP from bregma) was cut into 40–50 μm coronal sections using a vibratome (Leica VT100S) and collected in PBS. From each series, six sections were selected from Bregma −1.7 to −2.3 mm and incubated in blocking buffer (1× PBS, 0,3% TritonX, 5% goat serum) for 2 h at RT. Next, sections were placed in the primary antibody carrier solution (1× PBS, 0,3% TritonX, 1% goat serum, 1% BSA) and incubated overnight at 4 °C. After 3× washing with 1× PBS for 5 min, the sections were incubated for 2 h at RT in the secondary antibody carrier solution (1× PBS, 0.3% TritonX, 5% goat serum). Sections were washed 3 × 10 min in 1× PBS, stained with 4′,6-diamidino-2-phenylindole (DAPI, 1:1000) for 5 min and mounted on coverslips using Immu-Mount (Shandon). Complete antibody information in Supplementary Table 2.

Confocal imaging

Mounted brain slices were labeled with a code to blind the analyst. For cFos overlap experiments, immunostained slices were imaged with a confocal microscope (Olympus Fluoview FV 1000) using an oil immersion objective (UPLSAPO ×20/0.85). From each of the six slices per brain (left and right DG), 15 μm were imaged (stack of 10 images at 1024 × 1024 resolution, Z-step: 1.5 μm). Slices from BiPOLES-expressing animals were imaged with a Zeiss LSM 900 (Plan-Apochromat 20×/0.8). From each section, 18 μm were imaged (stack of six images at 1024 × 1024 resolution, Z-step: 3 μm). Excitation/emission filters were selected using the dye selection function of the Fluoview/Zen3.5 software (Alexa 405 (DAPI), Alexa 488 (shEGFP) and Alexa 568 (mKate2), Alexa 647 (cFos or FosB). The image acquisition settings were optimized once and kept constant for all images within an experimental data set. Images were not deconvolved or filtered for quantitative analysis. Exemplary images presented in the figures are median-filtered (2 × 2 kernel) and cropped. Each color channel was linearly adjusted (Image J).

Ensemble size calculation and overlap analysis

Confocal image stacks (pseudo-colored cyan: shEGFP; pseudo-colored magenta: mKate2; pseudo-colored gray: DAPI) were analyzed with Imaris (Oxford Instruments). The volume of the upper and lower blade of DG (granule cell layer, GCL) based on the DAPI channel was used to estimate the total GC number based on published cell densities[67] and to mask the cyan and the magenta channel to restrict analysis to the GCL. Automatic spot detection was used to identify shEGFP$^+$ cells in the cyan channel. The quality filter (round nuclei with a diameter of 8 μm) was adjusted once and then applied to every image stack of the same experiment. False positive spots (e.g., staining artifacts) were manually removed. It was not possible to detect mKate2-expressing GCs automatically as only the plasma membrane was labeled. To count mKate2-positive cells, spots were placed manually (spot size 12 μm) using the pseudo-colored magenta channel only. Double-positive cells (distance between shEGFP$^+$ and mKate2$^+$ spots <5 μm) were identified using a Matlab script. They were then manually inspected to check for artifacts and, if necessary, corrected. From the Imaris analysis, we calculated the following quantities:

$$(1)\quad \text{Number of granule cells} = \frac{\text{DAPI surface volume}}{\text{reported GC density}}$$

$$(2)\quad \text{Fraction of shEGFP tagged cells} = \frac{\text{number of shEGFP+ cells}}{\text{number of GCs}}$$

$$(3)\quad \text{Fraction of mKate2 tagged cells} = \frac{\text{number of mKate2+ cells}}{\text{number of GCs}}$$

$$(4)\quad \text{Fraction of double positive cells} = \frac{\text{number of double positive cells}}{\text{number of GCs}}$$

$$(5)\quad \text{expected overlap} = \text{fraction of shEGFP cells*} \text{ fraction of mKate2 cells}$$

$$(6)\quad \text{Overlap/chance} = \frac{\text{fraction of double positive cells}}{\text{expected overlap}}$$

Cluster analysis

Neurons were clustered by the Agglomerative Clustering algorithm implemented in the scikit-learn python library. For each image, we first computed the connection graph by using kneighbors_graph, which is also implemented in scikit-learn. The number of neighbors was fixed as one-tenth of the total number of neurons. First (mKate$^+$) and second set (shEGFP$^+$) of cFos-positive neurons were clustered separately (linkage criterion: "ward"). Clustering was performed for 16 different numbers of clusters $n_c \in [5, 20]$. To determine the optimal number of clusters (n_c) for each image, we generated 500 sets of artificial data from each image by randomly distributing the cFos$^+$ neurons within the cell body layer of DG. Double-positive neurons were treated as a

third type, keeping their numbers identical to the experimental data. The cell body layer area was defined by the DAPI channel, and the size of each neuron was standardized (16*16 pixels). Each set of artificial data was clustered with the same procedure as the empirical data. For each clustering result, a clustering index

$$(7)\quad C_c = \left\langle \frac{\text{median}(D_{ij})_{j\in\text{cluster}}}{\min(D_{ij})_{j\notin\text{cluster}}} \right\rangle_{i\in U}$$

was calculated, where D_{ij} is the distance between neurons i and j. Smaller c_c indicates stronger clustering. For each n_c, we calculated the proportion (of the 500 artificial sets) where c_c was smaller in the artificial data than in the empirical data. The optimal n_c was defined as the one with the smallest proportion, i.e., the strongest clustering compared to randomly distributed cells. In the case of multiple n_c with the same smallest proportion, the largest n_c was selected. The optimal n_c was determined for mKate2$^+$ and shEGFP$^+$ clusters separately (always including the double-positive cells).

The sphere of influence of a cluster was defined as the convex hull of all its neurons, calculated by using ConvexHull implemented in SciPy python library. The overlap index between mKate2$^+$ clusters M_i and shEGFP$^+$ clusters S_j was defined as

$$(8)\quad I_c = (M_i \cap S_j)/(M_i \cup S_j).$$

In case of overlap between multiple clusters, the largest overlap was scored. Another 200 sets of artificial data were generated from each image and analyzed in an identical fashion to create cumulative distributions of I_c values expected for randomly distributed cFos$^+$ cells (Fig. 5h).

Analysis of CaMPARI2 photoconversion

The antibody combinations (primary/secondary) used were Anti-CaMPARI2-Red (4F61)/rabbit-568 and cFos/rat-647. Due to the high scattering of 405 nm light by the brain tissue, only slices where the implant site was visible were analyzed (200–250 μm from the implant side, Supplementary Fig. 7). The DAPI channel was used to create a surface of the GCL to estimate the total number of GCs. 12 μm spots (Imaris) were manually placed on converted (red) and non-converted (green) CaMPARI2$^+$ GCs. Spots were exported to Matlab, the fluorescence intensities of all three channels were extracted, calcium-dependent conversion of each CaMPARI2$^+$ cell was calculated (R/R+G) and correlated with its cFos intensity.

Hippocampal slice culture

TetTag mice (male and female) or Wistar Unilever rats (Female, Envigo, HsdCpb:WU) were prepared at postnatal day 4–8[68]. Briefly, animals were anesthetized with 80% CO_2 20% O_2 and decapitated. Hippocampi were dissected in cold dissection medium containing (in mM): 248 sucrose, 26 $NaHCO_3$, 10 glucose, 4 KCl, 5 $MgCl_2$, 1 $CaCl_2$, 2 kynurenic acid, 0.001% phenol red (310–320 mOsm kg^{-1}, saturated with 95% O_2, 5% CO_2, pH 7.4). Tissue was cut into 400 μM thick sections on a tissue chopper and cultured on membranes (Millipore PICMORG50) at 37 °C in 5% CO_2. No antibiotics were added to the slice culture medium which was partially exchanged (60–70%) twice per week and contained 394 ml Minimal Essential Medium (for 500 ml), 20% horse serum, 1 mM L-glutamine, 0.01 mg ml^{-1} insulin, 1.45 ml 5 M NaCl, 2 mM $MgSO_4$, 1.44 mM $CaCl_2$, 0.00125% ascorbic acid, 13 mM D-glucose.

cFos expression induced by chemogenetic stimulation

Organotypic rat slice cultures were injected with AAV9-CaMKIIa-*hM3Dq-mCherry* at DIV 14 using a Picospritzer III (Parker Hannafin). Virus was injected into DG, CA3, and CA1 (1.8 bar pulses, 50 ms duration). After 4–5 days of expression, slices were stimulated either once or twice by applying a 10 μl drop of CNO (1 μM, Tocris) in buffer (in mM: 145 NaCl, 10 HEPES, 25 D-glucose, 1.25 NaH_2PO_4, 2.5 KCl, 1 MgCl, 2 $CaCl_2$, 0.01 TTX, pH 7.4) on top of the slice 24 h apart. Culture inserts were transferred to a new well containing only the buffer for 3 min to wash off the CNO and then returned to the incubator in culture medium. In twice-stimulated cultures, the first stimulation was done without TTX to avoid homeostatic plasticity. As controls, we included slices that were not treated (NT group) or treated with TTX-containing buffer without CNO (vehicle). All slices were fixed 70 min after the last treatment and stained against cFos and pan-FosB. Analysis was performed blind. DREADD-expressing cells were randomly selected based on their mCherry signal (20 spots for DG, 50 spots for CA1 per slice), nuclear cFos and pan-FosB fluorescence intensity was extracted.

Acute slice preparation and electrophysiology

Mice were decapitated under CO_2 anesthesia and the brains were dissected. Acute coronal slices (300 μm) were cut on a vibratome (Leica VT1000 S) in cold (4 °C) cutting solution containing (in mM): choline-chloride (110), KCl (2.5), NaH_2PO_4 (1.25), $NaHCO_3$ (25), $MgCl_2$ (7), $CaCl_2$ (0.5), glucose (25), sodium ascorbate (11.6), sodium pyruvate (3.1). Oxygenation and pH (7.4.) were maintained by bubbling (95% O_2, 5% CO_2). Slices were kept in a holding chamber with artificial cerebrospinal fluid (aCSF) containing (in mM): NaCl (125), KCl (2.5), NaH_2PO_4 (1.25), $NaHCO_3$ (26), $MgCl_2$ (1), $CaCl_2$ (2), glucose (10), saturated with 95% O_2, 5% CO_2. Brain slices recovered at 34 °C for at least 45 min before the start of whole-cell patch-clamp recordings (30–31 °C). Patch pipettes were pulled from borosilicate glass and had a resistance of 3–5 MΩ when filled with internal solution containing (in mM): K-gluconate (135), HEPES (10), $MgCl_2$ (4), Na_2-ATP (4), Na-GTP (0.4), Na_2-phosphocreatine (10), L-ascorbic acid (3), EGTA (0.2). Internal solution had pH 7.2 and 295 mOsm/L. The mKate2-positive cells in the DG were patched and signals acquired through an Axopatch 200B or Multiclamp 700B (Axon Instruments, Inc.), National Instruments A/D boards, and Matlab running Ephus software[69]. Action potential firing was electrically evoked by somatic current injection. Optogenetic stimulation was given through the objective (Olympus, ×60, 1.0 NA) at 473 or 594 nm (CoolLED, pE-4000). Data were analyzed with Matlab or Clampfit 10.7 (Molecular Devices).

Statistical analysis

Numerical data from individual experiments were collected and ensemble sizes were calculated in MS Excel (version 16.0). Statistical tests were conducted in GraphPad Prism (version 8) and assumed an alpha level of 0.05. To analyze differences, we used one and two-way analysis of variance and the Šídák method to correct for multiple comparisons. In some cases, we used two-sided t tests. A detailed description of experimental groups and statistical tests is provided in Supplementary Table 1. For all figures, $^*P < 0.05$, $^{**}P < 0.01$, $^{***}P < 0.001$, $^{****}P < 0.0001$.

Reporting summary

Further information on research design is available in the Nature Research Reporting Summary linked to this article.

Data availability

Source data are provided as a Source Data file. Other data are available upon request from the corresponding authors. Source data are provided with this paper.

Code availability

Custom code to generate kernel density estimates in Matlab and to simulate cFos suppression is provided via GitHub (https://github.com/toertner/Kernel-density-estimate).

References

1. Bird, C. M. & Burgess, N. The hippocampus and memory: insights from spatial processing. *Nat. Rev. Neurosci.* **9**, 182–194 (2008).
2. Morellini, F. Spatial memory tasks in rodents: what do they model? *Cell Tissue Res.* **354**, 273–286 (2013).
3. Aronov, D., Nevers, R. & Tank, D. W. Mapping of a non-spatial dimension by the hippocampal–entorhinal circuit. *Nature* **543**, 719–722 (2017).
4. Eichenbaum, H. Time cells in the hippocampus: a new dimension for mapping memories. *Nat. Rev. Neurosci.* **15**, 732–744 (2014).
5. Mau, W. et al. The same hippocampal CA1 population simultaneously codes temporal information over multiple timescales. *Curr. Biol.* **28**, 1499–1508.e4 (2018).
6. McCauley, J. P. et al. Circadian modulation of neurons and astrocytes controls synaptic plasticity in hippocampal area CA1. *Cell Rep.* **33**, 108255 (2020).
7. Deng, W., Mayford, M. & Gage, F. H. Selection of distinct populations of dentate granule cells in response to inputs as a mechanism for pattern separation in mice. *Elife* **2**, e00312 (2013).
8. Leutgeb, J. K., Leutgeb, S., Moser, M.-B. & Moser, E. I. Pattern separation in the dentate gyrus and CA3 of the hippocampus. *Science* **315**, 961–966 (2007).
9. Chavlis, S. & Poirazi, P. Pattern separation in the hippocampus through the eyes of computational modeling. *Synapse* **71**, e21972 (2017).
10. Hainmueller, T. & Bartos, M. Parallel emergence of stable and dynamic memory engrams in the hippocampus. *Nature* **558**, 292–296 (2018).
11. Danielson, N. B. et al. In vivo imaging of dentate gyrus mossy cells in behaving mice. *Neuron* **93**, 552–559.e4 (2017).
12. Pofahl, M. et al. Synchronous activity patterns in the dentate gyrus during immobility. *Elife* **10**, e65786 (2021).
13. GoodSmith, D. et al. Spatial representations of granule cells and mossy cells of the dentate gyrus. *Neuron* **93**, 677–690.e5 (2017).
14. Senzai, Y. & Buzsáki, G. Physiological properties and behavioral correlates of hippocampal granule cells and mossy cells. *Neuron* **93**, 691–704.e5 (2017).
15. van Dijk, M. T. & Fenton, A. A. On how the dentate gyrus contributes to memory discrimination. *Neuron* **98**, 832–845.e5 (2018).
16. Reijmers, L. G., Perkins, B. L., Matsuo, N. & Mayford, M. Localization of a stable neural correlate of associative memory. *Science* **317**, 1230–1233 (2007).
17. Josselyn, S. A. & Tonegawa, S. Memory engrams: recalling the past and imagining the future. *Science* **367**, eaaw4325 (2020).
18. Denny, C. A. et al. Hippocampal memory traces are differentially modulated by experience, time, and adult neurogenesis. *Neuron* **83**, 189–201 (2014).
19. Lacagnina, A. F. et al. Distinct hippocampal engrams control extinction and relapse of fear memory. *Nat. Neurosci.* **22**, 753–761 (2019).
20. Trouche, S. et al. Recoding a cocaine-place memory engram to a neutral engram in the hippocampus. *Nat. Neurosci.* **19**, 564–567 (2016).
21. Liu, X. et al. Optogenetic stimulation of a hippocampal engram activates fear memory recall. *Nature* **484**, 381–385 (2012).
22. Perusini, J. N. et al. Optogenetic stimulation of dentate gyrus engrams restores memory in Alzheimer's disease mice. *Hippocampus* **27**, 1110–1122 (2017).
23. Moser, E. I., Moser, M.-B. & McNaughton, B. L. Spatial representation in the hippocampal formation: a history. *Nat. Neurosci.* **20**, 1448–1464 (2017).
24. O'keefe, J. & Nadel, L. *The hippocampus as a cognitive map*. (Oxford university press, 1978).
25. Tanaka, K. Z. & McHugh, T. J. The hippocampal engram as a memory index. *J. Exp. Neurosci.* **12**, 1179069518815942 (2018).
26. Eagle, A. L. et al. Experience-dependent induction of hippocampal ΔFosB controls learning. *J. Neurosci.* **35**, 13773–13783 (2015).
27. Sheng, H. Z., Fields, R. D. & Nelson, P. G. Specific regulation of immediate early genes by patterned neuronal activity. *J. Neurosci. Res.* **35**, 459–467 (1993).
28. Trojanowski, N. F., Bottorff, J. & Turrigiano, G. G. Activity labeling in vivo using CaMPARI2 reveals intrinsic and synaptic differences between neurons with high and low firing rate set points. *Neuron* **109**, 663–676.e5 (2021).
29. Yassin, L. et al. An embedded subnetwork of highly active neurons in the neocortex. *Neuron* **68**, 1043–1050 (2010).
30. Lee, J. et al. FosGFP expression does not capture a sensory learning-related engram in superficial layers of mouse barrel cortex. *Proc. Natl. Acad. Sci. USA* **118**, e2112212118 (2021).
31. Lee, I. & Kesner, R. P. Encoding versus retrieval of spatial memory: double dissociation between the dentate gyrus and the perforant path inputs into CA3 in the dorsal hippocampus. *Hippocampus* **14**, 66–76 (2004).
32. Clark, R. E., Broadbent, N. J. & Squire, L. R. Impaired remote spatial memory after hippocampal lesions despite extensive training beginning early in life. *Hippocampus* **15**, 340–346 (2005).
33. Qin, H. et al. A visual-cue-dependent memory circuit for place navigation. *Neuron* **99**, 47–55.e4 (2018).
34. Masachs, N. et al. The temporal origin of dentate granule neurons dictates their role in spatial memory. *Mol. Psychiatry* **26**, 7130–7140 (2021).
35. Gu, Y. et al. Optical controlling reveals time-dependent roles for adult-born dentate granule cells. *Nat. Neurosci.* **15**, 1700–1706 (2012).
36. Andrews-Zwilling, Y. et al. Hilar GABAergic interneuron activity controls spatial learning and memory retrieval. *PLoS One* **7**, e40555 (2012).
37. Vierock, J. et al. BiPOLES is an optogenetic tool developed for bidirectional dual-color control of neurons. *Nat. Commun.* **12**, 4527 (2021).
38. Vogt, N. Tailoring optogenetic illumination through tapered fibers. *Nat. Methods* **14**, 763–763 (2017).
39. Spooner, R. I., Thomson, A., Hall, J., Morris, R. G. & Salter, S. H. The Atlantis platform: a new design and further developments of Buresova's on-demand platform for the water maze. *Learn. Mem.* **1**, 203–211 (1994).
40. Moeyaert, B. et al. Improved methods for marking active neuron populations. *Nat. Commun.* **9**, 4440 (2018).
41. Tanaka, K. Z. et al. The hippocampal engram maps experience but not place. *Science* **361**, 392–397 (2018).
42. Yuan, M. et al. Somatostatin-positive interneurons in the dentate gyrus of mice provide local- and long-range septal synaptic inhibition. *Elife* **6**, e21105 (2017).
43. Shen, Y. et al. CCR5 closes the temporal window for memory linking. *Nature* **606**, 146–152 (2022).
44. Corbett, B. F. et al. ΔFosB regulates gene expression and cognitive dysfunction in a mouse model of Alzheimer's disease. *Cell Rep.* **20**, 344–355 (2017).
45. Nestler, E. J. Transcriptional mechanisms of drug addiction. *Clin. Psychopharmacol. Neurosci.* **10**, 136–143 (2012).
46. Gajewski, P. A. et al. Epigenetic regulation of hippocampal fosb expression controls behavioral responses to cocaine. *J. Neurosci.* **39**, 8305–8314 (2019).
47. Poll, S. et al. Memory trace interference impairs recall in a mouse model of Alzheimer's disease. *Nat. Neurosci.* (2020) https://doi.org/10.1038/s41593-020-0652-4.
48. Mizuno, N. & Itoh, H. Functions and regulatory mechanisms of Gq-signaling pathways. *Neurosignals* **17**, 42–54 (2009).

49. Tyssowski, K. M. et al. Different neuronal activity patterns induce different gene expression programs. *Neuron* **98**, 530–546.e11 (2018).
50. Schoenenberger, P., Gerosa, D. & Oertner, T. G. Temporal control of immediate early gene induction by light. *PLoS One* **4**, e8185 (2009).
51. Khalaf, O. et al. Reactivation of recall-induced neurons contributes to remote fear memory attenuation. *Science* **360**, 1239–1242 (2018).
52. Pignatelli, M. et al. Engram cell excitability state determines the efficacy of memory retrieval. *Neuron* **101**, 274–284.e5 (2019).
53. Sun, X. et al. Functionally distinct neuronal ensembles within the memory engram. *Cell* **181**, 410–423 (2020).
54. Eagle, A. L., Williams, E. S., Beatty, J. A., Cox, C. L. & Robison, A. J. ΔFosb decreases excitability of dorsal hippocampal CA1 Neurons. *eNeuro* **5**, ENEURO.0104-18.2018 (2018).
55. Wittenberg, G. M. & Wang, S. S.-H. Malleability of spike-timing-dependent plasticity at the CA3-CA1 synapse. *J. Neurosci.* **26**, 6610–6617 (2006).
56. Vyleta, N. P., Borges-Merjane, C. & Jonas, P. Plasticity-dependent, full detonation at hippocampal mossy fiber-CA3 pyramidal neuron synapses. *Elife* **5**, e17977 (2016).
57. Pernía-Andrade, A. J. & Jonas, P. Theta-gamma-modulated synaptic currents in hippocampal granule cells in vivo define a mechanism for network oscillations. *Neuron* **81**, 140–152 (2014).
58. Guo, N. et al. Dentate granule cell recruitment of feedforward inhibition governs engram maintenance and remote memory generalization. *Nat. Med.* **24**, 438–449 (2018).
59. Cates, H. M., Lardner, C. K., Bagot, R. C., Neve, R. L. & Nestler, E. J. Fosb induction in nucleus accumbens by cocaine is regulated by E2F3a. *eNeuro* **6** (2019).
60. Rashid, A. J. et al. Competition between engrams influences fear memory formation and recall. *Science* **353**, 383–387 (2016).
61. Cai, D. J. et al. A shared neural ensemble links distinct contextual memories encoded close in time. *Nature* **534**, 115–118 (2016).
62. Tonegawa, S., Morrissey, M. D. & Kitamura, T. The role of engram cells in the systems consolidation of memory. *Nat. Rev. Neurosci.* **19**, 485–498 (2018).
63. Eagle, A. L. et al. Circuit-specific hippocampal ΔFosB underlies resilience to stress-induced social avoidance. *Nat. Commun.* **11**, 4484 (2020).
64. Rosenberg, M., Zhang, T., Perona, P. & Meister, M. Mice in a labyrinth show rapid learning, sudden insight, and efficient exploration. *Elife* **10**, e66175 (2021).
65. Wietek, J. et al. An improved chloride-conducting channelrhodopsin for light-induced inhibition of neuronal activity in vivo. *Sci. Rep.* **5**, 14807 (2015).
66. Hochbaum, D. R. et al. All-optical electrophysiology in mammalian neurons using engineered microbial rhodopsins. *Nat. Methods* **11**, 825–833 (2014).
67. Jinno, S. & Kosaka, T. Stereological estimation of numerical densities of glutamatergic principal neurons in the mouse hippocampus. *Hippocampus* **20**, 829–840 (2010).
68. Gee, C. E., Ohmert, I., Wiegert, J. S. & Oertner, T. G. Preparation of Slice Cultures from Rodent Hippocampus. *Cold Spring Harb. Protoc.* **2017** (2017).
69. Suter, B. A. et al. Ephus: multipurpose data acquisition software for neuroscience experiments. *Front. Neurosci.* **4**, 53 (2010). G.
70. Reference Atlas:: Allen Brain Atlas: Mouse Brain. https://mouse.brain-map.org/static/atlas. Accessed 30 July 2020.

Acknowledgements

We would like to thank Iris Ohmert, Jan Schröder, Katryn Sauter, Sabine Graf, Chantal-Joy Agbo, Tanja Stößner, and Karen Kesseler for excellent technical assistance. The pAAV-TRE3G-*BiPOLES-mKate2* construct (Addgene #192579) was a gift from J. Simon Wiegert. Ingke Braren from the UKE Vector Facility produced rAAV. We thank Mary Muhia, Irm Hermans-Borgmeyer, Silvia Rodriguez-Rozada, Brenna Fearey, and Sabine Hoffmeister-Ullerich for their discussions and helpful advice. This study was supported by the Deutsche Forschungsgemeinschaft (DFG) through Collaborative Research Center CRC 936 (#178316478) Projects B7 (F.M., T.G.O.), A2 (A.K.E.) and Z3 (C.C.H.), SFB TRR169-A2 (C.C.H., D.L.), Research Unit FOR 2419 (#278170285, MK; #282803474, CEG, TGO), and by Consejo Nacional para la Ciencia y Tecnología (CONACYT, Mexico, P.L.M).

Author contributions

P.L.M., A.F., A.K.E., F.M., and T.G.O. conceived and designed experiments. P.L.M., A.F., L.B., and L.A. performed behavioral experiments. A.F., T.F., J.A., L.L., and L.B. performed electrophysiological experiments. D.L. and C.C.H. applied cluster analysis. A.F. and C.E.G. performed slice culture experiments. P.L.M., L.B., L.A., and F.M. analyzed behavioral data. Confocal imaging, immunohistochemistry, and cFos scoring were done by A.F. and L.B. P.L.M., M.K., A.K.E., C.C.H., F.M., and G.O. obtained funding and provided infrastructure. P.L.M., C.E.G., F.M., and T.G.O. wrote the paper. All authors edited and approved the manuscript.

Funding

Open Access funding enabled and organized by Projekt DEAL.

Competing interests

The authors declare no competing interests.

Additional information

Supplementary information The online version contains supplementary material available at https://doi.org/10.1038/s41467-022-33947-w.

Correspondence and requests for materials should be addressed to Paul J. Lamothe-Molina or Thomas G. Oertner.

Peer review information *Nature Communications* thanks Steve Ramirez and the other, anonymous, reviewer(s) for their contribution to the peer review of this work. Peer reviewer reports are available.

Supplementary Information

ΔFosB accumulation in hippocampal granule cells drives cFos pattern separation during spatial learning

Paul J. Lamothe-Molina, Andreas Franzelin, Lennart Beck, Dong Li, Lea Auksutat, Tim Fieblinger, Laura Laprell, Joachim Alhbeck, Christine E. Gee, Matthias Kneussel, Andreas K. Engel, Claus C. Hilgetag, Fabio Morellini and Thomas G. Oertner

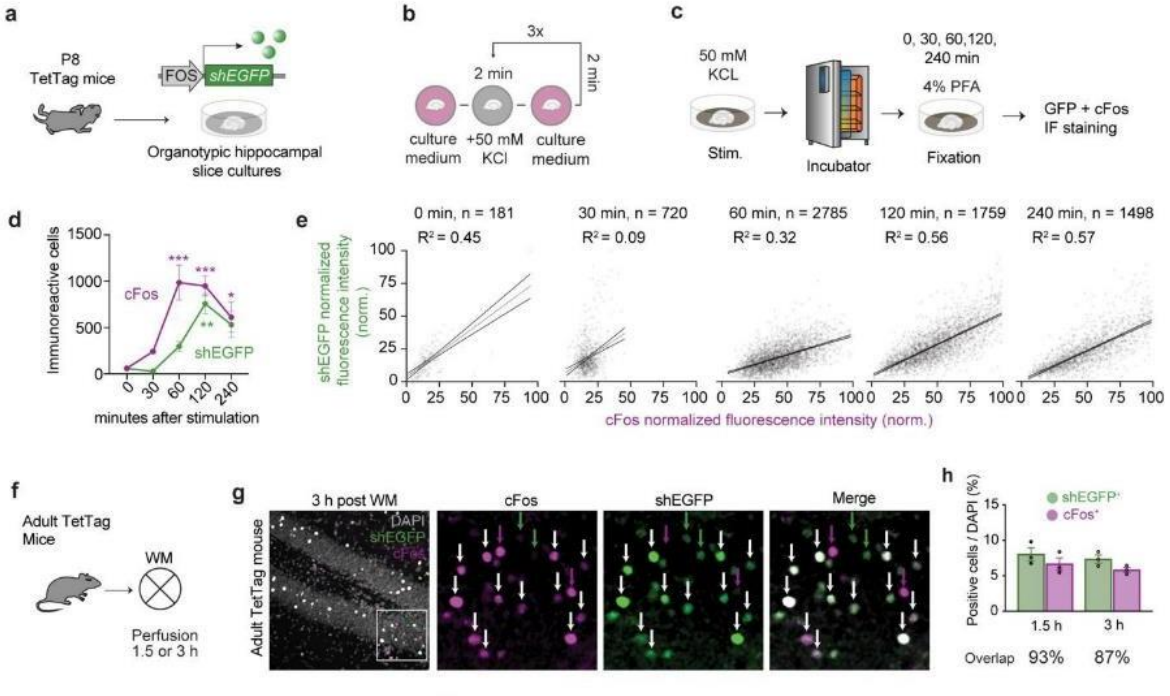

Supplementary Figure 1. Characterization of cFos reporter expression in TetTag mice. a, Hippocampal slice cultures were prepared from p8 TetTag mice in which *shEGFP* is expressed under the cFos promoter. **b**, cFos expression was induced by 50 mM potassium chloride (KCl) application. Slices were exposed to high KCl for 2 min, 3 times at 2 min intervals. **c**, Slices were returned to the incubator (37 °C) after stimulation and fixed with 4% paraformaldehyde (PFA) 0, 30, 60, 90, 120 or 240 min after the end of the stimulation. **d**, Time course of native cFos protein and shEGFP reporter expression. Immunoreactive (IR) cells were manually scored (shEGFP, n = 3 slices; cFos, n = 3 slices, mean ± SEM) inside the granule cell layer as determined by the DAPI signal. cFos$^+$ cells significantly increased after 60 min (****p < 0.0001) while shEGFP$^+$ cells significantly increased after 120 min (**p = 0.001) (two-way-ANOVA, Time Point x Protein interaction *p = 0.048. Šídák's multiple comparisons test) **e**, Anti-cFos vs. anti-shEGFP fluorescence intensity, using automatic detection of cFos+ cells (low detection threshold). High linear correlation was found 120 min and 240 min after stimulation. **f,** TetTag mice were trained in the WM to induce cFos and sacrificed 1.5 h or 3 h after the end of the last training session. **g,** Dentate gyrus from TetTag mouse stained against cFos (magenta) and shEGFP (green) 3 h after water maze (WM) training. Most fluorescent granule cells (GCs) are double-positive (white arrows). Magenta and green arrows correspond to cFos$^+$ or shEGFP$^+$ GCs, respectively. **h**, Fraction of positive cells and overlap of shEGFP reporter (green) and cFos protein (magenta) in animals sacrificed 1.5 h (n = 3 mice) and 3 h (n = 3 mice) after water maze training. Symbols correspond to individual animals, bars show mean +/- SEM.

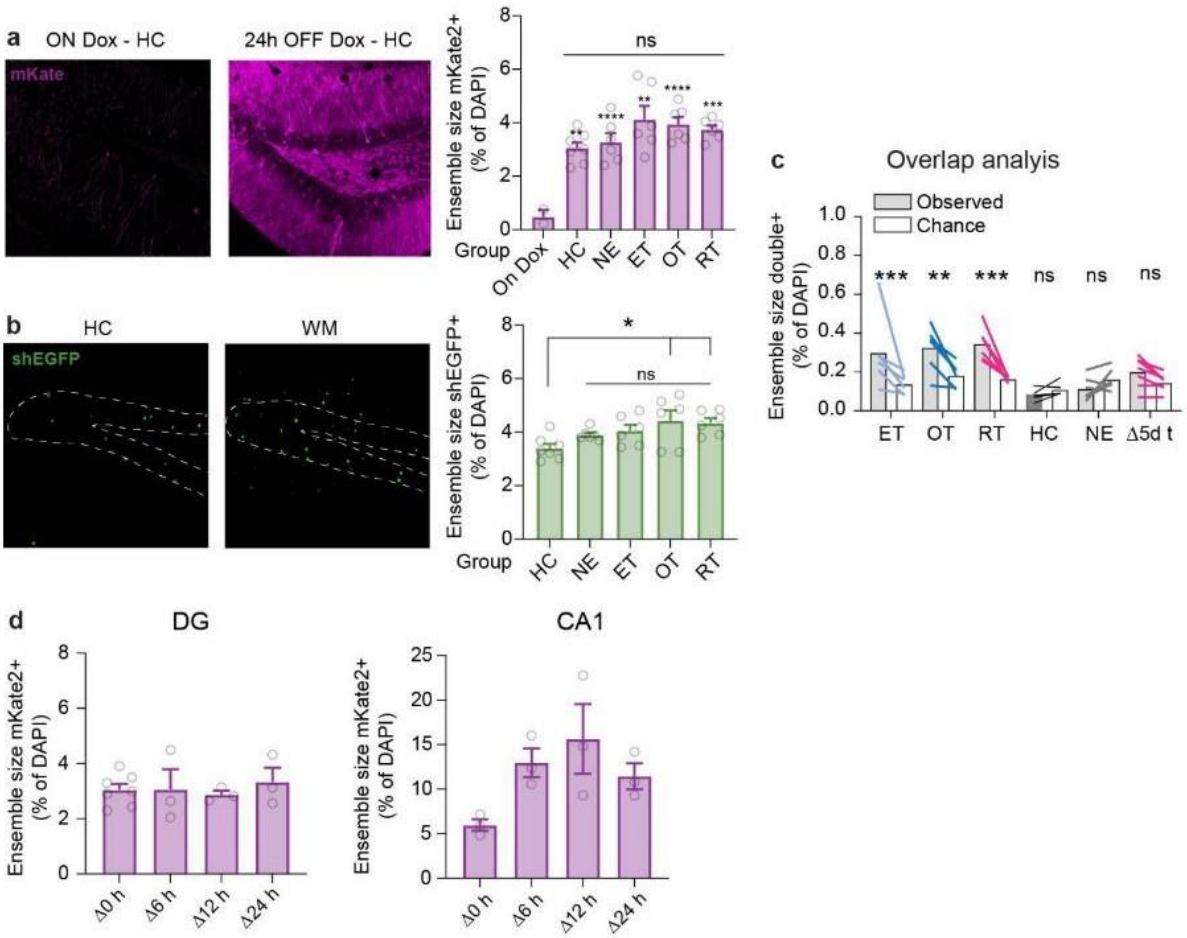

Supplementary Figure 2. Size of cFos ensembles in TetTag mice. a, Removal of Doxycline food induced cFos-dependent expression (cFos-tagged) of membrane-targeted mKate2 in the home cage (HC). The fraction of mKate2-positive neurons was not different in home-caged animals compared to novel environment (NE) and mice trained in the water maze (early training ET; overtrained OT; reversal training RT, mean +/- SEM). All groups showed significantly larger cFos$^+$ ensemble sizes than mice on Dox (HC **, n = 7; NE ****, n = 6; ET ***, n = 6; OT ****, n = 6; RT ***, n = 6. One-way-ANOVA, Sidak multiple comparison test). **b**, Nuclear shEGFP reports cFos-expression in the 2-3 hours before sacrifice. Ensemble size (mean +/- SEM) was significantly larger in the OT and RT groups compared to the HC group. Ensemble size was similar in all WM-trained groups (HC vs. OT *, n = 6; HC vs. RT *, n = 6; HC vs. NE ns, n = 6; HC vs. ET ns, n = 6. One-way-ANOVA, Sidak multiple comparison test). **c**, Observed (grey) and chance-level (white) overlap between mKate2 and shEGFP-tagged ensembles from different (Figs. 1, 2 and 5) experimental groups (HC ns, n = 7 (two sets of lines are overlapping); NE ns, n = 6; ET ***, n = 6; OT **, n = 6; RT ***, n = 6; Δ5d ns. Two-way-ANOVA, Sidak's multiple comparison test). **d**, Ensemble size (mKate2, mean +/- SEM) in home caged mice sacrificed at different times after the end of a 24 h off-Dox period (see Fig. 5). Note delayed increase of mKate2-positive pyramidal cells in CA1.

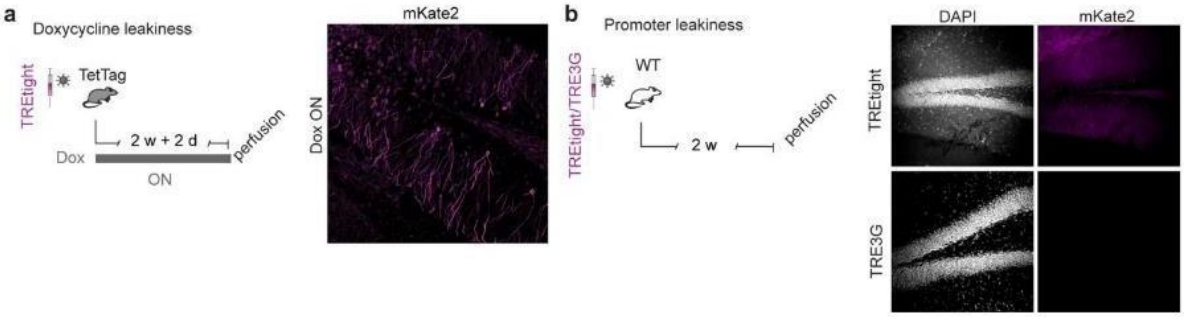

Supplementary Figure 3. Optimization of cFos tagging in TetTag mice. a, Doxycycline leakiness test. Mice were always ON Dox. They were injected with AAV9-TREtight-*iChloC-mKate2* bilaterally in DG and were always in their home cage (HC). Few mKate2-expressing granule cells (GCs) could be detected. **b**, Promoter leakiness test. Wild-type mice that do not express the tetracycline-transactivator (tTA) were injected with either TREtight or TRE3G-promoter region constructs using AAVs. Right: mKate2 expression was observed in TREtight, but not with TRE3G promoter.

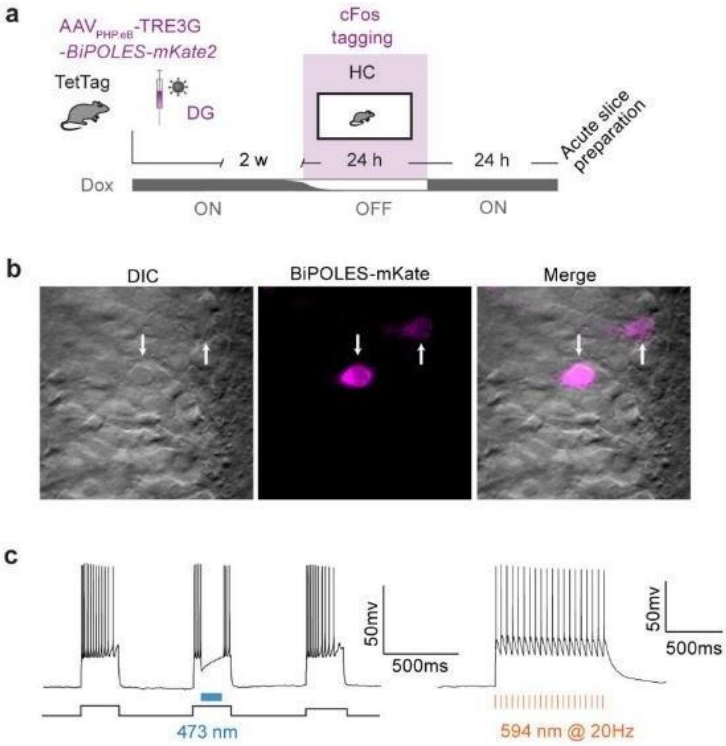

Supplementary Figure 4. BiPOLES characterization in granule cells (GCs). a, TetTag mice were injected with AAVPHP.eB-TRE3G-*BiPOLES-mKate2*. Mice were taken off Dox while they were in their home cage (HC). 24 h later, acute slices were prepared. **b,** Representative images showing the GC layer and BiPOLES-expressing cells. Left differential interference contrast (DIC) image, middle: fluorescent image showing mKate2 (arrows) in the soma of GCs, right: overlay. **c,** Whole cell patch-clamp recordings from BiPOLES-expressing GCs. 473 nm light prevents action potentials (APs) induced by somatic 150 pA (500 ms) current injection. 594 nm light pulses reliably elicit APs.

)

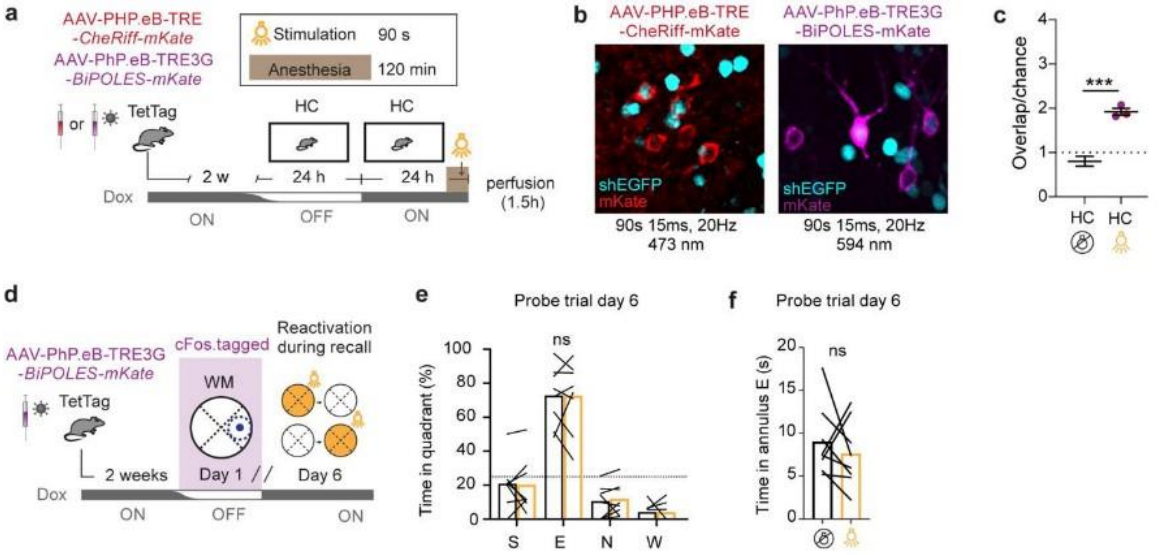

Supplementary Figure 5. Effect of optogenetic reactivation of cFos-tagged GCs on spatial memory recall. a, Testing the effect of optogenetic depolarization in home-caged (HC) mice. Mice were taken off Dox for 24 h to express the optogenetic construct in cFos$^+$ cells. Two different channelrhodopsins were tested, CheRiff(red) and Chrimson (magenta), the depolarizing actuator in the BiPOLES construct. Animals were light-stimulated under anesthesia (473 nm for CheRiff, 594 for BiPOLES) and sacrificed 1.5 h later. **b, c**, Light stimulation increased the overlap between the first set of cFos$^+$ neurons (red/magenta) and shEGFP expression (cyan). Lines show mean +/- SEM. The difference to unstimulated mice expressing mKate (HC group from Fig. 2) was significant (***p = 0.0003, two-sided, unpaired t test). **d**, Testing the effect of optogenetic reactivation of the cFos ensemble tagged on day 1 of WM training. All mice had two probe trials on day 6, one of which was performed under reactivation conditions (594 nm light pulses at 20 Hz). **e**, On day 6, performance in probe trials with optogenetic reactivation (orange bars) was not different from trials without reactivation (black bars) (ns, $p > 0.99$, matched two-way-ANOVA with Šídák's multiple comparisons test. **f**, Time spent in target (E) annulus was also not affected in trials with optogenetic reactivation (orange bar) (ns, $p = 0.49$, two-sided paired t test).

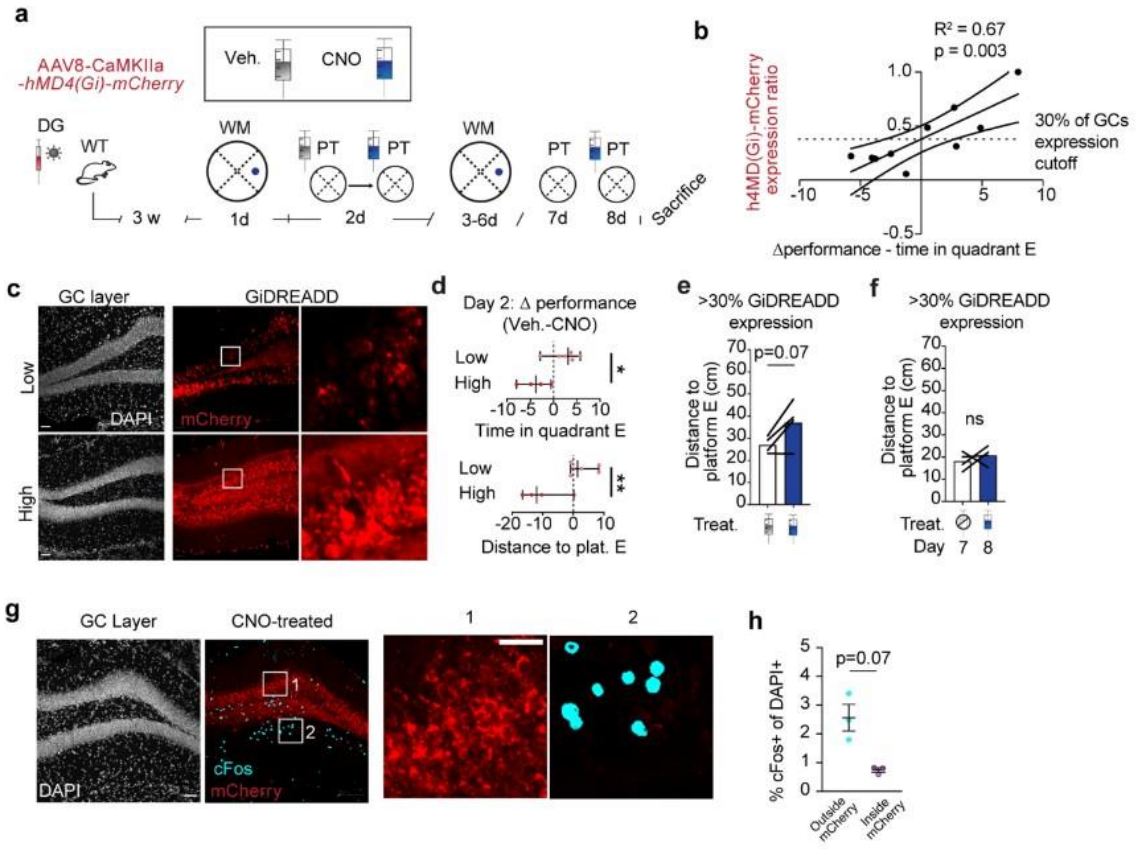

Supplementary Figure 6. Chemogenetic silencing of dentate gyrus affects spatial memory recall. a, Experimental design. Wild-type (WT) mice were injected with AAV_8-CaMKIIa-*hMD4(Gi)-mCherry* bilaterally in DG (n = 10 mice). 3 weeks after injection, mice were trained in the water maze (WM) on day 1. On day 2, mice were tested for reference memory with two probe trials (PT, no platform). All mice were injected with 0.9% NaCl (vehicle) before the first PT and then with clozapine-N-oxide (CNO, 5 mg/kg) before the second PT. Both injections were done intraperitoneally (i.p.) 40 min before each PT. Mice were trained further and tested again on day 7 for reference memory at the end of that session (no treatment) and on the following day (day 8) 40 min after CNO injection (without further training). Mice were sacrificed in different batches on different days with/without CNO application for immunohistochemistry. **b**, Expression of chemogenetic silencing receptors (hMD4(Gi)-mCherry) in DG strongly correlates with performance difference (with/without CNO) on day 2. For each mouse, we calculated the difference of time spent in quadrant E after CNO injection vs vehicle injection (Δ time) as a performance measure, with positive values indicating CNO-induced decrease in performance. **c**, Representative confocal images showing hMD4(Gi)-mCherry expression in DG. Upper row: low Gi-DREADD-expressing mouse; lower row: high Gi-DREADD-expressing mouse. Left, DAPI. Middle, mCherry. Right, magnification from GCs expressing mCherry in the upper blade of the DG. Mice were separated into two groups based on their mCherry expression ratio: high > 0.5 (n = 4), low < 0.5 (n = 6). **d**, Mice in the low expression group are unaffected or show better performance on the second PT, while mice in the high expression group perform worse (Markers: individual mice; Lines: median ± min/max; Distance to platform E: *p = 0.01; Time in quadrant E: **p = 0.007; two-sided unpaired t-test). **e**, Performance was worse during chemogenetic silencing in the high expression group, however, not statistically significant (ns p = 0.07, two-sided paired t-test). **f**, Spatial memory recall is not affected in expert mice. **g**, Example from a mouse where only the upper blade of DG was transduced with Gi-DREADD (red). No cFos expression (cyan) in granule cells of the upper blade (1), but strong cFos expression in GCs of the lower blade (2). This mouse received CNO before a PT and was sacrificed 1.5 h after. **h**, Data from three mice with uneven Gi-DREADD expression, comparing cFos expression outside and inside the (mCherry-labeled) Gi-DREADD expression area (mean +/- SEM, two-sided paired t test).

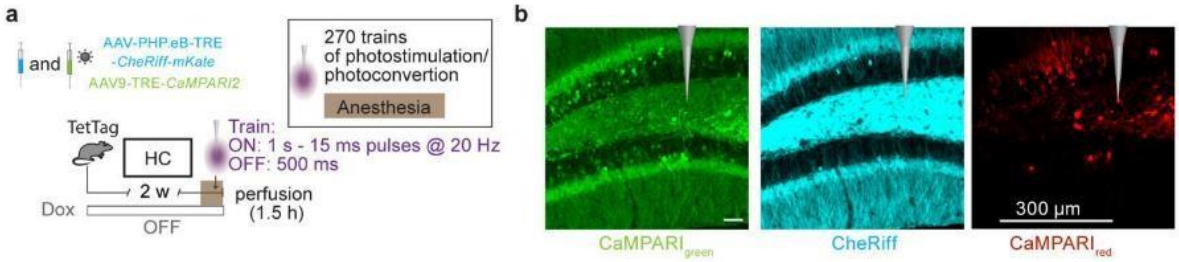

Supplementary Figure 7. Estimating the radius of photoconversion by coexpression of CaMPARI and channelrhodopsin. a Mice were injected a mix of two AAVs encoding CaMPARI2 and CheRiff, respectively. After 2 weeks, mice were anesthetized and stimulated with violet light through a tapered fiber positioned in the hilus, which depolarized the cells and photoconverted calcium-bound CaMPARI. **b** Immunohistochemistry of DG showed photoconverted neurons up to 300 µm away from the fiber tip (red). Based on these calibration experiments, we evaluated neurons within a 200 µm radius around the fiber tip in the behavioral experiments (Fig. 4).

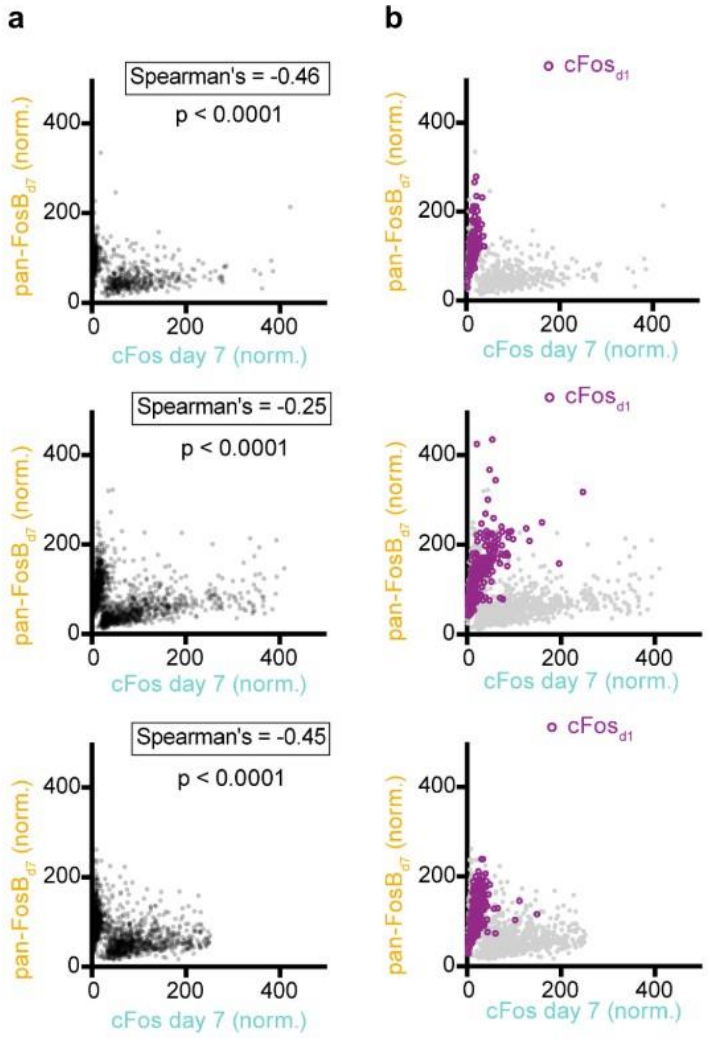

Supplementary Figure 8. Expression analysis in DG in individual mice. a Inverse correlation between cFos expression levels and FosB/ΔFosB on day 7 of WM training. **b** cFos-expressing neurons from day 1 (magenta) typically expressed FosB/ΔFosB, but rarely cFos on day 7.

These data are presented as pooled plots in main Fig. 6b and d.

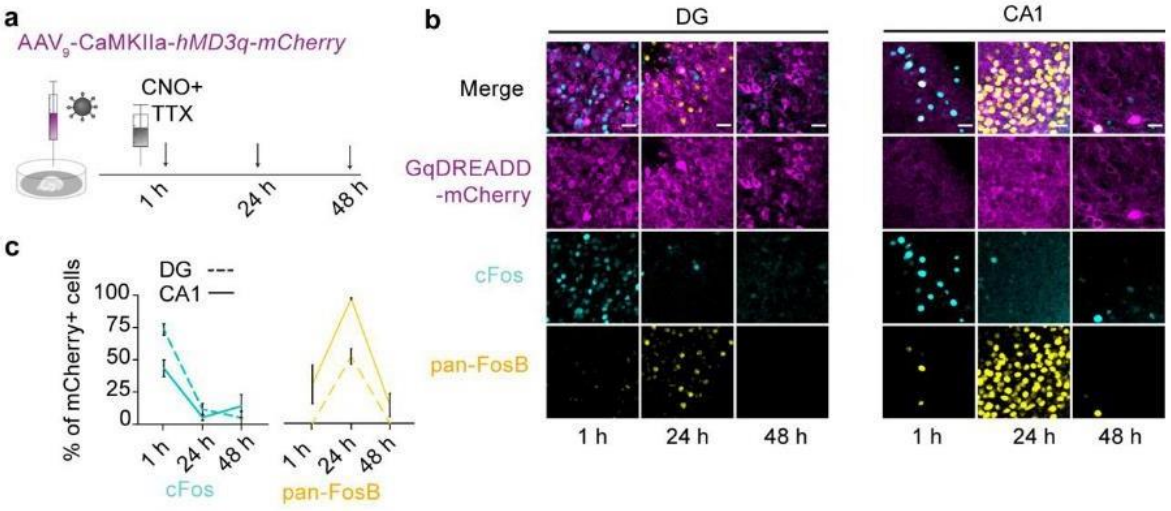

Supplementary Figure 9. Chemogenetic activation of cFos and pan FosB. a Hippocampal slice cultures were transduced with AAV8-CaMKIIa-*GqDREADD-mCherry*. Cultures were silenced with TXX, stimulated with CNO and fixed at 3 different time points. **b** Cultures were immunostained for cFos and pan-FosB. **c** cFos expression was strongly induced by CNO, but rapidly dropped to very low levels after 24 h in both DG and CA1 (mean +/- SEM). Pan-FosB immunoreactivity peaked after 24 h, with a higher fraction of CA1 neurons expressing FosB compared to DG. After 48 h, expression was down in both CA1 and DG.

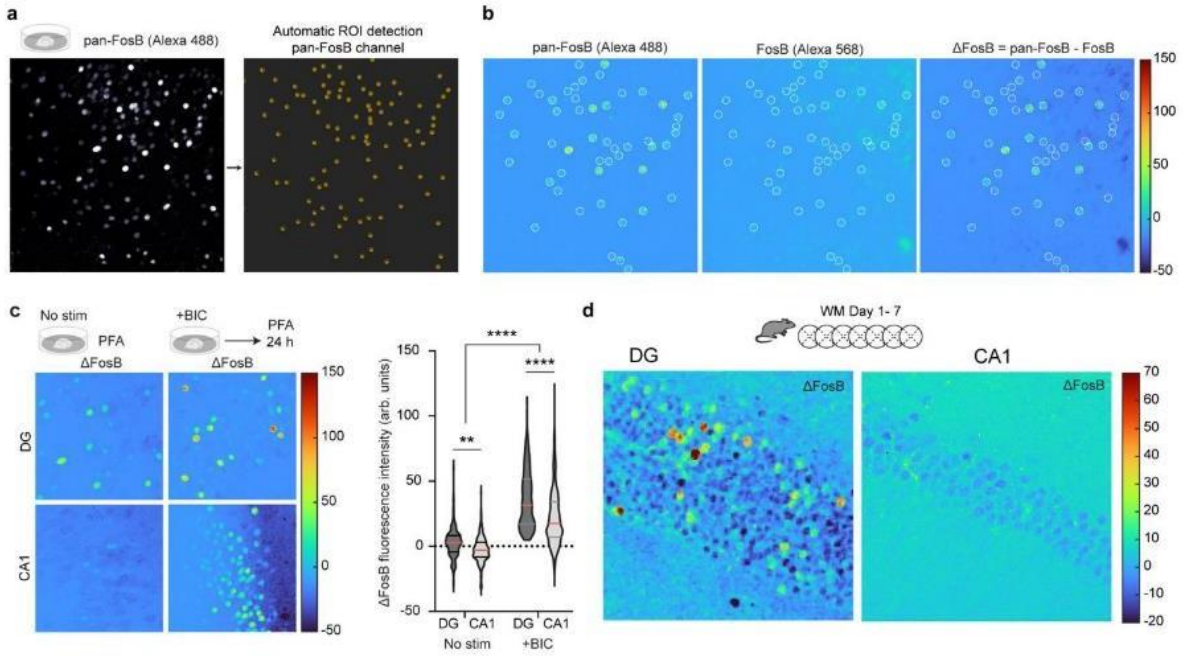

Supplementary Figure 10. Subtraction method to estimate ΔFosB expression. a, Example of an image (3D rendering from stack, Imaris) showing pan-FosB immunoreactive cells in the dentate gyrus (DG) from an organotypic rat slice culture taken at baseline without stimulation. An automated ROI selection was used to place spots (Imaris) on Pan-FosB immunoreactive cells. **b,** Same example image presented with Jet color look-up-table to represent fluorescence intensity of pan-FosB and FosB. Whole image fluorescence subtraction performed in Matlab allowing signed pixel values: pan-FosB channel – FosB channel = ΔFosB. White doted-line circles are placed to indicate the ROIs based on the Pan-FosB immunoreactive cells (placed manually on a single plane so not all spots from **a** appear in this image). **c,** Exemplary single plane images of DG and CA1 of organotypic slice cultures showing ΔFosB levels without stimulation (baseline) and 24 h after bicuculine (BIC) stimulation. Violin plots (range, median ± quartiles): ΔFosB intensities in defined ROIs (Imaris) are significantly higher in DG than in CA1 at baseline (** $p = 0.006$, DG: n = 228 cells, 3 slices; CA1: n = 298 cells, 3 slices, two-way-ANOVA) and 24 h after BIC stimulation (**** $p < 0.0001$, DG: n = 435 cells, 3 slices; CA1: n = 459 cells, 3 slices, two-way-ANOVA). **d,** Fluorescence subtraction method applied to brain slices from a mouse that was trained for 7 days in the water maze (WM). Image showing accumulation of ΔFosB in granule cells of the DG but not in pyramidal cells of the CA1 region. Complete statistics in Supplementary Table 1.

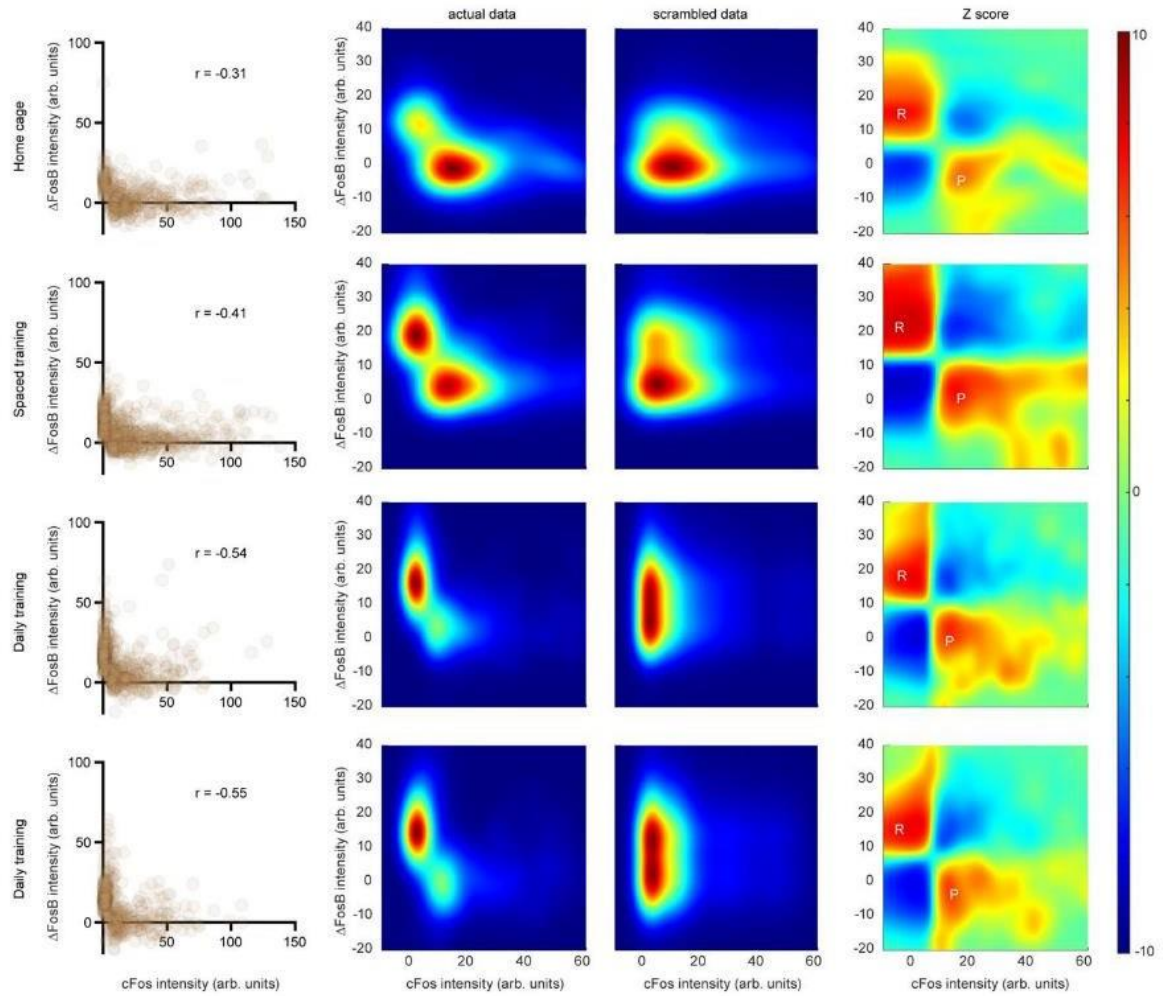

Supplementary Figure 11. Kernel density estimates in DG, more examples. Single cell analysis of cFos and ΔFosB expression in DG after 3 different training regimes. Each row shows data from one mouse (Home cage, spaced training, daily training, daily training). **First column:** Expression of cFos and ΔFosB in individual granule cells (brown circles). Spearman's r indicates inverse correlation. **Second column:** Kernel density estimate from actual single cell data (first column). **Third column:** Kernel density estimate, average of 100 randomized (scrambled) combinations of the actual data. **Fourth column:** Pixel-wise Z-score of actual data compared to scrambled data, scaled from -10 to +10. In every animal, we found two regions of overrepresented cells (positive Z-scores): Low cFos - high ΔFosB (R, repressed) and high cFos - low ΔFosB (P, permissive). In the homecage, most GC are in the permissive state. Spaced training resulted in a bimodal distribution. Daily training shifted the majority of GC to the repressed state.

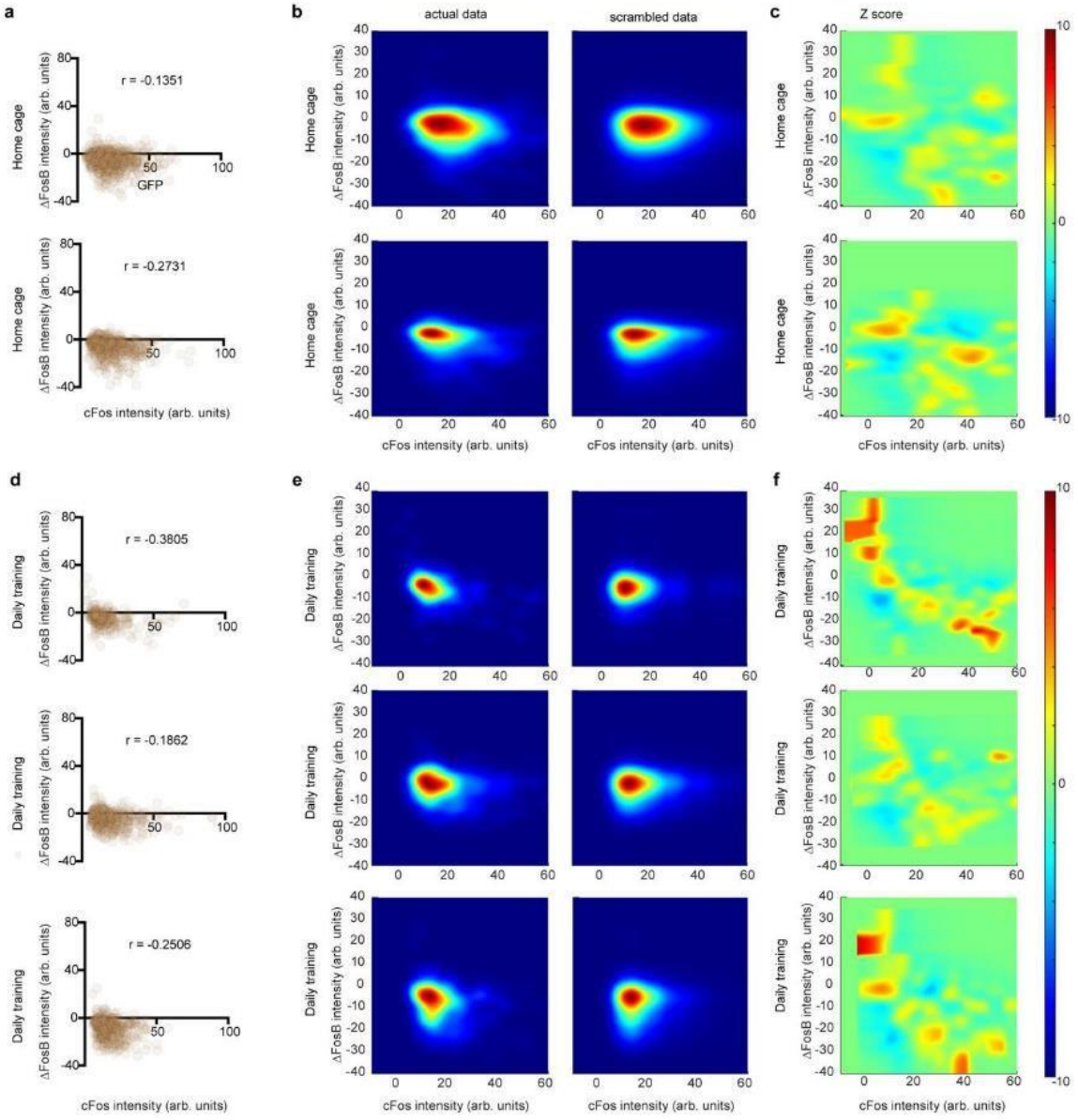

Supplementary Figure 12. Kernel density estimates from CA1 pyramidal cells. **a,** Two mice were kept in the homecage for 7 days. Expression of cFos and ΔFosB in individual CA1 cells (brown circles). Spearman's r indicates weak inverse correlation. **b,** Kernel density estimate from actual single cell data (first column) and average of 100 randomized (scrambled) combinations of the actual data. **c:** Pixel-wise Z-score of actual data compared to scrambled data, scaled from -10 to +10. **d,** Three mice were trained daily in the water maze for 7 days. Expression of cFos and ΔFosB in individual CA1 cells (brown circles). Spearman's r indicates inverse correlation. **e,** Kernel density estimate from actual single cell data (first column) and average of 100 randomized (scrambled) combinations of the actual data. **f,** Pixel-wise Z-score of actual data compared to scrambled data, scaled from -10 to +10. The actual distributions are similar to the scrambled distributions even after 7 days of WM training.

Supplementary Table 1

Figure	Panel	Groups	n	# replications	Test	Multiple comparison
1	c	ET (days 1-2) + OT (days 1-6)	12 mice (6 per group)	Pooled data from 4 different batches of mice	Mixed model ANOVA. Training (Days) fixed effect: *** p=0.0007	Sidak (Day 1 vs. 2, * p=0.02; day 5 vs. 6 P>0.98)
1	f	ET	6 mice	Pooled data from 4 different batches of mice	Matched, Two-way-ANOVA. Annulus effect: F (1, 5) = 28.68, P=0.0031. Annulus x Tagging Day interaction: F (1, 5) = 4.31, ns p=0.0925	Sidak (Day 1, annulus E vs. W, * p=0.03; Day 2 annulus E vs. W, ** p=0.001
1	h	OT	6 mice	Pooled data from 4 different batches of mice	Matched, Two-way-ANOVA. Annulus effect: F (1, 5) = 36.91, P=0.0017, Annulus x Tagging Day interaciton: F (1, 5) = 1.72, ns p=0.24	Sidak (Day 5, annulus E vs. W, **** p<0.0001; Day 6 annulus E vs. W, ** p<0.0001
1	i	ET and OT	6 mice per group	Pooled data from 4 different batches of mice	Mixed, Two-way-ANOVA. Group: F (1, 10) = 48.77, **** p<0.0001. Group x Tagging Day (learning) interaction: F (1, 10) = 5.28, * p=0.04	Sidak (ET group: day 1 vs. 2, distance to platform E, ** p=0.004; Group OT day 5 vs. 6 distance to platoform E, ns p=0.65.
1	k	ET and OT	6 mice per group	Pooled data from 4 different batches of mice	From SF 3	From SF 3
1 / 2	k / f	ET and OT / RT, NE and HC	6 mice per group	Pooled data from 4 different batches of mice	Ordinary one-way-ANOVA, Group: F (4, 26) = 9.567, **** p<0.0001	Sidak (HC vs. NE: ns p>0.99; HC vs. ET: **p=0.002; HC vs. OT: * p=0.01; ; HC vs. RT: ** p=0.024; NE vs. ET: ** p=0.03; NE vs. OT: * p=0.02; NE vs. RT: ** p=0.29; ET vs. OT: ns p=0.99; ET vs. RT: ns p>0.99; OT vs. RT: ns p=0.98
2	b	RT	6 mice	Pooled data from 4 different batches of mice	Matched, Two-way-ANOVA. Annulus effect: F (1, 5) = 54.68, *** P=0.0007. Annulus x Tagging day interaction: F (1, 5) = 7.49, * p=0.04	Sidak (Day 5, annulus E vs. W, * p=0.01; Day 6 annulus E vs. W, ns p=0.75
2	d	NE	6 mice	Pooled data from 4 different batches of mice	Two-sided paired t test. Annulus E vs. W. ns, p=0.16. CI -3.313 to 15.02	NA
2	f, g	ET, OT, RT, NE, HC	n=1815, 2209, 2524, 1531, 1575 cells	Pooled data from 4 different batches of mice	Ordinary two-way-ANOVA. Group effect: F(4, 40) = 13.19, **** p<0.0001	Sidak (HC vs. ET: **** p<0.0001; HC vs. OT: *** p=0.0003; HC vs. RT: ** p=0.001; ; HC vs. NE: ns p=0.75; ET vs. OT: ns p=0.6 ;ET vs. RT: ns p=0.26 ; ET vs. NE: *** p=0.0002; OT vs. RT: ns p>0.99 ; OT vs. NE: * p=0.03; RT vs. NE: ns p=0.11)
3	b	Optogenetic silencing group	15 mice	Pooled data from 2 different batches of mice	Repated measures one-way-ANOVA. Training (days) effect: F (2.9, 41), **** p<0.0001	Sidak (Escape Latency comparied to first training day. Day 2, *** p=0.0008; day 3, *** p=0.0006, day 4, *** p=0.0002; Day 5, **** p<0.0001
3	c	Tethered vs. Untethered	15 mice	Data from 2 different batches	Two-sided paired t test. Tethered vs. Untethered trials (Day 5) ns p=0.12	NA
3	d	473nm Light vs. No Light	15 mice	Data from 2 different batches	Two-sided paired t test. 473nm Light vs. No Light trials (Day 5) ns p=0.5	NA
3	d	594nm Light vs. No Light	8 mice	1 batch of mice	Two-sided paired t test. 594nm Light vs. No Light trials (Day 5) ns p=0.74	NA
3	g	473nm Light vs. No Light	8 mice (1 mouse excluded)	1 batch of mice	Matched two-way-ANOVA. Quadrant effect: F (3, 18) = 14.91, **** p<0.0001. 473nm Light x Quadrant interaction: F (1, 6) = 0.026, ns p=0.12	Sidak (Time in Quadrant, 473nm Light vs. No Light: South ns p=0.41; East ns p=0.35; North ns p=0.95, West ns p=0.92)
3	h	473nm Light vs. No Light	15 mice (3 mice excluded)	Data from 2 different batches of mice (dotted/solid lines)	Matched two-way-ANOVA. Quadrant effect: F (3, 33) = 68.41, **** p<0.0001. 473nm Light x Quadrant interaction: F (3, 33) = 6.93, *** p=0.001.	Sidak (Time in Quadrant, 473nm Light vs. No Light: South ns p=0.42; East ** p=0.002; North ns p=0.1, West ns p=0.99)
3	i	473nm Light vs. No Light	15 mice (4 mice excluded). Day 2 (n=8), Day 3 (n=7), & Day 5 (n=11)	Data from 2 different batches of mice (dotted/solid lines)	Two-sided paired t test. 473nm Light vs. No Light trials. Day 2: ns p=0.67; Day 3: ** p=0.004; Day 5: ** p=0.002	NA
5	c	Δ5d RT vs. Δ1d RT	Δ5d RT (n= 7 mice) Δ1d RT (n= 6 mice from Fig 2)	Pooled data from 2 different batches of mice	Two-sided unpaired t test. Δ5d RT vs. Δ1d RT overlap/chance. ** p=0.003	NA
5	g	DG: Δ0h, Δ6h,Δ12h, Δ24h	3 mice per group	Pooled data from 3 different batches of mice	Ordinary one-way-ANOVA. Group effect: F (3, 8) = 127, **** p<0.0001	Sidak (Δ0h vs Δ6h ** p=0.005; Δ0h vs. ,Δ12h **** p<0.0001, Δ0h vs., Δ24h **** p<0.0001, , Δ6h vs. Δ12h *** p=0.0005, Δ6h vs. Δ24h **** p<0.0001, Δ12h vs. Δ24h ** p=0.002)

Supplementary Table 1 (cont.)

Figure	Panel	Groups	n	# replications	Test	Multiple comparison
5	g	CA1: Δ0h, Δ6h,Δ12h, Δ24h	3 mice per group	Pooled data from 3 different batches of mice	Ordinary one-way-ANOVA. Group effect: F (3, 8) = 31.24, **** p<0.0001	Sidak (Δ0h vs Δ6h *** p=0.0005; Δ0h vs. ,Δ12h *** p=0.0002, Δ0h vs., Δ24h *** p=0.0003, , Δ6h vs. Δ12h ns p=0.89, Δ6h vs. Δ24h ns p=0.99, Δ12h vs. Δ24h ns p=0.99
6	b	Δ7d OT	6 mice	Data from 1 batch of mice	Spearman r = -0.36, CI: -0.3904 to -0.3358. **** p < 0.0001	NA
6	e	Δ7d OT	6 mice	Data from 1 batch of mice	Two-sided paired t test. Observed vs. Expected Overlap. ** p=0.002	NA
6	f	Δ7d OT	6 mice	Data from 1 batch of mice	Two-sided paired t test. Observed vs. Expected Overlap. *** p=0.0004	NA
7	a upper	NT, Veh., 1st CNO, 2nd CNO	NT (7 slices), Veh. (5 slices), 1st CNO (9 slices), 2nd CNO (14 slices)	Pooled data from 3 replications	Ordinary one-way-ANOVA, Group effect: F(3, 31) = 10.57. **** p<0.0001	Sidak (NT vs. Veh.: ns p>0.99; NT vs. 1st CNO: *** p=0.0003; NT vs. 2nd CNO: ns p=0.88; Veh. vs. 1st CNO: *** p=0.0006; Veh.. vs. 2nd CNO ns p=0.81; 1st CNO vs. 2nd CNO: *** p=0.0008)
7	a lower	NT, Veh., 1st CNO, 2nd CNO	NT (7 slices), Veh. (5 slices), 1st CNO (9 slices), 2nd CNO (14 slices)	Pooled data from 3 replications	Ordinary one-way-ANOVA, Group effect: F(3, 31) = 6.32 ** p=0.0036	Sidak (NT vs. Veh.: ns p>0.99; NT vs. 1st CNO: ns p=0.63; NT vs. 2nd CNO: * p=0.02; Veh.. vs. 1st CNO: ns p=0.77; Veh.. vs. 2nd CNO * p=0.003; 1st CNO vs. 2nd CNO: ns p>0.99)
7	b upper	NT, Veh., 1st CNO, 2nd CNO	NT (7 slices), Veh. (5 slices), 1st CNO (9 slices), 2nd CNO (14 slices)	Pooled data from 3 replications	Ordinary one-way-ANOVA, Group effect: F(3, 31) = 13.70. **** p<0.0001	Sidak (NT vs. Veh.: ns p>0.99; NT vs. 1st CNO: ** p=0.0069; NT vs. 2nd CNO: **** p<0.0001; Veh.. vs. 1st CNO: ** p=0.0067; Veh.. vs. 2nd CNO *** p=0.0002; 1st CNO vs. 2nd CNO: ns p=73)
7	b lower	NT, Veh., 1st CNO, 2nd CNO	NT (7 slices), Veh. (5 slices), 1st CNO (9 slices), 2nd CNO (14 slices)	Pooled data from 3 replications	Ordinary one-way-ANOVA, Group effect: F(3, 31) = 38.52 **** p<0.0001	Sidak (NT vs. Veh.: ns p=0.97; NT vs. 1st CNO: ns p=0.98; NT vs. 2nd CNO: **** p<0.0001; Veh.. vs. 1st CNO: ns p=0.87; Veh.. vs. 2nd CNO **** p<0.0001; 1st CNO vs. 2nd CNO: **** p<0.0001)
8	b	Home cage (HC), Spaced Training (ST), Daily Training (DT)	HC (n = 2), ST (n = 2), DT (n = 3)	Data from 1 batch of mice	Kruskal-Wallis test, **** p < 0.0001	Multiple Dunn's comparison test. HC vs. ST: **** p < 0.0001 ; HC vs. DT: **** p < 0.0001 ; ST vs. DT: ** p = 0.0094.
8	c	HC	1 mouse (example)	replicate in Supp. Fig. 11	Spearman r = -0.14, CI:-0.2284 to -0.05460. ** p = 0.0011	NA
8	c	ST	1 mouse (example)	replicate in Supp. Fig. 11	Spearman r = -0.44, CI: -0.4931 to -0.3944. **** p < 0.0001	NA
8	c	DT	1 mouse (example)	replicate in Supp. Fig. 11	Spearman r = -0.55, CI: -0.6054 to -0.4969. **** p < 0.0001	NA
SF 1	d	cFos and shEGFP	3 slices per time point per group	Data from 1 batch of slices	Matched two-way-ANOVA. Time Point effect: F (4, 16) = 19.74, **** p<0.0001. Time Point x Protein interaction: F (4, 16) = 3.02, * p=0.048	Sidak (cFos expression compared to baseline (0 min): 30 min ns p=0.69; 60 min **** p<0.0001; 120 min *** p=0.0001; 240 min ** p=0.009) (shEGFP expression compared to baseline (0 min): 30 min ns p=0.99; 60 min ns p=0.44; 120 min ** p=0.001; 240 min * p=0.02
SF 1	e	0, 30, 60, 120, 240 mins	n=181, 720, 2785, 1759, 1498 cells	Data from 1 batch of slices	Simple linear regression. R^2 = 0.45, 0.09, 0.32, 0.56, 0.57	NA
SF 2	a	On-Dox, HC, NE, ET, OT, RT	On-Dox (n=2), HC (n=7), NE, ET, OT, RT (n=6 per group)	Pooled data from 4 different batches of mice	Ordinary one-way-ANOVA. Group effect: F (5, 25) = 8.04 **** p<0.0001	Sidak (On-Dox vs. HC ** p=0.004, On-Dox vs. NE **** p>0.0001, On-Dox vs. ET ** p=0.001, On-Dox vs. OT *** p=0.0001, On-Dox vs. RT *** p=0.0003,HC vs. NE ns p=0.23, HC vs. ET ns p>0.99, , HC vs. OT ns p=0.49, HC vs. RT ns p=0.84, NE vs. ET ns p=0.64, NE vs. OT ns p>0.99, NE vs. RT ns. p=0.99, ET vs OT ns p=0.9, ET vs RT ns p=0.99, OT vs. RT ns p>0.99)
SF 2	b	HC, NE, ET, OT, RT	HC (n=7), NE, ET, OT, RT (n=6 per group)	Pooled data from 4 different batches of mice	Ordinary one-way-ANOVA. Group effect: F (4, 26) = 3.41 * p=0.027	Sidak ,HC vs. NE ns p=0.52, HC vs. ET ns p>0.26, , HC vs. OT * p=0.02, HC vs. RT * p=0.04, NE vs. ET ns p=0.98, NE vs. OT ns p=0.5, NE vs. RT ns. p=0.65, ET vs OT ns p=0.78, ET vs RT ns p=0.89, OT vs. RT ns p=0.99)
SF 2	c	ET, OT, RT, NE, HC, Δ5d RT	6 mice per group, except HC (7)	Pooled data from 4 different batches.	Matched, Two-way-ANOVA.Group effect: F (5, 32) = 7.21, *** p=0.0001. Group x Observed vs. Expected interaction F (4, 26) = 7.63, *** p=0.0003	Sidak (Observed vs. expected (chance), HC group: ns p=0.99; NE group: ns p=0.74; ET group: *** p=0.0008; OT group: ** p=0.003; RT group: *** p=0.0002; Δ5d RT: ns p=0.52

Supplementary Table 1 (cont.)

Figure	Panel	Groups	n	# replications	Test	Multiple comparison
SF 2	d	DG: Δ0h, Δ6h,Δ12h, Δ24h	3 mice per group	Pooled data from 4 different batches.	Ordinary one-way-ANOVA. Group effect: F (3, 8) = 0.53 ns p=0.67	Sidak (Δ0h vs Δ6h ns p=0.99; Δ0h vs. ,Δ12h ns p=0.99, Δ0h vs., Δ24h ns p=0.96, , Δ6h vs. Δ12h ns p=98, Δ6h vs. Δ24h ns p=0.99, Δ12h vs. Δ24h ns p=0.82
SF 2	d	CA1: Δ0h, Δ6h,Δ12h, Δ24h	3 mice per group	Pooled data from 4 different batches.	Ordinary one-way-ANOVA. Group effect: F (3, 8) = 3.25 ns p=0.08	Sidak (Δ0h vs Δ6h ns p=0.37; Δ0h vs. ,Δ12h ns p=0.96, Δ0h vs., Δ24h ns p=0.58, , Δ6h vs. Δ12h ns p=2, Δ6h vs. Δ24h ns p=0.06, Δ12h vs. Δ24h ns p=0.83
SF 5	c	HC vs HC + Optogenetic Reactivation	HC (n=7), HC + Opto ractivation (n=3)	Data from 1 batch of mice	Two-sided unpaired t test. HC overlap vs. HC overlap + Optogenetic Reactivation: *** p=0.003	NA
SF 5	e	594nm Light vs. No Light	8 mice	Data from 1 batch of mice	Matched two-way-ANOVA. Quadrant effect: F (3, 21) = 37.73, **** p<0.0001. 594nm Light x Quadrant interaction: F (1, 7) = 0.04, ns p=0.98	Sidak (Time in Quadrant, 595nm Light vs. No Light: South ns p=0.99; East ns p>0.99; North ns p=0.99, West ns p>0.99)
SF 5	f	594nm Light vs. No Light	8 mice	Data from 1 batch of mice	Two-sided paired t test. Time in Annulus E (594 nm light vs. No Light): ns p=0.49	NA
SF 6	b	WM Chemogenetic Silencing	10 mice	Data from 1 batch of mice	Simple linear regression. R square 0.67, ** p=0.003.	NA
SF 6	d	WM Chemogenetic Silencing: Low Expression & High Expression	Low Expression 6 mice, High Expression 4 mice	Data from 1 batch of mice	Two-sided unpaired t test. Low vs. High GiDREADD-mCherry Expression: * p=0.01	NA
SF 6	d	WM Chemogenetic Silencing: Low Expression & High Expression	Low Expression 6 mice, High Expression 4 mice	Data from 1 batch of mice	Two-sided unpaired t test. Low vs. High GiDREADD-mCherry Expression: ** p=0.007	NA
SF 6	e	WM Chemogenetic Silencing: High Expression Group	4 mice	Data from 1 batch of mice	Two-sided paired t test. Vehicle vs. CNO: ns p=0.07	NA
SF 6	f	WM Chemogenetic Silencing: High Expression Group	4 mice	Data from 1 batch of mice	Two-sided paired t test. day 7 (Vehicle) vs. day 8(CNO): ns p=0.53	NA
SF 6	h	Subset of mice from the WM Chemogenetic Silencing Group to test CNO effect on cFos expression	3 slices from 1 mouse	Data from 1 batch of mice	Two-sided paired t test. Inside vs. Outside of mCherry+ regions: ns p=0.07	NA
SF 8	a	Δ7d OT	1 mouse (example 1)	3	Spearman r = -0.46, CI: -0.5168 to -0.3938. **** p < 0.0001	NA
SF 8	a	Δ7d OT	1 mouse (example 2)		Spearman r = -0.25, CI: -0.2982 to -0.2075. **** p < 0.0001	NA
SF 8	a	Δ7d OT	1 mouse (example 3)		Spearman r = -0.45, CI: -0.4923 to -0.4146. **** p < 0.0001	NA
SF 10	c	No stimulation, Bicucculine (BIC)	3 slices per group		Unmatched, Two-way-ANOVA F (1, 1416). Region effect: **** p=0.0001. Stimulation effect **** p=0.0001. Region X Stimulation interaction **** p=0.0001	Sidak (DG-noStim. vs. DG-BIC: **** p < 0.0001; DG-noStim. vs. CA1-noStim.: ** p = 0.006; DG-noStim. vs. CA1-BIC: **** p < 0.0001; DG-BIC vs. CA1-noStim: **** p < 0.0001; CA1-noStim vs. CA1-BIC: **** p < 0.0001
SF 11	NA	HC	1 mouse (example)	replicate in Fig. 8	Spearman r = -0.31, CI: -0.3921 to -0.2197. **** p < 0.0001	NA
SF 11	NA	ST	1 mouse (example)	replicate in Fig. 8	Spearman r = -0.41, CI: -0.4661 to -0.3470. **** p < 0.0001	NA
SF 11	NA	DT	1 mouse (example)	replicate in Fig. 8	Spearman r = -0.54, CI: -0.5944 to -0.4766. **** p < 0.0001	NA
SF 11	NA	DT	1 mouse (example)	replicate in Fig. 8	Spearman r = -0.55, CI: -0.6124 to -0.4814. ** p = 0.0011	NA
SF 12	c	HC	1 mouse (example)		Spearman r = -0.14, CI: -0.2122 to -0.05640. *** p = 0.0006	NA
SF 12	c	HC	1 mouse (example)		Spearman r = -0.27, CI: -0.3477 to -0.1950. **** p < 0.0001	NA
SF 12	c	DT	1 mouse (example)		Spearman r = -0.38, CI: -0.4778 to -0.2739. **** p < 0.0001	NA
SF 12	c	DT	1 mouse (example)		Spearman r = -0.19, CI: -0.2732 to -0.09618. **** p < 0.0001	NA
SF 12	c	DT	1 mouse (example)		Spearman r = -0.25, CI: -0.3341 to -0.1631. **** p < 0.0001	NA

Supplementary Table 2

Primary and secondary antibodies

Immunogen	Host	Producer	Factory#	Dilution
cFos	Rat	Synaptic System	226017	1:1000
FosB/ΔFosB	Rabbit	Cell Signaling	#2251	1:1000
tRFP (mKate2)	Rabbit	Evrogen	AB233-EV	1:1000
GFP	Chicken	Invitrogen	A10262	1:1000
Anti-Campari2 red (4F61)	Rabbit	Absolute Antibody	AB1649-23.0	1:1000
FosB	Rabbit	Thermofisher	PA5-79280	1:300
FosB/ΔFosB	Mouse	Abcam	Ab11959	1:300

Immunogen/label	Host	Producer	Factory#	Dilution
Rabbit-488	Goat	Invitrogen	A11008	1:1000
Rabbit-568	Goat	Invitrogen	A11011	1:1000
Chicken-488	Goat	Invitrogen	A11039	1:1000
Rabbit-647	Goat	Invitrogen	A27040	1:1000
Rat-647	Goat	Invitrogen	A21247	1:1000
Mouse-488	Goat	Invitrogen	A11029	1:1000
Mouse-405	Goat	Invitrogen	A31553	1:1000

Publication (preprint) #2: Neuronal FOS reports synchronized activity of presynaptic neurons

Anisimova, Margarita, Paul J. Lamothe-Molina, **Andreas Franzelin**, Aman S. Aberra, Michael B. Hoppa, Christine E. Gee, and Thomas G. Oertner. 2023. “Neuronal FOS Reports Synchronized Activity of Presynaptic Neurons.” ***BioRxiv*.** https://doi.org/10.1101/2023.09.04.556168

Currently being prepared for re-submission

In this study, we clarified that cFOS is not an indicator of a neuron’s own spiking activity, but rather of synchronized activity in the population of presynaptic neurons. I designed and conducted a key experiment (Fig. 5) and was fully responsible for the data analysis and preparation of Fig. 5 and Fig. 6. I also contributed to literature research and manuscript writing.

Neuronal FOS reports synchronized activity of presynaptic neurons

Margarita Anisimova[1,3], Paul J. Lamothe-Molina[1,4], Andreas Franzelin[1], Aman S. Aberra[2], Michael B. Hoppa[2], Christine E. Gee[1]†, Thomas G. Oertner[1]*†

[1] Institute for Synaptic Physiology, Center for Molecular Neurobiology Hamburg (ZMNH), University Medical Center Hamburg-Eppendorf, Hamburg, 20251 Germany

[2] Department of Biological Sciences, Dartmouth College, Hanover, NH, 03755 USA

[3]Present address: Center for Neuroscience, 1544 Newton Court, Davis, CA 95618

[4]Present address: Institute of Pharmacology and Toxicology, University of Zürich, Zürich Switzerland

† these authors contributed equally to this work

* correspondence: thomas.oertner@zmnh.uni-hamburg.de

Abstract

The immediate early gene FOS is frequently used as a marker for highly active neurons. Implicit in this use is the assumption that there is a correlation between neuronal spiking and FOS expression. Here we use optogenetic stimulation of hippocampal neurons to investigate the relation between spike frequency and FOS expression, and report several surprising observations. First, FOS expression is cell-type specific, spiking CA2 pyramidal neurons rarely express FOS. Second, FOS has a U-shaped dependence on frequency: Spiking at 0.1 Hz is more effective than high frequency spiking (50 Hz) while intermediate frequencies do not induce FOS. Third, the pathway from spiking to FOS is not cell-autonomous. Instead, transmitter release and metabotropic glutamate receptor (mGluR) activation are required and, at 0.1 Hz, FOS is induced independently of CREB/calcineurin/MEK pathways. We propose that FOS does not primarily encode a neuron's own spike frequency but indicates repeated participation in highly synchronized activity, e.g. sharp wave ripples.

Introduction

More than 30 years ago, Morgan et al. reported that expression of FOS (Finkel–Biskis–Jinkins murine osteogenic sarcoma virus) protein increased in the brain following seizures (*1*). The ensuing search for activity-dependent genes yielded a large number of upregulated genes. The fastest upregulated (15 – 60 min), known as immediate early genes (IEG), are mostly transcription factors like FOS, which in turn increase expression of proteins involved in neuronal growth and synaptic plasticity (*2*, *3*). In addition to its role as a transcription factor, FOS also has direct effects on lipid synthesis in neurons (*4*). The availability of excellent antibodies popularized the use of FOS as a marker of neuronal activity not only in pathological conditions, but also during learning and memory recall. The creation of a transgenic mouse line using the FOS promoter to express a protein of interest specifically in active neurons was a revolutionary innovation (*5*). Expressing optogenetic tools under FOS control allowed manipulating the activity of a defined subset of neurons. For example, when channelrhodopsin expression is induced in mice during fear conditioning, light-induced reactivation of this subset of neurons produces a strong fear response (*6*, *7*). The functional importance of FOS-positive neurons is not restricted to fear memory; spatial memories are also affected when FOS-positive neurons are inhibited (*8*).

Despite the widespread use of FOS as a marker of active neurons, surprisingly little is known about the relationship between neuronal firing and FOS expression. The *fos* promoter is a point of convergence for several activity-dependent signaling pathways (*9*). Activity-dependent induction occurs when serine 133 phosphorylated calcium/cAMP response element binding protein (pCREB) dimerizes with CREB binding protein (CBP) and binds to the *cre* (cAMP response element) of the *fos* promoter. CREB is phosphorylated by several kinases including cAMP-dependent protein kinase A (PKA), calcium calmodulin dependent kinase IV (CaMKIV), protein kinase C (PKC), and ribosomal S6 kinases (RSKs). A second activity-dependent

regulator is the phosphatase calcineurin, which dephosphorylates Rb (Retinoblastoma) and de-represses *fos*. The SRE (serum response element) is a third site that may confer activity-dependence on the initiation of FOS expression. Some of these pathways are primarily activated by calcium, some by growth factors (via receptor tyrosine kinases) or G-protein coupled receptors (GPCRs). In most studies of FOS expression, neurons were activated by chemical stimulation (high K^+) or by pharmacologically induced seizures. The sodium channel blocker TTX efficiently blocks FOS expression, which led to the conclusion that high-frequency spiking is a key trigger for FOS expression (*10*). Accordingly, long high-frequency bursts of action potentials drive FOS expression in individual CA1 pyramidal neurons (*10*) but are arguably outside the envelope of physiological activity patterns. In cultured neurons, stimuli delivered in repetitive short bursts drive FOS more efficiently than long duration trains of single action potentials, but FOS induction was not correlated with intracellular calcium levels (*11–13*). In vivo calcium imaging studies also found surprisingly weak correlations between the frequency or amplitude of calcium transients and FOS expression in individual neurons during learning (*14–16*). As its complex transcriptional regulation already suggests, FOS seems to be more than a simple reporter of intracellular calcium or spike frequency.

We decided to investigate the relationship between neuronal spiking and FOS expression under highly controlled conditions in rat hippocampal slice culture. We used the red-light-sensitive channelrhodopsin ChrimsonR to drive action potentials in neurons while blocking fast synaptic transmission to prevent spontaneous and propagating activity. As anticipated, high frequency stimulation (50 Hz) drove FOS expression dependent on the number of action potentials, whereas frequencies between 1 and 10 Hz were ineffective. Unexpectedly, we observed the strongest and most consistent FOS expression following stimulation at 0.1 Hz. Pharmacological dissection revealed that FOS induction at all stimulation frequencies required mGluR activation and was therefore not cell-autonomous. Furthermore, glutamate application or chemogenetic

activation of G_q was sufficient to induce FOS in the absence of any action potentials (TTX). We conclude that FOS is best triggered by synchronized glutamate release events repeating roughly every 10 seconds. In vivo, such high synchrony events (sharp-wave ripples) occur frequently during periods of quiet rest and slow-wave sleep and have been causally linked to memory consolidation (*17*) and long-term potentiation (*18*, *19*). We propose that FOS and its downstream proteins are specifically upregulated in neurons that repeatedly participate in ripple events, even if they fire only a single action potential per ripple.

Results

To determine how neuronal activity relates to FOS expression, we needed to precisely induce action potentials (APs) across all hippocampal subfields. To prevent synaptically driven spiking, NBQX, CPPene and picrotoxin were added during optogenetic stimulation to block AMPA, NMDA and $GABA_A$ receptors, respectively. Pyramidal cell subtypes differ in their capacitance, input resistance and resting membrane potential (Fig. 1A), leading to a higher firing threshold in CA3 pyramidal neurons (PNs) when driven by somatic current injections (Fig. 1B). For non-invasive spike induction, we virally transduced organotypic slice cultures with the channelrhodopsin ChrimsonR (Fig. 1C). Using 1 ms flashes of a 625 nm LED (Fig. 1D), we found that the light intensity threshold for spike induction was not different for CA1 and CA3 PNs (Fig. 1E). This finding also held true for CA2 neurons and for a blue-light sensitive channelrhodopsin (CheRiff, fig. S1). Apparently, the larger membrane area of CA3 PNs contains proportionally more ChrimsonR channels, compensating for the differences in neuronal size and capacitance (*20*). At a light intensity of 7 mW/mm^2, we were able to drive AP trains in different hippocampal subfields with high reliability over a wide range of frequencies (Fig. 1F).

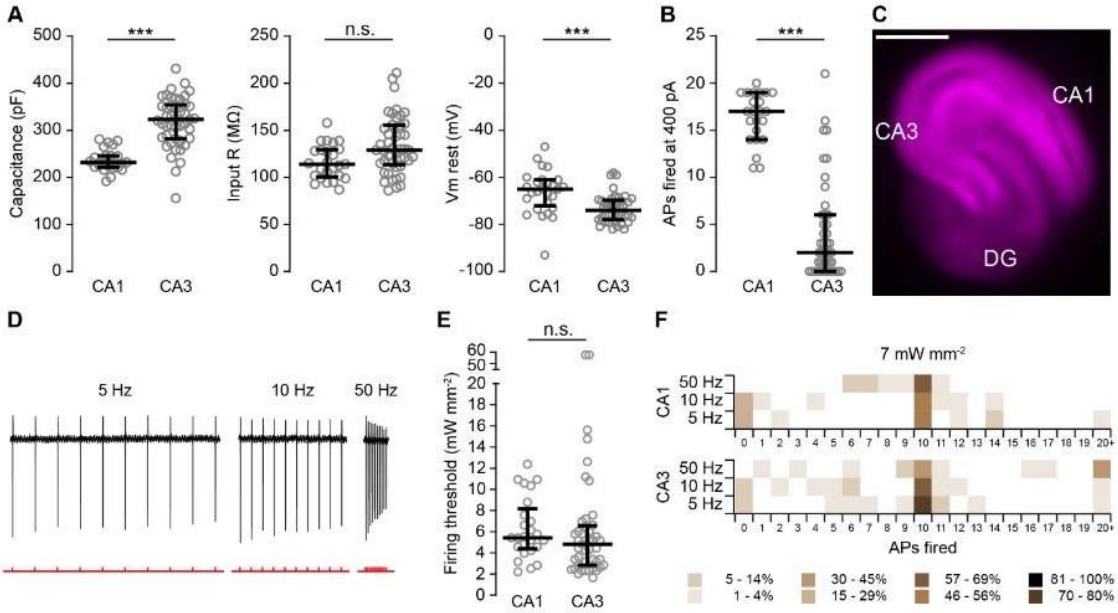

Figure 1: Optogenetic spike threshold is independent of cell size. (A) Whole-cell patch clamp recordings from pyramidal neurons in CA1 and CA3 show lower capacitance (*** $P < 0.0001$), similar input resistance ($P = 0.05$) and less negative membrane potential (V_m; *** $P < 0.0001$) of CA1 pyramidal neurons (CA3: $n = 45$; CA1: $n = 25$; Kolmogov-Smirnov tests). Capacitance and input resistance were measured in voltage clamp, V_m in current clamp. **(B)** The number of action potentials (APs) fired during a 600 ms, 400 pA somatic current injection (CA3: n = 44; CA1: n = 25; *** $P < 0.0001$). **(C)** Organotypic hippocampal culture transduced with AAV$^{2/Rh10}$-synapsin-ChrimsonR-tdTomato (magenta). Scale bar 500 µm. **(D)** Optogenetic stimulation of CA1 pyramidal neuron at different frequencies while recording in cell-attached mode. NBQX (10 µM), CPPene (1 µM) and picrotoxin (100 µM) were included to block AMPA, NMDA and $GABA_A$ receptors during optogenetic stimulation. **(E)** When driven to spike with light pulses of variable intensity, the firing threshold was not different in CA1 and CA3 pyramidal neurons (CA1: $n = 25$; CA3: $n = 45$; $P = 0.27$, K-S test). **(F)** The majority of pyramidal cells fired exactly 10 action potentials in response to 10 light pulses delivered at 5, 10, or 50 Hz. Plotted are individual data points, median and 25 % to 75 % interquartile range.

As a positive control, we applied high K^+ (2 x 2 min, 50 mM K^+ without inhibitors of postsynaptic receptors) and determined that fixing the slices 60 min later is a good compromise for detecting rapidly induced FOS in CA3 and DG neurons as well as the more slowly accumulating FOS in CA1 PNs (fig. S2). By 90 min, FOS immunoreactivity had almost disappeared from CA3 neurons whereas FOS was still increasing in CA1. We next compared the fraction of

ChrimsonR$^+$ neurons expressing FOS in different regions of the hippocampus after high K$^+$ stimulation and after optogenetic induction of 300 APs at 50 Hz inside a cell culture incubator (Fig. 2A). The CA2 region was identified by immunostaining against PCP4/PEP-19 (Fig. 2B), an established marker for CA2 (*21*). Both optogenetic and high K$^+$ stimulation produced strong FOS expression in CA1, CA3 and DG, but not in the CA2 region, where significantly fewer neurons expressed FOS (Fig. 2C, D). ChrimsonR expression was homogeneous across all areas and we confirmed that optogenetic stimulation reliably induced APs in all hippocampal subfields (Fig. 1, fig. S1). We conclude that the propensity for FOS expression, and also the time to peak FOS (fig. S2), are systematically different in different cell types. These findings indicate that absence of FOS may not indicate absence of activity, as we have previously observed in DG granule cells (*8*).

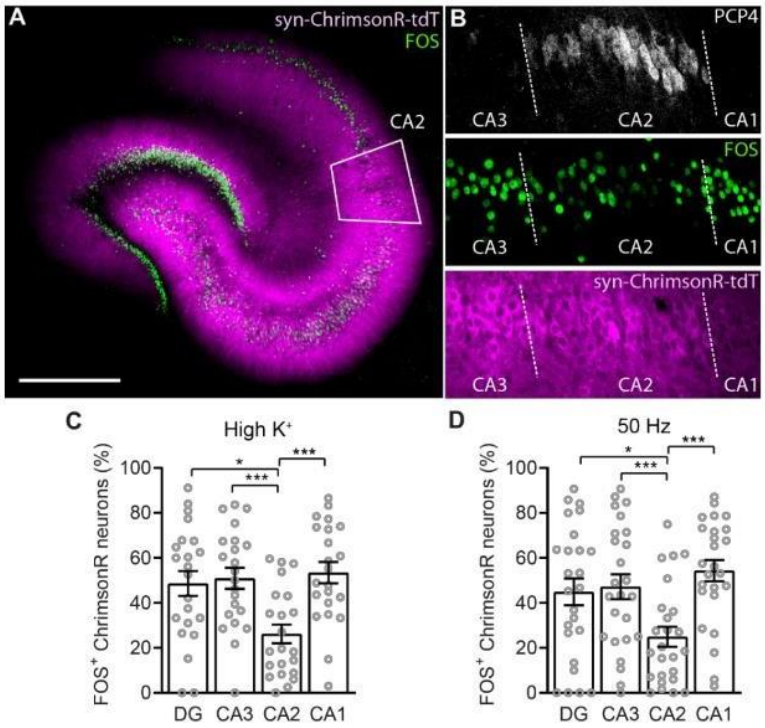

Fig. 2: Activity-induced FOS expression depends on cell type. (A) A hippocampal slice culture transduced with AAV$^{2/Rh10}$ syn-ChrimsonR-tdTomato (magenta) illustrating widespread high K$^+$ stimulated

FOS immunostaining (green) in all cell body layers except CA2 (white trapezoid). Slice was fixed 60 min after high K^+ stimulation. Scale bar 500 µm. **(B)** Single optical section confocal image of a slice stimulated to fire 300 action potentials at 50 Hz, fixed 60 min later and immuno-stained for PCP4 (Purkinje cell protein 4, a marker for CA2 neurons), FOS (green) and ChrimsonR-tdTomato (magenta). White dashed lines indicate the region defined as CA2. Optogenetic stimulation was always performed in the presence of AMPA, NMDA and $GABA_A$ receptor inhibitors to block fast synaptic transmission (see Fig. 1). **(C)** The proportion of ChrimsonR-tdTomato-expressing neurons in the dentate gyrus (DG), CA3, CA2 and CA1 that expressed FOS (FOS^+) one hour after stimulation with high K^+. Neurons were distinguished from other cell types by tdTomato fluorescence. *n* = 22 slices. Circles correspond to individual slices, bars show mean ± SEM. **(D)** same as C, but stimulation was 300 light flashes, 625 nm, 8 mW mm^{-2} at 50 Hz. *n* = 25 slices. * $p < 0.05$, *** $p < 0.001$, RM ANOVA, Tukey's multiple comparisons.

Next, we explored the number and frequency of APs required for FOS activation. Following in-incubator light stimulation and immunostaining, we counted the number of FOS-expressing neurons in fixed-size ROIs in CA1, CA3 and DG and normalized them to non-stimulated and high K^+ treated slices to correct for potential variability in the staining of batches (two-point normalization, see fig S3 for non-normalized counts). When stimulated at 50 Hz, FOS expression monotonically increased with the number of light-induced APs (Fig. 3A, B). As 300 light pulses reliably triggered FOS expression, we used this number of pulses to investigate the frequency dependence. To our surprise, the relationship between firing frequency and FOS expression was not monotonically increasing, but strongly bimodal (Fig. 3C). 50 Hz stimulation induced significant FOS expression in DG, CA3 and CA1 (fig. S3), but stimulation at 0.1 Hz was even more effective. To better mimic the stochastic occurrence of synchronized events in the brain, we generated trains of 300 light pulses with Poisson-like statistics (excluding ISIs < 40 ms). Poisson trains with a rate of 0.1 Hz were as effective as regular-spaced 0.1 Hz trains in inducing FOS (Fig. 3D), suggesting that the precise inter-pulse intervals are not critical. As the sodium channel blocker TTX prevented FOS expression at all frequencies (Fig. 3D), induction of FOS required active spiking.

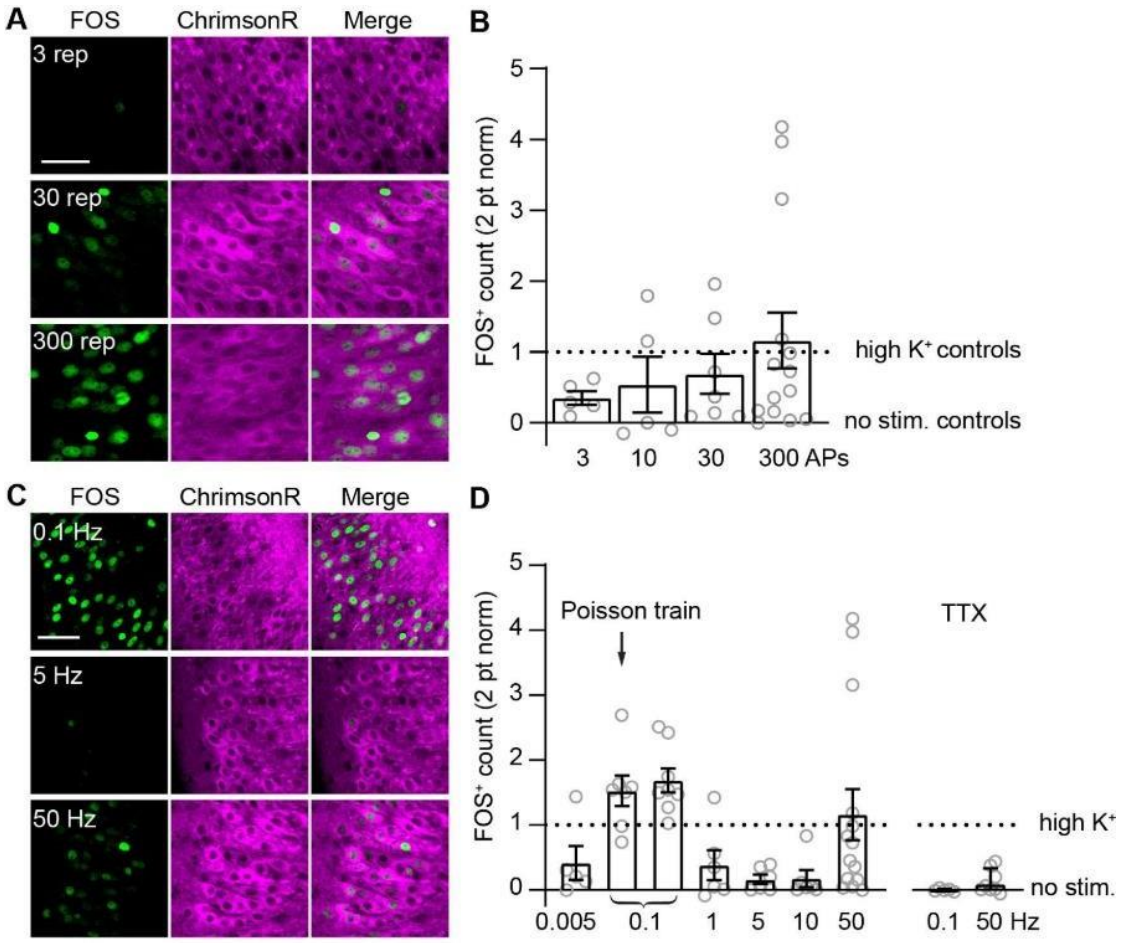

Figure 3: FOS is induced at high and low, not intermediate frequencies. (A) CA3 region of hippocampal slices expressing synapsin-ChrimsonR-tdTomato (magenta) and stimulated to fire 3 - 300 action potentials (APs) with AMPA, NMDA and $GABA_A$ receptors inhibited. The number of neurons expressing FOS (green) increased with the number of APs. Images are single optical confocal sections. Light stimulation: 1 ms, 625 nm, 50 Hz. **(B)** Total count of FOS^+ neurons normalized to high K^+ and non-stimulated control slices included in each batch according to: $x(norm) = (x - min(x))/(max(x) - min(x))$. Circles correspond to individual slice cultures (n = 5, 5, 7, 14), averaging FOS^+ count in DG, CA3 and CA1. Bars show mean ± SEM. **(C)** As in (A) but stimulated to fire 300 APs at different frequencies. **(D)** As in (B) but experiments as shown in (C) Note that 300 APs at 50 Hz is the same data as shown in (B). At 0.1 Hz the stimulation was applied either regularly or as a Poisson train (3 different trains, minimum interval 40 ms, 2-3 slices each). Tetrodotoxin (TTX 1 µM) blocks voltage gated sodium channels and prevents AP generation. n = 5, 7, 8, 6, 6, 6, 14, 5, 8. Scale bars 50 µm.

To better understand the molecular mechanism of FOS induction we targeted three candidate pathways known to induce FOS (Fig. 4A): 1) the phosphoCREB-CBP interaction (666-15), 2) MAPK/ERK - Elk-1/SRF (MEK inhibitor U0126), 3) calcineurin-mediated Rb dephosphorylation (cyclosporin A). As expected, a cocktail of these inhibitors completely blocked FOS induction by high K^+ and 50 Hz stimulation, while individual inhibitors had less consistent effects against 50 Hz induction (Fig. 4B, C). To our surprise, the same cocktail did not prevent FOS expression after 0.1 Hz stimulation, indicating that other signaling pathways are involved (Fig. 4D). Although we blocked activation of fast (ionotropic) postsynaptic receptors, glutamate and other transmitters would still be released by the synchronously spiking neurons. To maintain synchronous spiking but prevent transmitter release, we virally co-expressed ChrimsonR and a G_i-coupled DREADD (*22*, *23*). Under the chemogenetic block of transmitter release, 0.1 Hz stimulation no longer induced FOS, and unexpectedly, even high K^+-stimulated FOS depended on transmitter release (Fig. 4E, G). This finding strongly argues against the existence of a cell-autonomous spike-driven pathway that leads to FOS expression (*9*, *24*). A parsimonious explanation is that FOS is expressed when postsynaptic neurons receive synchronously released transmitter from many presynaptic neurons. The mGluRs, which respond to both glutamate transients from nearby release sites and spillover from distant synapses, are ideally suitable for detecting such events (*25*). Indeed, neuronal FOS absolutely required mGluR signaling, as antagonizing mGluRs prevented FOS induction by high K^+, 50 Hz and 0.1 Hz stimulation (Fig. 4E-G).

Group I mGluRs are found near postsynaptic densities and are G_q-coupled. We used a chemogenetic approach to test whether activation of G_q in neurons is sufficient induce FOS in the absence of electrical activity. Activating G_q-DREADD with CNO in the presence of TTX induced FOS in about half of transfected neurons (Fig. 4H, I). G_i activation and all other pharmacological treatments did not induce FOS in non-stimulated cultures (Fig S4). In

summary, FOS induction is not a cell-autonomous process (Fig. 4A), but involves communication between neurons via transmitter release (Fig. 4J).

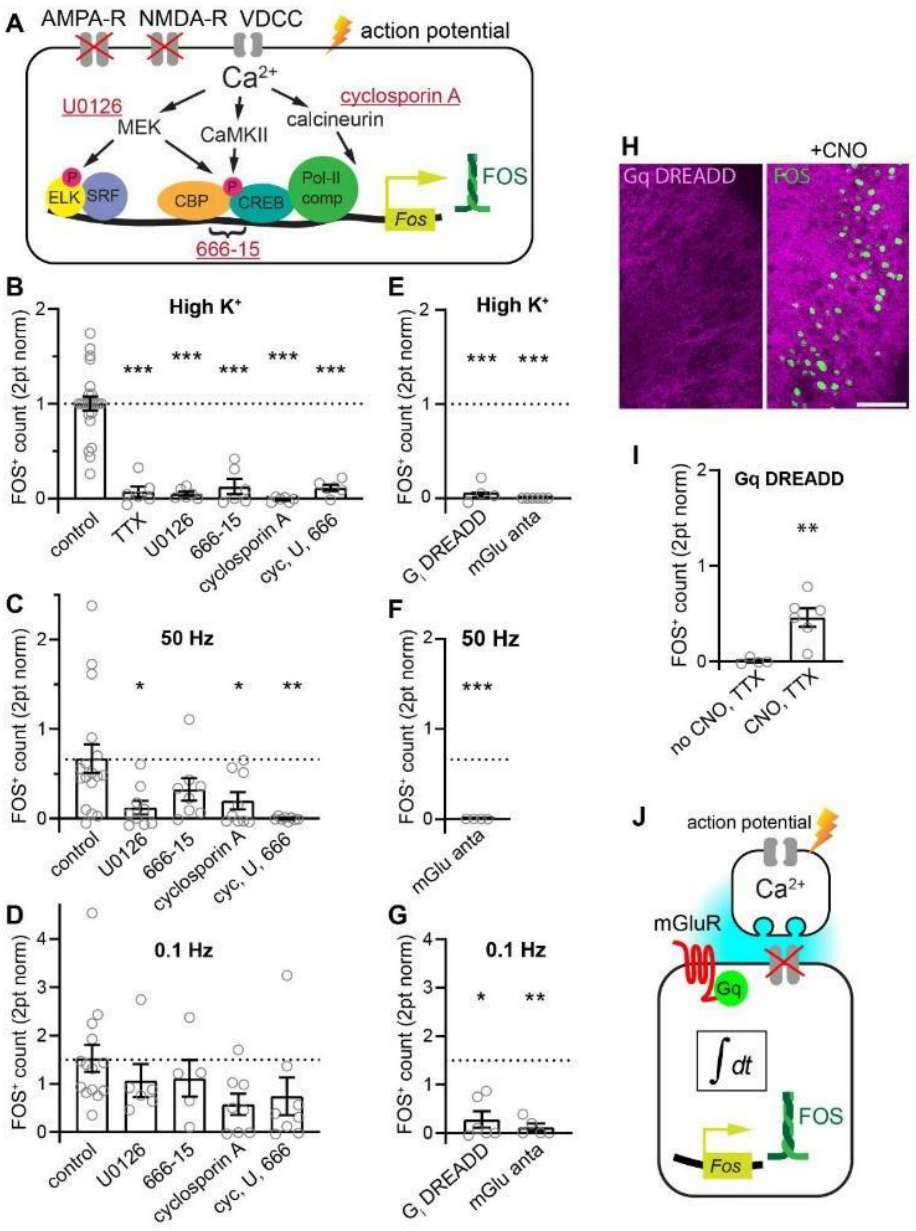

Figure 4: Low and high frequency-induced FOS use different pathways and depend on mGluRs. **(A)** Simplified scheme illustrating the presumed main activity-dependent pathways controlling FOS expression and the inhibitors used. Action potentials trigger calcium influx through voltage-dependent calcium channels (VDCC). U0126 (10 µM) antagonizes mitogen-activated protein kinase kinase 1/2

(MEK1/2) whose activity leads to activation of serum response factor (SRF) or phosphorylation of cAMP-dependent responsive element binding protein (CREB). 666-15 (666, 800 nM) blocks the interaction of pCREB and CREB binding protein (CBP) which initiates transcription of FOS. Cyclosporin A (cyc 500 nM) inhibits calcineurin which promotes FOS expression by dephosphorylating Rb and releasing transcription (not illustrated). The compounds were applied the evening before stimulating individually or together (cyc, U, 666). **(B)** Number of neurons expressing FOS one hour after stimulation (300 x 0.1 Hz). None of the compounds significantly inhibited FOS induced by 0.1 Hz firing. Normalization to positive (high K^+) and negative (no stim.) controls as in Fig. 3. Circles correspond to individual slice cultures, bars show mean ± SEM. AMPAR-, NMDAR- and $GABA_A$ inhibitors were present. **(C)** Number of neurons expressing FOS after high K^+ stimulation. FOS expression was inhibited by tetrodotoxin (TTX 1 µM) and by the inhibitors of the pathways illustrated in (A) n = 23, 6, 6, 6, 6, 6. **(D)** As in (B) except slices were fixed one hour after 50 Hz stimulation. n = 17, 9, 8, 9, 8. **(E)** Number of neurons expressing FOS one hour after stimulation to fire 300 APs x 0.1 Hz while transmitter release was inhibited by activation of co-expressed G_i-DREADD with clozapine-*N*-oxide (CNO) or metabotropic glutamate receptors were antagonized with 2 µM YM298198, 5 µM MPEP and 100 µM MSPG (mGlu anta). AMPAR-, NMDAR- and $GABA_A$ inhibitors were present. n = 4, 6 **(F, G)** As E) but after high K^+ (n = 4, 6) and 300 x 50 Hz stimulation (n = 4). **(H)** CA1 region of slices expressing G_qDREADD one hour after applying vehicle or CNO. TTX (1 µM) and inhibitors of AMPA-, NMDA- and $GABA_A$ receptors were applied the evening before. n = 4, 6. Scale bar 100 µm **I)** Quantification of experiments as in H). **(J)** Key steps in FOS activation missing from the schema in (A). Induction of FOS requires action potentials and glutamate release from presynaptic cells, activation of mGluRs and a temporal integration mechanism ($\int dt$). *P < 0.05; **P < 0.01; ***P < 0.001.

To test the hypothesis that solely firing presynaptic neurons is sufficient to induce FOS in postsynaptic neurons, we made use of the Schaffer collateral pathway. We locally injected ChrimsonR AAV to restrict spiking to CA3 neurons (Fig. 5A to C). With fast synaptic transmission inhibited, stimulation at 0.1 Hz induced FOS throughout the postsynaptic CA1 region (Fig. 5C to G). In contrast, very few ChrimsonR-expressing CA3 neurons expressed FOS (Fig. 5F). This experiment directly demonstrates that FOS is not an indicator of spiking neurons per se, rather, FOS expression indicates which neurons recently received synchronized glutamatergic input.

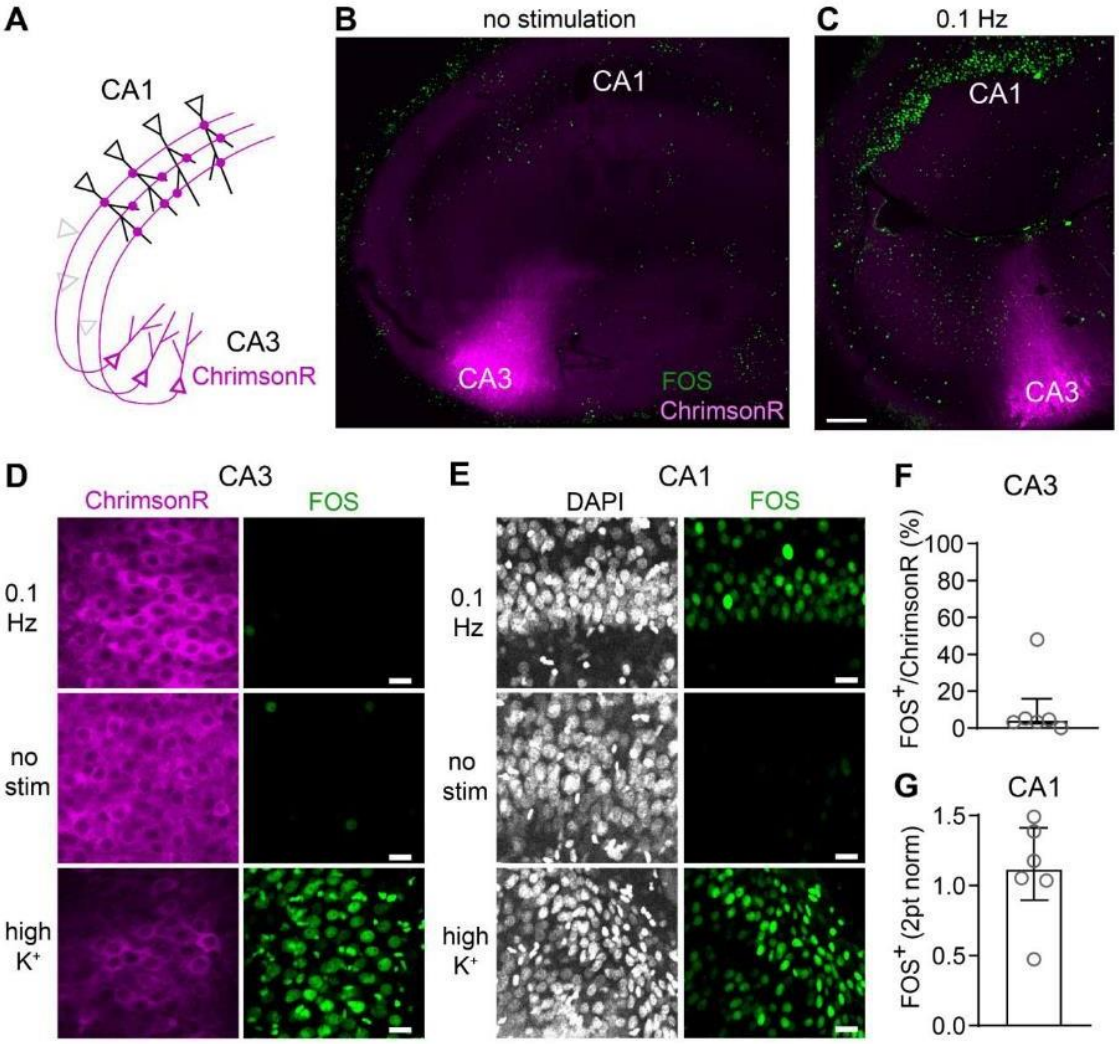

Figure 5: Presynaptic stimulation induces postsynaptic FOS. (A) Schema illustrating experiment designed to test whether synaptically released glutamate is sufficient to induce mGluR-dependent postsynaptic FOS. **(B)** Control non-stimulated organotypic culture with a cluster of ChrimsonR-expressing CA3 pyramidal neurons (magenta) stained for FOS (green) expression. **(C)** As in B but stained one hour after stimulation with 300 light pulses at 0.1 Hz. Scale bar: 100 µm applies to B and C. **(D, E)** FOS is not expressed in the optogenetically driven presynaptic neurons (CA3), but in the target region (CA1). Scale bars: 20 µm. **(F)** Following 0.1 Hz stimulation, FOS was expressed in a small fraction of the ChrimsonR-transfected CA3 neurons (3.2%, median with interquartile range, n = 6 cultures). **(G)** FOS expression in CA1 normalized to the non-stimulated and high K^+ treated cultures (median with interquartile range, n = 6 cultures).

Neuronal postsynaptic mGluRs are localized outside the synaptic cleft, in an annular region (~100 nm) around the postsynaptic density (*26*). We reasoned that if released glutamate was rapidly diluted from the interstitial space, synchronous spiking would not induce FOS. To create a situation with vastly increased extracellular volume, we applied our induction protocols to dissociated cultured hippocampal neurons in a laminar flow chamber, using electrical instead of optogenetic stimulation (*27*). One hour after the end of stimulation, there was no trace of FOS induction in neurons stimulated at 0.1, 5 or 50 Hz in the presence of antagonists of AMPA and NMDA receptors (Fig. 6A, B). In contrast, directly applying glutamate to stimulate mGluRs strongly induced FOS expression in the cultured neurons (Fig. 6C, D). The dependence on mGluRs was confirmed as there was no effect of inhibiting AMPA, NMDA and $GABA_A$ receptors during glutamate application. Similarly, inhibiting fast synaptic transmission did not reduce high K^+ induced FOS in slice cultures, in line with the requirement for mGluRs (Fig. S5, 4B). As the pan-mGluR agonist L-CCG-1 at both low (10 µM) and high (500 µM) concentrations induced FOS, high affinity (mGlu1-3, 5, 8) rather than low affinity mGluRs (mGlu4 and mGlu7 homomers) are required for FOS expression (Fig. 6C, D).

In the high K^+ experiments, both in slices and dissociated neuronal cultures we noted strong FOS immunoreactivity not only in neurons but also in glia cells (see Figs. 5, 6 and figs. S2, S3). Astrocytes become a powerful source of glutamate under such conditions (*28*) and may contribute to the neuronal mGluR-dependent FOS expression (Fig. 4E).

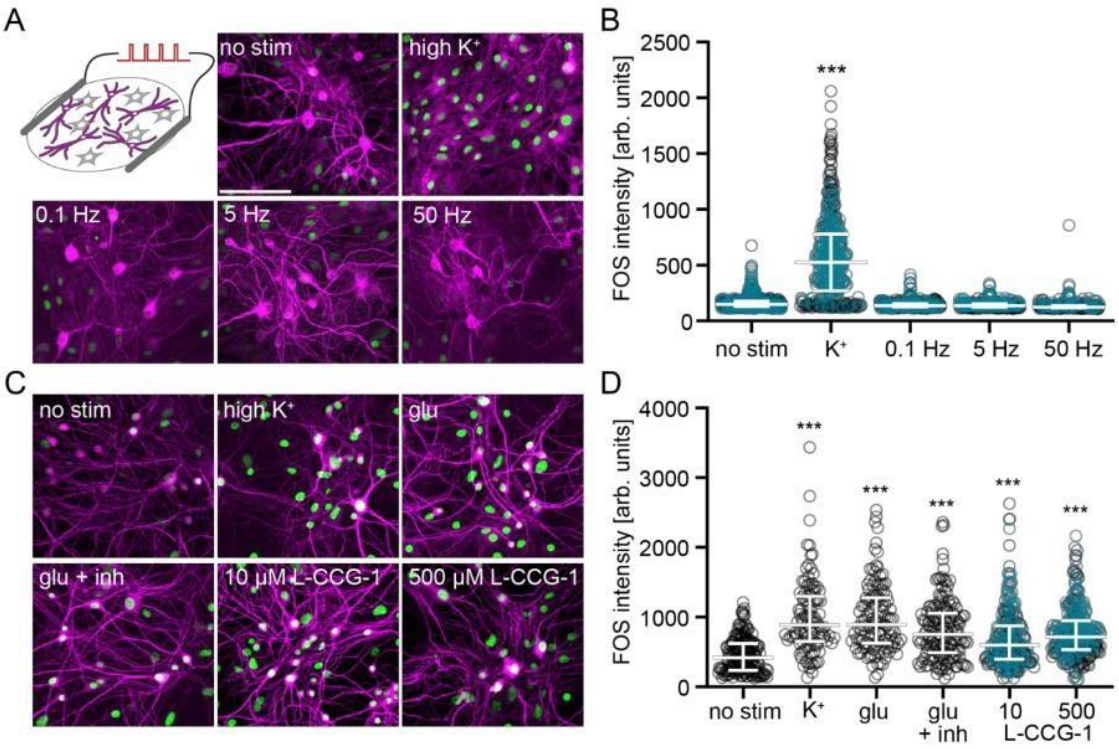

Figure 6: Activation of mGluRs rather than electrically-driven spiking drives FOS in cultured hippocampal neurons. (A) Exemplary FOS staining (green) of hippocampal neurons (magenta, MAP2 staining) 1 h after electrical stimulation, high K^+, or no stimulation (no stim). Note co-localized green and magenta nuclei appear white. **(B)** FOS intensity of MAP2 positive neurons from 2 independent experiments as in A. Circles are intensity of individual neurons, colors indicate different experiments. **(C)** Exemplary FOS staining (green) of MAP2 positive neurons exposed to 50 µM glutamate, 50 µM glutamate + CNQX, APV, picrotoxin to selectively stimulate mGluRs (glu + inh) and the broad-spectrum mGlu agonist L-CCG-1 in the presence of CNQX, APV, picrotoxin to prevent fast synaptic transmission. Different colors indicate independent plates of cultures. **(D)** FOS intensity of MAP2 positive neurons. *** significant increase in FOS compared with no stim ($p < 0.0001$), Kruskall-Wallis followed by Dunn's multiple comparisons. Shown are individual values, median and interquartile range. Scale bar 100 µM applies to all panels.

Discussion

Our study, which started as a simple calibration attempt to define the relationship between spiking and FOS expression, produced some unexpected results. We expected that a given spiking pattern would similarly drive FOS in all hippocampal principal cells, but we observed that some neurons, i.e., in CA2, express less FOS, whereas the time course of expression differs in others. Surprisingly, the very low frequency of 0.1 Hz stimulation produced more FOS than high frequency (50 Hz) stimulation when the number of action potentials remained at a constant 300. This observation was particularly notable as stimulating the neurons at intermediate frequencies (1 and 5 Hz) almost completely failed to induce FOS. In fact, spiking per se was neither necessary nor sufficient to induce FOS. Rather transmitter release and subsequent activation of mGluRs was necessary, and activation of neuronal G_q signaling was sufficient to induce FOS when spiking was prevented.

Thus, FOS induction is not a cell-autonomous integration of spike-induced calcium influx (*9*, *29*), but a network effect, where individual neurons use GPCRs to detect peaks of extracellular glutamate concentration, integrating this signal over long periods of time (~1 h). Of course, the same neurons which are receiving and sensing these waves of excitatory glutamatergic input will normally be participating and firing in phase with the input (*30*). The fact that neurons will usually be firing explains how the rather indirect, inter-cellular relationship between activity and FOS has been missed until now. The disconnect between activity (assessed by calcium imaging) and FOS expression at the single cell level has been noted in several studies (*11–13*, *31*). Without the ability to separate postsynaptic from presynaptic spiking afforded by optogenetic tools, however, it was difficult to determine which neurons had to be active to induce FOS (*32*).

As our aim was to define the relationship between simple neuronal spiking and FOS, we purposely inhibited both AMPA and NMDA type glutamate receptors together with $GABA_A$

receptors throughout most of this study. Certainly, these receptors contribute to FOS induction either indirectly, by increasing network activity and release of transmitter, or directly by permitting calcium influx (*32*, *33*). Speaking against a direct role of AMPA/NMDA receptors is, however, our observation that FOS induction by high K^+ was unaffected by their inhibition. Also, in dissociated cell cultures, exogenous glutamate induced the same amount of FOS with and without AMPA/NMDA inhibitors.

In addition to mGluRs, neuromodulators such as dopamine or acetylcholine, via their G_q-coupled receptors, likely contribute to FOS activation during behavior. We speculate these additional receptors may reduce the required fraction of synchronously active presynaptic neurons (and/or the number of repeats) to reach the threshold for FOS induction. Precedents for different types of GPCRs operating in an additive, mutually supporting fashion exist. For example, if mGluRs are blocked, muscarinic M1 receptor agonists restore LTP induced by sharp wave ripple (SWR) type activity (*19*). A candidate mechanism for integrating periodic mGlu activation involves the endoplasmic reticulum (ER). Recently identified mechanisms that link electrical activity with calcium accumulation in the ER (*34*) suggest that the ER could act as a cellular memory of past electrical activity. In this scenario, the magnitude of mGlu-mediated release events would be a function of past activity in that neuron.

What could be the physiological equivalent of our synchronized optogenetic stimulation? Synchrony at 50 Hz (gamma band) does occur during epileptic episodes and indeed leads to massive FOS expression, but is rather unlikely in healthy animals. A prominent activity pattern in the healthy hippocampus are sharp wave ripples (SWRs), high frequency field oscillations inside a short time window (20 – 100 ms) (*17*). Importantly, individual CA1 pyramidal cells typically fire only one or two APs during a single ripple (*35*). SWRs do not occur while the animal is moving, but during quiet wakefulness and slow-wave sleep, more frequently after learning (*17*, *36*). During SWRs, previously active place cells are reactivated (*37*). Strikingly,

during periods of immobility or drinking in a maze, mice produce one SWR every 10 seconds, on average (*35*). We propose that our 0.1 Hz optogenetic stimulation may have produced glutamate transients that resemble those experienced by neurons that repeatedly participate in SWRs. Interestingly, oscillations at 0.1 Hz are also prominent in the human electroencephalogram, consistent with cortical synchronization events repeating at this frequency (*38*, *39*).

Replay of activity sequences during SWRs is important for memory consolidation (*18*, *40*). Synaptic potentiation occurs when pre-before-postsynaptic spike sequences are repeatedly combined with ripple-like subthreshold synaptic input (*19*, *41*). Our findings suggest that activation of mGluRs could be the "third factor" promoting LTP induction in these experiments (*42*, *43*). Indeed, it has been shown that FOS^+ neurons are more strongly connected to other FOS^+ neurons compared to their neighbors, adding credibility to the idea that FOS may be a marker of the subnetworks that participate in ripples (*44*).

The current study raises some questions which merit further investigation. For instance, are the mGluRs required for FOS induction exclusively located on neurons, or are glial mGluRs also involved in FOS induction (*45*)? How is the activity of metabotropic receptors integrated over long periods of time and what signaling pathway connects the mGluR activation with FOS? Furthermore, we cannot explain why intermediate stimulation frequencies (1-10 Hz) failed to induce FOS in hippocampal neurons, but are reportedly effective in DRG neurons (*13*). Did these frequencies engage specific FOS suppression mechanisms, e.g. transcriptional repression by DREAM (*46*), or would we eventually see FOS expression if we continue to stimulate at 5 Hz? The parameter space of possible stimulation patterns is almost limitless, but we plan to address some of these questions in future experiments.

Our study has uncovered a GPCR-mediated mechanism that could inform individual neurons whether they are part of a well-synchronized active subnetwork and should ramp up synaptic

plasticity (*47*). When using FOS to identify and reactivate “engram ensembles” (*7*, *48*), it is important to keep in mind that these neurons may have never fired at high frequency, but are distinguished by the fact that they participated repeatedly in highly synchronized events. This insight puts a new perspective on optogenetic recall experiments (*6*, *48*), potentially explaining why simple synchronous activation, rather than recreating the precise temporal firing sequence, is sufficient to trigger memory recall.

Materials and Methods

Experimental animals

Wistar rats were housed and bred at the University Medical Center Hamburg-Eppendorf (UKE) animal facility and sacrificed according to German Law (Tierschutzgesetz der Bundesrepublik Deutschland, TierSchG) with approval from the Behörde für Justiz und Verbraucherschutz (BJV)-Lebensmittelsicherheit und Veterinärwesen Hamburg and the animal care committee of the UKE. Dissociated neuronal cultures were generated from Sprague–Dawley rat pups (p1) of either sex according to animal protocol number 0002115, approved by Dartmouth College’s Institutional Animal Care and Use Committee.

Hippocampal slice cultures

The procedure for preparing organotypic cultures (*49*) was modified using media without antibiotics (*50*). Briefly, P5-P6 rats of either sex were anesthetized with 80% CO_2 / 20% O_2 and decapitated. Using sterile procedures, the hippocampi were removed and 400 µm slices cut on a tissue chopper (McIlwain). Slices were placed on membrane inserts (Millipore, PICMORG50) in 6-well plates and maintained in an incubator at 37°C with 5% CO_2. Slice culture medium contained (for 500 ml): 394 ml Minimal Essential Medium (Sigma M7278), 100 ml heat inactivated donor horse serum (H1138 Sigma), 1 mM L-glutamine (Gibco 25030-024), 0.01 mg ml^{-1} insulin (Sigma I6634), 1.45 ml 5 M NaCl (S5150 Sigma), 2 mM $MgSO_4$ (Fluka

63126), 1.44 mM $CaCl_2$ (Fluka 21114), 0.00125% ascorbic acid (Fluka 11140), 13 mM D-glucose (Fluka 49152).

Primary neuronal culture, stimulation and immunohistochemistry

Primary hippocampal neurons were cultured from hippocampi with dentate gyrus removed, from postnatal day 1 Sprague–Dawley rats of both sexes. Briefly, hippocampal CA1-CA3 regions were digested with trypsin for 5 min at room temperature and dissociated into single cells. Cells were seeded inside a 6-mm-diameter cloning cylinder on polyornithine-coated glass coverslips. For the electrical stimulation experiments, coverslips were mounted in a laminar-flow perfusion and stimulation chamber. Cells were perfused continuously at a rate of 0.4 mL/min in Tyrode's solution containing the following (in mM): 119 NaCl, 2.5 KCl, 2 $CaCl_2$, 2 $MgCl_2$, 25 Hepes, and 30 glucose with 10 µM CNQX, 50 µM APV, and 100 µM picrotoxin during experiments. APs at 0.1, 5, or 50 Hz were evoked by passing 1 ms current pulses, yielding fields of ~12 V/cm, through the chamber via platinum/iridium electrodes. All experiments were performed at 34 - 35°C. After 300 APs were evoked, cultures remained in perfusion for an additional hour before fixation. As a positive control, cultures were placed in high potassium (70 mM KCl) Tyrode's solution lacking synaptic blockers (with equimolar substitution of NaCl) in an incubator for two 5 min periods, after which the cultures were placed back in normal culture media for one hour before fixation. For chemical stimulation, cultures were incubated for two 5 min periods in Tyrode's containing 50 µM L-glutamic acid (Sigma, G1251) or L-CCG-1 (Tocris, 0333) at 10 or 500 µM. Cultures were then placed in normal culture media with blockers of synaptic transmission (10 µM CNQX, 50 µM APV, and 100 µM picrotoxin) before fixation. Besides the positive controls, these blockers were also added to the cultures 12 h before electrical or chemical stimulation was applied. For immunohistochemistry, primary cultures were fixed in 4% PFA/4% sucrose in PBS for 15 min and washed in PBS (3x). Cultures were then permeabilized with 0.2% Triton X100, washed in PBS (3x), and blocked in 5% goat serum/5% bovine serum

albumin (1:1) for 30 minutes. Cultures were incubated overnight at 4°C in primary antibodies (Table 1). The following day, cultures were washed in PBS (3x) and incubated for 1 h at room temperature in secondary antibodies (Table 1) diluted in 5% goat serum in PBS. After a final set of PBS washes (3x), coverslips were mounted for imaging.

Viral vectors and transduction

Plasmids containing pAAV-hsyn-ChrimsonR-tdTomato (Addgene # 59171) (*51*) and AAV-hsyn-CheRiff-eGFP (Addgene #51697) (*52*) were packaged into AAV viral particles with serotype Rh10 (7.22×10^{13} vg ml^{-1}) at the Vector Core facility of the University Medical Center Hamburg-Eppendorf. For transduction, slice cultures (12-14 DIV) were transferred into sterile pre-warmed (37°C) HEPES-buffered solution containing: NaCl (145 mM, Sigma; S5886-500G), HEPES (10 mM, Sigma; H4034-100G), D-glucose (25 mM, Sigma; G7528-250G), KCl (2.5 mM, Fluka; 60121-1L), $MgCl_2$ (1 mM, Fluka; 63020-1L), $CaCl_2$ (2 mM, Honeywell; 21114-1L), pH 7.4, 318 mOsm kg^{-1}. A glass pipette was loaded with virus-containing buffer. For global transduction, a drop of virus-containing buffer from the tip of glass pipette was placed on top of the culture, and for local transduction, glass pipette was inserted into CA3 region under visual control for pressure injection (PicoSpritzer III).

Optogenetic stimulation in the CO_2 incubator

A closed 35 mm petri dish containing the membrane insert with a single slice culture in the center was placed on top of a 625 nm LED (Cree XP-E red) with collimation lens (Roithner LaserTechnik, 10034) as described (*53*). The LED was controlled from outside the incubator by a Grass S8800 stimulator, a constant-current driver (RECOM RCD-24-1.20) and a timer. LED power was adjusted to provide 7 mW mm^{-2} in the specimen plane. For Poisson stimulation at a rate of 0.1 Hz, we generated pulse trains with random inter-pulse intervals (ISIs) in Matlab, excluding ISIs < 40 ms to limit the peak frequency to 25 Hz. TTL pulse trains were sent to the LED driver via a DAQ board (PCIe-6321, National Instruments).

Slice culture immunohistochemistry

Slice cultures were fixed (30 min in ice-cold 4% paraformaldehyde in PBS) 60 min after stimulation. Slice cultures were washed in PBS (3 x 10 min) and blocked (2 h, 5% donor horse serum, 0.3 % TritonTM X-100 in PBS at RT), then incubated overnight with the primary antibodies (Table 1) in carrier solution (1% Bovine serum albumin, 0.3% TritonTM X-100 in PBS) at 4°C. On the next day, slice cultures were washed 3 x in PBS and incubated at room temperature for 2 h with secondary antibodies (Table 1) in carrier solution (same as above), then washed again (3 x 10 min) in PBS and mounted with Shandon Immu-Mount (Thermo Scientific; 9990402). Figure 5: slices were additionally stained with 4′,6-diamidino-2-phenylindole (DAPI, 1:1000) for 5 min during the last washing step.

	Primary AB				Secondary AB				
	Anti-	**Host**	**Producer (code)**	**Dilution**	**Anti-**	**Host**	**Label**	**Producer (code)**	**Dilution**
Fig. 2	FOS	rabbit	Santa Cruz Inc. (sc-52)	1:500	rabbit	goat	Alexa Fluor 647	Life Tech. (A27040)	1:2000
	PCP4	mouse	Sigma (AMAb91359)	1:500	mouse	goat	Alexa Fluor 488	Invitrogen (A11029)	1:1000
Fig. 3/4	FOS	rabbit	Santa Cruz Inc. (sc-52)	1:500	rabbit	goat	Alexa Fluor 647	Life Tech. (A27040)	1:2000
Fig. 5	FOS	rat	Syn. Systems (226017)	1:1000	rat	goat	Alexa Fluor 647	Invitrogen (A21247)	1:1000
Fig. 6	FOS	rabbit	Syn. System (226-008)	1:1000	rabbit	goat	Alexa Fluor 488	Life Tech. (A11034)	1:1000
	MAP2	guinea pig	Syn. Systems (188-004)	1:1000	guinea pig	goat	Alexa Fluor 647	Life Tech. (A21450)	1:1000
S2-S5	FOS	rabbit	Santa Cruz Inc. (sc-52)	1:500	rabbit	goat	Alexa Fluor 488	Live Tech. (A11008)	1:1000

Table 1: Primary and secondary antibodies

Confocal microscopy

The mounted slice cultures were imaged on an Olympus F1000 confocal microscope using a 20x oil immersion objective and 405, 488, 559, or 635 nm excitation. The imaging parameters

were adjusted for each set of experiments and kept unchanged throughout. Z-series (5 slices) stacks with 3 µm z-step at a 1024 × 1024 pixel resolution (zoom 1x) scanning at 12.5 µs per pixel were taken and analyzed in IMARIS software. Fiji/ImageJ was used to project the z-series and overlay channels. The mounted dissociated cultures were imaged on a Nikon Eclipse Ti spinning disk confocal microscope at 2048 × 2048 pixel resolution (20x air objective). Z-stacks with 0.9 µm steps were taken at 3-4 locations within the culture. Fig. 5B, C: Multiple stacks with 50 - 60 µm total depth (3 µm z-step) were imaged (512 × 512 pixel resolution, zoom 1x) with a scanning speed of 4 µs per pixel. The acquired stacks were stitched using Fiji/ImageJ. Fig. 5D, E: Single plane images (1024 × 1024 pixel) were acquired, scanning at 100 µs per pixel.

Image analysis

IMARIS software was used to count FOS^+ nuclei and to measure their intensity. FOS^+ spots (8 µm for CA1 and DG, 10 µm for CA2 and CA3) were automatically detected using the same quality filter threshold throughout all experiments. FOS^+ spots detected outside the pyramidal cell layer and FOS^+ nuclei of glial cells were manually removed. For $ChrimsonR^+$ neurons with no FOS signal, spots were manually added. Fig. 5: CA1: Six circular regions of interest (ROI, radius 30 µm, z-depth 9 µm) were placed on the CA1 pyramidal cell layer based on the DAPI signal. Within each ROI, all $DAPI^+$ neurons were manually selected (8 µm spots). In CA3, $ChrimsonR^+$ neurons were manually selected (8 µm spots). Fig. 6: All $MAP2^+$ cells were manually selected (8 µm spots). During manual spot addition, the FOS channel was turned off to avoid bias. A spot was defined as FOS^+ if the intensity was above a specific threshold defined by the negative control (no stimulation) images for each batch of experiments. The absolute number of FOS^+ neurons in each slice culture was two-point normalized to the number of FOS^+ neurons in positive (high K^+) and negative (no stimulation) controls.

Acknowledgments

We thank Iris Ohmert, Jan Schröder for excellent technical support, Ingke Braren of the UKE Vector facility for preparing the AAVs and Jack Mellor for helpful comments on the manuscript. pAAV-Syn-ChrimsonR-tdT was a gift from Edward S. Boyden, AAV-hsyn-CheRiff-eGFP was a gift from Adam E. Cohen.

Funding: This project was supported by Deutsche Forschungsgemeinschaft (DFG) grants SFB 936 #178316478 (TGO), SFB 1328 #335447717 #404539526 (CEG), FOR 2419 #278170285, #282803474 (TGO, CEG), Walter Benjamin program #468470832 (MA), European Research Council ERC Synergy 951515 (TGO), Neukom Scholars Program and Neukom CompX grant (ASA), P20-GM113132 NIH NIGMS (ASA, MBH), R01 NS112365/NS/NINDS NIH HHS/United States (MBH), NSF CAREER 1750199 (MBH).

Author contributions: Conceptualization: T.G.O. and C.E.G. Investigation and visualization: M.A., P.J.L.-M., A.F., and A.S.A. Funding acquisition and supervision: T.G.O., C.E.G. and M.B.H. Writing—original draft: T.G.O. and C.E.G.; review and editing: M.A., P.J.L.-M., A.F. and M.B.H.

Competing interests: The authors declare that they have no competing interests.

Data and materials availability: All data needed to evaluate the conclusions in the paper are present in the paper and/or the Supplementary Materials.

Supplementary Materials

Figs. S1 to S5.

References

1. J. I. Morgan, D. R. Cohen, J. L. Hempstead, T. Curran, Mapping patterns of c-fos expression in the central nervous system after seizure. *Science*. **237**, 192–197 (1987).

2. J. Tuvikene, P. Pruunsild, E. Orav, E.-E. Esvald, T. Timmusk, AP-1 Transcription Factors Mediate BDNF-Positive Feedback Loop in Cortical Neurons. *J. Neurosci.* **36**, 1290–1305 (2016).

3. C. M. Alberini, Transcription factors in long-term memory and synaptic plasticity. *Physiol. Rev.* **89**, 121–145 (2009).

4. L. Rodríguez-Berdini, G. O. Ferrero, F. Bustos Plonka, A. M. Cardozo Gizzi, C. G. Prucca, S. Quiroga, B. L. Caputto, The moonlighting protein c-Fos activates lipid synthesis in neurons, an activity that is critical for cellular differentiation and cortical development. *J. Biol. Chem.* **295**, 8808–8818 (2020).

5. L. G. Reijmers, B. L. Perkins, N. Matsuo, M. Mayford, Localization of a stable neural correlate of associative memory. *Science*. **317**, 1230–1233 (2007).

6. X. Liu, S. Ramirez, P. T. Pang, C. B. Puryear, A. Govindarajan, K. Deisseroth, S. Tonegawa, Optogenetic stimulation of a hippocampal engram activates fear memory recall. *Nature*. **484**, 381–385 (2012).

7. D. S. Roy, Y.-G. Park, M. E. Kim, Y. Zhang, S. K. Ogawa, N. DiNapoli, X. Gu, J. H. Cho, H. Choi, L. Kamentsky, J. Martin, O. Mosto, T. Aida, K. Chung, S. Tonegawa, Brain-wide mapping reveals that engrams for a single memory are distributed across multiple brain regions. *Nat. Commun.* **13**, 1799 (2022).

8. P. J. Lamothe-Molina, A. Franzelin, L. Beck, D. Li, L. Auksutat, T. Fieblinger, L. Laprell, J. Alhbeck, C. E. Gee, M. Kneussel, A. K. Engel, C. C. Hilgetag, F. Morellini, T. G. Oertner, ΔFosB accumulation in hippocampal granule cells drives cFos pattern separation during spatial learning. *Nat. Commun.* **13**, 6376 (2022).

9. E.-L. Yap, M. E. Greenberg, Activity-Regulated Transcription: Bridging the Gap between Neural Activity and Behavior. *Neuron*. **100**, 330–348 (2018).

10. P. Schoenenberger, D. Gerosa, T. G. Oertner, Temporal control of immediate early gene induction by light. *PLoS One*. **4**, e8185 (2009).

11. P. R. Lee, J. E. Cohen, D. A. Iacobas, S. Iacobas, R. D. Fields, Gene networks activated by specific patterns of action potentials in dorsal root ganglia neurons. *Sci. Rep.* **7**, 43765 (2017).

12. R. D. Fields, F. Eshete, B. Stevens, K. Itoh, Action potential-dependent regulation of gene expression: temporal specificity in ca2+, cAMP-responsive element binding proteins, and mitogen-activated protein kinase signaling. *J. Neurosci.* **17**, 7252–7266 (1997).

13. H. Z. Sheng, R. D. Fields, P. G. Nelson, Specific regulation of immediate early genes by patterned neuronal activity. *J. Neurosci. Res.* **35**, 459–467 (1993).

14. D. Mahringer, P. Zmarz, H. Okuno, H. Bito, G. B. Keller, Functional correlates of immediate early gene expression in mouse visual cortex. *Peer Community J.* **2**, e45 (2022).

15. S. Poll, M. Mittag, F. Musacchio, L. C. Justus, E. A. Giovannetti, J. Steffen, J. Wagner, L. Zohren, S. Schoch, B. Schmidt, W. S. Jackson, D. Ehninger, M. Fuhrmann, Memory trace interference impairs recall in a mouse model of Alzheimer's disease. *Nat. Neurosci.* **23**, 952–958 (2020).

16. D. Mahringer, A. V. Petersen, A. Fiser, H. Okuno, H. Bito, Expression of c-Fos and Arc in hippocampal region CA1 marks neurons that exhibit learning-related activity changes. *BioRxiv* (2019), doi:10.1101/644526.

17. A. Fernández-Ruiz, A. Oliva, E. Fermino de Oliveira, F. Rocha-Almeida, D. Tingley, G. Buzsáki, Long-duration hippocampal sharp wave ripples improve memory. *Science*. **364**, 1082–1086 (2019).

18. H. El Oussini, C.-L. Zhang, U. François, C. Castelli, A. Lampin-Saint-Amaux, M. Lepleux, P. Molle, L. Velez, C. Dejean, F. Lanore, C. Herry, D. Choquet, Y. Humeau, CA3 hippocampal synaptic plasticity supports ripple physiology during memory consolidation. *bioRxiv* (2023), p. 2023.03.28.534509, , doi:10.1101/2023.03.28.534509.

19. C. M. Tigaret, S. E. L. Chamberlain, J. H. L. P. Sadowski, J. Hall, M. C. Ashby, J. R. Mellor, Convergent Metabotropic Signaling Pathways Inhibit SK Channels to Promote Synaptic Plasticity in the Hippocampus. *J. Neurosci.* **38**, 9252–9262 (2018).

20. A. O. Komendantov, S. Venkadesh, C. L. Rees, D. W. Wheeler, D. J. Hamilton, G. A. Ascoli, Quantitative firing pattern phenotyping of hippocampal neuron types. *Sci. Rep.* **9**, 17915 (2019).

21. A. San Antonio, K. Liban, T. Ikrar, E. Tsyganovskiy, X. Xu, Distinct physiological and developmental properties of hippocampal CA2 subfield revealed by using anti-Purkinje cell protein 4 (PCP4) immunostaining. *J. Comp. Neurol.* **522**, 1333–1354 (2014).

22. T. J. Stachniak, A. Ghosh, S. M. Sternson, Chemogenetic synaptic silencing of neural circuits localizes a hypothalamus→midbrain pathway for feeding behavior. *Neuron*. **82**, 797–808 (2014).

23. B. N. Armbruster, X. Li, M. H. Pausch, S. Herlitze, B. L. Roth, Evolving the lock to fit the key to create a family of G protein-coupled receptors potently activated by an inert ligand. *Proc. Natl. Acad. Sci. U. S. A.* **104**, 5163–5168 (2007).

24. F. C. Cruz, E. Koya, D. H. Guez-Barber, J. M. Bossert, C. R. Lupica, Y. Shaham, B. T. Hope, New technologies for examining the role of neuronal ensembles in drug addiction and fear. *Nat. Rev. Neurosci.* **14**, 743–754 (2013).

25. C. H. Habrian, J. Levitz, V. Vyklicky, Z. Fu, A. Hoagland, I. McCort-Tranchepain, F. Acher, E. Y. Isacoff, Conformational pathway provides unique sensitivity to a synaptic mGluR. *Nat. Commun.* **10**, 5572 (2019).

26. R. Luján, J. D. Roberts, R. Shigemoto, H. Ohishi, P. Somogyi, Differential plasma membrane distribution of metabotropic glutamate receptors mGluR1 alpha, mGluR2 and mGluR5, relative to neurotransmitter release sites. *J. Chem. Neuroanat.* **13**, 219–241 (1997).

27. I. H. Cho, L. C. Panzera, M. Chin, S. A. Alpizar, G. E. Olveda, R. A. Hill, M. B. Hoppa, The potassium channel subunit Kvβ1 serves as a major control point for synaptic facilitation. *Proc. Natl. Acad. Sci. U. S. A.* **117**, 29937–29947 (2020).

28. E. B. Malarkey, V. Parpura, Mechanisms of glutamate release from astrocytes. *Neurochem. Int.* **52**, 142–154 (2008).

29. A. L. Eagle, P. A. Gajewski, A. J. Robison, Role of hippocampal activity-induced transcription in memory consolidation. *Rev. Neurosci.* **27**, 559–573 (2016).

30. Y. P. Guo, X. Sun, C. Li, N. Q. Wang, Y.-S. Chan, J. He, Corticothalamic synchronization leads to *c-fos* expression in the auditory thalamus. *Proc. Natl. Acad. Sci. U. S. A.* **104**, 11802–11807 (2007).

31. M. Peter, B. Bathellier, B. Fontinha, P. Pliota, W. Haubensak, S. Rumpel, Transgenic mouse models

enabling photolabeling of individual neurons in vivo. *PLoS One*. **8**, e62132 (2013).

32. A. E. West, W. G. Chen, M. B. Dalva, R. E. Dolmetsch, J. M. Kornhauser, A. J. Shaywitz, M. A. Takasu, X. Tao, M. E. Greenberg, Calcium regulation of neuronal gene expression. *Proc. Natl. Acad. Sci. U. S. A.* **98**, 11024–11031 (2001).

33. N. Holbro, A. Grunditz, J. S. Wiegert, T. G. Oertner, AMPA receptors gate spine Ca(2+) transients and spike-timing-dependent potentiation. *Proc. Natl. Acad. Sci. U. S. A.* **107**, 15975–15980 (2010).

34. L. C. Panzera, B. Johnson, J. A. Quinn, I. H. Cho, M. M. Tamkun, M. B. Hoppa, Activity-dependent endoplasmic reticulum Ca2+ uptake depends on Kv2.1-mediated endoplasmic reticulum/plasma membrane junctions to promote synaptic transmission. *Proc. Natl. Acad. Sci. U. S. A.* **119**, e2117135119 (2022).

35. G. Buzsáki, Hippocampal sharp wave-ripple: A cognitive biomarker for episodic memory and planning. *Hippocampus*. **25**, 1073–1188 (2015).

36. O. Eschenko, W. Ramadan, M. Mölle, J. Born, S. J. Sara, Sustained increase in hippocampal sharp-wave ripple activity during slow-wave sleep after learning. *Learn. Mem.* **15**, 222–228 (2008).

37. D. Dupret, J. O'Neill, B. Pleydell-Bouverie, J. Csicsvari, The reorganization and reactivation of hippocampal maps predict spatial memory performance. *Nat. Neurosci.* **13**, 995–1002 (2010).

38. V. V. Nikulin, T. Fedele, J. Mehnert, A. Lipp, C. Noack, J. Steinbrink, G. Curio, Monochromatic ultra-slow (~0.1 Hz) oscillations in the human electroencephalogram and their relation to hemodynamics. *Neuroimage*. **97**, 71–80 (2014).

39. G. Waterstraat, R. Körber, J.-H. Storm, G. Curio, Noninvasive neuromagnetic single-trial analysis of human neocortical population spikes. *Proc. Natl. Acad. Sci. U. S. A.* **118** (2021), doi:10.1073/pnas.2017401118.

40. G. Girardeau, K. Benchenane, S. I. Wiener, G. Buzsáki, M. B. Zugaro, Selective suppression of hippocampal ripples impairs spatial memory. *Nat. Neurosci.* **12**, 1222–1223 (2009).

41. J. H. L. P. Sadowski, M. W. Jones, J. R. Mellor, Sharp-Wave Ripples Orchestrate the Induction of Synaptic Plasticity during Reactivation of Place Cell Firing Patterns in the Hippocampus. *Cell Rep.* **14**, 1916–1929 (2016).

42. Ł. Kuśmierz, T. Isomura, T. Toyoizumi, Learning with three factors: modulating Hebbian plasticity with errors. *Curr. Opin. Neurobiol.* **46**, 170–177 (2017).

43. F. Lanté, M.-C. de Jésus Ferreira, J. Guiramand, M. Récasens, M. Vignes, Low-frequency stimulation induces a new form of LTP, metabotropic glutamate (mGlu5) receptor- and PKA-dependent, in the CA1 area of the rat hippocampus. *Hippocampus*. **16**, 345–360 (2006).

44. N. L. Pettit, E.-L. Yap, M. E. Greenberg, C. D. Harvey, Fos ensembles encode and shape stable spatial maps in the hippocampus. *Nature*. **609**, 327–334 (2022).

45. P. Devaraju, M.-Y. Sun, T. L. Myers, K. Lauderdale, T. A. Fiacco, Astrocytic group I mGluR-dependent potentiation of astrocytic glutamate and potassium uptake. *J. Neurophysiol.* **109**, 2404–2414 (2013).

46. P. Molinaro, L. Sanguigno, A. Casamassa, V. Valsecchi, R. Sirabella, G. Pignataro, L. Annunziato, L. Formisano, Emerging role of DREAM in healthy brain and neurological diseases. *Int. J. Mol. Sci.* **24**, 9177 (2023).

47. D. Kim, P. Park, X. Li, J. David Wong Campos, H. Tian, E. M. Moult, J. B. Grimm, L. Lavis, A. E.

Cohen, Mapping memories: pulse-chase labeling reveals AMPA receptor dynamics during memory formation. *bioRxiv* (2023), p. 2023.05.26.541296, , doi:10.1101/2023.05.26.541296.

48. K. K. Cowansage, T. Shuman, B. C. Dillingham, A. Chang, P. Golshani, M. Mayford, Direct reactivation of a coherent neocortical memory of context. *Neuron*. **84**, 432–441 (2014).

49. L. Stoppini, P. A. Buchs, D. Muller, A simple method for organotypic cultures of nervous tissue. *J. Neurosci. Methods*. **37**, 173–182 (1991).

50. C. E. Gee, I. Ohmert, J. S. Wiegert, T. G. Oertner, Preparation of Slice Cultures from Rodent Hippocampus. *Cold Spring Harb. Protoc.* **2017** (2017), doi:10.1101/pdb.prot094888.

51. N. C. Klapoetke, Y. Murata, S. S. Kim, S. R. Pulver, A. Birdsey-Benson, Y. K. Cho, T. K. Morimoto, A. S. Chuong, E. J. Carpenter, Z. Tian, J. Wang, Y. Xie, Z. Yan, Y. Zhang, B. Y. Chow, B. Surek, M. Melkonian, V. Jayaraman, M. Constantine-Paton, G. K.-S. Wong, E. S. Boyden, Independent optical excitation of distinct neural populations. *Nat. Methods*. **11**, 338–346 (2014).

52. D. R. Hochbaum, Y. Zhao, S. L. Farhi, N. Klapoetke, C. A. Werley, V. Kapoor, P. Zou, J. M. Kralj, D. Maclaurin, N. Smedemark-Margulies, J. L. Saulnier, G. L. Boulting, C. Straub, Y. K. Cho, M. Melkonian, G. K.-S. Wong, D. J. Harrison, V. N. Murthy, B. L. Sabatini, E. S. Boyden, R. E. Campbell, A. E. Cohen, All-optical electrophysiology in mammalian neurons using engineered microbial rhodopsins. *Nat. Methods*. **11**, 825–833 (2014).

53. M. Anisimova, B. van Bommel, R. Wang, M. Mikhaylova, J. S. Wiegert, T. G. Oertner, C. E. Gee, Spike-timing-dependent plasticity rewards synchrony rather than causality. *Cereb. Cortex*. **33**, 23–34 (2022).

Supplementary Material

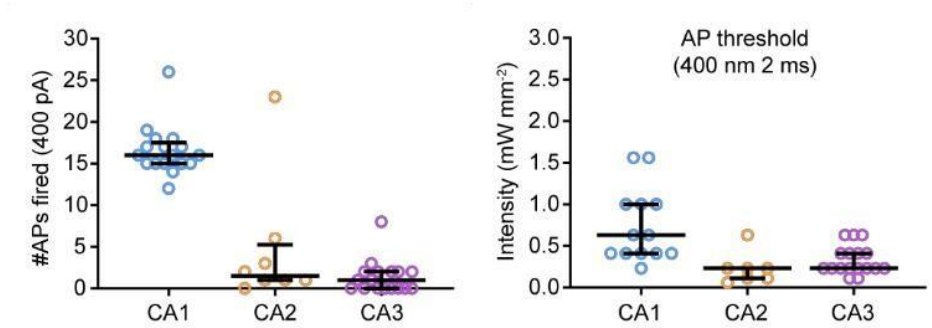

Figure S1: Action potential generation by current injection and light intensity threshold for action potential generation in CheRiff expressing hippocampal neurons. As in figure 1 except hippocampal slice cultures were transduced with AAV2/9-synapsin-CheRiff-eGFP. Light intensity threshold for action potential (AP) was determined in cell-attached mode. The number of action potentials fired in response to a 600 ms, 400 pA current injection from -70 mV was obtained after achieving whole-cell access. n = 17, 8, 19 neurons, respectively. Bars show median ± quartiles. Note that for some cells whole cell-access was obtained before light was applied, so the AP threshold was not measured.

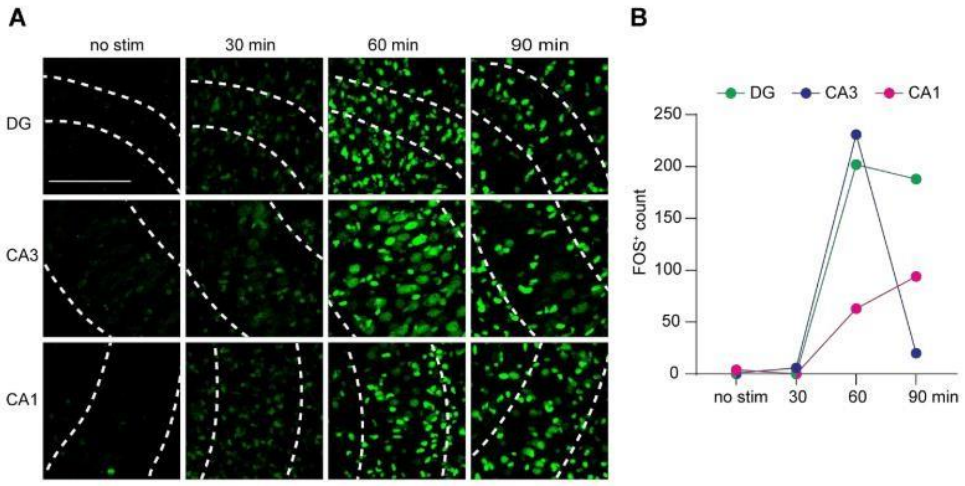

Figure S2: Time course of FOS expression after high K^+. A) Organotypic slice cultures of rat hippocampus fixed at different time points after K^+ stimulation and stained for FOS (green). Images are maximum intensity projections of 5 optical sections. Scale bar 100 µm. no stim = slice fixed without high K^+ stimulation. **B)** Count of FOS^+ neuronal nuclei in hippocampal subfields from slices fixed at different time points. 60 min was chosen as the optimal time point to fix slices after stimulation as expression peaked at this time point in dentate gyrus and CA3 and at 90 min FOS had almost disappeared from CA3.

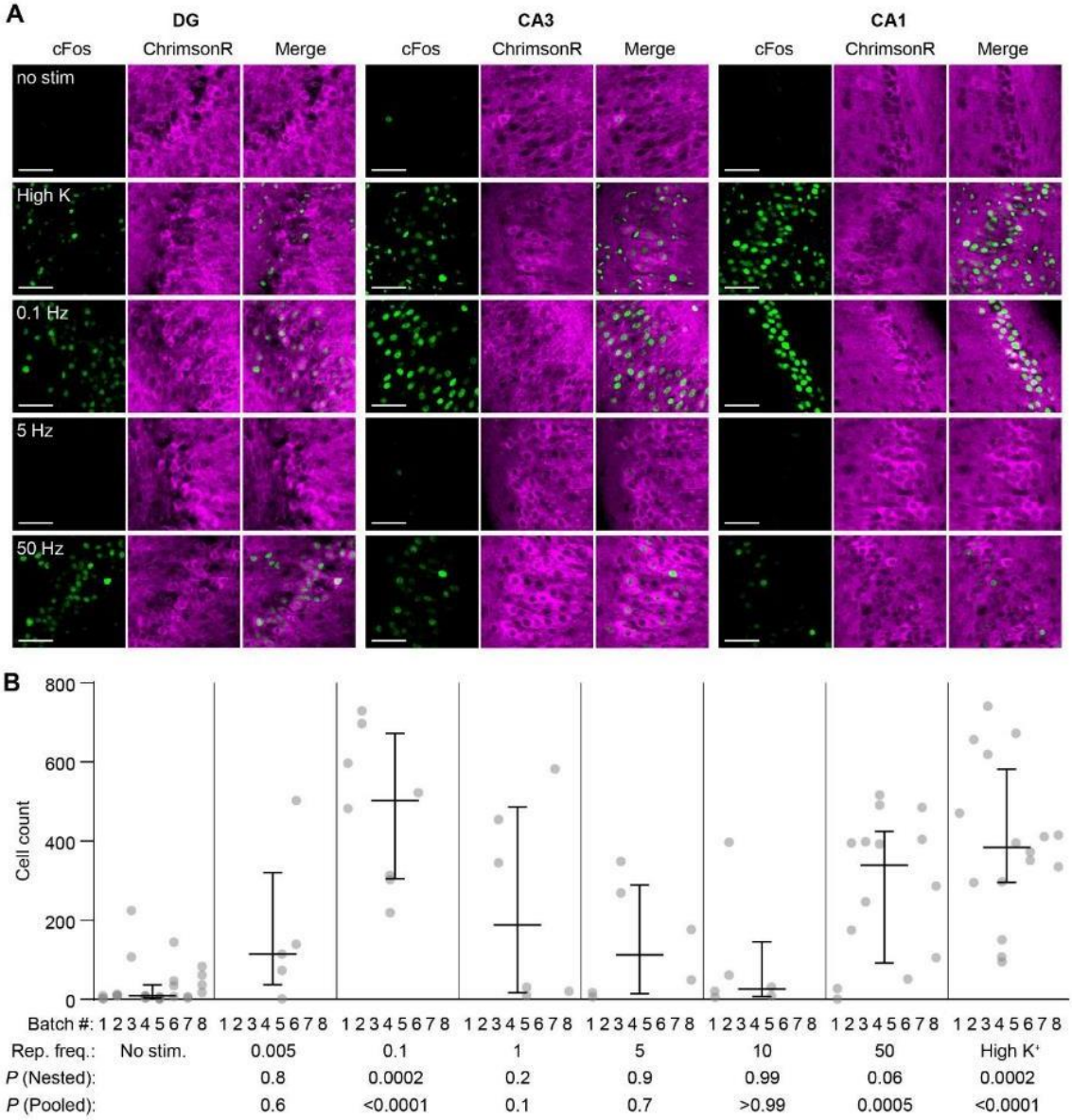

Figure S3: Bimodal relationship between firing frequency and FOS expression. A) Confocal images (single plane) of FOS expression pattern 60 min after light stimulation (300 pulses) at different frequencies in 3 hippocampal regions. Magenta: ChrimsonR-tdTomato. Green: anti-FOS. Scale bars: 50 µm. **B)** Quantification of FOS-positive neurons (88 cultures, 8 stimulation conditions, n = 8 biological repeats). Each dot represents one organotypic culture, averaging 3 FOVs (635 x 635 µm) in DG, CA3 and CA1, respectively. In addition to individual data points, median and 25 % to 75 % interquartile range are indicated. *P* (Nested): One-way ANOVA on nested data. *P* (Pooled): Kruskal-Wallis test on pooled data. *P* values are in comparison to 'No stim.' group. This set of experiments (stimulation + staining + imaging) were performed in 8 batches.

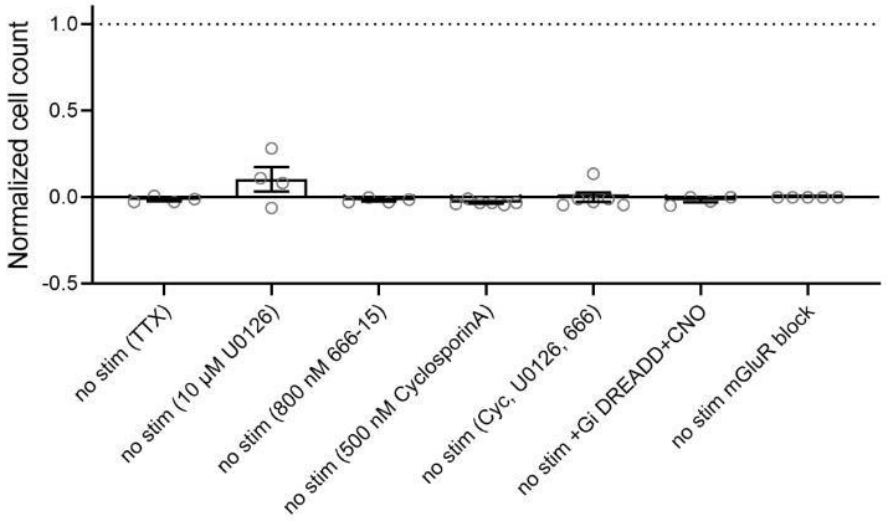

Figure S4: No effect of pharmacological agents tested on non-stimulated slice cultures. FOS+ neurons were counted in slice cultures (circles) incubated with blockers, counts were normalized to positive controls (high K^+). Bars show mean ± SEM.

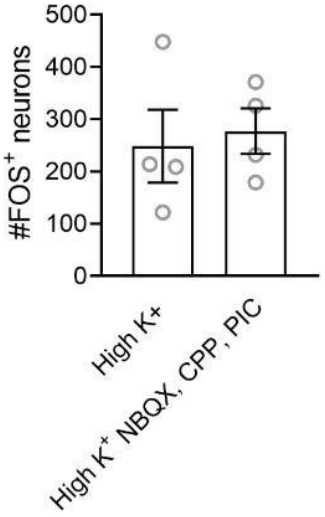

Figure S5: Inhibitors of fast synaptic transmission (NBQX, CPPene, picrotoxin) have no effect on high K^+ induced FOS. High K^+: n = 4 hippocampal slice cultures; High K^+ with synaptic blockers: n = 4 hippocampal slice cultures. Bars show mean ± SEM.

Publication (preprint) #3: Epigenetic repression of cFOS supports sequential formation of distinct spatial memories

Andreas Franzelin, Paul J. Lamothe-Molina, Christine E. Gee, Andrey Formozov, Eric Schreiter, Fabio Morellini, Thomas G. Oertner: 2024 “Epigenetic repression of cFOS supports sequential formation of distinct spatial memories ”. **Biorxiv**.

https://doi.org/10.1101/2024.02.16.580703

This manuscript contains the majority of my work. I discovered an epigenetic repression mechanism activated during learning and explored the behavioral consequences of disabling the repression by HDAC inhibition. I designed, conducted and analyzed all major experiments (Figs 1, 2, 3, 4, 7, 8). Stereotactic injections for the experiments in Figs 5 and 6) were performed by PJL and I performed the behavioral experiments and analyzed all data. I wrote the first draft of the manuscript and was fully responsible for the design of all figures.

Epigenetic repression of cFos supports sequential formation of distinct spatial memories

Andreas Franzelin[1], Paul J. Lamothe-Molina[1], Christine E. Gee[1], Andrey Formozov[1,2], Eric R. Schreiter[3], Fabio Morellini[4], Thomas G. Oertner[1*]

[1] Institute for Synaptic Physiology, Center for Molecular Neurobiology (ZMNH), University Medical Center Hamburg-Eppendorf, Hamburg, Germany
[2] present address: Department of Neurophysiology, MCTN, Medical Faculty Mannheim, Heidelberg University, 68167 Mannheim, Germany
[3] HHMI, Janelia Research Campus, Ashburn, VA 20147, USA
[4] Research Group Behavioral Biology, Center for Molecular Neurobiology (ZMNH), University Medical Center Hamburg-Eppendorf, Hamburg, Germany

*Correspondence: thomas.oertner@zmnh.uni-hamburg.de

Abstract

Expression of the immediate early gene cFos modifies the epigenetic landscape of activated neurons with downstream effects on synaptic plasticity. The production of cFos is inhibited by a long-lived isoform of another Fos family gene, ΔFosB. It has been speculated that this negative feedback mechanism may be critical for protecting episodic memories from being overwritten by new information. Here, we investigate the influence of ΔFosB inhibition on cFos expression and memory. Hippocampal neurons in slice culture produce more cFos on the first day of stimulation compared to identical stimulation on the following day. This downregulation affects all hippocampal subfields and requires histone deacetylation. Overexpression of ΔFosB in individual pyramidal neurons effectively suppresses cFos, indicating that accumulation of ΔFosB is the causal mechanism. Water maze training of mice over several days leads to accumulation of ΔFosB in granule cells of the dentate gyrus, but not in CA3 and CA1. Because the dentate gyrus is thought to support pattern separation and cognitive flexibility, we hypothesized that inhibiting the expression of ΔFosB would affect reversal learning, i.e., the ability to successively learn new platform locations in the water maze. The results indicate that pharmacological HDAC inhibition, which prevents cFos repression, impairs reversal learning, while learning and memory of the initial platform location remain unaffected. Our study supports the hypothesis that epigenetic mechanisms tightly regulate cFos expression in individual granule cells to orchestrate the formation of time-stamped memories.

Introduction

Current models of memory storage suggest that memory retrieval requires the reactivation of a subset of neurons that were active during the lived experience. Fear conditioning experiments in TetTag mice provide compelling experimental evidence for this concept (Liu et al. 2012; Reijmers et al. 2007). In these mice, cFos activation is used to label the most active neurons within a time window set by doxycycline withdrawal. cFos-expressing neurons ($cFos^+$) in the hippocampus appear to play a distinct role in the network. Calcium imaging in cFos reporter mice showed that $cFos^+$ neurons have very stable place fields and form ensembles with significantly correlated activity (Pettit et al. 2022). The goal of this study was to better understand the conditions for cFos activation, particularly the rapidly changing expression patterns seen in the dentate gyrus (DG) (Lamothe-Molina et al. 2022). It is well established that action potential firing leads to a proportional increase in intracellular calcium concentration ($[Ca^{2+}]_i$) (Maravall et al. 2000). Calcium release from the endoplasmic reticulum produces even larger $[Ca^{2+}]_i$ transients (Holbro, Grunditz, and Oertner 2009; Mellentin, Jahnsen, and Abraham 2007). Notably, nuclear $[Ca^{2+}]_i$ is a potent trigger for epigenetic modifications (Bading 2013; Mozolewski et al. 2021), making it a compelling parameter to study in the context of immediate early genes (Bengtson et al. 2010).

To examine the correlation between activity, nuclear calcium and cFos expression, we used organotypic slice cultures of the rat hippocampus. This culture system effectively preserves neuronal identities and connectivity between the different hippocampal subfields. To simultaneously record nuclear calcium in all neurons, we used CaMPARI2 - a recently improved calcium integrator (Moeyaert et al. 2018). CaMPARI2 contains a green fluorescent protein (mEOS), which irreversibly converts to a red fluorescent form when bound to calcium and exposed to violet illumination (405 nm). To measure calcium where it is most important for epigenetics, we used a nuclear-localized version, H2B-CaMPARI2. An additional advantage of nuclear targeting was the easy detection and segmentation of fluorescent nuclei with commercial image analysis software, a task that is challenging to automate when using cytoplasmic indicators. To obtain a permanent cell-specific record of activity, we illuminated the cultures with violet light inside the incubator during the stimulation period. Photoconversion of individual nuclei was quantified after fixation on a confocal microscope. This process allowed us to evaluate calcium transients that occurred one hour before fixation within a defined 60-second window.

Our experiments with slice cultures indicated that ΔFosB accumulation induces an epigenetic mechanism that prevents repeated expression of cFos in individual neurons. To determine whether this mechanism is actually evoked during learning, we tested whether inhibiting histone modification would affect performance in a complex spatial learning task (Morellini 2013). Indeed, we found that mice had no problem learning a single platform position under HDAC inhibition, but performed much worse when challenged with daily changing positions. Our findings support the concept that epigenetic mechanisms control the dynamic allocation of "fresh" neurons for memory storage, resulting in well-separated episodic memories (Watrous and Ekstrom 2014; Chowdhury and Caroni 2018).

Results

Nuclear calcium does not predict cFos expression level

To investigate the relationship between activity-induced increases in nuclear [Ca^{2+}] and cFos expression in many neurons in parallel, we virally transduced neurons with the photoconvertible calcium indicator CaMPARI2 fused to histone H2B for nuclear targeting (H2B-CaMPARI2). When bound to calcium, illumination of CaMPARI2 at 405 nm induces an irreversible conversion from a green to a red state, allowing calcium levels to be integrated in a precise time window defined by the photoconversion light. After five days of H2B-CaMPARI2 expression, we stimulated slice cultures with a drop of the $GABA_A$ antagonist bicuculline (Fig. 1A), which induces bursts of synchronized activity (Fig. S1). After 60 s of bicuculline treatment, the induced activity was terminated by pipetting the Na^+ channel blocker tetrodotoxin (TTX, 300 µl, 1 µM) onto the slice culture. During the stimulation period, the slice cultures were continuously illuminated (395 nm) to ensure photoconversion of calcium-bound H2B-CaMPARI2. Cultures were fixed 60 min after the end of the stimulation period and immunostained for cFos and the red-converted version of CaMPARI2. At a viral titer of 10^{12} vg/ml, cFos expression in H2B-CaMPARI2-expressing cultures was not different from non-transfected control cultures (Fig. S2). As negative controls, we included cultures that were treated with TTX instead of bicuculline (Fig. S3).

Sixty seconds of bicuculline stimulation with illumination resulted in H2B-CaMPARI2 photoconversion across all hippocampal subfields, indicating elevated nuclear Ca^{2+} levels during the stimulation period (Fig. 1B). This stimulation also led to widespread expression of cFos 60 min later (Fig. 1C), capturing the peak of endogenous cFos (Fig. S4). Quantitative analysis showed the strongest expression in CA1, DG and CA3, whereas neurons in CA2, hilus and subiculum expressed much less cFos (Fig. S5). To explore a range of activity levels, we varied the duration of bicuculline-driven activity by altering the timing of the TTX drop to terminate all electrical activity in the tissue. After fixation, CaMPARI2-positive nuclei were analyzed in a single image plane using Imaris (8 µm spots) to quantify CaMPARI2 conversion and cFos expression. Prolonging the period of high activity resulted in increased CaMPARI2 conversion (Fig. 1D) and increased cFos levels in DG, CA1 and CA3 (Fig. 1E). On the level of individual cultures, the correlation between CaMPARI2 conversion and cFos expression was very high (DG: $R^2 = 0.67$; CA3 & CA1: $R^2 = 0.99$, Fig. 1F). On the level of individual neurons, however, we found only weak or no correlations between these parameters at a given stimulation level (Fig. 1G). Even within a hippocampal subfield, neurons with intermediate photoconversion (0.4 to 0.6 [R/(R+G)]) showed a surprisingly large range of cFos levels, suggesting that there are additional parameters that control cFos expression in a cell-specific manner.

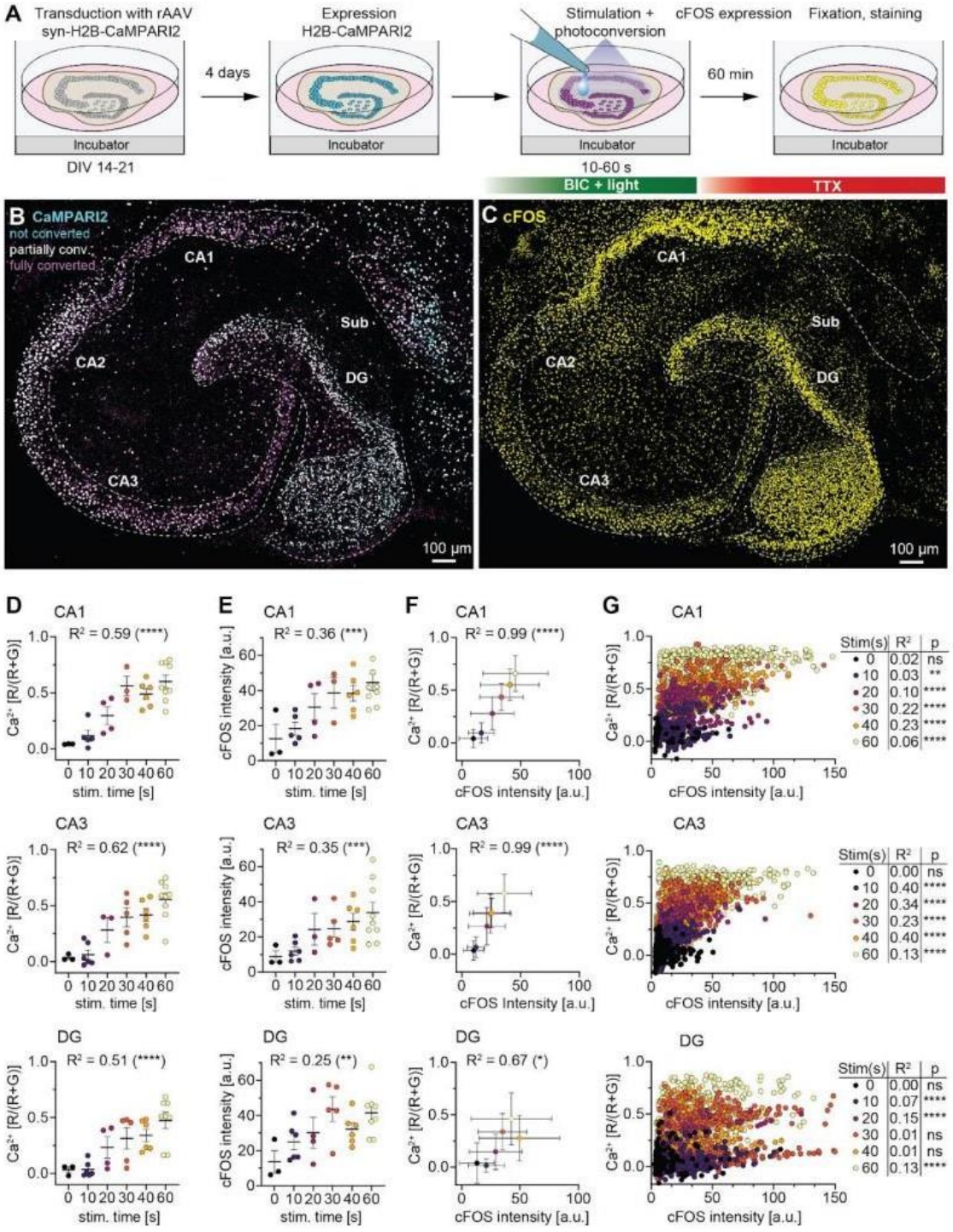

Figure 1: Correlations between nuclear calcium levels and cFos expression. A) Time line of in-incubator stimulation experiments using synapsin-H2B-CaMPARI2-transduced slice cultures, stimulated with bicuculline (BIC) followed by tetrodotoxin (TTX). **B)** Slice culture stimulated for 60 s with bicuculline, showing strong CaMPARI2 photoconversion (cyan = non-converted, white = partially converted, magenta = fully converted). **C)** Anti-cFos staining (yellow), same tissue as in B. **D)** CaMPARI2 photoconversion (Ca^{2+}, [R\(R+G)]) as a function of stimulation time. Circles represent averages from individual slice cultures (40 - 120 cells each). Bars show mean ± SEM for each stimulation condition. Coefficient of determination (R^2) and significance of linear regression shown for

hippocampal subfields CA1, CA3 and dentate gyrus (DG) (****p<0.0001). **E)** Expression of cFos (arbitrary units) as a function of stimulation time. Circles represent averages from individual slice cultures, bars show mean ± SEM. Coefficient of determination (R^2) and significance of linear regression is shown for each hippocampal subfield (CA1, ***p = 0.0009; CA3, ***p = 0.004; DG, **p = 0.0036). **F)** Correlations between CaMPARI2 photoconversion (Ca^{2+}) and cFos expression for different stimulation durations. Mean ± SD of cells collected from all cultures (n = 3-9) per stimulation duration. (CA1 and CA3: ****p < 0.0001; DG: *p = 0.045). **G)** CaMPARI2 photoconversion (Ca^{2+}) and cFos expression of individual neurons, color coded by stimulation time (same data as F). Note that for individual stimulation conditions, coefficients of determination are very low. **D-G)** For all correlations, Person's correlation coefficient was computed. Similar results were observed in two independent experiments.

cFos expression is dependent on the history of activity

Supraphysiological stimulation induced by cocaine consumption or epileptic seizures leads to cFos repression in the striatum and hippocampus (Cates et al. 2019; Renthal et al. 2008). Highly active regions share a common characteristic: they show substantial accumulation of ΔFosB, regardless of the specific stimulus. ΔFosB is a truncated variant of the FosB protein that has a very long lifespan. We evaluated ΔFosB expression levels at different time points after bicuculline stimulation. For each slice culture and hippocampal area, 20 neuronal nuclei were randomly selected based on the DAPI signal, their anti-ΔFosB fluorescence was evaluated and averaged (Fig. S6). Bicuculline stimulation induced strong ΔFosB expression in all hippocampal areas that lasted for at least 24 h (Fig. S6). To examine the interaction between ΔFosB and cFos, we stimulated cultures with a drop of bicuculline (10 µl, 20 µM) on day 1 (Fig. 2A). Since bicuculline is unstable at physiological pH and temperature, the period of increased activity is transient (Johnston 2013). The following day, the pre-stimulated cultures (referred to as 'BIC BIC') were re-stimulated along with non-pre-stimulated cultures ('- BIC'). As in the previous experiments, activity was terminated by a drop of TTX after 60 seconds. After 60 min, the stimulated cultures were fixed and stained for cFos and ΔFosB. We analyzed the mean levels of cFos and ΔFosB expression across all neurons within each hippocampal subregion. The pre-stimulated cultures had reduced cFos levels in all subregions compared to the single stimulation condition (Fig. 2A, B). Conversely, ΔFosB levels were significantly higher in the pre-stimulated condition compared to the single-stimulated cultures (Fig. 2A, C). In double stimulated cultures (BIC BIC), all neurons had low cFos and high ΔFosB (Fig. 2D, black dots). Neurons stimulated once (- BIC) expressed cFos at higher levels (Fig. 2D, green dots). Similar results were obtained in CA3 (Fig. 2E-H) and CA1 (Fig. 2I-L). These results underscore that a period of highly synchronized activity can repress the cFos promoter in the majority of neurons 24 h later, coinciding with substantial ΔFosB accumulation. To establish a causal relationship between ΔFosB and cFos suppression at the single cell level, a more direct manipulation of ΔFosB was required.

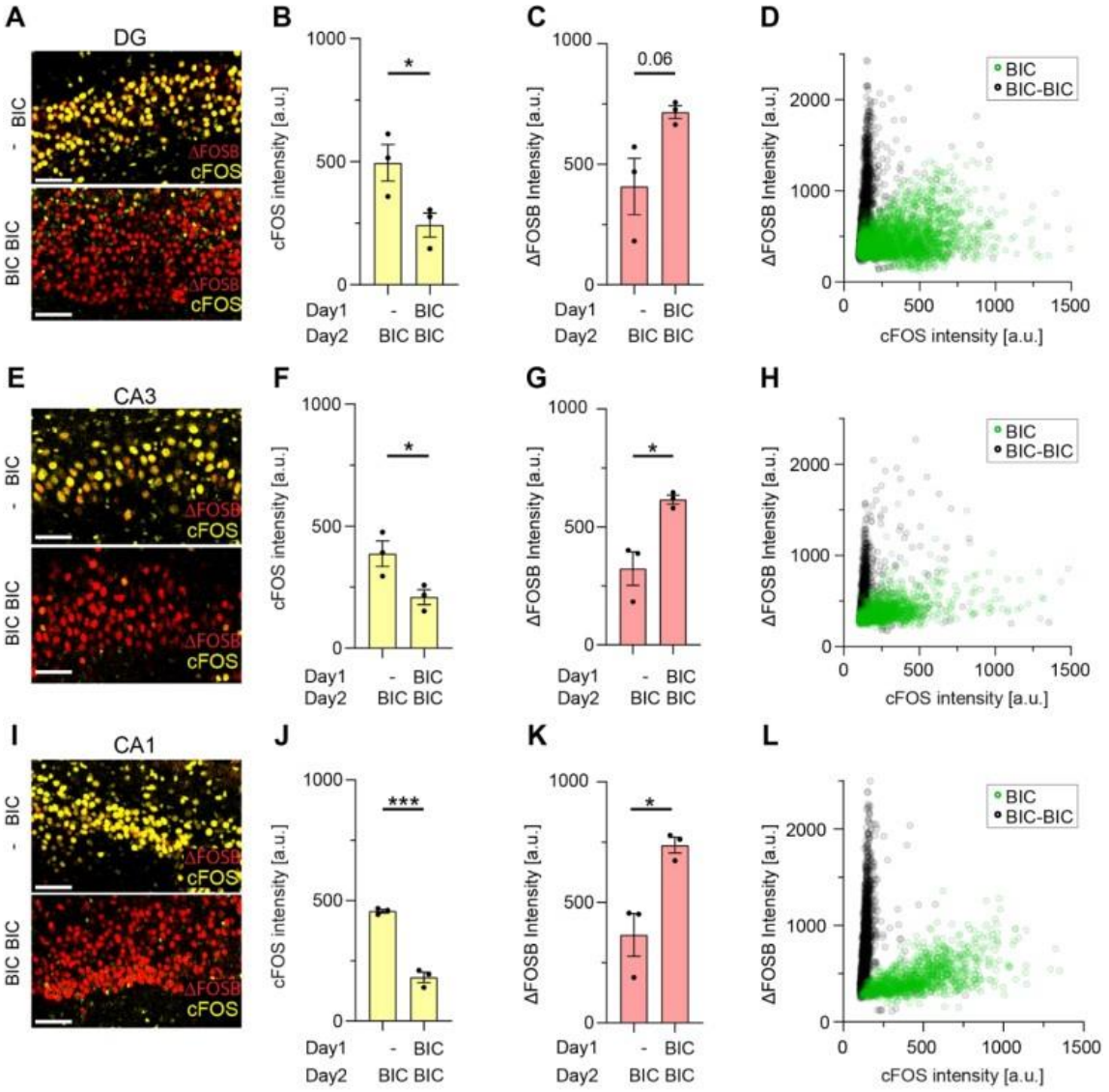

Figure 2: Bicuculline-induced activity increases ΔFosB expression in all hippocampal subregions. A) Confocal images of cFos (yellow) and ΔFosB (red) immunoreactivity in dentate gyrus (DG) after single (BIC) or two day-consecutive stimulation with bicuculline (BIC-BIC), scale bar 50 µm. **B)** Fluorescent intensity analysis (arbitrary units): cFos expression is decreased after consecutive (BIC-BIC) stimulation compared to single BIC stimulation (BIC) (*p = 0.046, t-test). Bars show mean ± SEM of all cells per culture (n = 3 slice cultures, black dots). **C)** Fluorescent intensity analysis (arbitrary units): ΔFosB expression is increased after consecutive (BIC-BIC) stimulation compared to single BIC stimulation (BIC) (ns p = 0.062, t-test). Bars show mean ± SEM of all cells per culture (n = 3 slice cultures, black spots). **D)** Single cell intensity plot of all cells of a single slice cultures per condition (green, BIC, n = 3177; black, BIC-BIC, n = 2605). **E-H)** Confocal images and analysis for CA3 neurons. cFos expression: *p = 0.042, t-test, BIC vs BIC-BIC. ΔFosB expression: *p = 0.016, t-test, BIC vs BIC-BIC. Single cell intensity plot: (green, BIC, n = 1265; black, BIC-BIC, n = 1219). **I-L)** Confocal images and analysis for CA1 neurons. cFos expression: ***p = 0.0003, t-test, BIC vs BIC-BIC. ΔFosB expression: *p = 0.017, t-test, BIC vs BIC-BIC. Single cell intensity plot: (green, BIC, n = 1077; black, BIC-BIC, n = 2081).

Constitutive ΔFosB expression reduces activity-induced cFos in CA1

To generate ΔFosB overexpression in a few identified neurons, we electroporated individual CA1 neurons with ΔFosB (0.1 ng/µl) and cerulean (10 ng/µl), both under the control of the constitutive synapsin-1 promoter. Phosphorylation of ΔFosB at the serine 27 residue plays a critical role in extending its lifespan (Ulery-Reynolds et al. 2009; Ulery, Rudenko, and Nestler 2006). As a control, we therefore electroporated a modified version of ΔFosB in which the serine residue at position 27 was replaced with alanine (S-27A). After 6 days of expression, cultures were stimulated with bicuculline for 60 s, at which point all activity was terminated with a drop of TTX (Fig. 3A). Sixty minutes later, the tissue was fixed and stained for cFos, ΔFosB and DNA (DAPI) (Fig. 3B). Nuclei of electroporated neurons (DAPI + cerulean) and neighboring non-electroporated neurons (DAPI only) were selected independently of any cFos or ΔFosB signal (Fig. 3B). In a second step, the nuclear cFos and ΔFosB intensity of each electroporated neuron was normalized to the respective intensities of three neighboring neurons. This normalization procedure eliminated the influence of variable antibody staining between batches and variable activity levels between cultures. Both constructs (S-27 and S-27A) resulted in increased ΔFosB levels and decreased cFos expression compared to non-electroporated neurons (Fig. 3C). The wild-type variant (S27) resulted in significantly higher ΔFosB levels compared to the less stable S-27A version, leading to correspondingly lower cFos expression. The single cell intensity plot shows a strong inverse correlation between cFos and ΔFosB in S-27 expressing neurons (R = -0.59), which is not the case for the S-27A (R = -0.04) or DAPI (R = 0.26) population. These results provide clear evidence for a causal relationship between ΔFosB expression and cFos repression in CA1 pyramidal cells. The single cell intensity plot (Fig. 3D) is reminiscent of the bimodal distribution observed in the populations of single or double bicuculline-stimulated cultures (Fig. 2L).

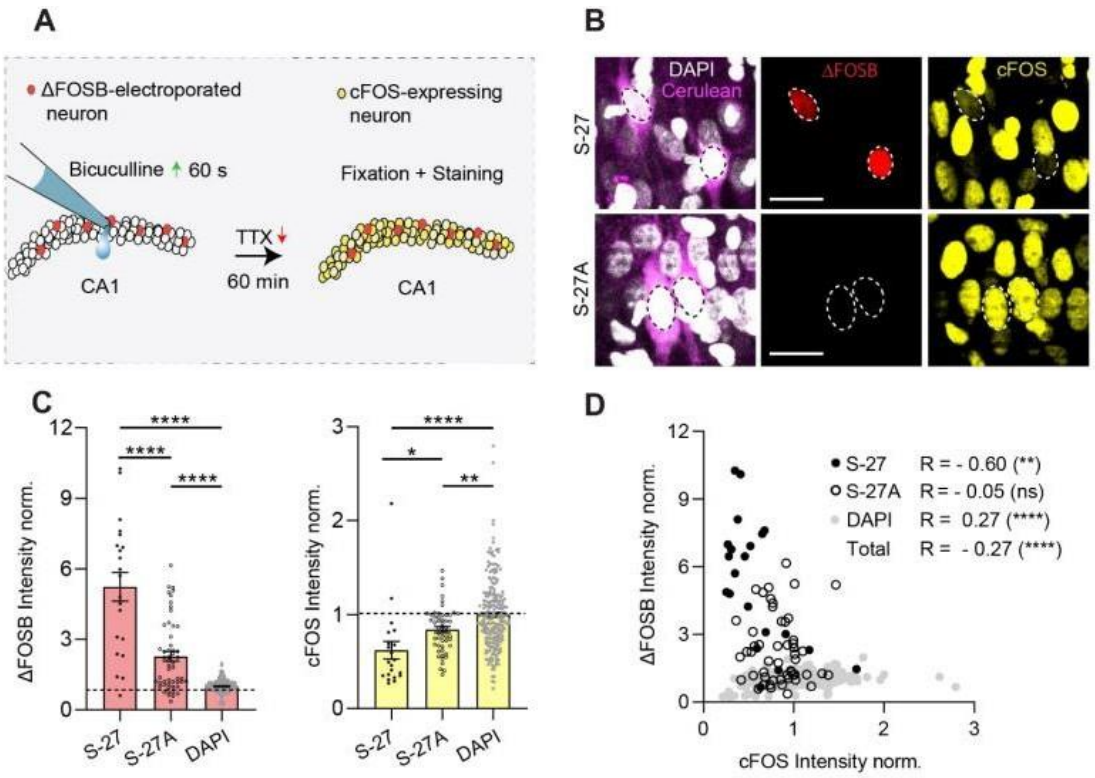

Figure 3: ΔFosB electroporation decreases bicuculline-induced cFos expression in CA1. **A)** Experimental design: slice cultures with single-cell electroporated CA1 neurons were stimulated with bicuculline for 60 seconds. Stimulation was terminated using TTX; cultures were fixed and stained for cFos (yellow) and ΔFosB (red) 60 minutes later. **B)** Confocal images of CA1 neurons expressing a non-modified version of ΔFosB (S27) and modified version of ΔFosB (S-27A) where the position serine 27 was exchanged with the amino acid alanine to prevent phosphorylation. In both conditions, neurons were co-electroporated with cerulean (10ng/µl, magenta) and the whole slice culture was stained for DNA (DAPI, gray) to allow unbiased cell selection for the intensity analysis. White circle show electroporated neurons. Scale bar = 20 µm **C)** Intensity analysis from neurons of n = 3 slice cultures per condition. Single spots represent a neuron and bars show mean ± SEM of all neurons. The cFos and ΔFosB intensities of electroporated neurons were normalized to neighboring DAPI⁺ neurons. Both protein versions (S-27, n = 21 neurons; S-27A, n = 53 neurons) show significantly higher ΔFosB expression (****p < 0.0001, S-27 vs DAPI; S-27A vs DAPI) compared to their neighboring DAPI⁺ neurons (n = 222). The wild type version leads to significantly more ΔFosB expression compared to the modified S-27A version (****p < 0.0001, S-27 vs S-27A). Neurons expressing both versions of ΔFosB have decreased cFos expression (****p < 0.0001, S-27 vs DAPI; **p = 0.01, S-27A vs DAPI) compared to neighboring DAPI⁺ neurons. Neurons expressing the S-27 version have decreased cFos intensities compared to the modified S-27A version (*p = 0.049, S-27 vs S27-A; 1-way ANOVA, Tukey's multiple comparison). **D)** Single cell intensity plot and intensity correlations between cFos and ΔFosB of different conditions (Pearson's). S-27 expressing neurons show a strong inverse correlation (R = - 60, ** p = 0.0043). S-27A (R = -0.05, ns p = 0.75), DAPI (R = 0.27, **** p < 0.0001), All (R = 0.27, **** p < 0.0001).

ΔFosB represses cFos via HDAC recruitment

ΔFosB is a splicing product of FosB (Robison and Nestler 2022). When phosphorylated by casein kinase 2 (CK2), ΔFosB becomes resistant to degradation and accumulates for several

days (Ulery-Reynolds et al. 2009; Ulery, Rudenko, and Nestler 2006). ΔFosB bineds directly to the cFos promoter and is able to recruit histone deacetylase class I enzymes (Renthal et al. 2008), setting the promoter to a repressed state (Fig 4A). We decided to test whether cFos suppression by bicuculline pre-stimulation (Fig. 2) indeed involves histone modification. Dentate gyrus neurons that were pre-stimulated with a drop of bicuculline (10 µl, 20 µM) 24 h before the second stimulation showed a CaMPARI2 conversion similar to that of non-prestimulated cultures, indicating that the network was still excitable (Fig. 4B, C). As in the previous experiments (Fig. 2), cFos expression was strongly suppressed by pre-stimulation (Fig. 4D). The HDAC inhibitor entinostat (MS 275) and the casein kinase II inhibitor DRB completely prevented the inhibitory effect of pre-stimulation in the dentate gyrus (Fig. 4D), but also increased nuclear calcium levels (Fig. 4C). Similar results were obtained in CA1 (Fig. 4E-J). In CA3, nuclear calcium levels were not affected by inhibition of CKII or HDAC (Fig. 4H,I) , but cFos inhibition was largely prevented (Fig. 4J). Taken together, we demonstrated that epigenetic repression of cFos after high activity occurs in all hippocampal subfields and is likely mediated by phosphorylated ΔFosB.

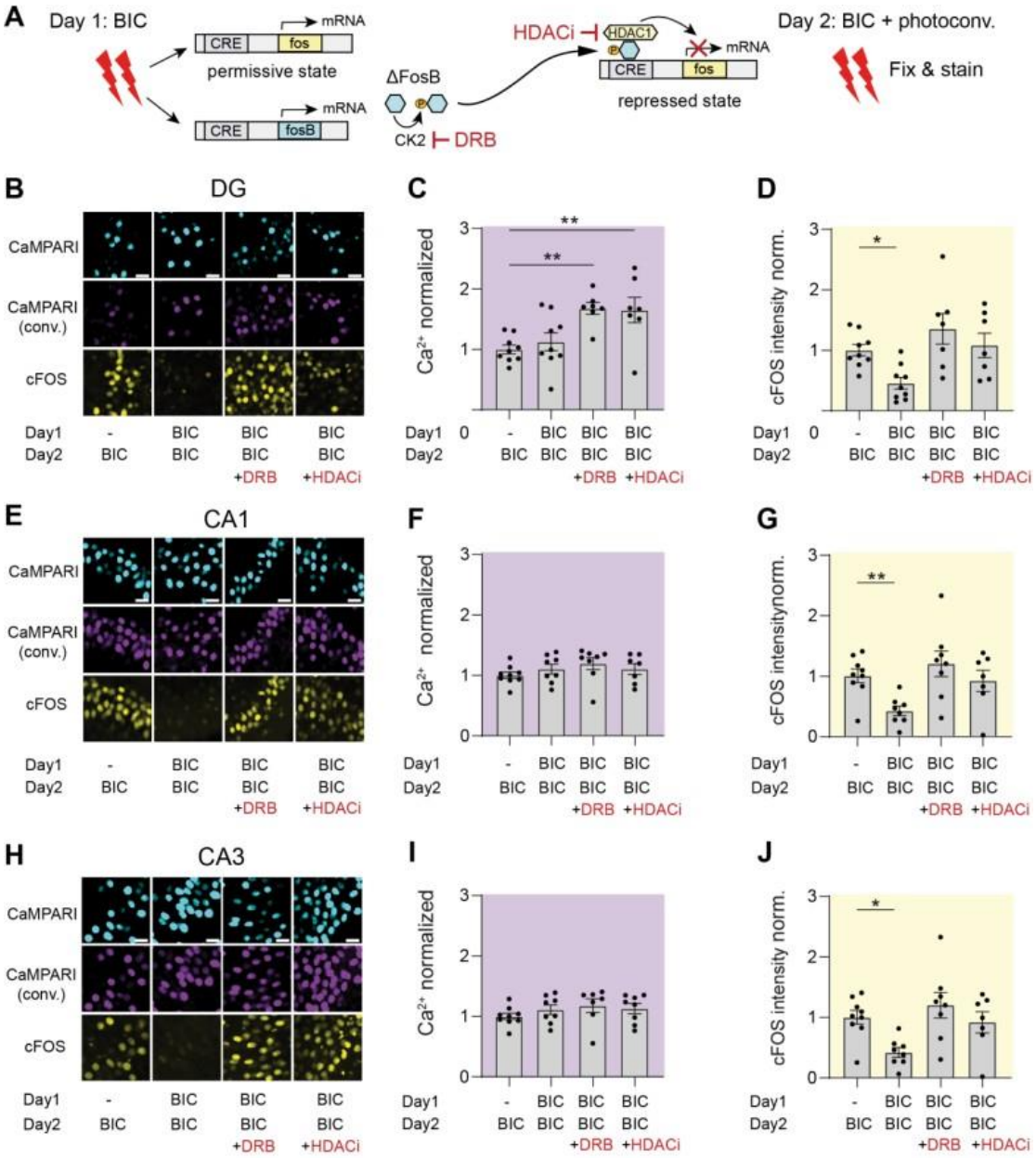

Figure 4: History of activity affects cFos expression. A) Bicuculline stimulation (BIC) on consecutive days, proposed mechanism of cFos inhibition. CK2, casein kinase 2; DRB, 5,6-Dichlor-benzimidazol-1-β-D-ribofuranosid; HDACi, histone deacetylase inhibitor Entinostat (MS 275). **B)** Confocal images of nuclear localized CaMPARI2 (native green fluorescence, cyan), photoconverted CaMPARI2 (immuno-enhanced, magenta) and anti-cFos staining (yellow) in dentate gyrus (DG), 1 h after bicuculline stimulation on day 2. Images show following conditions: BIC one-time stimulation on day 2 (BIC), BIC double stimulation on consecutive days (BIC-BIC), BIC double stimulation with CK_2 blocker (DRB) added on day 1 (BIC-BIC + DRB), BIC double stimulation with HDACi (MS275) (BIC-BIC + HDACi) added on day 2 together with second bicuculline stimulation. **C)** Analysis of Ca^{2+} level in dentate gyrus (DG) based on CaMPARI2 photoconversion during 60 seconds of BIC stimulation on day 2. Black dots represent the mean intensity in arbitrary units of 20 randomly selected $CaMPARI2^{+}$ nuclei. Gray bars represent mean ± SEM of n = 7 - 9 slice cultures per condition. All data points are normalized and statistically compared to the single stimulated condition (BIC). Double stimulated + HDACi or DRB treated cultures show increased calcium levels compared to BIC condition (**p = 0.005, BIC-BIC + DRB; **p = 0.0072, BIC-BIC + HDACi). Ca^{2+} level of

double stimulated cultures were not different from the BIC condition (ns p = 0.84, BIC). **D)** cFos intensity analysis in arbitrary units. All data points are normalized and statistically compared to the single stimulated condition (BIC). BIC-BIC condition shows decreased cFos expression compared to the single BIC condition (*p = 0.044). BIC-BIC + DRB or BIC-BIC + HDACi show no significant difference in cFos expression compared to BIC condition (ns p = 0.30, BIC-BIC + DRB; *p = 0.97, BIC-BIC + HDACi). The regions CA1 and CA3 were analyzed the same way. **E)** Confocal images of CA1 region. **F)** Analysis of Ca^{2+} levels in CA1. All conditions show similar Ca^{2+} levels compared to BIC condition (ns p = 0.82, BIC-BIC; ns p = 0.16, BIC-BIC + DRB; ns p = 0.23, BIC-BIC + HDACi; n = 7 - 11 cultures). **G)** cFos intensity analysis in CA1. Only double stimulated condition shows decreased cFos expression compared to the BIC condition (**p = 0.0094, BIC-BIC; ns p = 0.88, BIC-BIC + DRB; *p > 0.99, BIC-BIC + HDACi) **H)** Confocal images of CA3 region **I)** Analysis of Ca^{2+} levels in CA3. All conditions show similar Ca^{2+} levels compared to BIC condition (ns p = 0.68, BIB-BIC; ns p = 0.22, BIC-BIC + DRB; ns p = 0.70 BIC-BIC + HDACi) **J)** cFos intensity analysis in CA3. Only double stimulated condition shows decreased cFos expression compared to the BIC condition (*p = 0.025, BIC-BIC; ns p = 0.66, BIC-BIC + DRB; ns p = 0.97 BIC-BIC + HDACi). Statistical test: 2-way ANOVA, Dunett's multiple comparison.

Physiological activity drives ΔFosB expression in the dentate gyrus, but not in CA1

The role of ΔFosB as a protein influencing the epigenetic machinery has been studied mainly in the context of pathological conditions or drug abuse. These conditions are associated with supraphysiological activity and its negative consequences, such as memory impairment and compulsive behavior. In a previous study, we evaluated cFos and ΔFosB expression in water maze-trained mice using a subtractive method to quantify ΔFosB expression (Lamothe-Molina et al. 2022). Here, we use a recently developed antibody that directly detects ΔFosB (Fig. 5A). After two consecutive days of water maze training, a similar number of neurons in DG and CA1 express cFos (Fig. 5B). However, the accumulation of ΔFosB is largely limited to granule cells in the DG (Fig. 5C). Single neuron analysis revealed two subsets of DG granule cells, displaying either high ΔFosB / low cFos or low ΔFosB / high cFos, with an inverse correlation between the two proteins (Fig. 5D). Only a small number of neurons expressing ΔFosB were detected in CA1, and this group also had low cFos levels (Fig. 5E). Therefore, although the inhibitory mechanism is present in CA1 pyramidal cells (Fig. 2), it appears to be minimally active during physiological activity.

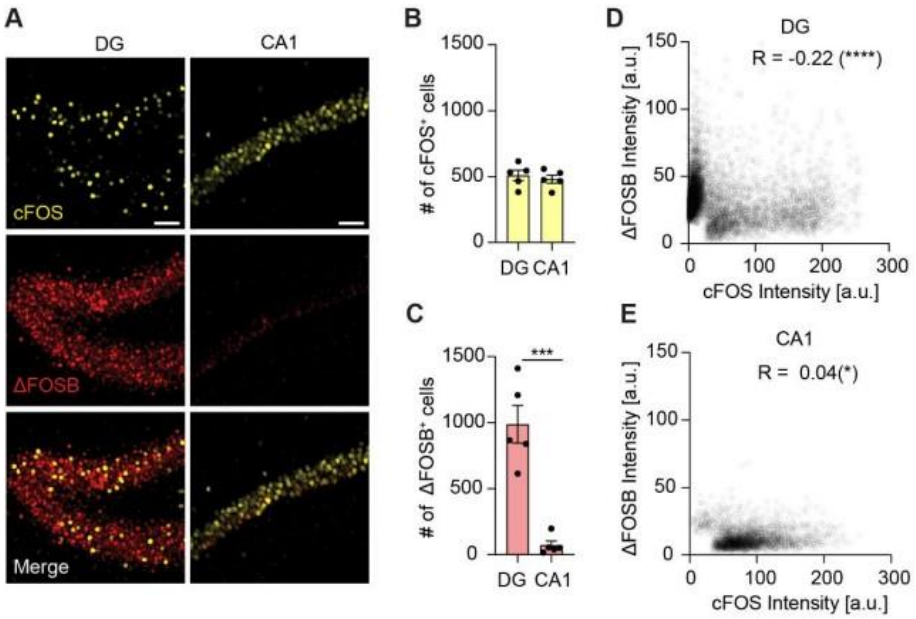

Figure 5: Expression of cFos and ΔFosB in the hippocampus after water maze training. A) In dentate gyrus (DG), sparse expression of cFos (yellow) and strong expression of ΔFosB (red). In CA1, dense expression of cFos and minor ΔFosB expression. Scale bar: 20 µm. **B)** No significant difference between cFos-expressing neurons in DG and CA1 (ns p = 0.60, t-test) after 2 days of water maze training (n = 5 mice). Dots show cell count (sum) of 4 analyzed images (18 µm z-stacks) per animal and region. Bars show mean ± SEM **C)** High number of ΔFosB-positive cells are found in DG, not in CA1 (***p = 0.0002, t-test) **D)** Single cell intensity analysis. Individual DG granule cell nuclei (circles) express either high cFos or high ΔFosB, rarely both (Pearson's R = -0.22; **** p < 0.0001; n (cells) = 6617). **E)** CA1 pyramidal cells express cFos, but hardly any ΔFosB (Pearson's R = 0.04; **** p < 0.0001; n (cells) = 2608).

Effect of HDAC inhibition on cFos re-expression in the dentate gyrus

The strong expression of ΔFosB in the DG after water maze training and its repressive effect on cFos led us to ask whether we could counteract cFos repression by inhibiting histone deacetylase class I. For these experiments, we injected Tet-tag mice with AAV-TRE-mKate2 and kept them on doxycycline (Dox) to prevent cFos tagging during the recovery period (Fig. 6A). The day before the mice learned to locate a hidden platform in the water maze (day 1), doxycycline was removed from the food to permanently label cFos-expressing neurons with mKate2 (cFos tagging). After the training, further cFos tagging was prevented by an intraperitoneal injection of Dox. On day 2, mice were retrained to find the platform and perfusion-fixed 1 h later. To assess cFos expression on day 2, tissue was stained for cFos (2^{nd} cFos ensemble, 647 nm), and cFos-tagged GC from day 1 were enhanced with anti-mKate2 staining (cFos-tagged, 568 nm). To test whether HDAC inhibition affects cFos repression, one group of mice was injected with HDACi (CI-994) immediately after training on day 1 and again 1 h before the training on day 2. The control group was injected with vehicle only (VEH, DMSO + 0.9% NaCl). As we and others previously reported, cFos expression in the DG was sparse on both days (Lamothe-Molina et al. 2022; Chatzi et al. 2019) (Fig 6B-C). HDACi treatment did not alter the size of cFos ensembles (Fig 5C, D). In HDACi-treated mice, 11% of day 1 Fos^{+}

cells re-expressed cFos on day 2, compared to 7% in the control group (Fig. 5E). The above-chance re-expression of cFos in HDACi-treated animals was normalized to the control group (VEH) of each experimental round. The above-chance re-expression in HDACi-treated mice was significantly higher compared to the control group (Fig 6F), demonstrating that HDAC inhibition indeed affects cFos repression in dentate granule cells.

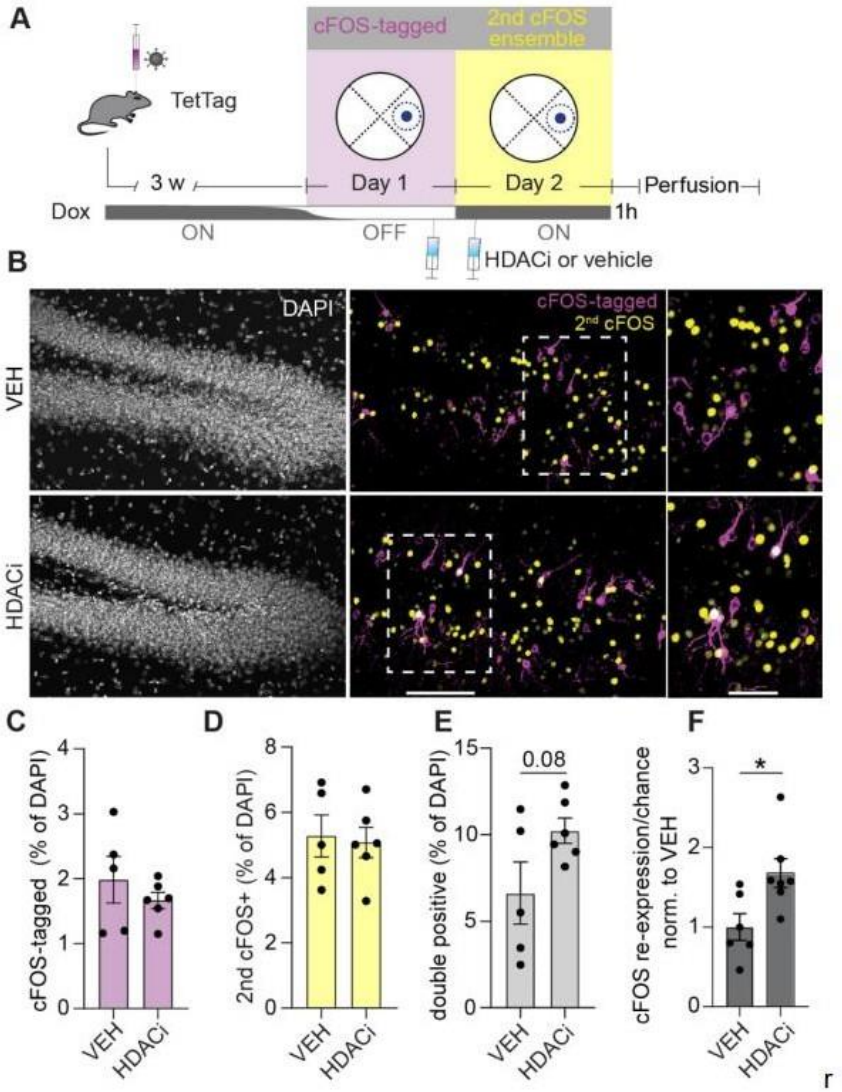

Figure 6: HDAC inhibitor increases cFos re-expression in dentate gyrus. A) Experimental time line: TetTag mice were injected with AAV-3TRE-mKate2 to tag cFos$^+$ granule cells with mKate2 when doxycycline is removed from chow (OFF Dox). During the OFF Dox period (Day 1), mice were trained to find a platform in the water maze. On day 2, mice performed the same training protocol again (ON Dox) and were perfused 1 h after training. One hour after WM training on day 1 and 1 h beforeWM training on day 2, mice were injected with HDACi solution (CI-994, 30 mg/kg in 90% 0.9% NaCl, 10% DMSO) or vehicle solution (90% 0.9% NaCl,10% DMSO). **B)** DAPI staining of dentate gyrus and immunofluorescence against mKate2 (magenta) and cFos (yellow). White square indicates zoomed section. **C)** No difference in percentage of granule cells expressing cFos on day 1 between HDACi and VEH treated animals (ns p = 0.37, t-test). **D)** No difference in percentage of granule cells expressing cFos on day 2 (ns p = 0.81, t-test). **E)** Increase in percentage of double positive GC in HDACi condition (ns p = 0.08, t-test). **F)** cFos re-expression above chance level normalized to VEH condition per experimental round, is significantly higher

in HDACi-treated mice (*p = 0.019, t-test). 1st experiment, n = 2 per condition; 2nd experiment, n = 4 (HDACi), n = 3 (VEH).

Inhibition of histone deacetylase during learning of multiple platform positions in the water maze

Multiple lines of evidence suggest that the DG plays a critical role in pattern separation, a key aspect of episodic memory and cognitive flexibility (Hainmueller and Bartos 2018; Leutgeb et al. 2007) Therefore, we tested whether the ΔFosB expression and cFos repression in the DG after water maze training is functional in facilitating reversal learning in the water maze, a cognitive ability known to rely on pattern separation and cognitive flexibility. To investigate the effects of HDAC inhibition during spatial reversal learning, we trained C57BL6/J mice to locate three different platform positions in the water maze over the course of 4 days. Some mice were orally treated with the HDAC inhibitor CI-994 (HDACi-treated, n = 12 mice) one hour before water maze (WM) training on each training day, while others were administered the vehicle solution only (90% corn oil and 10% DMSO, n = 15 mice). All mice were trained for three days to find the platform in the east quadrant of the WM. The learning curve of HDACi-treated animals did not differ from that of control animals (Fig. 7A). In addition, both groups showed identical performance in the day 1 probe trial (Fig 7B), indicating no effect of HDACi on short-term memory. HDACi-treated mice performed again equally well in the probe trial the next day (Fig. 7C), suggesting that long-term memory was also unaffected. Further training improved performance, but revealed no effect of HDAC inhibition in probe trials (Fig. S7).

Over the course of three days of training, mice developed a highly accurate memory for the platform location in the east quadrant. To test behavioral flexibility, mice underwent four reversal training trials to a new platform location on day 3 (platform in the west quadrant, Fig. 7D and E) and day 4 (platform in the north quadrant, Fig. 7F and G). After each reversal learning session, a probe trial was performed to evaluate the mice's search strategies. The mice in the control group quickly adapted their search strategy to the new positions of the platform, as shown by their improved performance in the training trials and their behavior during the probe trials. By the fourth trial on day 3, the control group mice had improved their learning performance (Fig. 7D), and by day 4, they needed only one trial to locate the platform promptly at the new location (Fig. 7F). It is important to note that on Day 3, the mice had to learn two things in order to switch their search strategy: first, the new position of the platform, and second, the "rule" that the platform could only be found at the most recent location, not at the location where they had previously found it on most of the training trials. Therefore, it is possible that the mice's rapid reversal learning on day 4 was facilitated by their prior understanding of this new rule. During the first 30 seconds of the probe trials, when mice are expected to search at the location with the higher probability of finding the platform, the control group spent more time at the newly learned platform location compared to the previously learned location (Fig. 7E and G, Fig. S8). Thus, the control mice exhibited adaptive behavioral flexibility and switched their strategy in response to the changing conditions experienced during reversal learning. In the HDACi-treated mice, however, this ability appeared to be

partially impaired. They showed weaker performance during the reversal training on day 4 compared to the control mice (Fig. 7F), and they did not show a preference for the newly learned platform over the previously learned one during the probe trials on days 3 and 4 (Fig. 7E and G).

Taken together, these results suggest that HDAC inhibition does not affect the learning or recall of a single spatial location. However, when mice are presented with a choice between multiple possible platform locations, the spatial memory formed under HDAC inhibition (first location) appears to interfere with the storage or recall of new information, thereby reducing behavioral flexibility.

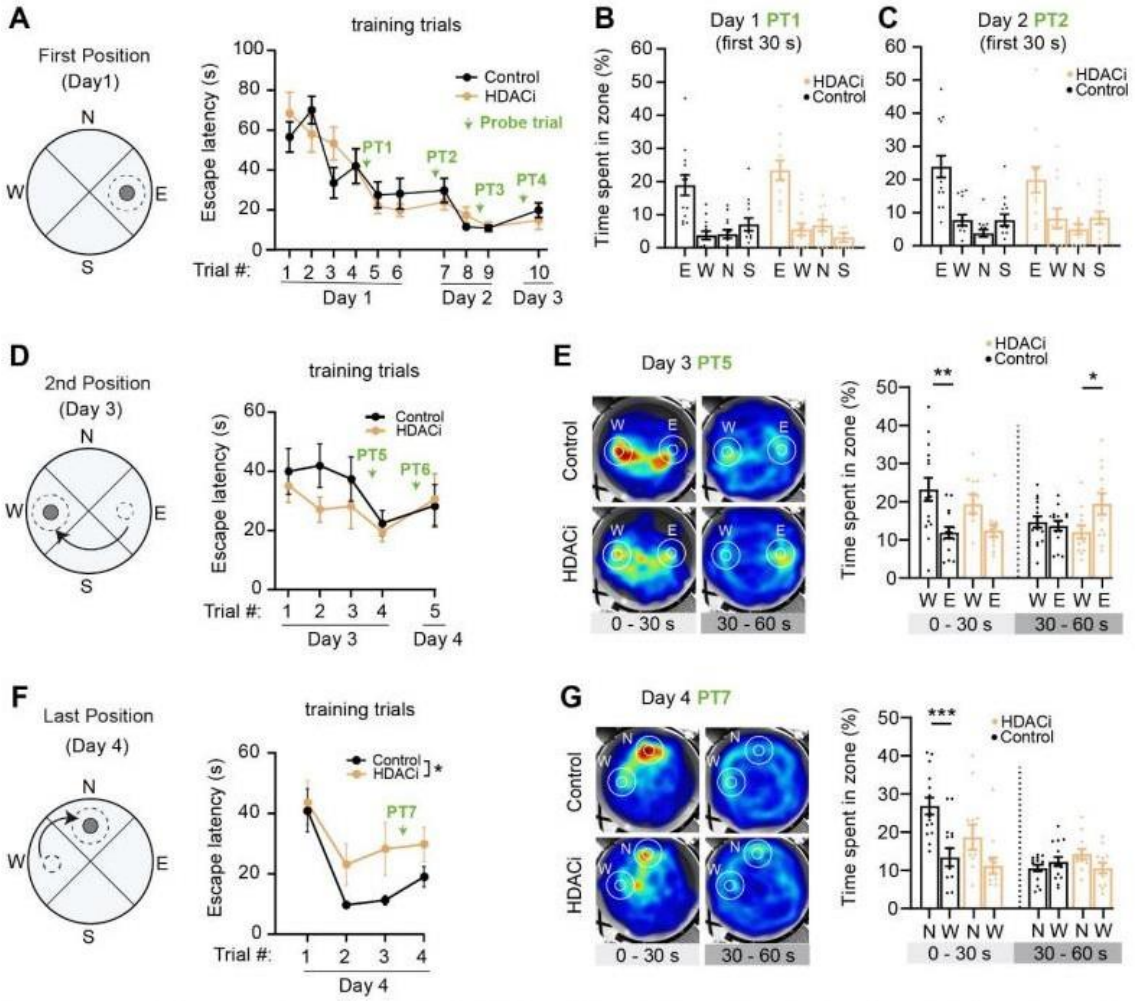

Figure 7: Spatial memory formation under HDAC inhibition. A) Day 1: The platform (gray circle) was located in the east quadrant of the maze. Escape latency to the platform was used for analysis of training trials (TT) and the dotted line (target zone, Ø = 42 cm) for probe trial analysis (PT). Mean escape latency (± SEM) improved over the course of 3 days during 10 TTs, with no difference between HDACi (ochre, n = 14-15) or VEH condition (black, n = 11-12) (ns, p = 0.99, 2-way ANOVA). Green arrows indicate probe trials. **B)** Performance during the first 30 s of the probe trail on day 1. Each point represents one animal (HDACi: n = 11, VEH: n = 13). Bars show percentage of time (mean ± SEM) spent in each target zone (east, E; west, W; north, N; south, S). No significant difference between HDACi and control group (ns p = 0.40, 2-way ANOVA). **C)** Probe trail performance (first 30 s) on day 2 to test for

long-term memory. Bars show mean ± SEM. No significant difference between both conditions (ns p = 0.81, 2-way ANOVA). **D)** On day 3, mice were trained to a novel platform location (west) in four TTs. Escape latency to platform west is shown as mean ± SEM. No significant difference between HDACi and control group (ns p = 0.17, 2-way ANOVA) **E)** Mean swim trajectories of all animals per condition for the first (0 - 30 s) and second half (30 - 60 s) of the probe trial (heat maps). Animals alternate between the old (E) and new (W) target zones. Bars show mean ± SEM. During the first 30 s, VEH-treated animals (black) show a significant preference for the new learned location (W) compared to the first learned location (E) (**p = 0.0016, 2-way ANOVA, Šídák). HDACi-treated mice (ns p = 0.89, 2-way ANOVA). In the second half of the probe trial, HDACi-treated animals show a significant preference for the old (E) platform location (*p = 0.016, 2-way ANOVA). VEH-treated mice (ns p = 0.89, 2-way ANOVA). **F)** On day 4, mice were trained to yet another platform location (north) in four TTs. The VEH condition shows better learning performance (mean ± SEM escape latency) compared to the HDACi group (*p = 0.029, 2-way ANOVA). Green arrow indicates probe trial. **G)** Mean swim trajectories of all animals per condition for the first (0 - 30 s) and second half (30 - 60 s) of the probe trial (hear maps). Bars show mean ± SEM. Control animals show a significant preference for the new platform position (N) compared to the previous (W) position (***p = 0.0004, 2-way ANOVA, Šídák). HDACi-treated mice (ns p = 0.01, 2-way ANOVA). During 30 - 60 s no condition showed preference for platform positions north vs west (VEH, ns p = 0.51; HDACi, ns p = 0.09; 2-way ANOVA, Šídák).

To further investigate the stability of spatial memories, all animals returned to the WM on day 5 for a long-term memory probe trial lasting 90 s. No HDACi was administered on this day. We split the total search path into three 30 s time periods and analyzed the number of entries into the three previously trained platform positions (Ø = 15 cm, Fig. 8A). In the first period, control animals had a strong preference for the last-learned platform position (green) compared to the second (red) and first (dark blue) position. Later in the probe trial (30 - 60 s), they sampled all three learned positions. In the last period (60 - 90 s), their search became more random, indicating that they adapted their strategy when they could not find the platform where they expected it to be. HDACi-treated mice (dotted lines) showed a slight preference for the last and second learned positions at the beginning of the trial (first period) and switched to random search in the later periods. Averaged over the total duration of the probe trial, HDACi-treated mice spent significantly less time in the 3 target zones (Ø = 42 cm) compared to controls (VEH vs HDACi, p = 0.02, Fig. 8B). In the first 30 s of the probe trial, control animals spend most of the time searching in the zone of the last trained platform position (Fig. 8C, D) while HDACi-treated mice did not. The effect of HDAC inhibition was even more pronounced when we tested the mice again on day 11, 6 days after the end of training (p = 0.001, Fig. 8E, F). The search strategy of control animals was remarkably consistent on day 5 and day 11 (Fig. 8G). After finding no platform at the last trained location, they went looking at the second and finally, at the first trained location. Mice that were trained under HDAC inhibition initially searched around the second trained location, but showed significant variance between day 5 and day 11 (Fig. 8H). In summary, the water maze experiments showed that HDAC inhibition during training of multiple platform positions leads to reduced performance in probe trials. Significant effects of HDACi treatment were detected immediately after training (Fig. 7) as well as 1, 4 (Fig S8) and 6 days later (Fig. 8).

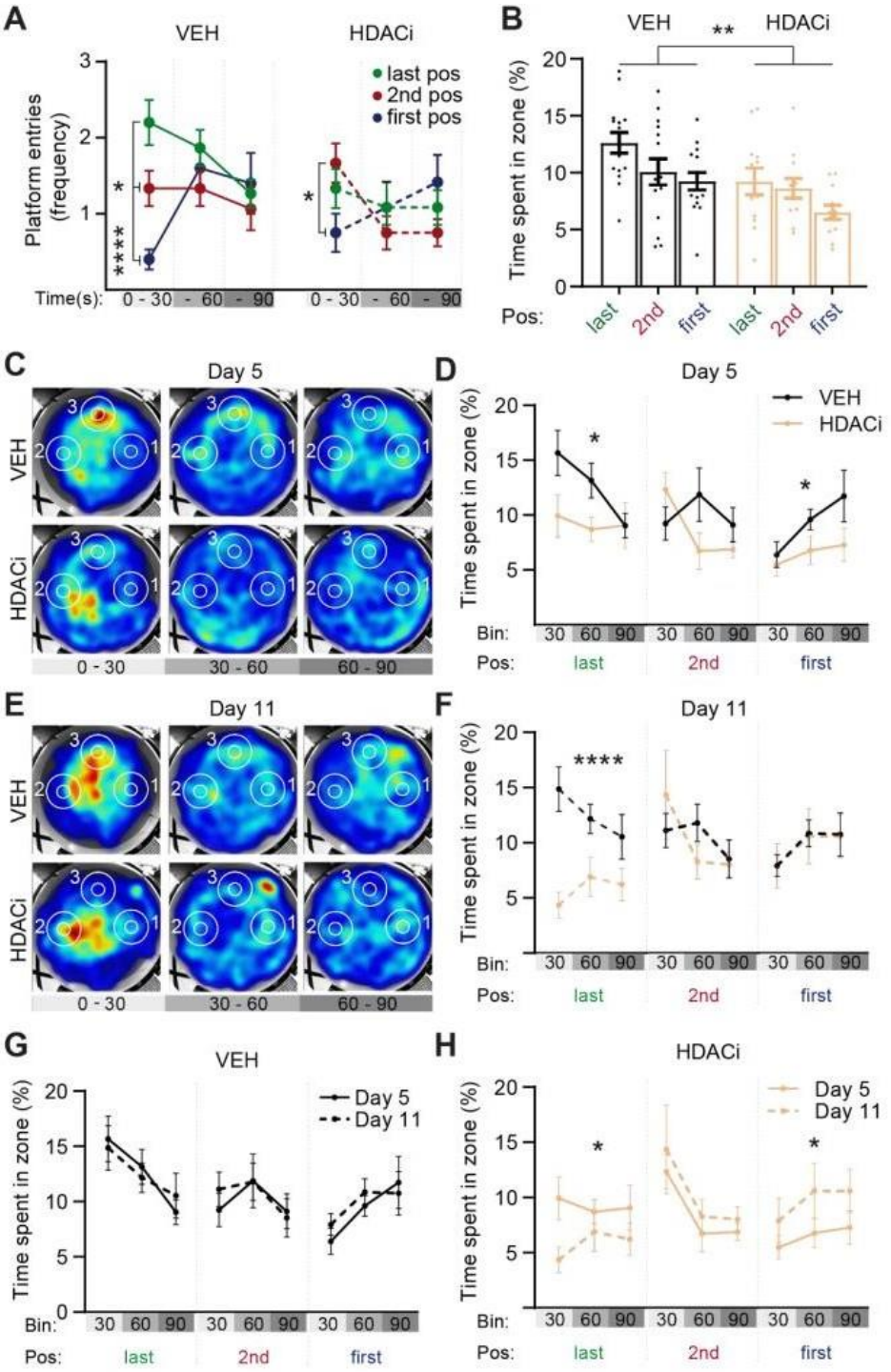

Figure 8: Spatial memory retrieval. A) Mean frequency of platform position entries for vehicle controls (VEH, n = 15 mice) and HDACi-treated mice (n = 12) during the probe trail on day 5. Last trained position (green, north), second trained position (red, west), first trained position (dark blue, east). The first 90 s were analyzed and divided into three periods: 0 - 30 s; 31 - 60 s; 61 - 90 s. Markers show mean ± SEM for each period. During the initial 30 s, control mice showed a strong preference for the last-trained platform location (last vs first, ****p < 0.0001; last vs 2nd, p = 0.051; 2nd vs first, *p = 0.033, 2-way ANOVA, Tukey). Mice that were HDACi-treated during training showed less preference for a particular position (last vs first, p = 0.64; last vs 2nd, p = 0.26; 2nd vs first, *p = 0.04, 2-way

ANOVA, Tukey). **B)** Total percentage of time spent in target zone (last, 2nd, first). Each point represents one animal (VEH, n = 15; HDACi, n = 12), bars show mean ± SEM. HDACi-treated mice spent significantly less time in all target zones (VEH vs. HDACi, **p = 0.018, 2-way ANOVA). **C)** Mean trajectory projections (heat maps) of all animals on day 5, divided into three 30 s periods. **D)** Percentage of time spent in the three target zones per condition (mean ± SEM). Compared to the HDACi condition, VEH-treated animals show an increased preference for the last (north) and first (east) but not for the second (west) position (last, * p = 0.017; 2nd, p = 0.32; first, * p = 0.031; 2-way ANOVA, Šídák). **E)** Mean trajectory projections (heat map) of all animals per condition on day 11, divided in three 30-s periods. **F)** Percentage of time spent in the target zones (order: last, first, second) for all three periods per condition on day 11 (mean ± SEM). Compared to the HDACi condition, VEH-treated animals show a high preference for the last (north) but not for the second (west) or first (east) position (last, **** p < 0.0001; 2nd, ns p = 0.88; first, * p = 0.092; 2-way ANOVA, Šídák). **G-H)** Plots compare probe trail data of both days (5 vs. 11) per condition (VEH, HDACi). VEH treated animals show similar performance on both days (last, ns p = 0.95; 2nd, ns p = 0.78; first, ns p = 0.63; 2-way ANOVA, Šídák). Compared to day 5, on day 11, HDACi-treated animals spent less time around the last position (north, * p = 0.013) but more time around the first position (east, * p = 0.033), with no difference for the 2nd learned position (west, ns p = 0.36; 2-way ANOVA, Šídák).

Discussion

When we examined the relationship between nuclear calcium levels and cFos expression, we were struck by the poor correlation between these two parameters in individual neurons. The complex regulation of the cFos promoter has been studied in great detail (Robison and Nestler 2022; Vanhoutte et al. 1999), and we realized that accumulation of ΔFosB could have suppressed cFos specifically in neurons with a history of spontaneous activity. In hippocampal slice cultures, we were able to produce this effect by pre-stimulation, resulting in increased ΔFosB and decreased cFos in response to a second round of stimulation on the next day. Causality was established by observing the same inhibitory effect following overexpression of ΔFosB in single neurons. Long-lasting cFos inhibition required phosphorylation of ΔFosB by CK2 and histone deacetylation by HDAC1, as expected (Robison and Nestler 2022). In these slice culture experiments, we induced rhythmic epileptiform activity by sequential application of bicuculline and TTX, thereby transiently blocking $GABA_A$-mediated inhibition. This supraphysiological stimulation caused ΔFosB accumulation and cFos inhibition in the DG, CA3, and CA1. Physiological activity, specifically water maze training, resulted in ΔFosB accumulation in DG granule cells, but not in CA3 and CA1 pyramidal cells. Thus, while the ΔFosB-based inhibitory mechanism appears to be operational and ubiquitous in all hippocampal neurons, spatial learning activates it specifically in the DG (Lamothe-Molina et al. 2022).

Our results indicate that ΔFosB accumulation in the DG during spatial learning restricts cFos expression to a subset of granule cells, namely cells that have not been strongly activated for several days. The specific activation of ΔFosB expression in the DG during spatial learning is intriguing given the role attributed to the DG in learning and memory. Multiple lines of evidence suggest that the DG plays a crucial role in pattern separation in both humans (Bakker et al. 2008; Berron et al. 2016) and rodents (Neunuebel and Knierim 2014; Madar, Ewell, and Jones 2019). Pattern separation allows for the discrimination between similar stimuli and memories, which is essential for cognitive flexibility and the ability to shift strategies when conditions change. A standard measure of cognitive flexibility and strategy shifting is reversal learning.

We speculated that learning-induced accumulation of FosB in granule cells may be relevant for reversal learning in the water maze.

To test this hypothesis, we developed a memory task that required memorization of three different spatial locations, each of which was trained on a different day. Since histone deacetylation was necessary to produce ΔFosB-mediated cFos inhibition in culture, we used an HDAC1 inhibitor to disable this epigenetic mechanism in vivo. Although both groups of mice were able to learn and remember a single platform position, HDAC-inhibited mice had significant difficulty remembering novel positions (reversal learning). Previous studies have reported improvements in memory following HDAC inhibition (Peixoto and Abel 2013; Ramirez-Mejia et al. 2021; Villain, Florian, and Roullet 2016) The deficit we report here is specific to reversal learning and can thus be reconciled with the aforementioned studies. Obviously, increased memory persistence could lead to reduced behavioral flexibility when an animal is faced with more complex tasks and changing environments. Furthermore, the duration of experimental HDAC inhibition appears to be critical, as acute and chronic inhibition have different effects on addiction memory (Nestler 2014).

In our experiments with TetTag mice, HDAC inhibition increased the proportion of granule cells expressing cFos on two consecutive days of water maze training. In these experiments, we used a relatively simple task of training TetTag mice to a single platform position. It remains to be seen how more complex tasks affect the overlap of cFos populations in the dentate gyrus with and without HDAC inhibition. The effects of HDAC inhibition on memory are due changes in the expression level of genes regulated by the CREB:CBP transcriptional complex (Vecsey et al. 2007). Despite this relatively specific effect, it should be noted that ΔFosB-mediated inhibition of cFos is not the only memory-relevant process controlled by HDAC1. Calbindin-D28k has also been shown to be downregulated by ΔFosB-mediated histone deacetylation (You et al. 2017).

The behavior of reversal-trained mice was intriguing and changed during the probe trials. Control mice not only learned the new platform locations as indicated by the reversal learning trials on days 3 and 4), but also changed their strategy. During the first reversal learning on day 3, mice still seemed to follow the rule “search at the position where you found the platform most often”, as their performance slowly improved over the four training trials. In contrast, on day 4, when they underwent a second set of reversal training trials, control mice started swimming directly to the new platform position after only one training trial, indicating a new behavioral rule: “search at the position where you last found the platform”. In addition, our analysis of probe trials on days 5 and 11 suggests that the control group of mice remembered platform locations in a sequential manner (Fig. 8G). An anthropomorphic interpretation of this ordered search could be a cognitive process that takes into account new information, such as the absence of the platform at the expected location: "Given that the platform is not where I last found it, where else could it be?" The reuse of the same set of neurons for memory storage on consecutive days could hinder the ability to recall different locations in sequence while updating prior beliefs about the platform’s location. This is evidenced by the behavior of mice trained under HDAC inhibition, which did not visit the platform locations in reverse order (Fig. 8H), suggesting a lack of clearly structured memory regarding possible escape locations.

ChIP-sequencing of mouse hippocampus revealed that ΔFosB regulates genes involved in neuron and dendrite development and synapse maturation (You et al. 2018), perhaps in a homeostatic manner to prevent seizure generation (Eagle et al. 2018). Our results highlight the importance of epigenetic mechanisms in the organization of complex contextual memories (Creighton et al. 2020; Eagle et al. 2015; Ramamoorthi et al. 2011; Weng et al. 2018) and explain why calcium levels are not sufficient to predict cFos activation in individual neurons. In contrast to CA1 pyramidal cells, DG granule cells exhibit a dramatic shift in transcription upon activation. The common perception of the DG as a quiet, sparsely active region is accurate in describing its electrophysiological responses, but not in describing its transcriptional responses (Jaeger et al. 2018). While there is strong electrical reactivation of granule cells when exposed to the same environment on consecutive days, readily measurable by monitoring somatic $[Ca^{2+}]_i$ (Hainmueller and Bartos 2018), the state of intracellular signaling pathways is completely altered compared to the first exposure (Coba et al. 2012; Jaeger et al. 2018). Granule cells are the only neurons in cortex that require regular replacement, and it is tempting to speculate that their high transcriptional activity and associated increases in excitability wear them down. The dentate gyrus evolved rapidly during the transition from reptiles to stem mammals (Hevner 2016), undoubtedly to support novel memory or thought processes specific to mammals. Determining how the epigenetic state of granule cells affects their input-output function is the next challenge in understanding the unique computations that require such unusual hardware.

Methods

Organotypic hippocampal slice cultures

Wistar rat pups were sacrificed at postnatal day 5-7, both hippocampi were dissected and cut into 400 µm thick sections using a tissue chopper. The hippocampal slices were cultured on 30 mm sterile membrane inserts (Millipore) in 6-well plates, each containing 1 ml of culture medium, in a cell culture incubator (37°C, 5% CO_2). The culture medium, consisting of 394 ml Minimal Essential Medium (Sigma), 100 ml heat-inactivated donor horse serum (Sigma), 1 mM L-glutamine (Gibco), 0.01 mg ml-1 insulin (Sigma), 1.45 ml 5 M NaCl (Sigma), 2 mM $MgSO_4$ (Fluka), 1.44 mM $CaCl_2$ (Fluka), 0.00125% ascorbic acid (Fluka), 13 mM D-glucose (Fluka), was partially (~70%) replaced twice a week. Antibiotics, which can induce seizure-like activity in hippocampal slice cultures, were not required due to sterile preparation conditions.

Single-cell electroporation

At DIV 14-16, CA1 neurons from slice cultures were transfected via single-cell electroporation (Wiegert, Gee, and Oertner 2017). Thin-walled pipettes (~10 MΩ) were loaded with plasmids diluted in intracellular solution (Table 1). Under visual control (IR-DIC), the pipette was advanced against the neuronal membrane. DNA was ejected with 12 hyperpolarizing pulses (-12 V, 0.5 ms) using an Axoporator 800A (Molecular Devices). Experiments were conducted 6 days after electroporation.

Plasmid	Short name	Concentration (final)
pAAV-hsyn1-H2B-CaMPARI2	H2B-CaMPARI2	Virus production
pAAV-CMV-ΔFosB (Addgene plasmid 68545)	ΔFosB(S27)	0.1ng/µl
pAAV-CMV-ΔFosB(S27A)	ΔFosB(S27A)	0.1ng/µl
pCI-syn1-CFP		10ng/µl

Table 1: Plasmid list

Viral vector production, dilution and transduction

Recombinant AAV were produced in the vector core facility of the University Medical Center Hamburg-Eppendorf. Virus particles were diluted to a working concentration of 1.13 x 10^{12} vector genomes / ml (vg/ml) in buffer solution containing (in mM) 145 NaCl, 10 HEPES, 25 D-glucose, 1.25 NaH_2PO_4, 2.5 KCl, 1 $MgCl_2$, 2 $CaCl_2$. In a laminar flow hood, 2 µl of the virus suspension was dropped on top of each slice culture at day in vitro (DIV) 14-19. After 5 days of expression, slice cultures were used for experiments.

Bicuculline-induced stimulation and H2B-CaMAPRI2 photoconversion in the incubator

Slice cultures were either virally transduced or electroporated with plasmid DNA before stimulation. Bicuculline (BIC) was applied to induce activity to analyze Ca^{2+} levels (H2B-CaMPARI2), cFos and ΔFosB expression (see Table 2). H2B-CaMPARI2 expressing cultures were illuminated with 395 nm light (0.4 mW/mm^2) during BIC stimulation. Three hippocampal slices were placed near the center of a single culture membrane in a 35 mm petri dish and transferred to the stimulation incubator at day 4 after transduction. At day 5 after transduction, the culture dish was placed into an LED illumination tower inside the incubator. To induce activity, slice cultures were treated by pipetting 100 µl bicuculline (BIC, 20 µM) on top of the cultures. After 10 - 60 s, tetrodotoxin (TTX, 300 µl, 1 µM) was added to prevent further spiking. The 395 nm LED (0.4 W/mm^2) was turned on 5 s before BIC application and turned off 5 s after TTX application to ensure conversion during potential activity bursts induced by handling. After 60 min of incubation, slice cultures were fixed and stained (see IHC section).

Figure	Virus/plasmid	BIC Stimulation		Stim. time	AB staining
		Day 1	Day 2		
1	H2B-CaMPARI2	No	Yes	10-60 s	cFos, CaMPARI2
2	none	No	Yes	60 s	cFos, ΔFosB
3	S27 / S27A	No	Yes	60 s	cFos, ΔFosB
4	H2B-CaMPARI2	Yes	Yes	60 s	cFos, CaMPARI2

Table 2: Slice culture experiments

Table 1 Plasmid list

Table 2 Slice culture experiments

Bicuculline stimulation on two consecutive days, DRB (CK2i) and MS-275 (HDACi) treatment

Slice cultures expressing H2B-CaMPARI2 were pre-stimulated with a drop of bicuculline (BIC, 10 µl, 20 µM, 2.7% DMSO, 97.3% buffer) the day (day 4) before the photo-conversion in the stimulation incubator. Additionally, some slice cultures were treated with BIC and 5,6-Dichlor-benzimidazol-1-β-D-ribofuranosid (DRB, Producer) (10 µl, BIC, 20 µM, DRB, 120 µM, 2.7% DMSO, 97.3% buffer). On day 5 slice cultures were stimulated with BIC again (100 µl, 20 µM, 2.7% DMSO, 97.3% buffer) in the presence of continuous 395 nm (0.4 mW/mm^2) light. Some conditions were treated with BIC and MS-275 (HDACi, Producer) (100 µl, BIC, 20 µM, MS-275, 10 µM, 2.7% DMSO, 97.3% buffer). 60 s after BIC application, TTX (300 µl, 1 µM) was applied to abolish activity and the cultures were fixed and stained 1 hour later (see IHC section).

Tissue fixation and Immunohistochemistry (IHC)

Slice cultures were fixed in 4% PFA/PBS solution for 25 min. Fixed cultures were cut off the membrane and washed in 1 × PBS for 10 min, incubated in blocking solution (500 µl, 1 × PBS, 0,3 % TritonX (Sigma-Aldrich), 5 % goat serum) for 2 h, then incubated in the primary antibody (Table 3) carrier solution (500 µl, 1 × PBS, 0,3 % Triton X-100, 1 % goat serum, 1 % BSA) overnight at 4°C. The next day, slice cultures were washed three times with 1 × PBS for 5 min, then incubated for 2 h in the secondary antibody (Table 3) carrier solution (500 µl, 1 × PBS, 0,3 % Triton X-100, 1 % goat serum, 1 % BSA) at RT. Slice cultures were washed 3 × 10 min in 1 × PBS, optionally stained with 4′,6-diamidino-2-phenylindole (DAPI, 1:1000) for 5 min, and mounted on coverslips using Immu-Mount (Shandon). This protocol was also used to stain acute hippocampal slices.

Figure	Primary AB (Producer, #)	Secondary AB (Producer, #)	Host	Dilution
1, 4, S3, S5	cFos (SySy, 226017)	647 (Invitrogen, A21247)	Rat	1:1000
	Campari2 red (4F61) (Abs. AB, AB1649-23.0)	568 (Invitrogen, A11011)	Rabbit	1:1000
2, 3, 5	cFos (SySy, 226017)	647 (Invitrogen, A21247)	Rat	1:1000
	ΔFosB (Cell Signaling, 2251)	568 (Invitrogen, A11011)	Rabbit	1:1000
6	cFos (SySy, 226017)	647 (Invitrogen, A21247)	Rat	1:1000
	tRFP/mKate2 (Evrogen, AB233-EV)	568 (Invitrogen, A11011)	Rabbit	1:1000
S2, S4	cFos (SySy, 226017)	647 (Invitrogen, A21247)	Rat	1:1000
S6	ΔFosB (Cell Signaling, 2251)	568 (Invitrogen, A11011)	Rabbit	1:1000

Table 3: Primary and secondary antibody combinations (SySy, Synaptic Systems)

Confocal imaging

To evaluate all hippocampal subfields (Fig. 1B-C, Fig. 2, Fig. S5), immunostained slice cultures were imaged in 3D with a confocal microscope (Olympus Fluoview FV 1000, UPLSAPO 20x/0.85) in 5×4 mosaic mode. Each stack contained up to 100 images (512 × 512 pixels, z-step: 3 µm). The following filter sets were used: Alexa 488 (CaMPARI2), Alexa 568 (CaMPARI2-converted, ΔFosB), Alexa 647 (cFos). Image stacks were stitched with ImageJ (Fig. 1A, B) (Preibisch, Saalfeld, and Tomancak 2009). Single plane images of hippocampal subregions (Fig. 1D-H, Fig. 4, Fig. S1, Fig. S2, Fig. S3, Fig. S4, Fig. S6) were acquired with a Zeiss LSM 900 (Plan-Apochromat 20×/0.8, 512 × 512 pixels). To image ΔFosB-electroporated CA1 neurons (Fig. 3), stacks of 7-9 image planes (1024 × 1024, z-step: 3 µm) were acquired using filter sets for Alexa 405 (DAPI, Cerulean), Alexa 488 (CaMPARI2), Alexa 568 (CaMPARI2-converted, ΔFosB), and Alexa 647 (cFos). The image acquisition settings were kept constant for all images within an experimental data set.

Imaris spot selection and analysis

For automated or manual selection of nuclei in single plane or image stacks, we used the Imaris Spot Detection tool (see Table 4). For automatic spot selection, the quality threshold was kept constant for all images within an experimental data set. Spots detected outside the principal cell layer (corresponding to inhibitory neurons) were manually removed. For single plane zoomed-in images, 20 spots were manually selected based on the green CaMPARI2 signal or the DAPI signal (depending on the experiment, see Table 4). The color channels containing the measured intensities (cFos, CaMPARI2 converted, or ΔFosB) were turned off to avoid biased spot selection. For background subtraction in CaMPARI2 experiments, 10 additional spots were manually placed in background regions (all color channels turned on). The mean intensity of background spots (green and red channel) was subtracted from the spot intensities of non-converted (green) and converted (red) CaMPARI2 nuclei using a Matlab script. For the experiment shown in figure 3, all electroporated CA1 neurons were selected based on the cerulean signal. For each electroporated neuron, three neighboring non-electroporated neurons were manually selected based on the DAPI signal. The nuclear intensity (cFos, ΔFosB) of electroporated CA1 neurons was normalized to the mean nuclear intensity of the neighboring DAPI$^+$ neurons (Matlab) to correct for variability in staining and bicuculline-induced stimulation intensity per culture.

Figure	Detection	Detection signal	Spot size	Spot selection
1, S2, S5	automatic	green CaMPARI2	8 µm	all spots analyzed
2	automatic	ΔFosB$^+$ nuclei	8 µm	all spots analyzed
3	manual	Cerulean$^+$ nuclei DAPI$^+$ nuclei	8 µm	three DAPI$^+$ spots per Cerulean$^+$ spot
4, S3	manual	green CaMPARI2	8 µm	20 spots selected

5	automatic	cFos⁺ nuclei ΔFosB⁺ nuclei	8 µm	all spots analyzed
6	automatic manual	cFos⁺ nuclei mKate2⁺ membrane	8 µm 10 µm	all spots analyzed all spots analyzed
S4, S6	manual	DAPI⁺ nuclei	8 µm	20 spots selected

Table 4: Imaris spot selection methods

Spot intensities were exported in csv files and further analyzed in Matlab. Nuclear [Ca^{2+}] was estimated by calculating CaMPARI2 conversion after fixation and immunostaining as

$$\left[\frac{R}{R+G}\right] = \frac{IF\ signal\ red\ CaMPARI2}{IF\ signal\ red\ CaMPARI2 + native\ fluorescence\ geen\ CaMPARI2}$$

yielding values between 0 (no conversion) and 1 (complete conversion).

Experimental animals

B6.Cg-Tg$^{(Fos\text{-}tTA,Fos\text{-}EGFP^*)1Mmay/J}$ (TetTag) mice were obtained from the Jackson Laboratory (Strain #018306) and bred to wild type (non-carrier) C57BL6/J mice from our colony. C57BL6/J (Jackson stock #:000664) were obtained from the UKE animal facility. Mice were group-housed with littermates until 2 weeks before rAAV injection or WM training and were then single caged. Mice had access to food and water ad libitum and were kept in an animal facility next to the behavioral rooms on a reversed light-dark cycle (dark 7 am - 7 pm) at 20 -23 °C with 45 - 65% humidity. Behavioral experiments were conducted during the dark phase of the cycle. Male and female TetTag mice between 20 - 40 weeks were included in the ΔFosB expression analysis (Fig 5) and cFos re-expression experiments (Fig 6). Male C57BL6/J mice between 20 - 40 weeks were used for HDAC inhibition experiments (Figs. 7 and 8). All experiments were conducted in accordance with German law and European Union directives on the protection of animals used for scientific purposes and were approved by the local authorities of the city of Hamburg (Behörde für Justiz und Verbraucherschutz, Lebensmittelsicherheit und Veterinärwesen, N 100/15 and N 046/2021).

Stereotactic virus injection

TetTag mice were virus-injected under analgesia and anesthesia using a stereotaxic drill and injection robot (Neurostar). Mice were fixed to the frame under isoflurane anesthesia (1.5% mixed in O^2), skin and connective tissue was removed, and two craniotomies were performed using an automated drill at the desired coordinates. We injected $AAV_{PHP.eB}$ (10^{12} vg/ml) encoding a red fluorescent protein fused to an opsin (pAAV-TRE3G-BiPOLES-mKate2 (Addgene # 192579)) to label the membrane of cFos⁺ neurons. For bilateral injections into the dorsal hippocampus, we used a glass micropipette attached to a 5 µl syringe (Hamilton). A single injection per site was performed using stereotaxic coordinates for DG (−2.2 AP, ± 1.37ML, −1.9 DV) with a volume of 500 nl on each side (injection speed: 100 nl/min). After the last injection, the pipette was retracted 200 µm and left for at least 5 min to minimize efflux of virus during withdrawal. After the injections, the bone surface was cleaned with 0.9% NaCl solution and the skin was stitched. To avoid hypothermia, a heated pad was placed under the

animal during surgery and under its cage for 1 h until full recovery. We provided post-surgery analgesia with Meloxicam mixed with softened Dox-food (see below) for 3 days after surgery. Animals recovered at least 2 weeks before behavioral experiments.

Doxycycline treatment

Animals were given doxycycline-containing food (Altromin-Dox, 50 mg per kg of body weight, red pellets). To tag the first cFos ensemble, animals were changed to doxycycline-free food (Altromin, light-brown pellets) 24 h before exposure to the water maze. Doxycycline (50 µg/g bodyweight) was injected I.P. immediately after WM training on day 2.

HDACi injection and oral delivery

For cFos re-expression analysis, Tet-Tag mice were I.P. injected with HDACi solution containing CI-994 (30 mg/kg, Tocris #2952), 30% Kolliphor (Sigma-Aldrich) and 10% DMSO (Roth) in 0.9% NaCl solution. The first injection was given on day 1 immediately after WM training (OFF-Dox) and again one hour before the first training trial on day 2. The control group was injected with vehicle solution (10% DMSO, 30% Kolliphor in 0.9% NaCl solution). For repetitive (4 days) HDAC inhibition during water maze training, CI-994 was orally administered 1 h before the first training trial for four consecutive days. Habituation: Mice were trained to drink corn oil from plastic syringes one week (for 2 days) before the start of the experiment. A syringe (1 ml) filled with 120 µl corn oil (10% DMSO) was hung into the home cage, the entire solution was consumed voluntarily within 5 min. HDACi during WM training: A syringe filled with 120 µl of HDACi solution (0.8 mg CI-994, 10% DMSO, 90% corn oil (Mazola)) or VEH solution (10% DMSO, 90% corn oil) was presented in front of the mouth until the entire solution was consumed.

Behavioral experiments

For cFos re-expression experiments, TetTag mice from our colony were injected in two batches (batch 1: n = 2 mice for each condition; batch 2: n = 4 mice (HDACi), n = 3 mice (VEH)). Repetitive HDAC inhibition experiments were conducted in two batches of C57BL6/J mice (batch 1: n = 8 mice for each condition; batch 2: n = 4 mice (HDACi), n = 7 mice (VEH)). All experiments were recorded on digital video, Ethovision XT 17.5 was used for automated tracking. Animals were handled for 1 week before the start of the pre-training sessions to reduce stress during behavioral tasks. Pre-training: Mice were pre-trained for 1 day before their first exposure to the WM arena. Sessions (2 trials of max. 60 s) were done in a small rectangular water tank in the dark, in the same room where the WM task was performed. Water level was 1 cm above the escape platform (Ø 15 cm). Once the animals found the platform, a grid was presented until the animals climbed onto it and were returned to their home cages in the waiting area of the behavioral room. Training: The WM consisted of a circular tank (Ø 1.45 m) with visual asymmetrical landmarks, filled with water with (non-toxic) white paint. A platform (Ø 15 cm, submerged by 1 cm) was placed in the center of the target quadrant (first position, east; second position, west; third position, north) during training trails (max. swim time: 90 s). Before mice were trained to a new position, they were placed onto the new platform for 10 s to enhance reversal training. To test spatial reference memory, a probe trial (PT) without a

platform was performed. PTs from day 1 until day 3 in the morning had a max. duration of 45 s (first 30 s are shown in the analysis, Fig. 7B,C; Fig. S7). After mice learned the second position, PT duration was increased to 60 s (Fig. 7E). After mice learned the third position, PT duration was further increased to 90 s (the first 60 s were analyzed, Fig. 7G). PTs on day 5 and day 11 had a duration of 120 s (the first 90 s were analyzed, Fig. 8). For the TTs, mice were lowered into the tank facing the wall in different, pseudo-randomized positions (avoiding the target quadrant). In PTs, mice were lowered in the center of the tank. An opaque cup attached to a pole was used to transfer the mice from their home cage to the drop position and a plastic grid attached to a pole was used to pick mice up. Mice were picked up 10 s after they found the platform and were returned to their home cage. Mice that did not find the platform during the TT were guided to it using the grid and were picked up after a 10 s on-platform waiting period. For both pre-training and WM, water temperature was 19 - 21°C and a heat lamp was placed over the waiting area to prevent hypothermia.

Confocal imaging

To capture cFos and ΔFosB expression (Fig. 5) or cFos re-expression in the hippocampus during WM training (Fig. 6), immunostained slices from perfusion-fixed brains were imaged with a Zeiss LSM 900 (Plan-Apochromat, 20×/0.8). From each mouse, 4 - 6 slices (left and right DG, CA1) were imaged (stack of 5 image planes, 512 × 512 pixels, z-step: 3 µm) using the following filter sets: Alexa 405 (DAPI), Alexa 568 (mKate2, ΔFosB), Alexa 647 (cFos). The image acquisition settings were kept constant within an experimental data set. For display purposes, color channels were linearly adjusted in ImageJ.

cFos re-expression analysis

Image stacks of the left and right hippocampus were analyzed with Imaris. The DAPI signal was used to create a volume for the upper and lower blade of the dentate gyrus. Based on reported cell densities (Jinno and Kosaka 2010), the volume was used to estimate the total number of granule cells. The cFos signal from both channels defined as cFos-tagged (568 nm) and 2nd cFos ensemble (647 nm) were masked based on the DAPI volume. The cFos-tagged neurons were manually selected (8 µm spots) when all other channels were turned off. The 2nd cFos ensemble was automatically detected using the quality filter function (see table 3). A Matlab based co-localization feature was used to identify overlapping spots from both populations (cFos-tagged, 2nd cFos ensemble, closer than 5 µm). Based on the script the spots were assigned to cFos^{+} neurons, cFos-tagged neurons and double positive neurons. False positive spots were removed and non-detected spots were added. Ensemble size calculation and overlap analysis was done with Matlab. Lower cFos intensity spots (< 40) were removed and following parameters were calculated

1. $Number\ of\ granule\ cells = \frac{DAPI\ surface\ volume}{reported\ GC\ density}$
2. $cFOS - tagged\ ensemble\ size = \frac{number\ of\ mKate2\ positive\ cells}{number\ of\ GC}$
3. $2nd\ cFOS\ ensamble\ size = \frac{number\ of\ cFOS\ positive\ cells}{number\ of\ GC}$

4. $Double\ positive\ cells = \frac{number\ of\ double\ positive\ cells}{number\ of\ GC}$
5. $Expected\ overlap = cFOS - tagged\ ensemble\ size * 2nd\ cFOS\ ensamble\ size$
6. $Re - expression/chance = \frac{Double\ positive\ cells}{expected\ overlap}$

Statistical analysis

Statistical tests were conducted in GraphPad Prism (version 9.01) and assumed an alpha level of 0.05. To analyze differences, we used one-way ANOVA, 2-way analysis of variance, and the Šídák method to correct for multiple comparisons. In some cases, we used two-sided t tests. A detailed description of experimental groups and statistical tests is provided as Supplementary Statistics. For all figures, *P < 0.05, **P < 0.01, ***P < 0.001, ****P < 0.0001.

Acknowledgements

We thank Jan Schöder, Iris Ohmert and Michaela Schweizer for excellent technical assistance and Ingke Braren from the UKE vector facility for the production of rAAV. The ΔFosB plasmid was a gift from Eric Nestler (Addgene # 68545). The pAAV-TRE3G-BiPOLES-mKate2 construct (Addgene #192579) was a gift from J. Simon Wiegert.

Funding: The project was supported by the German Research Foundation (DFG) through Collaborative Research Center CRC 936 Project B7 (#178316478, FM & TGO).

Author contributions: Conceptualization: T.G.O., F.M., C.E.G. and A.Fr. Experiments and data analysis: A.Fr. and P.J.L.M. Protein engineering: E.S. Fiber photometry: A.Fo. Writing—original draft: A.Fr. and T.G.O. Writing—review and editing: all authors.

Competing interests: The authors declare that they have no competing interests.

Data and materials availability: All data needed to evaluate the conclusions in the paper are present in the paper and/or the Supplementary Materials. Nuclear localized CaMPARI2 is available from the authors on request.

References

Bading, Hilmar. 2013. "Nuclear Calcium Signalling in the Regulation of Brain Function." *Nature Reviews. Neuroscience* 14 (9): 593–608.

Bakker, Arnold, C. Brock Kirwan, Michael Miller, and Craig E. L. Stark. 2008. "Pattern Separation in the Human Hippocampal CA3 and Dentate Gyrus." *Science (New York, N.Y.)* 319 (5870): 1640–42.

Bengtson, C. Peter, H. Eckehard Freitag, Jan-Marek Weislogel, and Hilmar Bading. 2010. "Nuclear Calcium Sensors Reveal That Repetition of Trains of Synaptic Stimuli Boosts Nuclear Calcium Signaling in CA1 Pyramidal Neurons." *Biophysical Journal* 99 (12): 4066–77.

Berron, D., H. Schutze, A. Maass, A. Cardenas-Blanco, H. J. Kuijf, D. Kumaran, and E. Duzel. 2016. "Strong Evidence for Pattern Separation in Human Dentate Gyrus." *The Journal of Neuroscience: The Official Journal of the Society for Neuroscience* 36 (29): 7569–79.

Cates, Hannah M., Casey K. Lardner, Rosemary C. Bagot, Rachael L. Neve, and Eric J. Nestler. 2019. "Fosb Induction in Nucleus Accumbens by Cocaine Is Regulated by E2F3a." *ENeuro* 6 (2): ENEURO.0325-18.2019.

Chatzi, Christina, Yingyu Zhang, Wiiliam D. Hendricks, Yang Chen, Eric Schnell, Richard H. Goodman, and Gary L. Westbrook. 2019. "Exercise-Induced Enhancement of Synaptic Function Triggered by the Inverse BAR Protein, Mtss1L." *ELife* 8 (June). https://doi.org/10.7554/eLife.45920.

Chowdhury, Ananya, and Pico Caroni. 2018. "Time Units for Learning Involving Maintenance of System-Wide CFos Expression in Neuronal Assemblies." *Nature Communications* 9 (1): 4122.

Coba, Marcelo P., Noboru H. Komiyama, Jess Nithianantharajah, Maksym V. Kopanitsa, Tim Indersmitten, Nathan G. Skene, Ellie J. Tuck, et al. 2012. "TNiK Is Required for Postsynaptic and Nuclear Signaling Pathways and Cognitive Function." *The Journal of Neuroscience: The Official Journal of the Society for Neuroscience* 32 (40): 13987–99.

Creighton, Samantha D., Gilda Stefanelli, Anas Reda, and Iva B. Zovkic. 2020. "Epigenetic Mechanisms of Learning and Memory: Implications for Aging." *International Journal of Molecular Sciences* 21 (18): 6918.

Eagle, Andrew L., Paula A. Gajewski, Miyoung Yang, Megan E. Kechner, Basma S. Al Masraf, Pamela J. Kennedy, Hongbing Wang, Michelle S. Mazei-Robison, and Alfred J. Robison. 2015. "Experience-Dependent Induction of Hippocampal ΔFosB Controls Learning." *The Journal of Neuroscience: The Official Journal of the Society for Neuroscience* 35 (40): 13773–83.

Eagle, Andrew L., Elizabeth S. Williams, Joseph A. Beatty, Charles L. Cox, and Alfred J. Robison. 2018. "ΔFosB Decreases Excitability of Dorsal Hippocampal CA1 Neurons." *ENeuro* 5 (4): ENEURO.0104-18.2018.

Hainmueller, Thomas, and Marlene Bartos. 2018. "Parallel Emergence of Stable and Dynamic Memory Engrams in the Hippocampus." *Nature* 558 (7709): 292–96.

Hevner, Robert F. 2016. "Evolution of the Mammalian Dentate Gyrus." *The Journal of Comparative Neurology* 524 (3): 578–94.

Holbro, Niklaus, Asa Grunditz, and Thomas G. Oertner. 2009. "Differential Distribution of Endoplasmic Reticulum Controls Metabotropic Signaling and Plasticity at Hippocampal Synapses." *Proceedings of the National Academy of Sciences of the United States of America* 106 (35): 15055–60.

Jaeger, Baptiste N., Sara B. Linker, Sarah L. Parylak, Jerika J. Barron, Iryna S. Gallina, Christian D. Saavedra, Conor Fitzpatrick, et al. 2018. "A Novel Environment-Evoked Transcriptional Signature Predicts Reactivity in Single Dentate Granule Neurons." *Nature Communications* 9 (1): 3084.

Jinno, Shozo, and Toshio Kosaka. 2010. "Stereological Estimation of Numerical Densities of Glutamatergic Principal Neurons in the Mouse Hippocampus." *Hippocampus* 20 (7): 829–40.

Johnston, Graham A. R. 2013. "Advantages of an Antagonist: Bicuculline and Other GABA Antagonists." *British Journal of Pharmacology* 169 (2): 328–36.

Lamothe-Molina, Paul J., Andreas Franzelin, Lennart Beck, Dong Li, Lea Auksutat, Tim Fieblinger, Laura Laprell, et al. 2022. "ΔFosB Accumulation in Hippocampal Granule Cells Drives CFos Pattern Separation during Spatial Learning." *Nature Communications* 13 (1): 6376.

Leutgeb, Jill K., Stefan Leutgeb, May-Britt Moser, and Edvard I. Moser. 2007. "Pattern Separation in the Dentate Gyrus and CA3 of the Hippocampus." *Science* 315 (5814): 961–66.

Liu, Xu, Steve Ramirez, Petti T. Pang, Corey B. Puryear, Arvind Govindarajan, Karl Deisseroth, and Susumu Tonegawa. 2012. "Optogenetic Stimulation of a Hippocampal Engram Activates Fear Memory Recall." *Nature* 484 (7394): 381–85.

Madar, Antoine D., Laura A. Ewell, and Mathew V. Jones. 2019. "Pattern Separation of Spiketrains in Hippocampal Neurons." *Scientific Reports* 9 (1): 5282.

Maravall, M., Z. F. Mainen, B. L. Sabatini, and K. Svoboda. 2000. "Estimating Intracellular Calcium Concentrations and Buffering without Wavelength Ratioing." *Biophysical Journal* 78 (5): 2655–67.

Mellentin, C., H. Jahnsen, and W. C. Abraham. 2007. "Priming of Long-Term Potentiation Mediated by Ryanodine Receptor Activation in Rat Hippocampal Slices." *Neuropharmacology* 52 (1): 118–25.

Moeyaert, Benjamien, Graham Holt, Rajtarun Madangopal, Alberto Perez-Alvarez, Brenna C. Fearey, Nicholas F. Trojanowski, Julia Ledderose, et al. 2018. "Improved Methods for Marking Active Neuron Populations." *Nature Communications* 9 (1): 4440.

Morellini, Fabio. 2013. "Spatial Memory Tasks in Rodents: What Do They Model?" *Cell and Tissue Research* 354 (1): 273–86.

Mozolewski, Pawel, Maciej Jeziorek, Christoph M. Schuster, Hilmar Bading, Bess Frost, and Radek Dobrowolski. 2021. "The Role of Nuclear Ca2+ in Maintaining Neuronal Homeostasis and Brain Health." *Journal of Cell Science* 134 (8). https://doi.org/10.1242/jcs.254904.

Nestler, Eric J. 2014. "Epigenetic Mechanisms of Drug Addiction." *Neuropharmacology* 76 (January): 259–68.

Neunuebel, Joshua P., and James J. Knierim. 2014. "CA3 Retrieves Coherent Representations from Degraded Input: Direct Evidence for CA3 Pattern Completion and Dentate Gyrus Pattern Separation." *Neuron* 81 (2): 416–27.

Peixoto, Lucia, and Ted Abel. 2013. "The Role of Histone Acetylation in Memory Formation and Cognitive Impairments." *Neuropsychopharmacology: Official Publication of the American College of Neuropsychopharmacology* 38 (1): 62–76.

Pettit, Noah L., Ee-Lynn Yap, Michael E. Greenberg, and Christopher D. Harvey. 2022. "Fos Ensembles Encode and Shape Stable Spatial Maps in the Hippocampus." *Nature* 609 (7926): 327–34.

Preibisch, Stephan, Stephan Saalfeld, and Pavel Tomancak. 2009. "Globally Optimal Stitching of Tiled 3D Microscopic Image Acquisitions." *Bioinformatics (Oxford, England)* 25 (11): 1463–65.

Ramamoorthi, Kartik, Robin Fropf, Gabriel M. Belfort, Helen L. Fitzmaurice, Ross M. McKinney, Rachael L. Neve, Tim Otto, and Yingxi Lin. 2011. "Npas4 Regulates a Transcriptional Program in CA3 Required for Contextual Memory Formation." *Science (New York, N.Y.)* 334 (6063): 1669–75.

Ramirez-Mejia, Gerardo, Elvi Gil-Lievana, Oscar Urrego-Morales, Ernesto Soto-Reyes, and Federico Bermúdez-Rattoni. 2021. "Class I HDAC Inhibition Improves Object Recognition Memory Consolidation through BDNF/TrkB Pathway in a Time-Dependent Manner." *Neuropharmacology* 187 (108493): 108493.

Reijmers, Leon G., Brian L. Perkins, Naoki Matsuo, and Mark Mayford. 2007. "Localization of a Stable Neural Correlate of Associative Memory." *Science (New York, N.Y.)* 317 (5842): 1230–33.

Renthal, William, Tiffany L. Carle, Ian Maze, Herbert E. Covington 3rd, Hoang-Trang Truong, Imran Alibhai, Arvind Kumar, Rusty L. Montgomery, Eric N. Olson, and Eric J. Nestler. 2008. "Delta FosB Mediates Epigenetic Desensitization of the C-Fos Gene after Chronic Amphetamine Exposure." *The Journal of Neuroscience: The Official Journal of the Society for Neuroscience* 28 (29): 7344–49.

Robison, Alfred J., and Eric J. Nestler. 2022. "ΔFOSB: A Potentially Druggable Master Orchestrator of Activity-Dependent Gene Expression." *ACS Chemical Neuroscience* 13 (3): 296–307.

Ulery, Paula G., Gabby Rudenko, and Eric J. Nestler. 2006. "Regulation of DeltaFosB Stability by Phosphorylation." *The Journal of Neuroscience: The Official Journal of the Society for Neuroscience* 26 (19): 5131–42.

Ulery-Reynolds, P. G., M. A. Castillo, V. Vialou, S. J. Russo, and E. J. Nestler. 2009. "Phosphorylation of DeltaFosB Mediates Its Stability in Vivo." *Neuroscience* 158 (2): 369–72.

Vanhoutte, Peter, Jean-Vianney Barnier, Bernard Guibert, Christiane Pagès, Marie-Jo Besson, Robert A. Hipskind, and Jocelyne Caboche. 1999. "Glutamate Induces Phosphorylation of Elk-1 and CREB, along with c *-Fos* Activation, via an Extracellular Signal-Regulated Kinase-Dependent Pathway in Brain Slices." *Molecular and Cellular Biology* 19 (1): 136–46.

Vecsey, Christopher G., Joshua D. Hawk, K. Matthew Lattal, Joel M. Stein, Sara A. Fabian, Michelle A. Attner, Sara M. Cabrera, et al. 2007. "Histone Deacetylase Inhibitors Enhance Memory and Synaptic Plasticity via CREB:CBP-Dependent Transcriptional Activation." *The Journal of Neuroscience: The Official Journal of the Society for Neuroscience* 27 (23): 6128–40.

Villain, Hélène, Cédrick Florian, and Pascal Roullet. 2016. "HDAC Inhibition Promotes Both Initial Consolidation and Reconsolidation of Spatial Memory in Mice." *Scientific Reports* 6 (1). https://doi.org/10.1038/srep27015.

Watrous, Andrew J., and Arne D. Ekstrom. 2014. "The Spectro-Contextual Encoding and Retrieval Theory of Episodic Memory." *Frontiers in Human Neuroscience* 8 (February): 75.

Weng, Feng-Ju, Rodrigo I. Garcia, Stefano Lutzu, Karina Alviña, Yuxiang Zhang, Margaret Dushko, Taeyun Ku, et al. 2018. "Npas4 Is a Critical Regulator of Learning-Induced Plasticity at Mossy Fiber-CA3 Synapses during Contextual Memory Formation." *Neuron* 97 (5): 1137-1152.e5.

Wiegert, J. Simon, Christine E. Gee, and Thomas G. Oertner. 2017. "Single-Cell Electroporation of Neurons." *Cold Spring Harbor Protocols* 2017 (2): db.prot094904.

You, Jason C., Kavitha Muralidharan, Jin W. Park, Iraklis Petrof, Mark S. Pyfer, Brian F. Corbett, John J. LaFrancois, et al. 2017. "Epigenetic Suppression of Hippocampal Calbindin-D28k by ΔFosB Drives Seizure-Related Cognitive Deficits." *Nature Medicine* 23 (11): 1377–83.

You, Jason C., Gabriel S. Stephens, Chia-Hsuan Fu, Xiaohong Zhang, Yin Liu, and Jeannie Chin. 2018. "Genome-Wide Profiling Reveals Functional Diversification of ΔFosB Gene Targets in the Hippocampus of an Alzheimer's Disease Mouse Model." *PloS One* 13 (2): e0192508.

Supplementary Figures 1-8

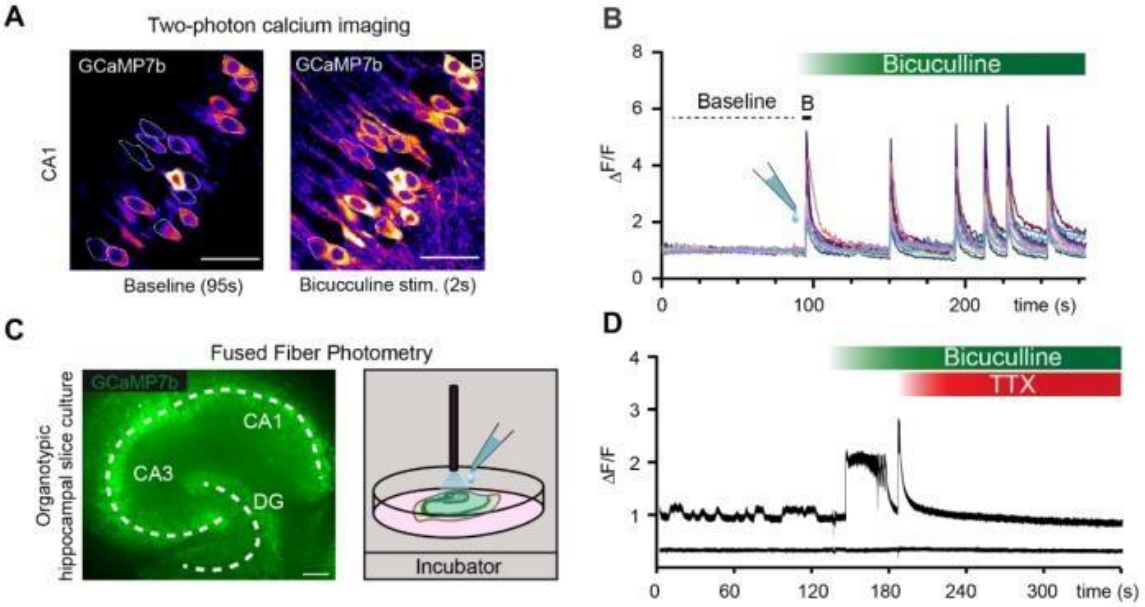

Supplementary figure 1: Synchronized bursting after $GABA_A$ receptor block. A) Organotypic hippocampal slice culture (rat) transduced with AAV9-Syn-jGCaMP7b ($7x10^{12}$ in buffer) (Dana et al. 2019). Left: GCaMP7b fluorescence at baseline, average of 190 images (256 x 256 pixels) acquired at 2 frames/s on a two-photon microscope at RT, peak-scaled to the brightest pixels. White lines around cell bodies show regions of interest (ROIs, n = 14). Right: Fluorescence after addition of bicuculline (20 µM), peak-scaled average of 4 images. Images were median-filtered (2-pixel radius), scale bars are 20 µm. **B)** GCaMP7b fluorescence intensity changes ($\Delta F/F_0$) relative to baseline fluorescence (F_0) in 14 neurons (ROIs shown in A) during bicuculline stimulation. Thick line 'B' indicates the first synchronous increase in jGCaMP7b intensity (right image in A). Six bursts of activity occurred within 200 s. **C)** Fused-fiber photometry (Formozov, Dieter, and Wiegert 2023) of jGCaMP7b fluorescence during bicuculline stimulation inside the incubator (37°C). Hippocampal slice cultures were virally transduced with jGCaMP7b and placed directly (1 mm) under the optical fiber inside the incubator. **D)** jGCaMP7b fluorescence intensity changes ($\Delta F/F_0$) during sequential application of bicuculline (20 µM, t = 140 s) and TTX (1 µM , t = 190 s) relative to baseline (F_0), 470 nm excitation. Note spontaneous activity at baseline, but not after TTX. The trace below the jGCaMP7b signal was recorded quasi-simultaneously with temporally interleaved 405 nm light pulses (isosbestic wavelength) to control for possible artifacts induced by application of bicuculline and TTX. Both functional and isosbestic signals were corrected by subtracting the autofluorescence of the optical fiber.

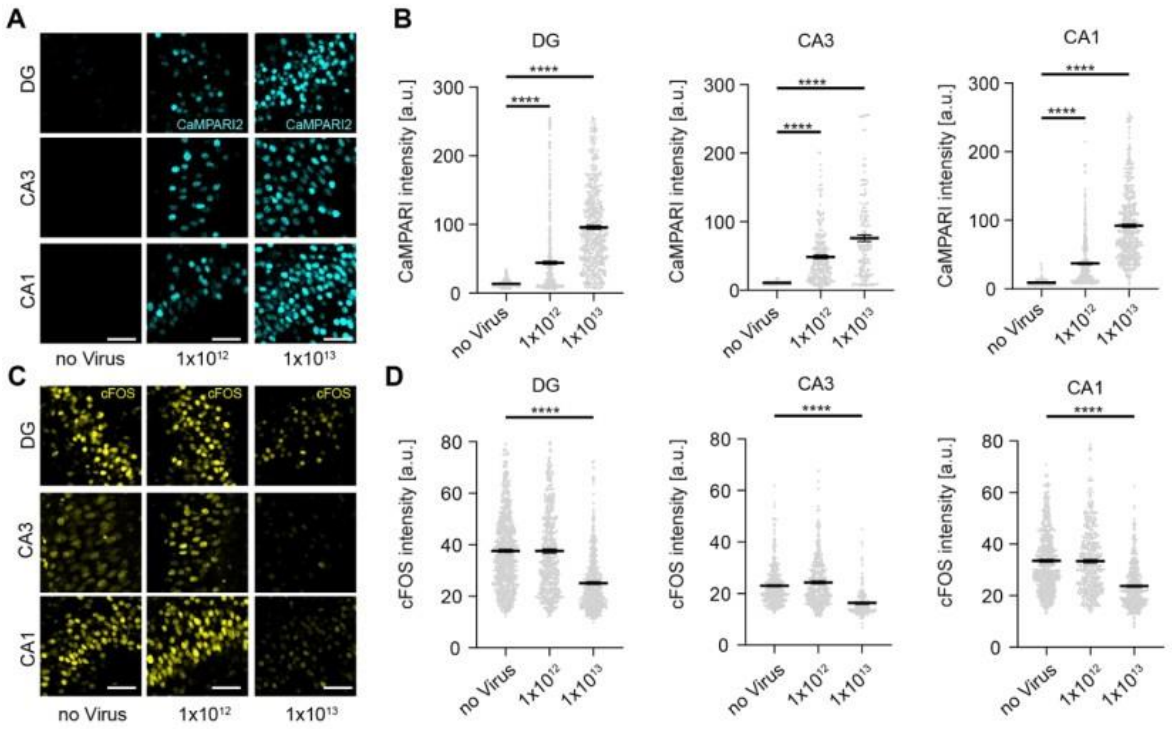

Supplementary figure 2: Low H2B-CaMPARI2 level does not affect bicuculline-induced cFOS expression. **A)** Confocal images of hippocampal subfields (DG, CA3, CA1) in slice cultures transfected with high (10^{13} vg/ml) or low (10^{12} vg/ml) titer of AAV.PhP.eb-syn-H2B-CaMPARI2 (cyan). Non-transfected cultures were used as controls. Scale bars = 20 µm. **B)** Single cell intensity analysis of H2B-CaMPARI2 expression (arbitrary units) in hippocampal subfields. For each condition, cells from 3 slice cultures were pooled. Gray dots show individual cells, black lines indicate mean ± SEM (DG, no virus, n = 585 cells; 10^{12}, n = 428 cells, 10^{13}, n = 427 cells; CA3, no virus, n = 704 cells; 10^{12}, n = 510 cells, 10^{13}, n = 468 cells; CA1, no virus, n = 370 cells; 10^{12}, n = 233 cells, 10^{13}, n = 158 cells). In all hippocampal subfields, expression level increased with virus titer (****p < 0.0001, 1x10^{13} vs no virus; ****p < 0.0001, 1x10^{12} vs no virus, 1-way-ANOVA, Dunett's multiple comparison). **C)** Bicuculline-induced cFOS expression (yellow), same regions as in panel A. Scale bars = 20 µm. **D)** Single cell intensity analysis of cFOS expression (same cells as in B). For all subfields, low virus titer (1x10^{12}) did not affect cFOS expression (DG, ns p = 0.99; CA3, ns p = 0.053; CA1, ns p = 0.97) whereas high virus titer (1x10^{13}) significantly reduced cFOS expression (DG, CA3, CA1, ****p < 0.0001, 1-way-ANOVA, Dunett's multiple comparison).

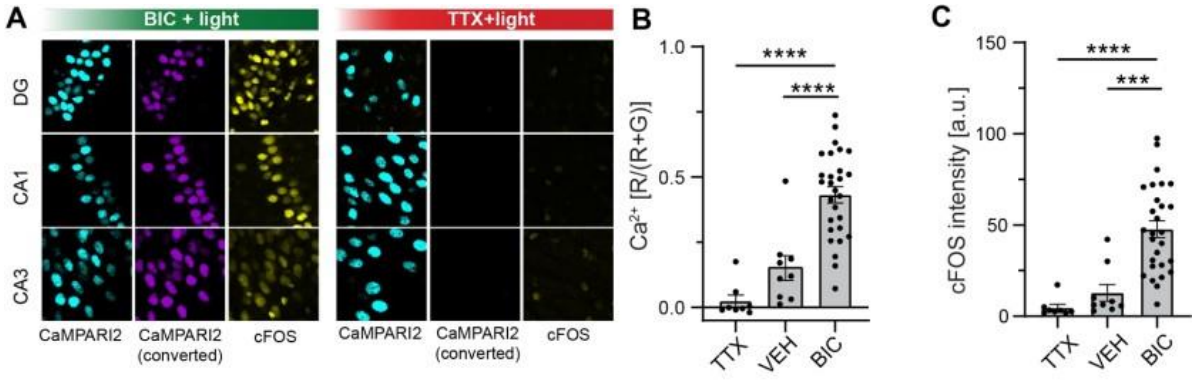

Supplementary figure 3: No conversion of H2B-CaMPARI2 in the absence of activity. A) Left: Confocal images of hippocampal subfields (DG, CA1, CA3) expressing H2B-CaMPARI2 after bicuculline stimulation (60 s, 20 µM, 100 µl in buffer) and continuous photoconversion with 395 nm light (green bar). Activity was terminated after 60 s by adding TTX (1 µM, 100 µl in buffer). Slice cultures were fixed 60 min later and stained for converted CaMPAIR2 (magenta) and cFOS (yellow). Green CaMPARI2 signal (cyan) was not immuno-enhanced. Right: Slice cultures treated with TTX (60 s, 1 µM, 100 µl) and illuminated for 60 s. **B)** Analysis of H2B-CaMPARI2 conversion (R/(R+G)) during 60 s of illumination after treatment with TTX, vehicle (VEH, 2.7% DMSO in buffer), or bicuculline. Based on the baseline fluorescence of CaMPARI2, 20 nuclei per subfield were selected for analysis (ROIs). Each black dot represents the mean of 20 ROIs, gray bars indicate mean of means ± SEM (TTX, n = 8; VEH, n = 9; BIC, n = 28). Photoconversion was significantly stronger after bicuculline stimulation compared to TTX (****$p < 0.0001$) or vehicle-treated cultures (****$p < 0.0001$). Th difference between VEH and TTX conditions was not significant (ns, $p = 0.20$, 1-way-ANOVA, Dunett's multiple comparison). **C)** cFOS intensity analysis, same ROIs as in B). cFOS levels in bicuculline-stimulated slice cultures were significantly higher compared to TTX (****$p < 0.0001$) or vehicle-treated cultures (***$p = 0.0002$). The difference between VEH and TTX conditions was not significant ($p = 0.69$, 1-way-ANOVA, Dunett's multiple comparison). Note: BIC data are identical to the one-time stimulated cultures presented in Fig. 4.

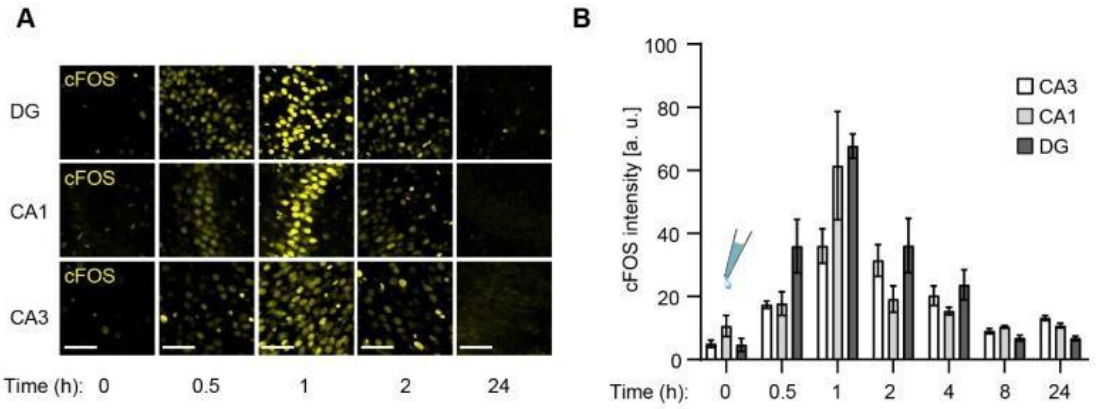

Supplementary figure 4: Temporal profile of cFOS expression after bicuculline stimulation at t = 0.
A) Confocal images of hippocampal subfields (DG, CA1, CA3) stimulated with bicuculline (100 µl, 20 µM in buffer). Stimulation was terminated after 60 s by adding TTX (tetrodotoxin, 300 µl, 1 µM in buffer). Slice cultures were fixed after t = 0, 0.5, 1, 2 or 24 hours and stained for cFOS (yellow) and DAPI (not displayed). Scale bar = 50 µm. **B)** cFOS intensity analysis (arbitrary units). Bars (white = CA3, gray = CA1, dark gray = DG) represent mean ± SEM from n = 3 slice cultures per time point. From each hippocampal subfield, 20 ROIs were randomly selected based on the DAPI signal. During ROI selection, the cFOS channel was turned off. In all subfields, cFOS intensity peaked 1 h after bicuculline stimulation.

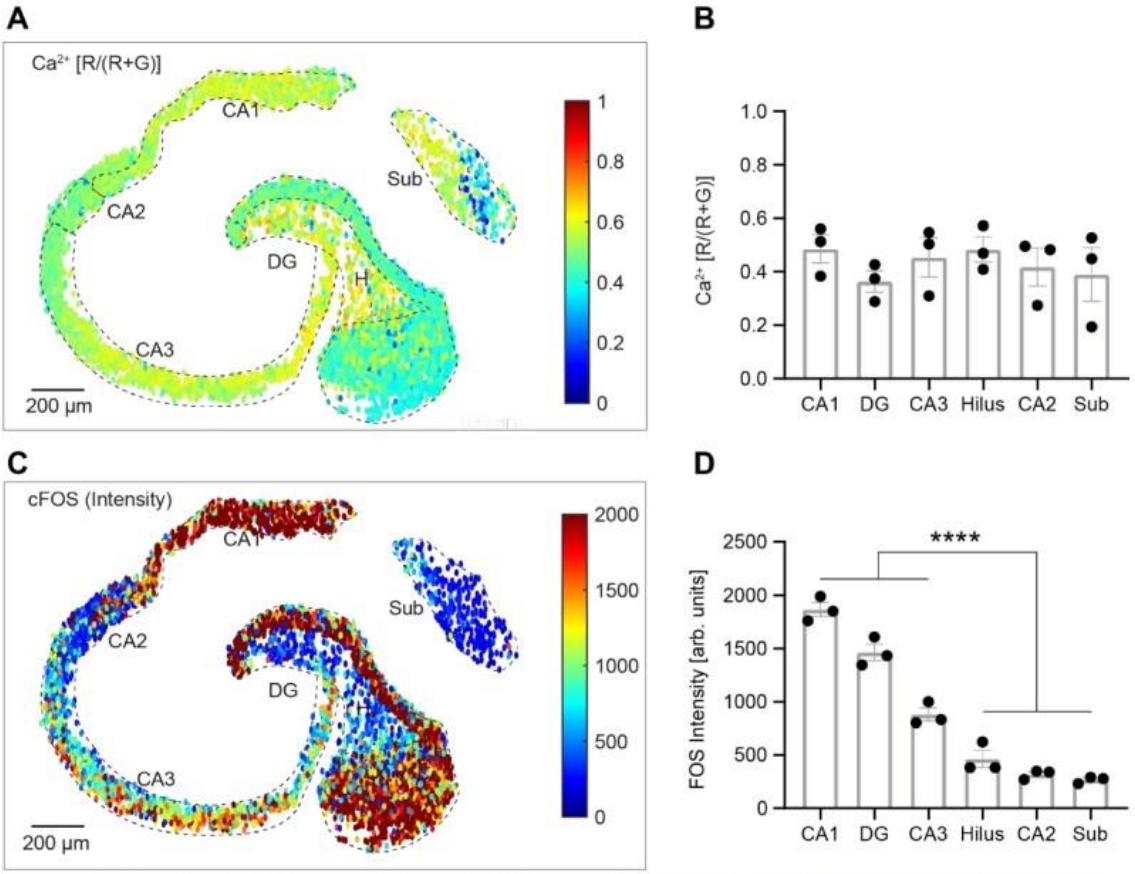

Supplementary figure 5: Spatial analysis of Ca^{2+} and cFOS expression after bicuculline stimulation.
A) H2B-CaMPARI2-positive nuclei were automatically detected using Imaris (Spot size: 8 µm). For each spot, the conversion ratio (R/(R+G)), corresponding to nuclear Ca^{2+} levels, was calculated in Matlab. Spots were color-coded according to the normalized conversion ratio (ranging from 0 to 1) and plotted at their spatial coordinates (CA1, n = 606 nuclei; CA2, n = 247 nuclei; CA3, n = 830 nuclei; DG, n = 2245 nuclei; hilus (H), n = 294 nuclei; subiculum (Sub), n = 343 nuclei). Scale bar = 200 µm. **B)** Analysis of mean Ca^{2+} level ± SEM per region (n = 3 slice cultures). Neurons of all regions showed similar Ca^{2+} levels. **C)** Same analysis procedure like in panel A, but spots are color-coded based on their cFOS intensity (0-2000, arbitrary units). Scale bar = 200 µm. **D)** Analysis of mean cFOS level ± SEM per region (n = 3 slice cultures). Principal neurons in CA1, CA3 and DG show significantly higher cFOS expression compared to neurons in CA2, the hilus and the subiculum (****$p < 0.0001$; t-test).

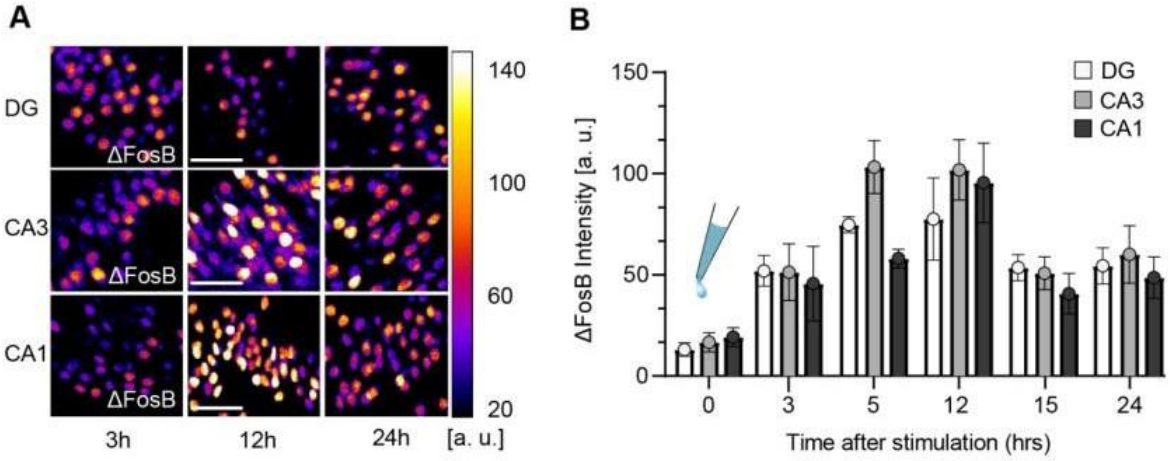

Supplementary figure 6: Temporal profile of ΔFosB expression after bicuculline stimulation at t = 0.
A) Confocal images of hippocampal subfields (DG, CA1, CA3) stimulated with bicuculline (100 µl, 20 µM in buffer). Stimulation was terminated after 60 s by adding TTX (300 µl, 1 µM in buffer). Slice cultures were fixed after t = 0, 3, 5, 12, 15 and 24 hours and stained for ΔFosB (fire color scale, arbitrary units) and DAPI (not displayed). Scale bar = 50 µm. B) ΔFosB intensity analysis. Bars (white = DG, gray = CA3, dark gray = CA1) represent mean ± SEM from 3 - 8 slice cultures per time point. ΔFosB intensity peaked 5 -12 hours after bicuculline stimulation and was still elevated after 24 h.

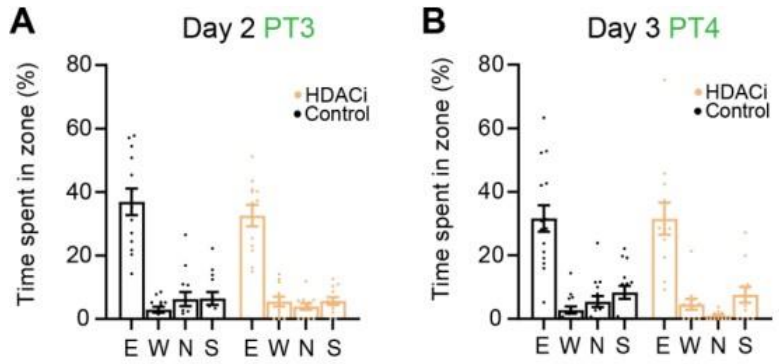

Supplementary figure 7: Spatial memory recall on day 2 and day 3. A) Third probe trail for platform position east (E, first trained position) on day 2. Each dot represents one animal, bars show mean ± SEM. Both groups (VEH, black, n = 14; HDACi, ocher, n = 12) show the same preference for the trained target zone (E) during the first 30 s of a 45-second probe trail (E, east, p = 0.2; W, west, p = 0.91; N, north, p = 0.97; S, south, p = 0.99). **B)** Fourth probe trail for platform position east (E, first position) on day 3. Each dot represents one animal, bars show mean ± SEM. Both groups (VEH, black, n = 15; HDACi, ocher, n = 12) show the same preference for the trained target zone (E) during the first 30 s of a 45-second probe trail (E, p > 0.99; W, p = 0.98; N, p = 0.68; S, p = 0.99, 2-way ANOVA, Šídák's multiple comparisons).

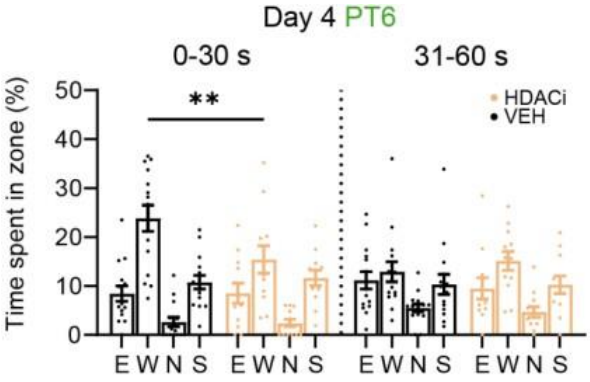

Supplementary figure 8: Spatial memory recall on day 4. Second probe trail (60 s) in the morning of day 4, last trained platform position west (W). Each dot represents one animal, bars show mean ± SEM. Behavior during the first and second half of the probe trial was analyzed separately (dotted line). During the first 30 s, vehicle-treated mice (n = 15) spent significantly more time around the last trained platform position (W) compared the HDACi group (n = 12) (E, east, p > 0.99; W, west, ** p = 0.0073; N, north, p > 0.99; S, south, p = 0.99). No difference in position preference was observed during the last 30 s between both conditions (E, p = 0.94; W, p = 0.86; N, p = 0.99; S, p > 0.99; 2-way ANOVA, Šídák's multiple comparison).

Supplementary References

Dana, Hod, Yi Sun, Boaz Mohar, Brad K. Hulse, Aaron M. Kerlin, Jeremy P. Hasseman, Getahun Tsegaye, et al. 2019. "High-Performance Calcium Sensors for Imaging Activity in Neuronal Populations and Microcompartments." *Nature Methods* 16 (7): 649–57.

Formozov, Andrey, Alexander Dieter, and J. Simon Wiegert. 2023. "A Flexible and Versatile System for Multi-Color Fiber Photometry and Optogenetic Manipulation." *Cell Reports Methods* 3 (3): 100418.

General Discussion

cFOS labels engram neurons during first memory encounter but cannot be predicted by Ca^{2+}

Over the past few decades, cFOS has become a widely used marker of neuronal activity. In particular, it has been used to label and identify neurons in specific behavioural contexts and to drive the expression of optogenetic tools that are then used to manipulate the activity of these neurons during memory retrieval. (Denny et al., 2014; Liu et al., 2012, 2014; Ramirez et al., 2013). This use of cFOS is based on the assumption that there is a causal relationship between neuronal activity and cFOS expression and that this relationship holds true for all neurons throughout the brain. Whereas I present clear evidence that cFOS increases following spatial learning or novel environmental exposure (Publication1: Fig. 2g, SF2), we also observed that dentate granule cells that once expressed cFOS, rarely re-express cFOS (Publication1: Fig. 1k, 2f) when they are reactivated as indicated by elevated Ca^{2+} levels (Publication1: Fig. 4). On closer examination, I found a strong correlation between Ca^{2+} and cFOS at the population level in all hippocampal subregions, (CA1, CA3, DG) (Publication3: Fig. 1D-F), but no predictive relationship between Ca^{2+} and cFOS at the single cell level (Discussion: Fig. D1A). Our data show that there is a complex relationship between neuronal spiking, intracellular Ca^{2+} and cFOS. The absence of cFOS does not mean the absence of activity.

Although not widely appreciated, several other studies contain similar findings. For example, mice performing a two-alternative forced choice task show similar weak correlations between Ca^{2+} and two IEGs (cFOS, Arg1/Arc) in CA1 pyramidal using two-photon Ca^{2+} imaging (Mahringer et al., 2019) (Discussion: Fig. D1B-C). A study using cytosolic CaMPARI2 also showed weak correlations between Ca^{2+} and cFOS in the visual cortex of mice under standard 12/12-hour light/dark cycle conditions. (Discussion: Fig. D1D) (Trojanowski et al., 2021). However, when mice were exposed to a prolonged dark cycle before photoconversion, the

correlation improved. Thus, a prolonged period of quiescence followed by a sudden onset of activity increases the likelihood of cFOS expression (Discussion: Fig. D1E). Also, exposure to novel environments induces cFOS in multiple brain areas, but cFOS expression is reduced upon repeated exposure to the same context (Papa et al., 1993; Struthers et al., 2005). These findings mean that using cFOS to identify 'engram cells' during subsequent recall of the memory is ill-advised.

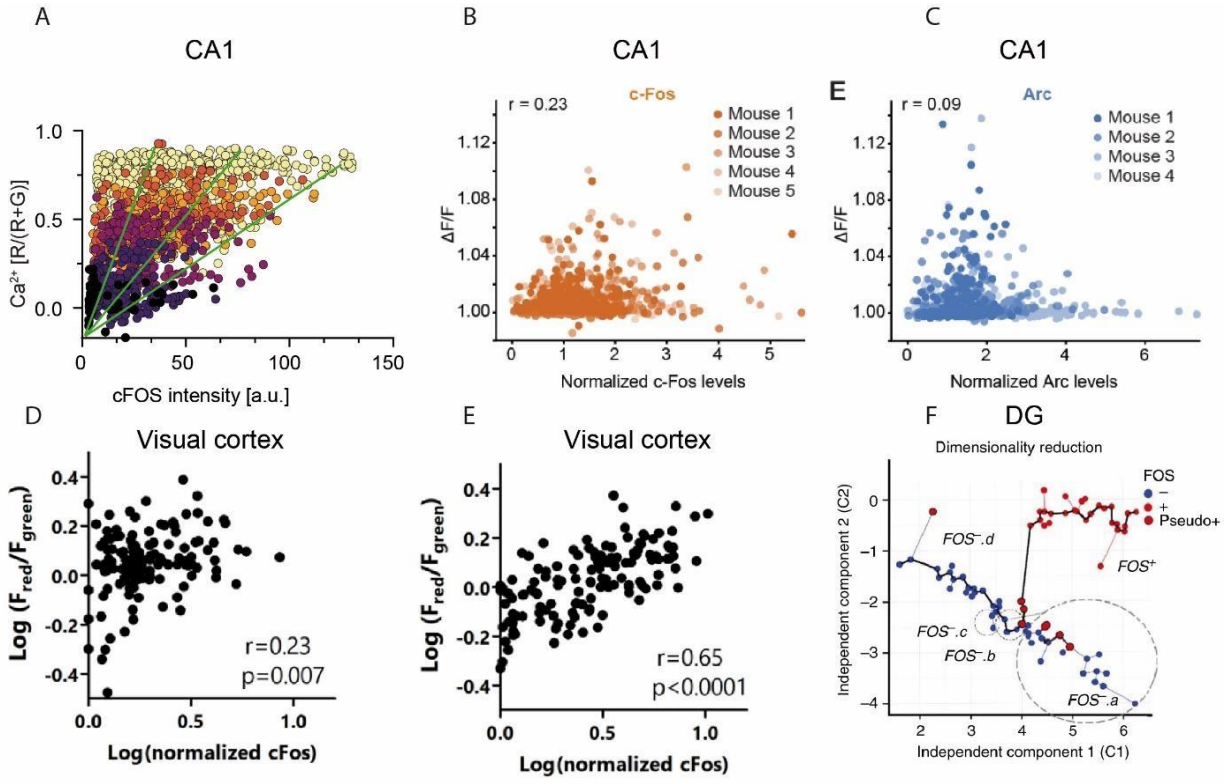

Figure D1 Correlation of Ca^{2+} and cFOS in the CA1 and DG. A) *Analysis of CA1 neurons with nuclear CaMPARI2 stimulated with bicuculline for up to 60 seconds shows minimal correlation at the single cell level.* ***B-C)*** *Similarly low correlations are observed in CA1 neurons expressing jRGECO and cFOS-GFP or Arg1/Arc fusion proteins during a two-alternative forced choice task (Mahringer et al., 2019)* ***D-E)*** *Visual cortex neurons with cytosolic CaMPARI2 also show a weak correlation between Ca^{2+} and cFOS during 12h/12h light/dark cycles. The introduction of a 60 h dark period before photoconversion in the following light cycle increases the correlation (Trojanowski et al., 2021). F) Gene activity status of dentate granule cells. (Lacar et al., 2016)*

A requirement for a neuron to be called a potential engram cell is that it should be active both when forming a memory and when retrieving that memory, as when a mouse is returned to the same context in which something was previously learned (Josselyn & Tonegawa, 2020; Khalaf et al., 2018; Lacagnina et al., 2019). Importantly, almost all previous studies looking for 'engram cells' have used single-trial aversive stimuli such as footshocks; to my knowledge, we

were the first to perform such studies in the water maze. Entering the field rather naively, my colleagues and I were surprised to find that only a small fraction (2-8%) of dentate granule cells re-expressed cFOS during memory retrieval in the water maze (Publication1: Fig.1k, 2f). This result differed from our initial expectation that we would be able to identify individual DG engrams encoding specific memories: We thought that each memory would be associated with a different but highly reproducible pattern of cFOS-expressing neurons. We hoped to be able to use cFOS patterns to tell which memory, in our design different platform positions, a mouse was recalling. Although the overlap, i.e. the number of DG neurons expressing cFOS during training and recall, was always higher than chance, there was no way of using cFOSexpression to distinguish between the remembered locations (Publication1: Fig.2). Although still quite speculative, my answer to the question: What do cFOS+ ensembles represent in thedentate gyrus, would be that the cFOS-expressing neurons that are expressed in a similar context on successive days are those that are involved in learning the differences between days. In this way, they are involved in registering the temporal sequence of events.

An important feature of neurons that are part of an engram ensemble is their intrinsic excitability, which is enhanced by learning (Sehgal et al., 2014; Zhou et al., 2009). In the lateral amygdala, the likelihood of neurons being incorporated into an Arc/Arg3.1-positive engram is increased when CREB is overexpressed and excitability is increased (Han et al., 2007). Neuronal excitability changes over time. When cells express cFOS, they have increased excitability (Pignatelli et al., 2019; Sun et al., 2020; Yassin et al., 2010). Following cFOS expression, dentate granule cells undergo an intrinsic excitability switch, driven by the downregulation of genes encoding K+ channels (Rao-Ruiz et al., 2019). This suggests that the integration of a given cell into an engram depends on its intrinsic excitability, which is predetermined by its gene expression status. This leads to a testable prediction: Neurons with similar Ca^{2+}-to-cFOS ratios (positioned on a line through the origin in Figure D1A) will have similar gene expression profiles.

Evidence supporting this hypothesis comes from a study using single cell nuclear-RNA sequencing of dentate granule cells from mice at time points from 30 minutes to 4 hours after exploration of a novel environment for 15 minutes (Lacar et al., 2016). Expression profiles of cFOS+ and cFOS- dentate granule neurons were different. Interestingly, there was a small population of cFOS-positive neurons with expression profiles more like the cFOS-negative neurons (Discussion: Fig. D1F). It is tempting to speculate that these "pseudo" cFOS-positive cells correspond to the small population of neurons that are able to re-express cFOS on consecutive days in our experiments (Publication1: Fig. 1j, 4).

As there are many immediate early genes (IEGs), it is interesting to examine their activity-dependent expression in more detail and whether their expression habituates during repeated activation. Following exposure to contextual fear conditioning, expression of the IEG Arg3.1/Arc is detected in a sparse but distinct population of dentate granule cells, mirroring the expression pattern of cFOS (Marco et al., 2020; Rao-Ruiz et al., 2019). In contrast to cFOS, Arg3.1/Arc remains upregulated in 70% of dentate granule cells 24 hours later (Rao-Ruiz et al., 2019). But similar to cFOS (Publication1: Fig.6e), 5 days later during memory recall a new ensemble of Arg1/Arc-positive cells emerged, showing low overlap with the previously tagged cell ensemble (Marco et al., 2020). Interestingly, Arg3.1/Arc expression is not sustained in CA1 and CA3 neurons and returns to basal levels 5 hours later (Rao-Ruiz et al., 2019). This is again in contrast to cFOS, which I found to be persistently upregulated in 27% of CA1 neurons 24 hours after the neurons were tagged in mice in their home cage (Publication1: Fig. 5f). Thus, depending on the cell type, the temporal dynamics of Arg3.1/Arc expression is opposed to that of cFOS. Therefore, neither can be used as a surrogate for neuronal activity unless the cell type and temporal characteristics for that cell type are known.

This conclusion is further supported by our observation that some neuronal cell types do not express cFOS even with high activity. PCP4 (Purkinje cell protein 4)-expressing cells within CA2, hilus, and the fasciola cinerea (labeled as Sub) do not express FOS when driven to spike (Publication2: Fig.2; Publication3: SF.5). In addition to PCP4, these cell types also express

Amigo2 (Amphoterin Induced Gene and ORF) (Evans et al., 2018; Laeremans et al., 2013; Sanders et al., 2022). Both proteins inhibit Ca^{2+}/calmodulin signaling (Kanazawa et al., 2008; Recabarren & Alarcón, 2017), which could prevent activity-dependent gene expression. Additionally, CA2 neurons express a protein called 'regulator of G protein signaling 14' (RGS14) (Evans et al., 2018). RGS14 has been shown to negatively regulate long-term structural plasticity of dendritic spines by limiting postsynaptic calcium signaling. Calcium-positive, cFOS-negative neurons could therefore represent neuronal phenotypes with restricted synaptic plasticity.

As the correlation between calcium levels and cFOS expression is very weak, and in some hippocampal regions (CA2) completely absent, a better marker of active neurons is necessary before engram ensembles assembled from neurons in different brain areas can be detected. As demonstrated in this thesis, CaMPARI2 is useful for capturing active neurons, but delivering photoconversion light throughout the brain is difficult if not impossible. NPAS4, a transcription factor closely associated with Ca^{2+} influx, could be a plausible candidate to identify engram cells during recall although its expression may also differ depending on cell type (Lissek et al., 2021; Ramamoorthi et al., 2011; S.-J. Zhang et al., 2009).

Our results further challenge the traditional link between neuronal activity/ Ca^{2+} and cFOS expression. We found that 300 action potentials delivered at frequencies of 1, 5, or 10 Hz failed to induce cFOS expression in hippocampal neurons (Publication2: Fig. 3D). Surprisingly, cFOS induction was strong when the same number of action potentials was delivered at high (50 Hz) and strongest at very low (0.1 Hz) frequencies (Publication2: Fig. 3D). Furthermore, we found that it was not the spiking cells per se but postsynaptic cells that primarily express cFOS (Publication2: Fig.5). This raises the question: Is there a physiological process similar to our presynaptic optogenetic stimulation that can induce cFOS in vivo?

The mean firing rate of hippocampal neurons during immobility, sleep, or consummatory behaviors ranges from 0.001 to 10 Hz (Mizuseki & Buzsáki, 2013). Field recordings show that the hippocampus has periodic high frequency network oscillations at around 200 Hz called

sharp wave ripples (SPW-R) (Ylinen et al., 1995). Only a fraction of CA1 pyramidal neurons participate in each ripple. These CA1 neurons fire 1-2 action potentials during a ripple, whereas the firing rates of interneurons often match the high frequency of the ripple oscillations (Buzsáki, 2015; Ylinen et al., 1995). SPW-R are observed in states of quiet wakefulness, slow-wave sleep and especially following learning sessions and occur semi-regularly at around 0.1 to 3 s^{-1} (Eschenko et al., 2008; Fernández-Ruiz et al., 2019). We propose that our 0.1 Hz optogenetic stimulation may have produced glutamate transients that are similar to those experienced by neurons that repeatedly participate in SWRs.

Even if principal hippocampal neurons can fire at 50 Hz, it is very unlikely to occur in healthy animals. The 50 Hz stimulation might simulate an epileptic episode, which causes massive cFOS expression similar to what I found in bicuculline-stimulated slice cultures. We consistently observed that 50 Hz stimulation caused an intermediate number of neurons to express cFOS. Interestingly, cFOS elimination in the hippocampus increases the rate of neuronal death following seizures (J. Zhang et al., 2002) and cFOS expression in cerebellar granule neurons is necessary for neuronal survival during low potassium treatment (Rawat et al., 2016). This suggests that cFOS might be part of or orchestrate a neuroprotective mechanism when induced by high pathological frequencies. Also pointing to a fundamental difference between the high and ultra-low frequency cFOS are the pharmacological findings. An inhibitor cocktail that inhibits cFOS expressed by 50 Hz and high K+ treatment is relatively ineffective at 0.1 Hz (Publication2: Fig.4).

We are not the first to observe that intermediate frequency optogenetic stimulation is inefficient for cFOS induction. 5 Hz stimulation of the lateral amygdala induces cFOS in only 15 - 25% of neurons (Rogerson et al., 2016). In medium spiny neurons of the nucleus accumbens, optogenetic stimulation fails to induce cFOS but successfully induces other IEGs such as NPAS4, Arc, and Egr1 (Bepari et al., 2012). Interestingly, in dorsal root ganglion neurons, 0.1 - 10 Hz frequencies induce high cFOS expression (Sheng et al., 1993). Again, I must conclude that IEG expression differs among brain regions.

Several lines of evidence I present point to the importance of presynaptic glutamate release and postsynaptic mGluR signaling for cFOS induction. I showed that cFOS can be induced in CA1 neurons by optogenetically stimulating a sparse population of CA3 neurons. Notably, this stimulation did not result in cFOS expression within the CA3 neurons themselves (Publication2: Fig. 5; Discussion Fig. D2A). In the same experimental setting, blocking metabotropic glutamate receptors (mGluRs) or simultaneously inhibiting neurotransmitter release by Gi-DREADD activation eliminates cFOS expression (Publication2: Fig. 4; Discussion: Fig. D2B-C). Gq stimulation in the presence of TTX demonstrates that cFOS canbe induced in a spike-independent manner (Publication2: Fig. 4H; Discussion: Fig. D2D). If presynaptic glutamate release is a major driver of cFOS induction, optogenetic stimulation mayinduce cFOS primarily

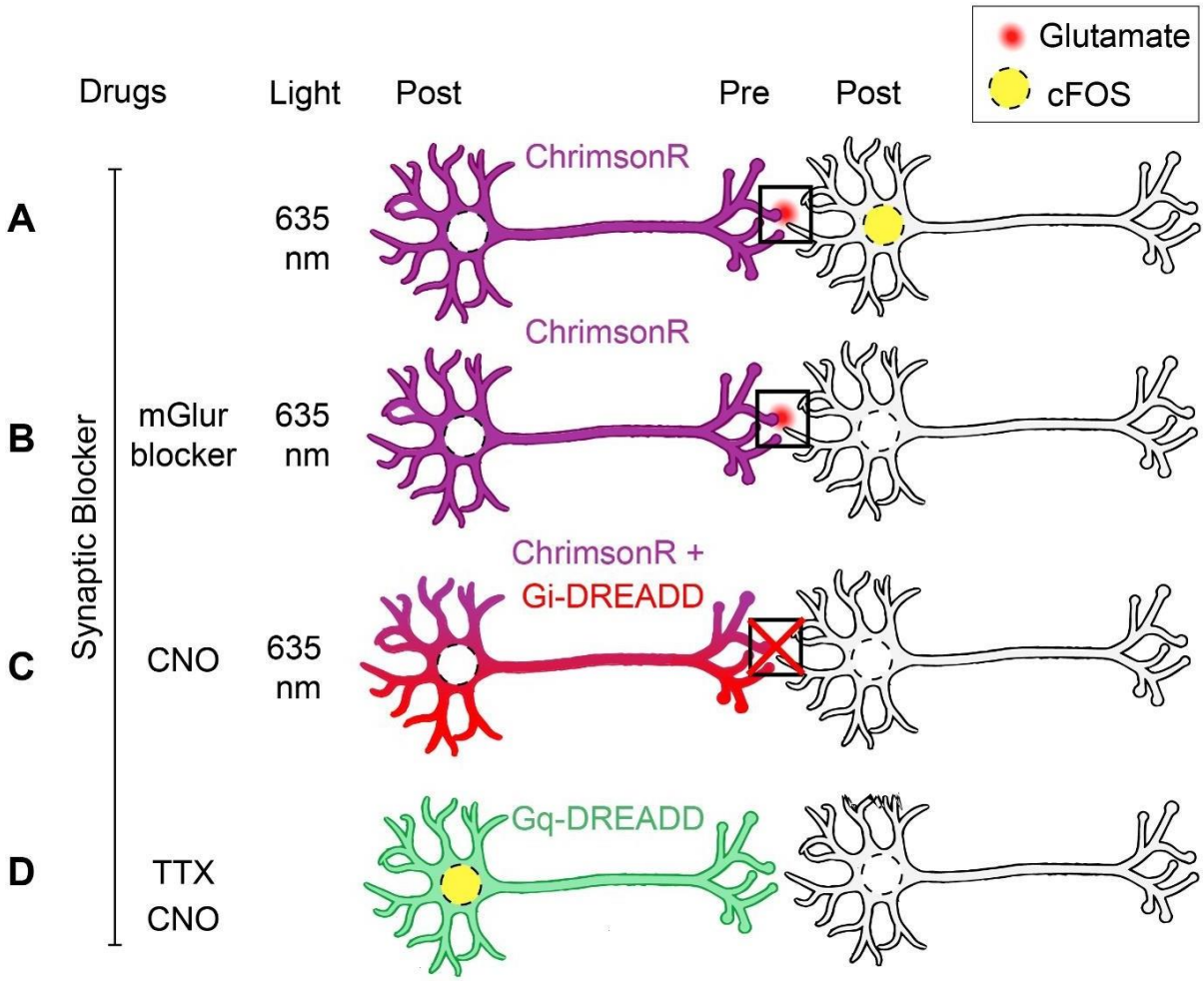

Figure D2 Effects of opto- or chemogenetic stimulation on pre- and postsynaptic neurons. A) *Optogenetic stimulation of ChrimsonR-expressing neurons with 300 635nm light flashes at 0.1 Hz in the*

presence of fast synaptic blockers (picrotoxin, NBQX, CPPene). cFOS is induced in the postsynaptic neuron. ***B)*** *A combination of antagonists of the metabotropic glutamate receptor (mGluR) eliminates cFOS expression.* ***C)*** *Activation of Gi-DREADDS has the same effect on cFOS induction.* ***D)*** *Gq-DREADD stimulation in the presence of TTX induces cFOS in the presynaptic neuron.*

in regions with strong interconnectivity or recurrent collateral networks. For example, intense optogenetic stimulation (50 Hz, 30 s) induces cFOS in the highly interconnected pre- and infralimbic cortex but not in CA1 neurons (Benn et al., 2016). When using optogenetic tools, the stimulating effect on the postsynaptic neurons should be taken into account (Pignatelli et al., 2019). A transient increase in intracellular activity was observed in cFOS-tagged dentate granule neurons during contextual re-exposure, associated with the internalization of Kir2.1 inward rectifier potassium channels. Interestingly, the same effect was not observed when the neurons were activated optogenetically. These data suggest that presynaptic glutamate release, rather than spiking alone, is the cause of the observed change in excitability.

Why has this important distinction in the relationship between neuronal activity and cFOS expression been missed for so long? Many of the studies that have implicated AMPA/NMDAR/VSCC and Ca^{2+} as key pathways for cFOS induction have used pharmacological treatments that are powerful but affect all cells equally, i.e. both pre- and postsynaptic neurons (Cohen & Greenberg, 2008; Griffiths et al., 1998; Jinnah et al., 2003; Murphy et al., 1991; Zhao et al., 2007). Since Ca^{2+} levels directly cause neurotransmitter release, we suggest that this is why the role of glutamate in cFOS induction has been overlooked for so long.

In our experiments, we blocked fast synaptic transmission by blocking AMPA, NMDA, and $GABA_A$ receptors. Two of our findings argue against a direct role for AMPA and NMDA receptors. First, the blockade of AMPA/NMDA receptors did not prevent cFOS expression by high K+ (Publication2: SF 5). Second, cFOS induction in dissociated cell cultures was not reduced by blocking NMDA/AMPA receptors (Publication2: Fig 6). Interestingly, genes associated with NMDA and AMPA receptors, like L-N/Q and T-type calcium channels, as well as the ERK/MAPK pathway, are not differentially upregulated in cFOS-positive neurons compared to cFOS-negative neurons after novel environment exposure (Lacar et al., 2016).

In comparison to ionotropic glutamate receptors, group I mGluRs are extrasynaptic (S. J. Kim et al., 2003; Kumar et al., 2012). Once released, glutamate is quickly taken up by presynaptic or postsynaptic transporters and the nearby glial cells (Auger & Attwell, 2000; Kanai et al.,

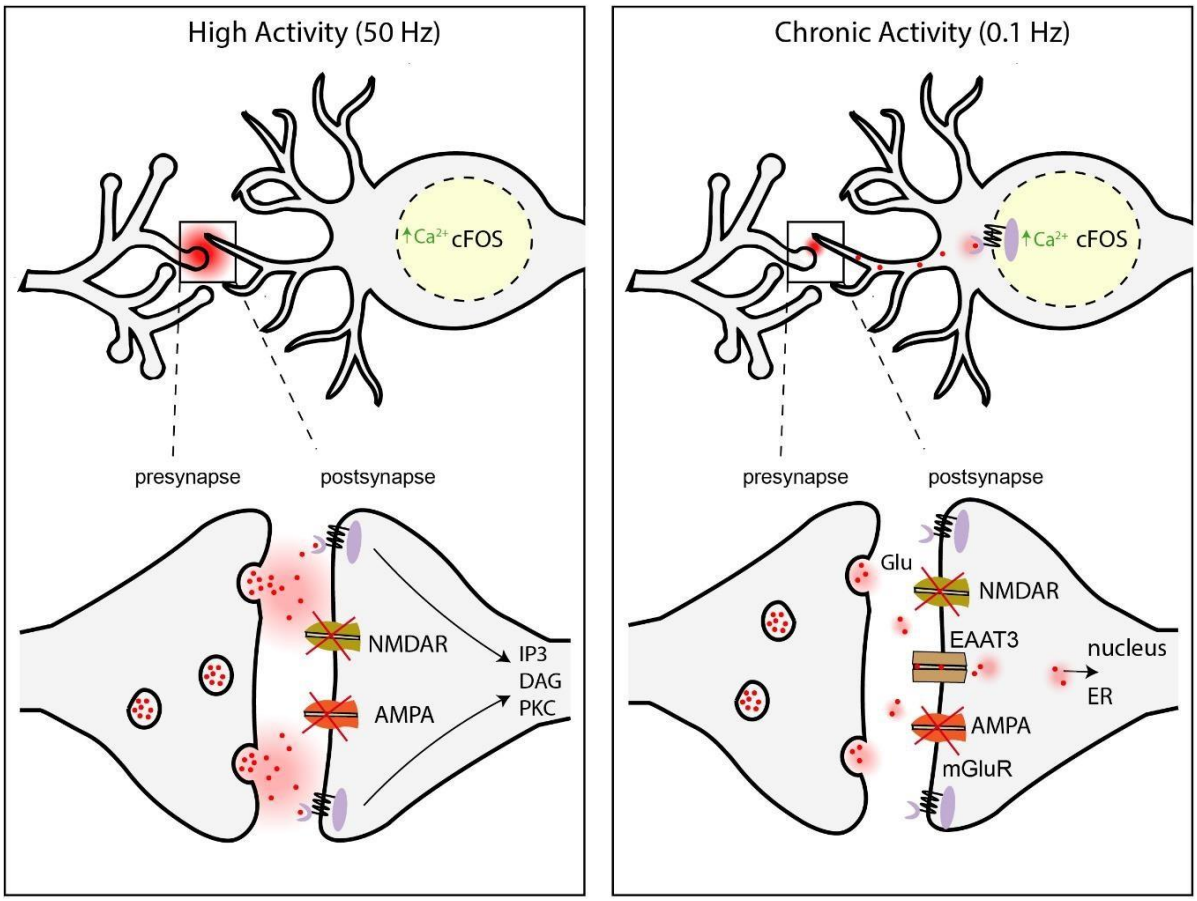

Figure D3 Possible pathways of cFOS induction after high and chronic stimulation

1993). High-frequency activity, such as seizures, significantly increases the extracellular concentration of neurotransmitters such as glutamate and dopamine (Meurs et al., 2008). In the 50 Hz condition, these uptake mechanisms may have been temporarily oversaturated, allowing glutamate to reach mGluRs localized in the extrasynaptic space (Discussion: Figure 3D, left). However, this does not explain mGluR-dependent cFOS induction during low-frequency stimulation, as neurons only fire once every 10 seconds. Multiple studies show that over half of the mGluR5 receptors are localized to intracellular membranes (Hubert et al., 2001; Jong et al., 2009; O'Malley et al., 2003). In the CA1 region mGlu5 is expressed on the membrane of the ER and the nucleus (Purgert et al., 2014). Uncaging of glutamate in the presence of cell surface ionotropic or metabotropic receptor inhibitors or selective activation of

intracellular mGlu5 induces a sustained increase in cytoplasmic calcium, cFOS induction and long-term depression (Kumar et al., 2012; Purgert et al., 2014). Most of these effects are prevented with the membrane-permeable 2-Methyl-6-(phenylethynyl)-pyridine (MPEP), a selective mGlu5 antagonist (Purgert et al., 2014). MPEP was part of the mGluR antagonist cocktail we used to block cFOS induction by 0.1 Hz stimulation.

But how does presynaptic glutamate release activate intracellular mGlu5 receptors? In CA1 neurons glutamate is taken up by aspartate/glutamate transporter 3 (EAAT3) (Purgert et al., 2014). These transporters are present in the synaptic zone (Cheng et al., 2002; D'Amico et al., 2010). This suggests that intracellular mGlu5 receptors may be stimulated by intracellular glutamate and may play an important role in cFOS induction after 0.1 Hz stimulation (Discussion: Fig. D3, right). Future experiments can test this hypothesis.

ΔFOS repressive action is an epigenetic feedback mechanism important for memory formation

cFOS expression depends not only on upstream signaling cascades, but also on how previous activities have shaped the epigenetic state of a cell. I found that hippocampal neurons experiencing repeated supraphysiological activity reduce cFOS expression and accumulate a second FOS family protein: ΔFOSB. After spatial learning, ΔFOSB is elevated in the hippocampus, particularly in the dentate gyrus (Eagle et al., 2015). We observed that dentate granule neurons, in particular the first training cFOS-tagged ones, accumulate ΔFOSB during repeated spatial learning (Publication1: Fig. 6; Publication3: Fig. 5). After repeated training, the proteins are expressed in an anti-correlated manner meaning the cFOS ensemble has shifted (Publication1: Fig. 6; Publication3: Fig. 5). We speculate that physiologically induced cFOS repression may serve an important function for learning and memory. We hypothesize that cFOS repression via ΔFOSB reflects a time-dependent epigenetic mechanism to facilitatethe formation of episodic memories. Indeed, I showed that interfering with ΔFOSB-induced histone deacetylation causes severe learning and memory problems, apparently disrupting memory of episodes.

ΔFOSB is a long-lasting, very stable isoform of the FOSB protein and has been termed "a sustained molecular switch for addiction" (Nestler et al., 2001). Eric Nestler and colleagues demonstrated that accumulation of ΔFOSB occurs after compulsive behavior and chronic drug consumption, especially in the nucleus accumbens and dorsal striatum. Drug-associated stimuli are extremely resistant to extinction, and addiction can be considered an extreme case of learning and memory (Kutlu & Gould, 2016). FOSB knockout mice fail to develop sensitization to cocaine (Hiroi et al., 1997), while overexpression of ΔFOSB in areas related to addiction promotes drug-related behavior (M. B. Kelz et al., 1999). Interestingly, transcription of ΔFOSB is increased in the dorsal hippocampus after chronic cocaine exposure, and inhibition of the ΔFOSB binding partner JUND impairs cocaine-conditioned place preference (Gajewski et al., 2019). These data indicate that ΔFOSB expression is relevant for the persistent nature of a memory of addiction.

I performed several experiments designed to determine whether there is a causal relationship between ΔFOSB and cFOS repression in subregions of the hippocampus. As a consequence of repeated supraphysiological stimulation with bicuculline, slice cultures show decreased cFOS expression and increased ΔFOSB in most subregions (Publication3: Fig. 2, 4). I observed that cFOS repression is prevented by an inhibitor of casein kinase II, which phosphorylates and stabilizes ΔFOSB (Publication3: Fig. 4). Interestingly, repeated activation of Gq-DREADD selectively suppresses cFOS expression in the dentate gyrus but not in CA1 (Publication1: Fig. 7). This raises the question why repetitive stimulation with Gq-DREADDs does not repress cFOS in CA1 whereas after a second bicuculline stimulation there is less cFOS in CA1. A possibility is of course that in CA1 Gq DREADD activation does not increase ΔFOSB. An additional possibility is that mGlu5 receptors are downregulated after bicuculline-induced epileptiform activity, as was seen in vivo after kainate-induced epilepsy (Crans et al., 2020). The Gq signaling pathway may no longer be activated by the second bicuculline stimulation in CA1, and no cFOS can be expressed. When Gq is directly stimulated via CNO activation of the Gq DREADD, cFOS is expressed in CA1 as there is no strong repressive

pathway active in CA1. Therefore, my favorite hypothesis is that ΔFOSB is not readily accumulating in CA1 neurons, as we saw after repeated water maze training. Indeed, I demonstrated a causal relationship between ΔFOSB and repression of cFOS by overexpressing ΔFOSB and the non-phosphorylatable ΔFOSB (S27A) in CA1 neurons. As expected, more cFOS was expressed when the S27A version was overexpressed. Unfortunately, I could not perform the same experiment in dentate granule cells, as these cells did not survive single-cell electroporation. Thus, when ΔFOSB is high in CA1, it *is* able to repress cFOS expression.

So why does ΔFOSB accumulate specifically in the dentate granule cell layer in vivo? One plausible explanation is that the dentate gyrus exhibits a more robust transcriptional response, in contrast to the even more active CA1 region (Jaeger et al., 2018; Marco et al., 2020). Increased FOSB expression leads to increased ΔFOSB levels, as splicing of ΔFOSB mRNAis regulated by the amount of unspliced FOSB transcripts (Alibhai et al., 2007). In return, ΔFOSB has a stimulating effect on FOSB gene transcription, which leads to a tremendous increase (4.5-fold) in FOSB protein levels when overexpressed (Chen et al., 2000).

The epigenetic state of genes is partially controlled by histone modification enzymes. Histone deacetylase (HDAC) removes acetyl residues from histones to cause region-specific chromatin condensation, which prevents gene expression (Klemm et al., 2019). In seizure-prone mice, ΔFOSB accumulates, binds to the cFOS promoter, and recruits HDAC class I, leading to repression of the cFOS promoter through histone deacetylation (Corbett et al. 2017a (Discussion: Fig. D4A). These mice exhibited severe memory impairment. Treatment with HDACi restored cFOS expression and rescued memory deficits.

Supporting this idea, I showed that by treating hippocampal slice cultures with HDAC inhibitors, cFOS expression can be restored following repetitive bicuculline stimulation (Publication3: Fig. 4). Additionally, the administration of HDAC inhibitors before memory retrieval in the water maze (WM) resulted in increased cFOS re-expression in cFOS-tagged dentate granule cells (Publication3: Fig. 6). These findings suggest that HDAC class I is responsible for cFOS

repression in the hippocampus and that the HDAC inhibitor I used effectively crosses the blood-brain barrier after oral administration. Interestingly, healthy mice show improved memoryrecall when treated with HDAC inhibitors (Burns et al., 2022; Burns & Gräff, 2021). Based on the memory-restoring effects of HDAC inhibitors in pathological conditions (Corbett et al., 2017; Kilgore et al., 2010) and the memory-enhancing effects in healthy mice (Burns & Gräff, 2021), HDAC inhibitors are considered as potential memory enhancing treatments.

Given that the ensemble of cFOS+ cells in the dentate gyrus appears to change with each new exposure to the water maze, we hypothesized that HDAC inhibitors, by removing the repression of cFOS, might affect memory of the temporal relationships between episodes. Enhancing memory of one episode by HDAC inhibition might come with a decreased ability to subsequently learn a slightly modified version of the task and impaired performance when recalling a sequence of memories (Discussion: Fig. 5 B-C).

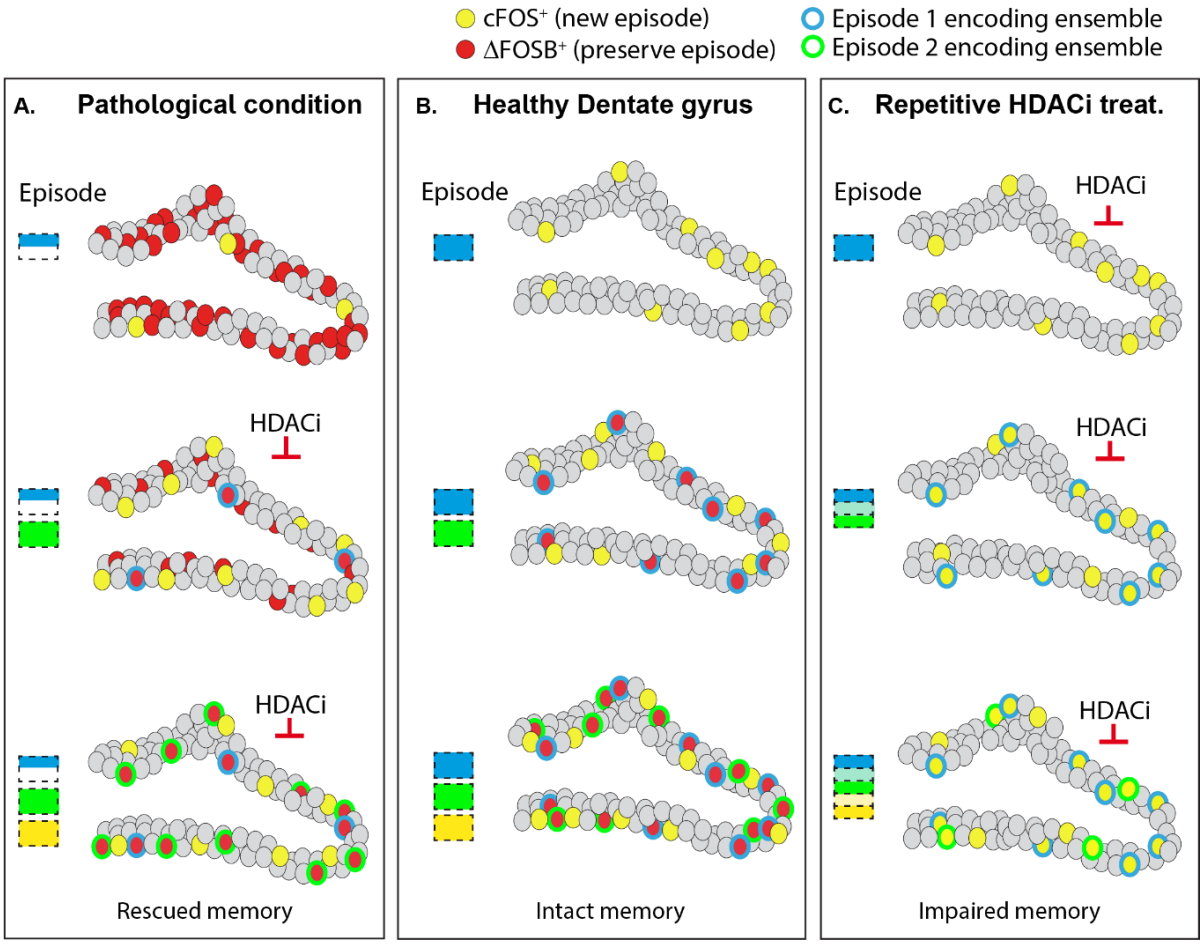

Figure D4 Schematic illustration of cFOS and ΔFOSB expression in the hippocampus of

***pathological, healthy, and HDACi-treated mice**. **A)** In pathological conditions such as Alzheimer's disease or epilepsy, ΔFOSB accumulates affecting cFOS expression and memory. Cyan, green, and yellow squares represent well-established episodic memories in separate neuronal ensembles. Memory deficits can be restored by inhibiting histone-deacetylation enzymes. **B)** Intact cFOS pattern separation in healthy dentate gyrus and optimal episodic memory **C)** Repetitive HDACi treatment affects the repression of cFOS and impairs episodic memory formation.*

To test this hypothesis, we designed a complex water maze experiment in which mice were trained to learn a new platform position daily with HDAC inhibition. As expected, I observed that HDAC inhibition did not affect learning and short-term memory recall in the water maze (Villain et al., 2016) (Publication3: Fig. 7AB). We did not, however, observe improved memory performance in HDACi-treated mice during long-term memory recall (Publication3: Fig. C), as suggested in the literature (Gräff et al., 2014; Valiati et al., 2017; Villain et al., 2016; Whittle et al., 2016). Supporting my hypothesis, I observed that during the probe trial on day 3, HDACi-treated mice spent less time at the newly learned location and instead primarily searched for the platform at the first learned location (Publication3: Fig. G). This suggests that the first memory formed under HDAC inhibition is indeed enhanced and interferes with the acquisition of new information. On day 4, the platform was again moved to a new quadrant. HDACi-treated mice showed reduced learning of the new position suggesting that HDAC inhibition reduced the ability to sequentially learn platform position (Publication3: Fig. 4H).

On day 5, we analyzed the animal's search behavior during a 90-second probe trial without a platform. We expected normal mice would search for the missing platform first in the last learned position, then in the second-to-last position, etc. If our hypothesis that HDAC inhibition would impair memory of the temporal order of events is correct, the expectation was that treated mice would search first in the initially learned position or fail to target their search. WhatI observed was that the control mice showed the expected preference first by searching in the last learned platform location and then searching in the reverse order they were learned in (Publication3: Fig. 8). Even six days after the end of training, the vehicle-treated control mice used the same search strategy, demonstrating a remarkably robust memory of the temporal sequence (Publication3: Fig. 8G). The animals treated with HDACi were clearly deficient in their memory of temporal sequence. On day 5, they did not concentrate their search at either

the last or the first learned positions (Publication3: Fig. 8D). And 6 days later, there was no consistent search strategy (Publication3: Fig. 8H). Thus, repeated HDAC inhibition does not adversely affect learning or recall of a single memory but impairs the ability to update the memory and learn a new position as well as the ability to remember a sequence of memories. Two important caveats prevent us from concluding that cFOS in dentate granule cells is critical for memory of sequences. First, the HDAC inhibitor affects the expression of many genes in addition to cFOS (Burns et al., 2022), and second, our manipulation is body-wide. The epigenetic effects of ΔFOSB in other brain regions were also affected and these might also be associated with memory (Beloate et al., 2016; Dietz et al., 2014; Huggett & Stallings, 2020; L. I. Perrotti et al., 2008; Werme et al., 2002). Nevertheless, I propose that activity-dependent epigenetic mechanisms are crucial for flexibility and remembering sequences of events. Future experiments with targeted inhibition of HDACs in dentate granule cells will determine whether they are the critical cell type involved.

References

Agís-Balboa, R. C., Pinheiro, P. S., Rebola, N., Kerimoglu, C., Benito, E., Gertig, M., Bahari-Javan, S., Jain, G., Burkhardt, S., Delalle, I., Jatzko, A., Dettenhofer, M., Zunszain, P. A., Schmitt, A., Falkai, P., Pape, J. C., Binder, E. B., Mulle, C., Fischer, A., & Sananbenesi, F. (2017). Formin 2 links neuropsychiatric phenotypes at young age to an increased risk for dementia. *The EMBO Journal*, *36*(19), 2815–2828.

Alibhai, I. N., Green, T. A., Potashkin, J. A., & Nestler, E. J. (2007). Regulation of fosB and DeltafosB mRNA expression: in vivo and in vitro studies. *Brain Research*, *1143*, 22–33.

Amaral, D. G., Scharfman, H. E., & Lavenex, P. (2007). The dentate gyrus: fundamental neuroanatomical organization (dentate gyrus for dummies). *Progress in Brain Research*, *163*, 3–22.

Amatniek, J. C., Hauser, W. A., DelCastillo-Castaneda, C., Jacobs, D. M., Marder, K., Bell, K., Albert, M., Brandt, J., & Stern, Y. (2006). Incidence and predictors of seizures in patients with Alzheimer's disease. *Epilepsia*, *47*(5), 867–872.

Andersson, M., Westin, J. E., & Cenci, M. A. (2003). Time course of striatal DeltaFOSB-like immunoreactivity and prodynorphin mRNA levels after discontinuation of chronic dopaminomimetic treatment. *The European Journal of Neuroscience*, *17*(3), 661–666.

Angel, P., & Karin, M. (1991). The role of Jun, FOS and the AP-1 complex in cell-proliferation and transformation. *Biochimica et Biophysica Acta. Reviews on Cancer*, *1072*(2–3), 129–157.

Auger, C., & Attwell, D. (2000). Fast removal of synaptic glutamate by postsynaptic transporters. *Neuron*, *28*(2), 547–558.

Barbas, H., Gustafson, E. L., & Greengard, P. (1993). Comparison of the immunocytochemical localization of DARPP-32 and I-1 in the amygdala and hippocampus of the rhesus monkey. *The Journal of Comparative Neurology*, *334*(1), 1–18.

Beloate, L. N., Weems, P. W., Casey, G. R., Webb, I. C., & Coolen, L. M. (2016). Nucleus accumbens NMDA receptor activation regulates amphetamine cross-sensitization and deltaFOSB expression following sexual experience in male rats. *Neuropharmacology*, *101*, 154–164.

Benn, A., Barker, G. R. I., Stuart, S. A., Roloff, E. v. L., Teschemacher, A. G., Warburton, E. C., & Robinson, E. S. J. (2016). Optogenetic stimulation of prefrontal glutamatergic neurons enhances recognition memory. *The Journal of Neuroscience: The Official Journal of the Society for Neuroscience*, *36*(18), 4930–4939.

Benton, M. D., & Raman, I. M. (2009). Stabilization of Ca current in Purkinje neurons during high-frequency firing by a balance of Ca-dependent facilitation and inactivation. *Channels (Austin, Tex.)*, *3*(6), 393–401.

Bepari, A. K., Sano, H., Tamamaki, N., Nambu, A., Tanaka, K. F., & Takebayashi, H. (2012). Identification of optogenetically activated striatal medium spiny neurons by Npas4 expression. *PloS One*, *7*(12), e52783.

Bernstein, H. L., Lu, Y.-L., Botterill, J. J., & Scharfman, H. E. (2019). Novelty and novel objects increase c-FOS immunoreactivity in mossy cells in the mouse dentate gyrus. *Neural Plasticity*, *2019*, 1815371.

Biagini, G., D'Arcangelo, G., Baldelli, E., D'Antuono, M., Tancredi, V., & Avoli, M. (2005). Impaired activation of CA3 pyramidal neurons in the epileptic hippocampus. *Neuromolecular Medicine*, *7*(4), 325–342.

Bibb, J. A., Snyder, G. L., Nishi, A., Yan, Z., Meijer, L., Fienberg, A. A., Tsai, L. H., Kwon, Y. T., Girault, J. A., Czernik, A. J., Huganir, R. L., Hemmings, H. C., Jr, Nairn, A. C., & Greengard, P. (1999). Phosphorylation of DARPP-32 by Cdk5 modulates dopamine signalling in neurons. *Nature*, *402*(6762), 669–671.

Bing, G., Wang, W., Qi, Q., Feng, Z., Hudson, P., Jin, L., Zhang, W., Bing, R., & Hong, J. S. (1997). Long-term expression of FOS-related antigen and transient expression of delta FOSB associated with seizures in the rat hippocampus and striatum. *Journal of Neurochemistry*, *68*(1), 272–279.

Bito, H., Deisseroth, K., & Tsien, R. W. (1996). CREB phosphorylation and dephosphorylation: A Ca^{2+}- and stimulus duration–dependent switch for hippocampal gene expression. *Cell*, *87*(7), 1203–1214.

Blackstad, T. W. (1956). Commissural connections of the hippocampal region in the rat, with special reference to their mode of termination. *The Journal of Comparative Neurology*, *105*(3), 417–537.

Bodzęta, A., Scheefhals, N., & MacGillavry, H. D. (2021). Membrane trafficking and positioning of mGluRs at presynaptic and postsynaptic sites of excitatory synapses. *Neuropharmacology*, *200*(108799), 108799.

Bourgeois, J.-P., Meas-Yeadid, V., Lesourd, A.-M., Faure, P., Pons, S., Maskos, U., Changeux, J.-P., Olivo-Marin, J.-C., & Granon, S. (2012). Modulation of the mouse prefrontal cortex activation by neuronal nicotinic receptors during novelty exploration but not by exploration of a familiar environment. *Cerebral Cortex (New York, N.Y.: 1991)*, *22*(5), 1007–1015.

Bousiges, O., Vasconcelos, A. P. de, Neidl, R., Cosquer, B., Herbeaux, K., Panteleeva, I., Loeffler, J.-P., Cassel, J.-C., & Boutillier, A.-L. (2010). Spatial memory consolidation is associated with induction of several lysine-acetyltransferase (histone acetyltransferase) expression levels and H2B/H4 acetylation-dependent transcriptional events in the rat hippocampus. *Neuropsychopharmacology: Official Publication of the American College of Neuropsychopharmacology*, *35*(13), 2521–2537.

Bowers, M. E., Xia, B., Carreiro, S., & Ressler, K. J. (2015). The Class I HDAC inhibitor RGFP963 enhances consolidation of cued fear extinction. *Learning & Memory (Cold Spring Harbor, N.Y.)*, *22*(4), 225–231.

Brenna, A., Olejniczak, I., Chavan, R., Ripperger, J. A., Langmesser, S., Cameroni, E., Hu, Z., De Virgilio, C., Dengjel, J., & Albrecht, U. (2019). Cyclin-dependent kinase 5 (CDK5) regulates the circadian clock. *ELife*, *8*. https://doi.org/10.7554/eLife.50925

Bullitt, E. (1990). Expression of c-fos-like protein as a marker for neuronal activity following noxious stimulation in the rat. *The Journal of Comparative Neurology*, *296*(4), 517–530.

Burns, A. M., Farinelli-Scharly, M., Hugues-Ascery, S., Sanchez-Mut, J. V., Santoni, G., & Gräff, J. (2022). The HDAC inhibitor CI-994 acts as a molecular memory aid by facilitating synaptic and intracellular communication after learning. *Proceedings of the National Academy of Sciences of the United States of America*, *119*(22), e2116797119.

Burns, A. M., & Gräff, J. (2021). Cognitive epigenetic priming: leveraging histone acetylation for memory amelioration. *Current Opinion in Neurobiology*, *67*, 75–84.

Butler, C. R., & Zeman, A. Z. (2008). Recent insights into the impairment of memory in epilepsy: transient epileptic amnesia, accelerated long-term forgetting and remote memory impairment. *Brain: A Journal of Neurology*, *131*(Pt 9), 2243–2263.

Buzsáki, G. (2015). Hippocampal sharp wave-ripple: A cognitive biomarker for episodic memory and planning. *Hippocampus*, *25*(10), 1073–1188.

Buzsáki, G., & Moser, E. I. (2013). Memory, navigation and theta rhythm in the hippocampal-entorhinal system. *Nature Neuroscience*, *16*(2), 130–138.

Carle, T. L., Ohnishi, Y. N., Ohnishi, Y. H., Alibhai, I. N., Wilkinson, M. B., Kumar, A., & Nestler, E. J. (2007). Proteasome-dependent and -independent mechanisms for FOSB destabilization: identification of FOSB degron domains and implications for DeltaFOSB stability. *The European Journal of Neuroscience*, *25*(10), 3009–3019.

Catterall, W. A. (2011). Voltage-gated calcium channels. *Cold Spring Harbor Perspectives in Biology*, *3*(8), a003947.

Chandramohan, Y., Droste, S. K., & Reul, J. M. H. M. (2007). Novelty stress induces phospho-acetylation of histone H3 in rat dentate gyrus granule neurons through coincident signalling via the N-methyl-D-aspartate receptor and the glucocorticoid receptor: relevance for c-fos induction. *Journal of Neurochemistry*, *101*(3), 815–828.

Chaudhuri, A., Zangenehpour, S., Rahbar-Dehgan, F., & Ye, F. (2000). Molecular maps of neural activity and quiescence. *Acta Neurobiologiae Experimentalis*, *60*(3), 403–410.

Chavlis, S., & Poirazi, P. (2017). *Pattern separation in the hippocampus through the eyes of computational modeling*. *March*. https://doi.org/10.1002/syn.21972

Chen, J., Zhang, Y., Kelz, M. B., Steffen, C., Ang, E. S., Zeng, L., & Nestler, E. J. (2000). Induction of cyclin-dependent kinase 5 in the hippocampus by chronic electroconvulsive seizures: Role of ΔFOSB. *The Journal of Neuroscience: The Official Journal of the Society for Neuroscience*, *20*(24), 8965–8971.

Cheng, C., Glover, G., Banker, G., & Amara, S. G. (2002). A novel sorting motif in the glutamate transporter excitatory amino acid transporter 3 directs its targeting in Madin-Darby canine kidney cells and hippocampal neurons. *The Journal of Neuroscience: The Official Journal of the Society for Neuroscience*, *22*(24), 10643–10652.

Chin, J., & Scharfman, H. E. (2013). Shared cognitive and behavioral impairments in epilepsy and Alzheimer's disease and potential underlying mechanisms. *Epilepsy & Behavior: E&B*, *26*(3), 343–351.

Chung, L. (2015). A Brief Introduction to the Transduction of Neural Activity into FOS Signal. *Development & Reproduction*, *19*(2), 61–67.

Cohen, S., & Greenberg, M. E. (2008). Communication between the synapse and the nucleus in neuronal development, plasticity, and disease. *Annual Review of Cell and Developmental Biology*, *24*(1), 183–209.

Colby, C. R., Whisler, K., Steffen, C., Nestler, E. J., & Self, D. W. (2003). Striatal cell type-specific overexpression of DeltaFOSB enhances incentive for cocaine. *The Journal of Neuroscience: The Official Journal of the Society for Neuroscience*, *23*(6), 2488–2493.

Corbett, B. F., You, J. C., Zhang, X., Pyfer, M. S., Tosi, U., Iascone, D. M., Petrof, I., Hazra, A., Fu, C.-H., Stephens, G. S., Ashok, A. A., Aschmies, S., Zhao, L., Nestler, E. J., & Chin, J. (2017). ΔFOSB regulates gene expression and cognitive dysfunction in a mouse model of Alzheimer's disease. *Cell Reports*, *20*(2), 344–355.

Cruz, F. C., Javier Rubio, F., & Hope, B. T. (2015). Using c-fos to study neuronal ensembles in corticostriatal circuitry of addiction. *Brain Research*, *1628*, 157–173.

Cruz-Mendoza, F., Jauregui-Huerta, F., Aguilar-Delgadillo, A., García-Estrada, J., & Luquin, S. (2022). Immediate early gene c-fos in the brain: Focus on glial cells. *Brain Sciences*, *12*(6), 687.

Curran, T., Miller, A. D., Zokas, L., & Verma, I. M. (1984). Viral and cellular fos proteins: a comparative analysis. *Cell*, *36*(2), 259–268.

Curran, T., & Morgan, J. I. (1985). Superinduction of c-fos by nerve growth factor in the presence of peripherally active benzodiazepines. *Science (New York, N.Y.)*,*229*(4719), 1265–1268.

Curran, T., & Teich, N. M. (1982). Identification of a 39,000-dalton protein in cells transformed by the FBJ murine osteosarcoma virus. *Virology*, *116*(1), 221–235.

D'Amico, A., Soragna, A., Di Cairano, E., Panzeri, N., Anzai, N., Vellea Sacchi, F., & Perego, C. (2010). The surface density of the glutamate transporter EAAC1 is controlled by interactions with PDZK1 and AP2 adaptor complexes. *Traffic (Copenhagen, Denmark)*, *11*(11), 1455–1470.

Davis, H. P., & Squire, L. R. (1984). Protein synthesis and memory: a review. *Psychological Bulletin*, *96*(3), 518–559.

Day, H. E., Badiani, A., Uslaner, J. M., Oates, M. M., Vittoz, N. M., Robinson, T. E., Watson, S. J., Jr, & Akil, H. (2001). Environmental novelty differentially affects c-fos mRNA expression induced by amphetamine or cocaine in subregions of the bed nucleus of the stria terminalis and amygdala. *The Journal of Neuroscience: The Official Journal of the Society for Neuroscience*, *21*(2), 732–740.

Dede, A. J. O., Frascino, J. C., Wixted, J. T., & Squire, L. R. (2016). Learning and remembering real-world events after medial temporal lobe damage. *Proceedings of the National Academy of Sciences of the United States of America*, *113*(47), 13480–13485.

Deisseroth, K., Mermelstein, P. G., Xia, H., & Tsien, R. W. (2003). Signaling from synapse to nucleus: the logic behind the mechanisms. *Current Opinion in Neurobiology*, *13*(3), 354–365.

Del-Bel, E. A., Borges, C. A., Defino, H. L., & Guimarães, F. S. (2000). Induction of FOS protein immunoreactivity by spinal cord contusion. *Brazilian Journal of Medical and Biological Research*, *33*(5), 521–528.

Denny, C. A., Kheirbek, M. A., Alba, E. L., Tanaka, K. F., Brachman, R. A., Laughman, K. B., Tomm, N. K., Turi, G. F., Losonczy, A., & Hen, R. (2014). Hippocampal memory traces are differentially modulated by experience, time, and adult neurogenesis. *Neuron*, *83*(1), 189–201.

Derkach, V. A., Oh, M. C., Guire, E. S., & Soderling, T. R. (2007). Regulatory mechanisms of AMPA receptors in synaptic plasticity. *Nature Reviews. Neuroscience*, *8*(2), 101–113.

Die Mneme als erhaltendes Prinzip im Wechsel des organischen Geschehens. (1906). *Nature*, *73*(1893), 338–338.

Dietz, D. M., Kennedy, P. J., Sun, H., Maze, I., Gancarz, A. M., Vialou, V., Koo, J. W., Mouzon, E., Ghose, S., Tamminga, C. A., & Nestler, E. J. (2014). ΔFOSB induction in prefrontal cortex by antipsychotic drugs is associated with negative behavioral outcomes. *Neuropsychopharmacology: Official Publication of the American College of Neuropsychopharmacology*, *39*(3), 538–544.

Dobrazanski, P., Noguchi, T., Kovary, K., Rizzo, C. A., Lazo, P. S., & Bravo, R. (1991). Both products of the fosB gene, FOSB and its short form, FOSB/SF, are transcriptional activators in fibroblasts. *Molecular and Cellular Biology*, *11*(11), 5470–5478.

Eagle, A. L., Gajewski, P. A., Yang, M., Kechner, M. E., Al Masraf, B. S., Kennedy, P. J., Wang, H., Mazei-Robison, M. S., & Robison, A. J. (2015). Experience-dependent induction of hippocampal ΔFOSB controls learning. *The Journal of Neuroscience: The Official Journal of the Society for Neuroscience*, *35*(40), 13773–13783.

Eagle, A. L., Manning, C. E., Williams, E. S., Bastle, R. M., Gajewski, P. A., Garrison, A., Wirtz, A. J., Akguen, S., Brandel-Ankrapp, K., Endege, W., Boyce, F. M., Ohnishi, Y. N., Mazei-Robison, M., Maze, I., Neve, R. L., & Robison, A. J. (2020). Circuit-specific

hippocampal ΔFOSB underlies resilience to stress-induced social avoidance. *Nature Communications*, *11*(1), 4484.

Eagle, A. L., Williams, E. S., Beatty, J. A., Cox, C. L., & Robison, A. J. (2018). ΔFOSB decreases excitability of dorsal hippocampal CA1 neurons. *ENeuro*, *5*(4), ENEURO.0104-18.2018.

Eichenbaum, H. (2017). The role of the hippocampus in navigation is memory. *Journal of Neurophysiology*, *117*(4), 1785–1796.

Ekstrom, A. D., & Ranganath, C. (2017). Space, Time and Episodic Memory: the Hippocampus is all over the Cognitive Map. In *bioRxiv*. bioRxiv. https://doi.org/10.1101/150177

Eschenko, O., Ramadan, W., Mölle, M., Born, J., & Sara, S. J. (2008). Sustained increase in hippocampal sharp-wave ripple activity during slow-wave sleep after learning. *Learning & Memory (Cold Spring Harbor, N.Y.)*, *15*(4), 222–228.

Espinoza, C., Guzman, S. J., Zhang, X., & Jonas, P. (2018). Parvalbumin+ interneurons obey unique connectivity rules and establish a powerful lateral-inhibition microcircuit in dentate gyrus. *Nature Communications*, *9*(1), 4605.

Evans, P. R., Parra-Bueno, P., Smirnov, M. S., Lustberg, D. J., Dudek, S. M., Hepler, J. R., & Yasuda, R. (2018). RGS14 restricts plasticity in hippocampal CA2 by limiting postsynaptic calcium signaling. *ENeuro*, *5*(3), ENEURO.0353-17.2018.

Fernández-Ruiz, A., Oliva, A., Fermino de Oliveira, E., Rocha-Almeida, F., Tingley, D., & Buzsáki, G. (2019). Long-duration hippocampal sharp wave ripples improve memory. *Science (New York, N.Y.)*, *364*(6445), 1082–1086.

Fienberg, A. A., Hiroi, N., Mermelstein, P. G., Song, W.-J., Snyder, G. L., Nishi, A., Cheramy, A., O'Callaghan, J. P., Miller, D. B., Cole, D. G., Corbett, R., Haile, C. N., Cooper, D. C., Onn, S. P., Grace, A. A., Ouimet, C. C., White, F. J., Hyman, S. E., Surmeier, D. J., … Greengard, P. (1998). DARPP-32: Regulator of the efficacy of dopaminergic neurotransmission. *Science (New York, N.Y.)*, *281*(5378), 838–842.

Fischer, A., Sananbenesi, F., Wang, X., Dobbin, M., & Tsai, L.-H. (2007). Recovery of learning and memory is associated with chromatin remodelling. *Nature*, *447*(7141), 178–182.

Fleischmann, A., Hvalby, O., Jensen, V., Strekalova, T., Zacher, C., Layer, L. E., Kvello, A., Reschke, M., Spanagel, R., Sprengel, R., Wagner, E. F., & Gass, P. (2003). Impaired long-term memory and NR2A-type NMDA receptor-dependent synaptic plasticity in mice lacking c-FOS in the CNS. *The Journal of Neuroscience: The Official Journal of the Society for Neuroscience*, *23*(27), 9116–9122.

Fortin, N. J., Agster, K. L., & Eichenbaum, H. B. (2002). Critical role of the hippocampus in memory for sequences of events. *Nature Neuroscience*, *5*(5), 458–462.

Francis, T. C., Chandra, R., Friend, D. M., Finkel, E., Dayrit, G., Miranda, J., Brooks, J. M., Iñiguez, S. D., O'Donnell, P., Kravitz, A., & Lobo, M. K. (2015). Nucleus accumbens medium spiny neuron subtypes mediate depression-related outcomes to social defeat stress. *Biological Psychiatry*, *77*(3), 212–222.

Gajewski, P. A., Eagle, A. L., Williams, E. S., Manning, C. E., Lynch, H., McCornack, C., Maze, I., Heller, E. A., & Robison, A. J. (2019). Epigenetic regulation of hippocampal FOSB expression controls behavioral responses to cocaine. *The Journal of Neuroscience: The Official Journal of the Society for Neuroscience*, *39*(42), 8305–8314.

Ghosh, A., Ginty, D. D., Bading, H., & Greenberg, M. E. (1994). Calcium regulation of gene expression in neuronal cells. *Journal of Neurobiology*, *25*(3), 294–303.

Giovagnoli, A. R., & Avanzini, G. (1999). Learning and memory impairment in patients with temporal lobe epilepsy: relation to the presence, type, and location of brain lesion. *Epilepsia*, *40*(7), 904–911.

Gonzalez, J. C., Lee, H., Vincent, A. M., Hill, A. L., Goode, L. K., King, G. D., Gamble, K. L., Wadiche, J. I., & Overstreet-Wadiche, L. (2023). Circadian regulation of dentate gyrus excitability mediated by G-protein signaling. *Cell Reports*, *42*(2), 112039.

Gräff, J., Joseph, N. F., Horn, M. E., Samiei, A., Meng, J., Seo, J., Rei, D., Bero, A. W., Phan, T. X., Wagner, F., Holson, E., Xu, J., Sun, J., Neve, R. L., Mach, R. H., Haggarty, S. J., & Tsai, L.-H. (2014). Epigenetic priming of memory updating during reconsolidation to attenuate remote fear memories. *Cell*, *156*(1–2), 261–276.

Greenberg, M. E., & Ziff, E. B. (1984). Stimulation of 3T3 cells induces transcription of the c-fos proto-oncogene. *Nature*, *311*(5985), 433–438.

Greengard, P., Allen, P. B., & Nairn, A. C. (1999). Beyond the dopamine receptor: the DARPP-32/protein phosphatase-1 cascade. *Neuron*, *23*(3), 435–447.

Griffiths, R., Ritchie, L., Lidwell, K., Grieve, A., Malcolm, C. S., Scott, M., & Meredith, C. (1998). Calcium influx via L-type voltage-gated channels mediates the delayed, elevated increases in steady-state c-fos mRNA levels in cerebellar granule cells exposed to excitotoxic levels of glutamate. *Journal of Neuroscience Research*, *52*(6), 641–652.

Grueter, B. A., Robison, A. J., Neve, R. L., Nestler, E. J., & Malenka, R. C. (2013). ΔFOSB differentially modulates nucleus accumbens direct and indirect pathway function. *Proceedings of the National Academy of Sciences of the United States of America*, *110*(5), 1923–1928.

Gustems, M., Woellmer, A., Rothbauer, U., Eck, S. H., Wieland, T., Lutter, D., & Hammerschmidt, W. (2014). c-Jun/c-FOS heterodimers regulate cellular genes via a newly identified class of methylated DNA sequence motifs. *Nucleic Acids Research*, *42*(5), 3059–3072.

Hafting, T., Fyhn, M., Molden, S., Moser, M.-B., & Moser, E. I. (2005). Microstructure of a spatial map in the entorhinal cortex. *Nature*, *436*(7052), 801–806.

Hagenston, A. M., & Bading, H. (2011). Calcium signaling in synapse-to-nucleus communication. *Cold Spring Harbor Perspectives in Biology*, *3*(11), a004564.

Halazonetis, T. D., Georgopoulos, K., Greenberg, M. E., & Leder, P. (1988). c-Jun dimerizes with itself and with c-FOS, forming complexes of different DNA binding affinities. *Cell*, *55*(5), 917–924.

Han, J.-H., Kushner, S. A., Yiu, A. P., Cole, C. J., Matynia, A., Brown, R. A., Neve, R. L., Guzowski, J. F., Silva, A. J., & Josselyn, S. A. (2007). Neuronal competition and selection during memory formation. *Science (New York, N.Y.)*, *316*(5823), 457–460.

Handa, R. J., Nunley, K. M., & Bollnow, M. R. (1993). Induction of c-fos mRNA in the brain and anterior pituitary gland by a novel environment. *Neuroreport*, *4*(9), 1079–1082.

Hardingham, G. E., Chawla, S., Johnson, C. M., & Bading, H. (1997). Distinct functions of nuclear and cytoplasmic calcium in the control of gene expression. *Nature*, *385*(6613), 260–265.

Hartley et al. (2013). Space in the brain: how the hippocampal formation supports spatial cognition. *Philosophical Transactions of the Royal Society of London. Series B, Biological Sciences*, *369*(1635), 20120510–20120510.

Hebb. (1949). *The Organisation of Behavior*.

Herdegen, T., Kovary, K., Buhl, A., Bravo, R., Zimmermann, M., & Gass, P. (1995). Basal expression of the inducible transcription factors c-Jun, JunB, JunD, c-FOS, FOSB, and Krox-24 in the adult rat brain. *The Journal of Comparative Neurology*, *354*(1), 39–56.

Herdegen, T., & Leah, J. D. (1998). Inducible and constitutive transcription factors in the mammalian nervous system: control of gene expression by Jun, FOS and Krox, and CREB/ATF proteins. *Brain Research Reviews*, *28*(3), 370–490.

Herrmann, N., Lanctôt, K. L., Rothenburg, L. S., & Eryavec, G. (2007). A placebo-controlled trial of valproate for agitation and aggression in Alzheimer's disease. *Dementia and Geriatric Cognitive Disorders*, *23*(2), 116–119.

Hirai, S., Bourachot, B., & Yaniv, M. (1990). Both Jun and FOS contribute to transcription activation by the heterodimer. *Oncogene*, *5*(1), 39–46.

Hiroi, N., Brown, J. R., Haile, C. N., Ye, H., Greenberg, M. E., & Nestler, E. J. (1997). FOSB mutant mice: loss of chronic cocaine induction of FOS-related proteins and heightened sensitivity to cocaine's psychomotor and rewarding effects. *Proceedings of the National Academy of Sciences of the United States of America*, *94*(19), 10397–10402.

Hiroi, N., Fienberg, A. A., Haile, C. N., Alburges, M., Hanson, G. R., Greengard, P., & Nestler, E. J. (1999). Neuronal and behavioural abnormalities in striatal function in DARPP-32-mutant mice. *The European Journal of Neuroscience*, *11*(3), 1114–1118.

Hiroi, N., & Graybiel, A. M. (1996). Atypical and typical neuroleptic treatments induce distinct programs of transcription factor expression in the striatum. *The Journal of Comparative Neurology*, *374*(1), 70–83.

Hope, B. T., Kelz, M. B., Duman, R. S., & Nestler, E. J. (1994). Chronic electroconvulsive seizure (ECS) treatment results in expression of a long-lasting AP-1 complex in brain with altered composition and characteristics. *The Journal of Neuroscience: The Official Journal of the Society for Neuroscience*, *14*(7), 4318–4328.

Hope, B. T., Nye, H. E., Kelz, M. B., Self, D. W., Iadarola, M. J., Nakabeppu, Y., Duman, R. S., & Nestler, E. J. (1994). Induction of a long-lasting AP-1 complex composed of altered FOS-like proteins in brain by chronic cocaine and other chronic treatments. *Neuron*, *13*(5), 1235–1244.

Hsu, C.-L., Kikuchi, K., & Kondo, M. (2007). Activation of mitogen-activated protein kinase kinase (MEK)/extracellular signal regulated kinase (ERK) signaling pathway is involved in myeloid lineage commitment. *Blood*, *110*(5), 1420–1428.

Hubert, G. W., Paquet, M., & Smith, Y. (2001). Differential subcellular localization of mGluR1a and mGluR5 in the rat and monkey Substantia nigra. *The Journal of Neuroscience: The Official Journal of the Society for Neuroscience*, *21*(6), 1838–1847.

Hudson, A. E. (2018). Genetic reporters of neuronal activity: C-FOS and G-CaMP6. *Methods in Enzymology*, *603*, 197–220.

Huggett, S. B., & Stallings, M. C. (2020). Genetic architecture and molecular neuropathology of human cocaine addiction. *The Journal of Neuroscience: The Official Journal of the Society for Neuroscience*, *40*(27), 5300–5313.

Jackson, M. J., Papa, S., Bolaños, J., Bruckdorfer, R., Carlsen, H., Elliott, R. M., Flier, J., Griffiths, H. R., Heales, S., Holst, B., Lorusso, M., Lund, E., Øivind Moskaug, J., Moser, U., Di Paola, M., Polidori, M. C., Signorile, A., Stahl, W., Viña-Ribes, J., & Astley, S. B. (2002). Antioxidants, reactive oxygen and nitrogen species, gene induction and mitochondrial function. *Molecular Aspects of Medicine*, *23*(1–3), 209–285.

Jaeger, B. N., Linker, S. B., Parylak, S. L., Barron, J. J., Gallina, I. S., Saavedra, C. D., Fitzpatrick, C., Lim, C. K., Schafer, S. T., Lacar, B., Jessberger, S., & Gage, F. H. (2018). A novel environment-evoked transcriptional signature predicts reactivity in single dentate granule neurons. *Nature Communications*, *9*(1), 3084.

Janczura, K. J., Volmar, C.-H., Sartor, G. C., Rao, S. J., Ricciardi, N. R., Lambert, G., Brothers, S. P., & Wahlestedt, C. (2018). Inhibition of HDAC3 reverses Alzheimer's disease-

related pathologies in vitro and in the 3xTg-AD mouse model. *Proceedings of the National Academy of Sciences of the United States of America*, *115*(47), E11148–E11157.

Jinnah, H. A., Egami, K., Rao, L., Shin, M., Kasim, S., & Hess, E. J. (2003). Expression of c-FOS in the brain after activation of L-type calcium channels. *Developmental Neuroscience*, *25*(6), 403–411.

Jong, Y.-J. I., Kumar, V., & O'Malley, K. L. (2009). Intracellular metabotropic glutamate receptor 5 (mGluR5) activates signaling cascades distinct from cell surface counterparts. *The Journal of Biological Chemistry*, *284*(51), 35827–35838.

Josselyn, S. A., & Tonegawa, S. (2020). Memory engrams: Recalling the past and imagining the future. *Science*, *367*(6473). https://doi.org/10.1126/science.aaw4325

Kanai, Y., Smith, C. P., & Hediger, M. A. (1993). A new family of neurotransmitter transporters: the high-affinity glutamate transporters. *FASEB Journal: Official Publication of the Federation of American Societies for Experimental Biology*, *7*(15), 1450–1459.

Kanazawa, Y., Makino, M., Morishima, Y., Yamada, K., Nabeshima, T., & Shirasaki, Y. (2008). Degradation of PEP-19, a calmodulin-binding protein, by calpain is implicated in neuronal cell death induced by intracellular Ca^{2+} overload. *Neuroscience*, *154*(2), 473–481.

Kelz, M. B., Chen, J., Carlezon, W. A., Jr, Whisler, K., Gilden, L., Beckmann, A. M., Steffen, C., Zhang, Y. J., Marotti, L., Self, D. W., Tkatch, T., Baranauskas, G., Surmeier, D. J., Neve, R. L., Duman, R. S., Picciotto, M. R., & Nestler, E. J. (1999). Expression of the transcription factor deltaFOSB in the brain controls sensitivity to cocaine. *Nature*, *401*(6750), 272–276.

Kelz, Max B., & Nestler, E. J. (2000). ΔFOSB: a molecular switch underlying long-term neural plasticity. *Current Opinion in Neurology*, *13*(6), 715–720.

Kesner, R. P., Gilbert, P. E., & Barua, L. A. (2002). The role of the hippocampus in memory for the temporal order of a sequence of odors. *Behavioral Neuroscience*, *116*(2), 286–290.

Khalaf, O., Resch, S., Dixsaut, L., Gorden, V., Glauser, L., & Gräff, J. (2018). Reactivation of recall-induced neurons contributes to remote fear memory attenuation. *Science*, *360*(6394), 1239–1242.

Kilgore, M., Miller, C. A., Fass, D. M., Hennig, K. M., Haggarty, S. J., Sweatt, J. D., & Rumbaugh, G. (2010). Inhibitors of class 1 histone deacetylases reverse contextual memory deficits in a mouse model of Alzheimer's disease. *Neuropsychopharmacology: Official Publication of the American College of Neuropsychopharmacology*, *35*(4), 870–880.

Kim, K.-R., Jeong, H.-J., Kim, Y., Lee, S. Y., Kim, Y., Kim, H.-J., Lee, S.-H., Cho, H., Kang, J.-S., & Ho, W.-K. (2021). Calbindin regulates Kv4.1 trafficking and excitability in dentate granule cells via CaMKII-dependent phosphorylation. *Experimental & Molecular Medicine*, *53*(7), 1134–1147.

Kim, K.-R., Lee, S. Y., Yoon, S. H., Kim, Y., Jeong, H.-J., Lee, S., Suh, Y. H., Kang, J.-S., Cho, H., Lee, S.-H., Kim, M.-H., & Ho, W.-K. (2020). Kv4.1, a key ion channel for low frequency firing of dentate granule cells, is crucial for pattern separation. *The Journal of Neuroscience: The Official Journal of the Society for Neuroscience*, *40*(11), 2200–2214.

Kim, S. J., Kim, Y. S., Yuan, J. P., Petralia, R. S., Worley, P. F., & Linden, D. J. (2003). Activation of the TRPC1 cation channel by metabotropic glutamate receptor mGluR1. *Nature*, *426*(6964), 285–291.

Klemm, S. L., Shipony, Z., & Greenleaf, W. J. (2019). Chromatin accessibility and the regulatory epigenome. *Nature Reviews. Genetics*, *20*(4), 207–220.

Krapacher, F. A., Fernández-Suárez, D., Andersson, A., Carrier-Ruiz, A., & Ibáñez, C. F. (2022). Convergent dopamine and ALK4 signaling to PCBP1 controls FOSB alternative splicing and cocaine behavioral sensitization. *The EMBO Journal*, *41*(15), e110721.

Kraus, B. J., Robinson, R. J., 2nd, White, J. A., Eichenbaum, H., & Hasselmo, M. E. (2013). Hippocampal "time cells": time versus path integration. *Neuron*, *78*(6), 1090–1101.

Kumar, V., Fahey, P. G., Jong, Y.-J. I., Ramanan, N., & O'Malley, K. L. (2012). Activation of intracellular metabotropic glutamate receptor 5 in striatal neurons leads to up-regulation of genes associated with sustained synaptic transmission including arc/Arg3.1 protein. *The Journal of Biological Chemistry*, *287*(8), 5412–5425.

Kutlu, M. G., & Gould, T. J. (2016). Effects of drugs of abuse on hippocampal plasticity and hippocampus-dependent learning and memory: contributions to development and maintenance of addiction. *Learning & Memory (Cold Spring Harbor, N.Y.)*, *23*(10), 515–533.

Kwak, Y., Jeong, J., Lee, S., Park, Y.-U., Lee, S.-A., Han, D.-H., Kim, J.-H., Ohshima, T., Mikoshiba, K., Suh, Y.-H., Cho, S., & Park, S. K. (2013). Cyclin-dependent kinase 5 (Cdk5) regulates the function of CLOCK protein by direct phosphorylation. *The Journal of Biological Chemistry*, *288*(52), 36878–36889.

Kwapis, J. L., Alaghband, Y., López, A. J., White, A. O., Campbell, R. R., Dang, R. T., Rhee, D., Tran, A. V., Carl, A. E., Matheos, D. P., & Wood, M. A. (2017). Context and auditory fear are differentially regulated by HDAC3 activity in the lateral and basal subnuclei of the amygdala. *Neuropsychopharmacology: Official Publication of the American College of Neuropsychopharmacology*, *42*(6), 1284–1294.

Lacagnina, A. F., Brockway, E. T., Crovetti, C. R., Shue, F., McCarty, M. J., Sattler, K. P., Lim, S. C., Santos, S. L., Denny, C. A., & Drew, M. R. (2019). Distinct hippocampal engrams control extinction and relapse of fear memory. *Nature Neuroscience*, *22*(5), 753–761.

Lacar, B., Linker, S. B., Jaeger, B. N., Krishnaswami, S. R., Barron, J. J., Kelder, M. J. E., Parylak, S. L., Paquola, A. C. M., Venepally, P., Novotny, M., O'Connor, C., Fitzpatrick, C., Erwin, J. A., Hsu, J. Y., Husband, D., McConnell, M. J., Lasken, R., & Gage, F. H. (2016). Nuclear RNA-seq of single neurons reveals molecular signatures of activation. *Nature Communications*, *7*(1), 11022.

Laeremans, A., Nys, J., Luyten, W., D'Hooge, R., Paulussen, M., & Arckens, L. (2013). AMIGO2 mRNA expression in hippocampal CA2 and CA3a. *Brain Structure & Function*, *218*(1), 123–130.

Larimer, P., & Strowbridge, B. W. (2008). Nonrandom local circuits in the dentate gyrus. *The Journal of Neuroscience: The Official Journal of the Society for Neuroscience*, *28*(47), 12212–12223.

Larimer, P., & Strowbridge, B. W. (2010). Representing information in cell assemblies: persistent activity mediated by semilunar granule cells. *Nature Neuroscience*, *13*(2), 213–222.

Larner, A. J. (2010). Epileptic seizures in AD patients. *Neuromolecular Medicine*, *12*(1), 71–77.

Lashley. (1925). *The relation of learning and retention to the extent of cerebral lesions in the rat*.

Lashley, K. (1950). In search of the engram. In *Experimental Biology Symposium No. 4: Physiological Mechanisms in Animal Behaviour* (pp. 454–482). https://doi.org/10.1097/00008877-199204001-00015

Lau, C. G., & Zukin, R. S. (2007). NMDA receptor trafficking in synaptic plasticity and neuropsychiatric disorders. *Nature Reviews. Neuroscience*, *8*(6), 413–426.

Lee, S.-J. R., Escobedo-Lozoya, Y., Szatmari, E. M., & Yasuda, R. (2009). Activation of CaMKII in single dendritic spines during long-term potentiation. *Nature*, *458*(7236), 299–304.

Lee, T.-S., Li, A. Y., Rapuano, A., Mantis, J., Eid, T., Seyfried, T. N., & de Lanerolle, N. C. (2021). Gene expression in the epileptic (EL) mouse hippocampus. *Neurobiology of Disease*, *147*(105152), 105152.

Levenson, J. M., O'Riordan, K. J., Brown, K. D., Trinh, M. A., Molfese, D. L., & Sweatt, J. D. (2004). Regulation of histone acetylation during memory formation in the hippocampus. *The Journal of Biological Chemistry*, *279*(39), 40545–40559.

Lisman, J., Buzsáki, G., Eichenbaum, H., Nadel, L., Ranganath, C., & Redish, A. D. (2017). Viewpoints: how the hippocampus contributes to memory, navigation and cognition. *Nature Neuroscience*, *20*(11), 1434–1447.

Lissek, T., Andrianarivelo, A., Saint-Jour, E., Allichon, M.-C., Bauersachs, H. G., Nassar, M., Piette, C., Pruunsild, P., Tan, Y.-W., Forget, B., Heck, N., Caboche, J., Venance, L., Vanhoutte, P., & Bading, H. (2021). Npas4 regulates medium spiny neuron physiology and gates cocaine-induced hyperlocomotion. *EMBO Reports*, *22*(12), e51882.

Liu, X., Ramirez, S., Pang, P. T., Puryear, C. B., Govindarajan, A., Deisseroth, K., & Tonegawa, S. (2012). Optogenetic stimulation of a hippocampal engram activates fear memory recall. *Nature*, *484*(7394), 381–385.

Liu, X., Ramirez, S., & Tonegawa, S. (2014). Inception of a false memory by optogenetic manipulation of a hippocampal memory engram. *Philosophical Transactions of the Royal Society of London. Series B, Biological Sciences*, *369*(1633), 20130142.

Lobo, M. K., Zaman, S., Damez-Werno, D. M., Koo, J. W., Bagot, R. C., DiNieri, J. A., Nugent, A., Finkel, E., Chaudhury, D., Chandra, R., Riberio, E., Rabkin, J., Mouzon, E., Cachope, R., Cheer, J. F., Han, M.-H., Dietz, D. M., Self, D. W., Hurd, Y. L., … Nestler, E. J. (2013). ΔFOSB induction in striatal medium spiny neuron subtypes in response to chronic pharmacological, emotional, and optogenetic stimuli. *The Journal of Neuroscience: The Official Journal of the Society for Neuroscience*, *33*(47), 18381–18395.

Lorente. (1932). Studies on the structure of the celebral cortex. II. Continuation of the study of ammonic system. *Journal of Psychology and Neurology*, *46*, 113–177.

Lozsadi, D. A., & Larner, A. J. (2006). Prevalence and causes of seizures at the time of diagnosis of probable Alzheimer's disease. *Dementia and Geriatric Cognitive Disorders*, *22*(2), 121–124.

Lucibello, F. C., Lowag, C., Neuberg, M., & Müller, R. (1989). trans-repression of the mouse c-fos promoter: a novel mechanism of FOS-mediated trans-regulation. *Cell*, *59*(6), 999–1007.

Mahringer, D., Petersen, A. V., Fiser, A., Okuno, H., Bito, H., Perrier, F., & Keller, G. B. (2019). *Expression of c-FOS and Arc in hippocampal region CA1 marks neurons that exhibit learning-related activity changes*. https://doi.org/10.1101/644526

Mandelzys, A., Gruda, M. A., Bravo, R., & Morgan, J. I. (1997). Absence of a persistently elevated 37 kDa fos-related antigen and AP-1-like DNA-binding activity in the brains of kainic acid-treated fosB null mice. *The Journal of Neuroscience: The Official Journal of the Society for Neuroscience*, *17*(14), 5407–5415.

Marco, A., Meharena, H. S., Dileep, V., Raju, R. M., Davila-Velderrain, J., Zhang, A. L., Adaikkan, C., Young, J. Z., Gao, F., Kellis, M., & Tsai, L.-H. (2020). Mapping the

epigenomic and transcriptomic interplay during memory formation and recall in the hippocampal engram ensemble. *Nature Neuroscience*, *23*(12), 1606–1617.

Matthies, H. (1989). In search of cellular mechanisms of memory. *Progress in Neurobiology*, *32*(4), 277–349.

McAvoy, K., Besnard, A., & Sahay, A. (2015). Adult hippocampal neurogenesis and pattern separation in DG: a role for feedback inhibition in modulating sparseness to govern population-based coding. *Frontiers in Systems Neuroscience*, *9*, 120.

McClung, C. A., & Nestler, E. J. (2003). Regulation of gene expression and cocaine reward by CREB and DeltaFOSB. *Nature Neuroscience*, *6*(11), 1208–1215.

Meurs, A., Clinckers, R., Ebinger, G., Michotte, Y., & Smolders, I. (2008). Seizure activity and changes in hippocampal extracellular glutamate, GABA, dopamine and serotonin. *Epilepsy Research*, *78*(1), 50–59.

Minkeviciene, R., Rheims, S., Dobszay, M. B., Zilberter, M., Hartikainen, J., Fülöp, L., Penke, B., Zilberter, Y., Harkany, T., Pitkänen, A., & Tanila, H. (2009). Amyloid beta-induced neuronal hyperexcitability triggers progressive epilepsy. *The Journal of Neuroscience: The Official Journal of the Society for Neuroscience*, *29*(11), 3453–3462.

Mizuseki, K., & Buzsáki, G. (2013). Preconfigured, skewed distribution of firing rates in the hippocampus and entorhinal cortex. *Cell Reports*, *4*(5), 1010–1021.

Monfil, T., Vázquez Roque, R. A., Camacho-Abrego, I., Tendilla-Beltran, H., Iannitti, T., Meneses-Morales, I., Aguilar-Alonso, P., Flores, G., & Morales-Medina, J. C. (2018). Hyper-response to novelty increases c-FOS expression in the hippocampus and prefrontal cortex in a rat model of schizophrenia. *Neurochemical Research*, *43*(2), 441–448.

Moratalla, R., Elibol, B., Vallejo, M., & Graybiel, A. M. (1996). Network-level changes in expression of inducible FOS-Jun proteins in the striatum during chronic cocaine treatment and withdrawal. *Neuron*, *17*(1), 147–156.

Moratalla, R., Vallejo, M., Elibol, B., & Graybiel, A. M. (1996). D1-class dopamine receptors influence cocaine-induced persistent expression of FOS-related proteins in striatum. *Neuroreport*, *8*(1), 1–5.

Morgan, J. I., Cohen, D. R., Hempstead, J. L., & Curran, T. (1987). Mapping patterns of c-fos expression in the central nervous system after seizure. *Science (New York, N.Y.)*, *237*(4811), 192–197.

Morgan, J. I., & Curran, T. (1986). Role of ion flux in the control of c-fos expression. *Nature*, *322*(6079), 552–555.

Morgan, J. I., & Curran, T. (1991). Stimulus-transcription coupling in the nervous system: involvement of the inducible proto-oncogenes fos and jun. *Annual Review of Neuroscience*, *14*(1), 421–451.

Murphy, T. H., Worley, P. F., & Baraban, J. M. (1991). L-type voltage-sensitive calcium channels mediate synaptic activation of immediate early genes. *Neuron*, *7*(4), 625–635.

Nakabeppu, Y., & Nathans, D. (1991). A naturally occurring truncated form of FOSB that inhibits FOS/Jun transcriptional activity. *Cell*, *64*(4), 751–759.

Naya, Y., & Suzuki, W. A. (2011). Integrating what and when across the primate medial temporal lobe. *Science (New York, N.Y.)*, *333*(6043), 773–776.

Nestler, E. J., Barrot, M., & Self, D. W. (2001). DeltaFOSB: a sustained molecular switch for addiction. *Proceedings of the National Academy of Sciences of the United States of America*, *98*(20), 11042–11046.

Neunuebel; Knierim. (2014). *CA3 Retrieves Coherent Representations from Degraded Input: Direct Evidence for CA3 Pattern Completion and Dentate Gyrus Pattern Separation*. *81*(2), 416–427.

Nye, H. E., Hope, B. T., Kelz, M. B., Iadarola, M., & Nestler, E. J. (1995). Pharmacological studies of the regulation of chronic FOS-related antigen induction by cocaine in the striatum and nucleus accumbens. *The Journal of Pharmacology and Experimental Therapeutics*, *275*(3), 1671–1680.

Nye, H. E., & Nestler, E. J. (1996). Induction of chronic FOS-related antigens in rat brain by chronic morphine administration. *Molecular Pharmacology*, *49*(4), 636–645.

O'Keefe, J., & Dostrovsky, J. (1971). The hippocampus as a spatial map. Preliminary evidence from unit activity in the freely-moving rat. *Brain Research*, *34*(1), 171–175.

Olivera, B. M., Miljanich, G. P., Ramachandran, J., & Adams, M. E. (1994). Calcium channel diversity and neurotransmitter release: the omega-conotoxins and omega-agatoxins. *Annual Review of Biochemistry*, *63*(1), 823–867.

O'Malley, K. L., Jong, Y.-J. I., Gonchar, Y., Burkhalter, A., & Romano, C. (2003). Activation of metabotropic glutamate receptor mGlu5 on nuclear membranes mediates intranuclear Ca^{2+} changes in heterologous cell types and neurons. *The Journal of Biological Chemistry*, *278*(30), 28210–28219.

Onodera, H., Kogure, K., Ono, Y., Igarashi, K., Kiyota, Y., & Nagaoka, A. (1989). Proto-oncogene c-fos is transiently induced in the rat cerebral cortex after forebrain ischemia. *Neuroscience Letters*, *98*(1), 101–104.

Ouimet, C. C., Miller, P. E., Hemmings, H. C., Jr, Walaas, S. I., & Greengard, P. (1984). DARPP-32, a dopamine- and adenosine 3':5'-monophosphate-regulated phosphoprotein enriched in dopamine-innervated brain regions. III. Immunocytochemical localization. *The Journal of Neuroscience: The Official Journal of the Society for Neuroscience*, *4*(1), 111–124.

Palop, J. J., & Mucke, L. (2009). Epilepsy and cognitive impairments in Alzheimer disease. *Archives of Neurology*, *66*(4), 435–440.

Pang, Y., Kiba, H., & Jayaraman, A. (1993). Acute nicotine injections induce c-fos mostly in non-dopaminergic neurons of the midbrain of the rat. *Brain Research. Molecular Brain Research*, *20*(1–2), 162–170.

Panikker, P., Xu, S.-J., Zhang, H., Sarthi, J., Beaver, M., Sheth, A., Akhter, S., & Elefant, F. (2018). Restoring Tip60 HAT/HDAC2 balance in the neurodegenerative brain relieves epigenetic transcriptional repression and reinstates cognition. *The Journal of Neuroscience: The Official Journal of the Society for Neuroscience*, *38*(19), 4569–4583.

Papa, M., Pellicano, M. P., Welzl, H., & Sadile, A. G. (1993). Distributed changes in c-FOS and c-Jun immunoreactivity in the rat brain associated with arousal and habituation to novelty. *Brain Research Bulletin*, *32*(5), 509–515.

Pastalkova, E., Itskov, V., Amarasingham, A., & Buzsáki, G. (2008). Internally generated cell assembly sequences in the rat hippocampus. *Science (New York, N.Y.)*, *321*(5894), 1322–1327.

Paz, R., Gelbard-Sagiv, H., Mukamel, R., Harel, M., Malach, R., & Fried, I. (2010). A neural substrate in the human hippocampus for linking successive events. *Proceedings of the National Academy of Sciences of the United States of America*, *107*(13), 6046–6051.

Peakman, M.-C., Colby, C., Perrotti, L. I., Tekumalla, P., Carle, T., Ulery, P., Chao, J., Duman, C., Steffen, C., Monteggia, L., Allen, M. R., Stock, J. L., Duman, R. S., McNeish, J. D., Barrot, M., Self, D. W., Nestler, E. J., & Schaeffer, E. (2003). Inducible, brain region-

specific expression of a dominant negative mutant of c-Jun in transgenic mice decreases sensitivity to cocaine. *Brain Research*, *970*(1–2), 73–86.

Peixoto, L., & Abel, T. (2013). The role of histone acetylation in memory formation and cognitive impairments. *Neuropsychopharmacology: Official Publication of the American College of Neuropsychopharmacology*, *38*(1), 62–76.

Penfield, W., & Milner, B. (1958). Memory deficit produced by bilateral lesions in the hippocampal zone. *A.M.A. Archives of Neurology and Psychiatry*, *79*(5), 475–497.

Perrotti, L. I., Weaver, R. R., Robison, B., Renthal, W., Maze, I., Yazdani, S., Elmore, R. G., Knapp, D. J., Selley, D. E., Martin, B. R., Sim-Selley, L., Bachtell, R. K., Self, D. W., & Nestler, E. J. (2008). Distinct patterns of DeltaFOSB induction in brain by drugs of abuse. *Synapse (New York, N.Y.)*, *62*(5), 358–369.

Perrotti, Linda I., Hadeishi, Y., Ulery, P. G., Barrot, M., Monteggia, L., Duman, R. S., & Nestler, E. J. (2004). Induction of deltaFOSB in reward-related brain structures after chronic stress. *The Journal of Neuroscience: The Official Journal of the Society for Neuroscience*, *24*(47), 10594–10602.

Pich, E. M., Pagliusi, S. R., Tessari, M., Talabot-Ayer, D., Hooft van Huijsduijnen, R., & Chiamulera, C. (1997). Common neural substrates for the addictive properties of nicotine and cocaine. *Science (New York, N.Y.)*, *275*(5296), 83–86.

Pignatelli, M., Ryan, T. J., Roy, D. S., Lovett, C., Smith, L. M., Muralidhar, S., & Tonegawa, S. (2019). Engram Cell Excitability State Determines the Efficacy of Memory Retrieval. *Neuron*, *101*(2), 274-284.e5.

Purgert, C. A., Izumi, Y., Jong, Y.-J. I., Kumar, V., Zorumski, C. F., & O'Malley, K. L. (2014). Intracellular mGluR5 can mediate synaptic plasticity in the hippocampus. *The Journal of Neuroscience: The Official Journal of the Society for Neuroscience*, *34*(13), 4589–4598.

Rajadhyaksha, A., Barczak, A., Macıas, W., Leveque, J.-C., Lewis, S. E., & Konradi, C. (1999). L-type ca^{2+}channels are essential for glutamate-mediated CREB phosphorylation and*c-fos*gene expression in striatal neurons. *The Journal of Neuroscience: The Official Journal of the Society for Neuroscience*, *19*(15), 6348–6359.

Ramamoorthi, K., Fropf, R., Belfort, G. M., Fitzmaurice, H. L., McKinney, R. M., Neve, R. L., Otto, T., & Lin, Y. (2011). Npas4 regulates a transcriptional program in CA3 required for contextual memory formation. *Science (New York, N.Y.)*, *334*(6063), 1669–1675.

Ramirez et al. (2013). Creating a False Memory in the Hippocampus. *Science*, *339*(6121), 816–819.

Rao-Ruiz, P., Couey, J. J., Marcelo, I. M., Bouwkamp, C. G., Slump, D. E., Matos, M. R., van der Loo, R. J., Martins, G. J., van den Hout, M., van IJcken, W. F., Costa, R. M., van den Oever, M. C., & Kushner, S. A. (2019). Engram-specific transcriptome profiling of contextual memory consolidation. *Nature Communications*, *10*(1), 2232.

Rawat, V., Goux, W., Piechaczyk, M., & D'Mello, S. R. (2016). C-FOS protects neurons through a noncanonical mechanism involving HDAC3 interaction: Identification of a 21-amino acid fragment with neuroprotective activity. *Molecular Neurobiology*, *53*(2), 1165–1180.

Recabarren, D., & Alarcón, M. (2017). Gene networks in neurodegenerative disorders. *Life Sciences*, *183*, 83–97.

Renthal, W., Carle, T. L., Maze, I., Covington, H. E., 3rd, Truong, H.-T., Alibhai, I., Kumar, A., Montgomery, R. L., Olson, E. N., & Nestler, E. J. (2008). Delta FOSB mediates epigenetic desensitization of the c-fos gene after chronic amphetamine exposure. *The Journal of Neuroscience: The Official Journal of the Society for Neuroscience*, *28*(29), 7344–7349.

Robison, A. J., Vialou, V., Mazei-Robison, M., Feng, J., Kourrich, S., Collins, M., Wee, S., Koob, G., Turecki, G., Neve, R., Thomas, M., & Nestler, E. J. (2013). Behavioral and structural responses to chronic cocaine require a feedforward loop involving ΔFOSB and calcium/calmodulin-dependent protein kinase II in the nucleus accumbens shell. *The Journal of Neuroscience: The Official Journal of the Society for Neuroscience*, *33*(10), 4295–4307.

Rogerson, T., Jayaprakash, B., Cai, D. J., Sano, Y., Lee, Y.-S., Zhou, Y., Bekal, P., Deisseroth, K., & Silva, A. J. (2016). Molecular and cellular mechanisms for trapping and activating emotional memories. *PloS One*, *11*(8), e0161655.

Rylski, M., & Kaczmarek, L. (2004). Ap-1 targets in the brain. *Frontiers in Bioscience*, *9*(1–3), 8–23.

Ryseck, R. P., & Bravo, R. (1991). c-JUN, JUN B, and JUN D differ in their binding affinities to AP-1 and CRE consensus sequences: effect of FOS proteins. *Oncogene*, *6*(4), 533–542.

Saha, R. N., & Dudek, S. M. (2013). Splitting Hares and Tortoises: A classification of neuronal immediate early gene transcription based on poised RNA polymerase II. *Neuroscience*, *247*, 175–181.

Sanders, M., Petrasch-Parwez, E., Habbes, H.-W., Düring, M. V., & Förster, E. (2022). Corrigendum: Postnatal developmental expression profile classifies the indusium griseum as a distinct subfield of the hippocampal formation. *Frontiers in Cell and Developmental Biology*, *10*, 856519.

Sargolini, F., Fyhn, M., Hafting, T., McNaughton, B. L., Witter, M. P., Moser, M.-B., & Moser, E. I. (2006). Conjunctive representation of position, direction, and velocity in entorhinal cortex. *Science (New York, N.Y.)*, *312*(5774), 758–762.

Scharfman, H. E., & Myers, C. E. (2016). Corruption of the dentate gyrus by "dominant" granule cells: Implications for dentate gyrus function in health and disease. *Neurobiology of Learning and Memory*, *129*, 69–82.

Scheff, S. W., Price, D. A., Schmitt, F. A., & Mufson, E. J. (2006). Hippocampal synaptic loss in early Alzheimer's disease and mild cognitive impairment. *Neurobiology of Aging*, *27*(10), 1372–1384.

Scoville, W. B., & Milner, B. (1957). Loss of recent memory after bilateral hippocampal lesions. *Journal of Neurology, Neurosurgery, and Psychiatry*, *20*(1), 11–21.

Sehgal, M., Ehlers, V. L., & Moyer, J. R., Jr. (2014). Learning enhances intrinsic excitability in a subset of lateral amygdala neurons. *Learning & Memory (Cold Spring Harbor, N.Y.)*, *21*(3), 161–170.

Semon, R. W., & Semon, R. W. (1909). *Die mnemischen Empfindungen in ihren Beziehungen zu den Originalempfindungen / von Richard Semon*. W. Engelmann,.

Sheng, H. Z., Fields, R. D., & Nelson, P. G. (1993). Specific regulation of immediate early genes by patterned neuronal activity. *Journal of Neuroscience Research*, *35*(5), 459–467.

Shneker, B. F., & Fountain, N. B. (2003). Epilepsy. *Disease-a-Month: DM*, *49*(7), 426–478.

Silver, P. A. (1991). How proteins enter the nucleus. *Cell*, *64*(3), 489–497.

Simms, B. A., & Zamponi, G. W. (2014). Neuronal voltage-gated calcium channels: structure, function, and dysfunction. *Neuron*, *82*(1), 24–45.

Spiers, H. J., Burgess, N., Hartley, T., Vargha-Khadem, F., & O'Keefe, J. (2001). Bilateral hippocampal pathology impairs topographical and episodic memory but not visual pattern matching. *Hippocampus*, *11*(6), 715–725.

Squire, L. R., Stark, C. E. L., & Clark, R. E. (2004). the Medial Temporal Lobe. *Annual Review of Neuroscience*, *27*(1), 279–306.

Stent, G. S. (1973). A physiological mechanism for Hebb's postulate of learning. *Proceedings of the National Academy of Sciences of the United States of America*, *70*(4), 997–1001.

Stiles, C. D. (1985). The biological role of oncogenes--insights from platelet-derived growth factor: Rhoads Memorial Award lecture. *Cancer Research*, *45*(11 Pt 1), 5215–5218.

Struthers, W. M., DuPriest, A., & Runyan, J. (2005). Habituation reduces novelty-induced FOS expression in the striatum and cingulate cortex. *Experimental Brain Research*, *167*(1), 136–140.

Sun, X., Bernstein, M. J., Meng, M., Rao, S., Sørensen, A. T., Yao, L., Zhang, X., Anikeeva, P. O., & Lin, Y. (2020). Functionally Distinct Neuronal Ensembles within the Memory Engram. *Cell*, *181*, 410–423.

Takuma, K., Hara, Y., Kataoka, S., Kawanai, T., Maeda, Y., Watanabe, R., Takano, E., Hayata-Takano, A., Hashimoto, H., Ago, Y., & Matsuda, T. (2014). Chronic treatment with valproic acid or sodium butyrate attenuates novel object recognition deficits and hippocampal dendritic spine loss in a mouse model of autism. *Pharmacology, Biochemistry, and Behavior*, *126*, 43–49.

Taube, J. S., Muller, R. U., & Ranck, J. B., Jr. (1990). Head-direction cells recorded from the postsubiculum in freely moving rats. II. Effects of environmental manipulations. *The Journal of Neuroscience: The Official Journal of the Society for Neuroscience*, *10*(2), 436–447.

Thind, K. K., Ribak, C. E., & Buckmaster, P. S. (2008). Synaptic input to dentate granule cell basal dendrites in a rat model of temporal lobe epilepsy. *The Journal of Comparative Neurology*, *509*(2), 190–202.

Tolman, E. C. (1948). Cognitive maps in rats and men. *Psychological Review*, *55*(4), 189–208.

Trojanowski, N. F., Bottorff, J., & Turrigiano, G. G. (2021). Activity labeling in vivo using CaMPARI2 reveals intrinsic and synaptic differences between neurons with high and low firing rate set points. *Neuron*, *109*(4), 663-676.e5.

Tulving, E., Voi, M. E. L., Routh, D. A., & Loftus, E. (1983). Ecphoric processes in episodic memory. *Philosophical Transactions of the Royal Society of London*, *302*(1110), 361–371.

Turrigiano, G. G., Leslie, K. R., Desai, N. S., Rutherford, L. C., & Nelson, S. B. (1998). Activity-dependent scaling of quantal amplitude in neocortical neurons. *Nature*, *391*(6670), 892–896.

Ulery, P. G., Rudenko, G., & Nestler, E. J. (2006). Regulation of ΔFOSB Stability by Phosphorylation. *The Journal of Neuroscience: The Official Journal of the Society for Neuroscience*, *26*(19), 5131–5142.

Ulery-Reynolds, P. G., Castillo, M. A., Vialou, V., Russo, S. J., & Nestler, E. J. (2009). Phosphorylation of ΔFOSB mediates its stability in vivo. *Neuroscience*, *158*(2), 369–372.

Valiati, F. E., Vasconcelos, M., Lichtenfels, M., Petry, F. S., de Almeida, R. M. M., Schwartsmann, G., Schröder, N., de Farias, C. B., & Roesler, R. (2017). Administration of a histone deacetylase inhibitor into the basolateral amygdala enhances memory consolidation, delays extinction, and increases hippocampal BDNF levels. *Frontiers in Pharmacology*, *8*, 415.

van Strien, Cappaert, & Witter. (2009). The anatomy of memory: an interactive overview of the parahippocampal–hippocampal network. *Nature Reviews. Neuroscience*, *10*(4), 272–282.

Vialou, V., Robison, A. J., Laplant, Q. C., Covington, H. E., 3rd, Dietz, D. M., Ohnishi, Y. N., Mouzon, E., Rush, A. J., 3rd, Watts, E. L., Wallace, D. L., Iñiguez, S. D., Ohnishi, Y. H., Steiner, M. A., Warren, B. L., Krishnan, V., Bolaños, C. A., Neve, R. L., Ghose, S., Berton, O., … Nestler, E. J. (2010). DeltaFOSB in brain reward circuits mediates resilience to stress and antidepressant responses. *Nature Neuroscience*, *13*(6), 745–752.

Villain, H., Florian, C., & Roullet, P. (2016). HDAC inhibition promotes both initial consolidation and reconsolidation of spatial memory in mice. *Scientific Reports*, *6*(1). https://doi.org/10.1038/srep27015

Vossel, K. A., Ranasinghe, K. G., Beagle, A. J., Mizuiri, D., Honma, S. M., Dowling, A. F., Darwish, S. M., Van Berlo, V., Barnes, D. E., Mantle, M., Karydas, A. M., Coppola, G., Roberson, E. D., Miller, B. L., Garcia, P. A., Kirsch, H. E., Mucke, L., & Nagarajan, S. S. (2016). Incidence and impact of subclinical epileptiform activity in Alzheimer's disease. *Annals of Neurology*, *80*(6), 858–870.

Wang, J. Q., Fibuch, E. E., & Mao, L. (2007). Regulation of mitogen-activated protein kinases by glutamate receptors. *Journal of Neurochemistry*, *100*(1), 1–11.

Werme, M., Messer, C., Olson, L., Gilden, L., Thorén, P., Nestler, E. J., & Brené, S. (2002). Delta FOSB regulates wheel running. *The Journal of Neuroscience: The OfficialJournal of the Society for Neuroscience*, *22*(18), 8133–8138.

Westenbroek, R. E., Ahlijanian, M. K., & Catterall, W. A. (1990). Clustering of L-type Ca^{2+} channels at the base of major dendrites in hippocampal pyramidal neurons. *Nature*, *347*(6290), 281–284.

Wheeler, D. G., Groth, R. D., Ma, H., Barrett, C. F., Owen, S. F., Safa, P., & Tsien, R. W. (2012). Ca(V)1 and Ca(V)2 channels engage distinct modes of $Ca(^{2+})$ signaling to control CREB-dependent gene expression. *Cell*, *149*(5), 1112–1124.

Whitlock, J. R., Sutherland, R. J., Witter, M. P., Moser, M.-B., & Moser, E. I. (2008). Navigating from hippocampus to parietal cortex. *Proceedings of the National Academy of Sciences of the United States of America*, *105*(39), 14755–14762.

Whittle, N., Maurer, V., Murphy, C., Rainer, J., Bindreither, D., Hauschild, M., Scharinger, A., Oberhauser, M., Keil, T., Brehm, C., Valovka, T., Striessnig, J., & Singewald, N. (2016). Enhancing dopaminergic signaling and histone acetylation promotes long-term rescue of deficient fear extinction. *Translational Psychiatry*, *6*(12), e974–e974.

Wible, C. (2013). Hippocampal Physiology, Structure and Function and the Neuroscience of Schizophrenia: A Unified Account of Declarative Memory Deficits, Working Memory Deficits and Schizophrenic Symptoms. *Behavioral Sciences*, *3*(2), 298–315.

Wilson, C. B., McLaughlin, L. D., Ebenezer, P. J., Nair, A. R., & Francis, J. (2014). Valproic acid effects in the hippocampus and prefrontal cortex in an animal model of post-traumatic stress disorder. *Behavioural Brain Research*, *268*, 72–80.

Wisdom, R. (1999). AP-1: one switch for many signals. *Experimental Cell Research*, *253*(1), 180–185.

Witter, M. P., Canto, C. B., Couey, J. J., Koganezawa, N., & O'Reilly, K. C. (2013). Architecture of spatial circuits in the hippocampal region. *Philosophical Transactions of the Royal Society of London. Series B, Biological Sciences*, *369*(1635), 20120515–20120515.

Xing, J., Ginty, D. D., & Greenberg, M. E. (1996). Coupling of the RAS-MAPK pathway to gene activation by RSK2, a growth factor-regulated CREB kinase. *Science (New York, N.Y.)*, *273*(5277), 959–963.

Xu, Y., Zheng, Z., Ho, K. P., & Qian, Z. (2006). Effects of spinal cord injury on c-fos expression in hypothalamic paraventricular nucleus and supraoptic nucleus in rats. *Brain Research*, *1087*(1), 175–179.

Yang, K., Broussard, J. I., Levine, A. T., Jenson, D., Arenkiel, B. R., & Dani, J. A. (2017). Dopamine receptor activity participates in hippocampal synaptic plasticity associated with novel object recognition. *The European Journal of Neuroscience*, *45*(1), 138–146.

Yang, X.-J., & Seto, E. (2008). The Rpd3/Hda1 family of lysine deacetylases: from bacteria and yeast to mice and men. *Nature Reviews. Molecular Cell Biology*, *9*(3), 206–218.

Yassin, L., Benedetti, B. L., Jouhanneau, J.-S., Wen, J. A., Poulet, J. F. A., & Barth, A. L. (2010). An Embedded Subnetwork of Highly Active Neurons in the Neocortex. *Neuron*, *68*(6), 1043–1050.

Ylinen, A., Bragin, A., Nadasdy, Z., Jando, G., Szabo, I., Sik, A., & Buzsaki, G. (1995). Sharp wave-associated high-frequency oscillation (200 Hz) in the intact hippocampus: network and intracellular mechanisms. *The Journal of Neuroscience: The Official Journal of the Society for Neuroscience*, *15*(1), 30–46.

Yokoyama, K., Hiyama, A., Arai, F., Nukaga, T., Sakai, D., & Mochida, J. (2013). C-FOS regulation by the MAPK and PKC pathways in intervertebral disc cells. *PloS One*, *8*(9), e73210.

You, J. C., Muralidharan, K., Park, J. W., Petrof, I., Pyfer, M. S., Corbett, B. F., LaFrancois, J. J., Zheng, Y., Zhang, X., Mohila, C. A., Yoshor, D., Rissman, R. A., Nestler, E. J., Scharfman, H. E., & Chin, J. (2017). Epigenetic suppression of hippocampal calbindin-D28k by ΔFOSB drives seizure-related cognitive deficits. *Nature Medicine*, *23*(11), 1377–1383.

Yuan, R. K., Hebert, J. C., Thomas, A. S., Wann, E. G., & Muzzio, I. A. (2015). HDAC I inhibition in the dorsal and ventral hippocampus differentially modulates predator-odor fear learning and generalization. *Frontiers in Neuroscience*, *9*, 319.

Yutsudo, N., Kamada, T., Kajitani, K., Nomaru, H., Katogi, A., Ohnishi, Y. H., Ohnishi, Y. N., Takase, K.-I., Sakumi, K., Shigeto, H., & Nakabeppu, Y. (2013). fosB-null mice display impaired adult hippocampal neurogenesis and spontaneous epilepsy with depressive behavior. *Neuropsychopharmacology: Official Publication of the American College of Neuropsychopharmacology*, *38*(5), 895–906.

Zachariou, V., Bolanos, C. A., Selley, D. E., Theobald, D., Cassidy, M. P., Kelz, M. B., Shaw-Lutchman, T., Berton, O., Sim-Selley, L. J., Dileone, R. J., Kumar, A., & Nestler, E. J. (2006). An essential role for DeltaFOSB in the nucleus accumbens in morphine action. *Nature Neuroscience*, *9*(2), 205–211.

Zhang, J., Zhang, D., McQuade, J. S., Behbehani, M., Tsien, J. Z., & Xu, M. (2002). c-fos regulates neuronal excitability and survival. *Nature Genetics*, *30*(4), 416–420.

Zhang, S.-J., Zou, M., Lu, L., Lau, D., Ditzel, D. A. W., Delucinge-Vivier, C., Aso, Y., Descombes, P., & Bading, H. (2009). Nuclear calcium signaling controls expression of a large gene pool: identification of a gene program for acquired neuroprotection induced by synaptic activity. *PLoS Genetics*, *5*(8), e1000604.

Zhao, R., Liu, L., & Rittenhouse, A. R. (2007). Ca^{2+} influx through both L- and N-type Ca^{2+} channels increases c-fos expression by electrical stimulation of sympathetic neurons. *The European Journal of Neuroscience*, *25*(4), 1127–1135.

Zhou, Y., Won, J., Karlsson, M. G., Zhou, M., Rogerson, T., Balaji, J., Neve, R., Poirazi, P., & Silva, A. J. (2009). CREB regulates excitability and the allocation of memory to subsets of neurons in the amygdala. *Nature Neuroscience*, *12*(11), 1438–1443.

Zhu, H., Yan, H., Tang, N., Li, X., Pang, P., Li, H., Chen, W., Guo, Y., Shu, S., Cai, Y., Pei, L., Liu, D., Luo, M.-H., Man, H., Tian, Q., Mu, Y., Zhu, L.-Q., & Lu, Y. (2017). Impairments of spatial memory in an Alzheimer's disease model via degeneration of hippocampal cholinergic synapses. *Nature Communications*, *8*(1), 1676.

Zimmer. (1971). Ipsilateral afferents to the commissural zone of the fascia dentata, demonstrated in decommissurated rats by silver impregnation. *Journal of Comparative Neurology, 142 (1971), Pp. 393–416*.

Appendix

Publication #4: Tool development Freeze-frame imaging of dendritic Ca^{2+} signals with TubuTag

Alberto Perez-Alvarez*, Florian Huhn, Céline D. Dürst, **Andreas Franzelin**, Paul J. Lamothe-Molina, and Thomas G. Oertner*, Frontiers Molecular Neurosci. 2021; 14: 635820

https://doi.org/10.3389/fnmol.2021.635820

In this project, we developed a new indicator for dendritic Ca^{2+} signals. I was responsible for immunohistological staining and confocal imaging (Fig. 4). I successfully tested antibodies against converted TubuTag and participated in writing of the manuscript.

frontiers in Molecular Neuroscience

ORIGINAL RESEARCH
published: 04 March 2021
doi: 10.3389/fnmol.2021.635820

Freeze-Frame Imaging of Dendritic Calcium Signals With TubuTag

Alberto Perez-Alvarez[1,2], Florian Huhn[2], Céline D. Dürst[1,2], Andreas Franzelin[1], Paul J. Lamothe-Molina[1] and Thomas G. Oertner[1]**

[1] Institute for Synaptic Physiology, Center for Molecular Neurobiology, University Medical Center Hamburg-Eppendorf, Hamburg, Germany, [2] Rapp OptoElectronic GmbH, Wedel, Germany

The extensive dendritic arbor of neurons is thought to be actively involved in the processing of information. Dendrites contain a rich diversity of ligand- and voltage-activated ion channels as well as metabotropic receptors. In addition, they are capable of releasing calcium from intracellular stores. Under specific conditions, large neurons produce calcium spikes that are locally restricted to a dendritic section. To investigate calcium signaling in dendrites, we introduce TubuTag, a genetically encoded ratiometric calcium sensor anchored to the cytoskeleton. TubuTag integrates cytoplasmic calcium signals by irreversible photoconversion from green to red fluorescence when illuminated with violet light. We used a custom two-photon microscope with a large field of view to image pyramidal neurons in CA1 at subcellular resolution. Photoconversion was strongest in the most distal parts of the apical dendrite, suggesting a gradient in the amplitude of dendritic calcium signals. As the read-out of fluorescence can be performed several hours after photoconversion, TubuTag will help investigating dendritic signal integration and calcium homeostasis in large populations of neurons.

Keywords: calcium imaging, dendritic integration, two-photon (2p), hippocampus, genetically encoded activity indicators

OPEN ACCESS

Edited by:
Marco Mainardi,
Institute of Neuroscience, National Research Council (CNR), Italy

Reviewed by:
Anna Letizia Allegra Mascaro,
National Research Council (CNR), Italy
Tommaso Fellin,
Italian Institute of Technology (IIT), Italy

****Correspondence:***
Alberto Perez-Alvarez
alberto.perez-alvarez@zmnh.uni-hamburg.de
Thomas G. Oertner
thomas.oertner@zmnh.uni-hamburg.de

Received: *30 November 2020*
Accepted: *09 February 2021*
Published: *04 March 2021*

Citation:
Perez-Alvarez A, Huhn F, Dürst CD, Franzelin A, Lamothe-Molina PJ and Oertner TG (2021) Freeze-Frame Imaging of Dendritic Calcium Signals With TubuTag. Front. Mol. Neurosci. 14:635820. doi: 10.3389/fnmol.2021.635820

INTRODUCTION

When a cluster of excitatory synapses is simultaneously activated on a basal dendrite of a pyramidal neuron, the combined depolarization triggers a local NMDA spike (Schiller et al., 2000). In addition to NMDA receptors, voltage-gated calcium channels also contribute to local dendritic depolarization and calcium spikes (Losonczy and Magee, 2006; Remy and Spruston, 2007; Takahashi et al., 2020). These non-linear processes may endow dendrites with the capability to serve as computational subunits (Polsky et al., 2004) and gate the output of cortical neurons during perception of sensory stimuli (Takahashi et al., 2020). As the dendritic arbor of even a single cortical neuron spans several square millimeters and dendritic calcium spikes are stochastic, capturing these rare events with laser scanning microscopy is technically challenging. Most of our knowledge is based on painstaking patch-clamp recordings from individual dendrites or simulating synaptic activity by local glutamate uncaging (Antic et al., 2010; Major et al., 2013). Optical recording *in vivo* is possible in head-fixed animals, but typically limited to a single plane containing a few dendrites (Helmchen et al., 1999; Takahashi et al., 2016). Several approaches to speed up volumetric imaging have been demonstrated (Bouchard et al., 2015; Szalay et al., 2016; Yang and Yuste, 2017), but the fundamental trade-off between the desired high spatial resolution in a large volume of tissue and the temporal resolution required to capture brief calcium transients cannot be solved by ever-faster

scanning mechanisms (Lecoq et al., 2019). Fast multiphoton imaging requires high laser power, and the resulting local heating can affect brain physiology (Schmidt and Oheim, 2020). Thus, to analyze dendritic calcium signals in thousands of neurons under physiological conditions, it would be very attractive to temporally separate the labeling event from the read-out.

To generate a lasting record of synaptic activity that can be read-out later, we previously developed SynTagMA (Perez-Alvarez et al., 2020), a synaptically targeted variant of CaMPARI-2 (Moeyaert et al., 2018). This calcium integrator photoconverts irreversibly from green to red if it is bound to calcium and simultaneously illuminated by violet light (Fosque et al., 2015; Moeyaert et al., 2018). We reasoned that immobilizing the calcium integrator by targeting it to the dendritic cytoskeleton would allow generating a similarly conserved record (freeze frame) of dendritic calcium events. Here we show that a fusion of α-tubulin with CaMPARI2 provides stable cytoskeletal anchoring and very low turnover, essential features to preserve information about subcellular calcium distributions for later read-out. Using hippocampal slice cultures virally transduced with TubuTag as a test system, we show that electrical stimulation of Schaffer collateral axons induces calcium gradients in the apical dendrites, the distal tips reaching the highest concentrations. In fixed tissue, the contrast between active and inactive neurons and dendrites was further enhanced by an antibody that recognizes only the red form of TubuTag.

RESULTS

Our new sensor is based on the fluorescent protein mEos (Wiedenmann et al., 2004) that undergoes irreversible photoconversion from green to red when illuminated with violet light (405 nm). Previously, mEos had been fused to a calcium-dependent conformation switch (calmodulin-M13) to create integrating sensors that can only be photoconverted when bound to calcium (CaMPARI, CaMPARI2) (Fosque et al., 2015; Moeyaert et al., 2018). To generate TubuTag, we fused CaMPARI2 in-frame to α-tubulin. We also created a high affinity version based on CaMPARI2_F391W_L398V (Moeyaert et al., 2018). Expressed in hippocampal neurons by single cell electroporation, dendrites, and somata showed bright green fluorescence. Dendritic spines, which rarely contain microtubules and are stabilized by f-actin instead, were largely invisible (**Figure 1A**). As the green fluorescence of the CaMPARI moiety dims upon calcium binding, it can be used as an acute calcium sensor. To characterize the calcium sensitivity of TubuTag, we induced back-propagating action potentials (bAPs) by somatic current injections and simultaneously measured green fluorescence intensity in the apical dendrite by two-photon microscopy (**Figure 1B**). Interleaved trials with no stimulation (0 APs) allowed distinguishing bleaching and wash-out of TubuTag from calcium-induced dimming (**Figure 1C**). The dimming response increased with the number of bAPs in a 100 Hz burst, following a sigmoidal curve in a log dose-response plot. We found that our tubulin fusion constructs followed the binding curves of the parent CaMPARI variants (**Figure 1D**) up to 10 bAPs, but reached saturation slightly earlier (−62% ΔF/F after 30 bAPs). For this study, we used the lowest affinity TubuTag (with CaMPARI2) to minimize baseline photoconversion in inactive cells. CaMPARI2 is also much brighter and shows more efficient photoconversion (larger dynamic range) than CaMPARI1 (Moeyaert et al., 2018).

Illumination with long violet light (405 nm) pulses during extracellular high-frequency stimulation of CA3 axons induced strong photoconversion of CA1 neurons expressing TubuTag (**Figure 1E**). The red label showed no sign of decay after 3 h, indicating irreversible photoconversion and slow protein turnover. Therefore, we expect red/green ratio differences between active and inactive neurons to be stable for several hours. To determine the fraction of TubuTag integrated in stable microtubules vs. soluble TubuTag monomers, we measured fluorescence recovery after photobleaching (FRAP, **Figure 1F**). After 3 h, ∼50% of the bleached fluorescence had recovered (**Figure 1G**), consistent with the slow turnover of microtubules in neurons (Kahn et al., 2018). Adjacent regions showed a small and transient dip in fluorescence intensity, consistent with diffusional exchange of bleached and unbleached monomers. Thus, if subcellular resolution is the goal of the experiment and 5% loss of contrast is acceptable, the red/green ratio (R/G) should be determined within ∼40 min after photoconversion.

To image large populations of neurons at high resolution, low-magnification high-NA water immersion objectives are available from all major microscope manufacturers. However, it is challenging to integrate them into commercial two-photon microscopes as they require a large diameter laser beam scanned at large angles with minimal wave front error. In addition, the detection pathway has to conserve the etendue of the objective (or condenser, respectively) in order to detect all emitted photons that enter the optical system. We custom-built a two-photon microscope designed to meet the following requirements: (1) 800 × 800 μm field of view (FoV); (2) efficient detection of green and red fluorescence, simultaneously through the objective and through the condenser; (3) resonant-galvo-galvo scanning for fast frame rates; (4) protection of photomultiplier tubes (PMTs) during photoconversion (405 nm light). In our system, the scan lens – tube lens assembly provides 4.3 × magnification and is horizontally oriented, allowing for a compact detection assembly directly on top of the objective (**Figures 2a,b**). Below the stage, a second optical system detects fluorescence through a 1.4 NA oil immersion condenser. For patch-clamp experiments, a CCD camera is coupled in by a sliding 45° mirror and the condenser provides Dodt contrast illumination. During photoconversion, both light detection pathways are protected by electronic shutters with 45 mm free aperture (NS45B, Uniblitz, United States).

To maintain the brain tissue at 37°C throughout the experiment, the temperature of the perfusate was controlled by an in-line heater and the oil-immersion condenser was heated to 33°C by a ring of Peltier elements, with the cool side in contact with the PMT assembly. A magnetic holder allows switching objectives with different working distances for different types of experiments. For most experiments, we used a Nikon 16 × 0.8 NA objective which provides a good compromise between FoV,

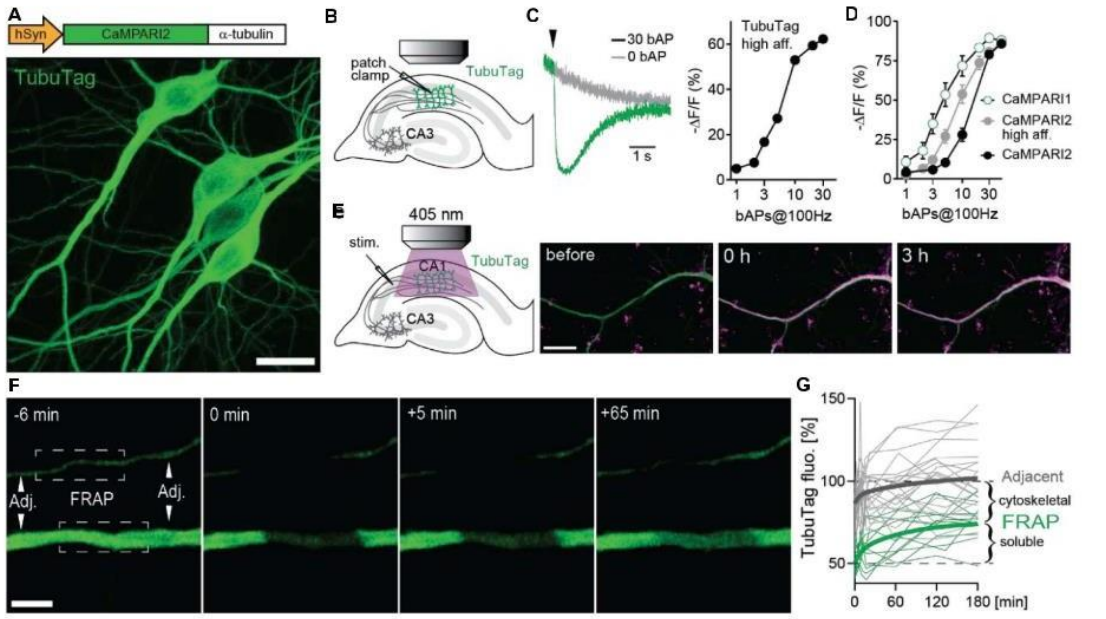

FIGURE 1 | Design and performance of TubuTag. **(A)** TubuTag was created by fusing α-tubulin driven by the human synapsin-1 promoter to the calcium integrator CaMPARI2. Expression was tested by single-cell electroporation in CA1. Note absence of TubuTag from dendritic spines that are stabilized by f-actin. Scale bar: 20 μm. **(B)** Back-propagating action potentials (bAP) were induced in a TubuTag-expressing neuron while monitoring green fluorescence in the apical dendrite. **(C)** Dimming of high affinity TubuTag upon bAP generation through whole-cell patch clamp (2 neurons). Arrowhead indicates time of AP burst. Dimming increases with the number of bAPs. **(D)** Dimming of three soluble CaMPARI variants upon bAP induction. **(E)** High frequency synaptic stimulation via extracellular electrode (three 0.2 ms pulses, 100 Hz) in *stratum radiatum* followed by a long violet light pulse (405 nm, 14 mW/mm^2, 500 ms duration, 1 s delay) led to strong photoconversion of TubuTag (10 pair repeats at 0.033 Hz). Converted TubuTag signal (red) in dendrites remained stable for over 3 h (2 neurons). Scale bar: 20 μm. **(F)** Turnover of TubuTag was assessed by fluorescence recovery after photobleaching (FRAP). Fluorescence at bleached (squares) and adjacent (arrowheads) dendritic areas was measured and followed over time. Scale bar: 5 μm. **(G)** Dendritic fluorescence normalized to F_0 fitted by a double exponential for bleached (τ_{fast} = 8 min; τ_{slow} = 75 min, *n* = 12 dendrites, 6 neurons) and adjacent areas.

optical resolution (**Figures 2c,d**) and 45-degree approach angle for patch-clamp or stimulation electrodes.

In order to express our sensor in a population of neurons, we packaged TubuTag into an AAV9 vector and injected it into the CA1 region of hippocampal organotypic slices using a Picospritzer (**Figures 3a–c**). Schaffer collateral axons were stimulated with an extracellular electrode in *stratum radiatum* (paired pulses at 20 Hz), shortly followed by a short violet light pulse delivered through the imaging objective (**Figure 3d**). After repeating this protocol 50 times, many dendrites in the vicinity of the electrode turned red while somata showed little photoconversion (**Figure 3a**). Strongly converted dendrites could be found next to non-converted dendrites, suggesting that not all neurons produced dendritic calcium spikes (**Figure 3e**). Conversion efficiency was not different in superficial vs. deep dendrites, indicating good penetration of the 405 nm photoconversion light (**Figure 3f**). The high transduction efficiency of AAV9 allowed us to monitor compartmentalized calcium signals at full density in a large volume fraction of CA1 in a single experiment. We used a tracking algorithm (see the section "Materials and Methods") to trace apical dendrites from the soma to the distal tips (**Figure 3g**). Not surprisingly, the density of strongly photoconverted dendrites increased toward the stimulation electrode. Evaluating photoconversion along individual dendrites revealed that distal tips were more strongly converted, even in neurons where little or no photoconversion was detected in the proximal apical dendrite (**Figure 3h**). The large surface-to-volume ratio of thin distal dendrites would be expected to favor large amplitude calcium signals. As thin dendrites are much smaller than the point-spread function of a two-photon microscope, the amplitude of these signals may have been systematically underestimated in acute calcium imaging experiments with single wavelength indicators.

It would be attractive to induce TubuTag conversion in intact animals during behavior and image the frozen calcium signal at high resolution *ex vivo*. Chemical fixation, however, invariably leads to some loss of fluorescence, reducing image contrast. For *ex-vivo* detection of active dendrites, it would be advantageous to specifically enhance the red fluorescence by immunostaining. A specific antibody against the red form of CaMPARI has been developed (Moeyaert et al., 2018). As a proof of principle, we tested this antibody on slices where TubuTag-expressing neurons had been strongly stimulated and illuminated with violet light, resulting in layer-specific photoconversion across the whole

Figure 1 Design and performance of TubuTag

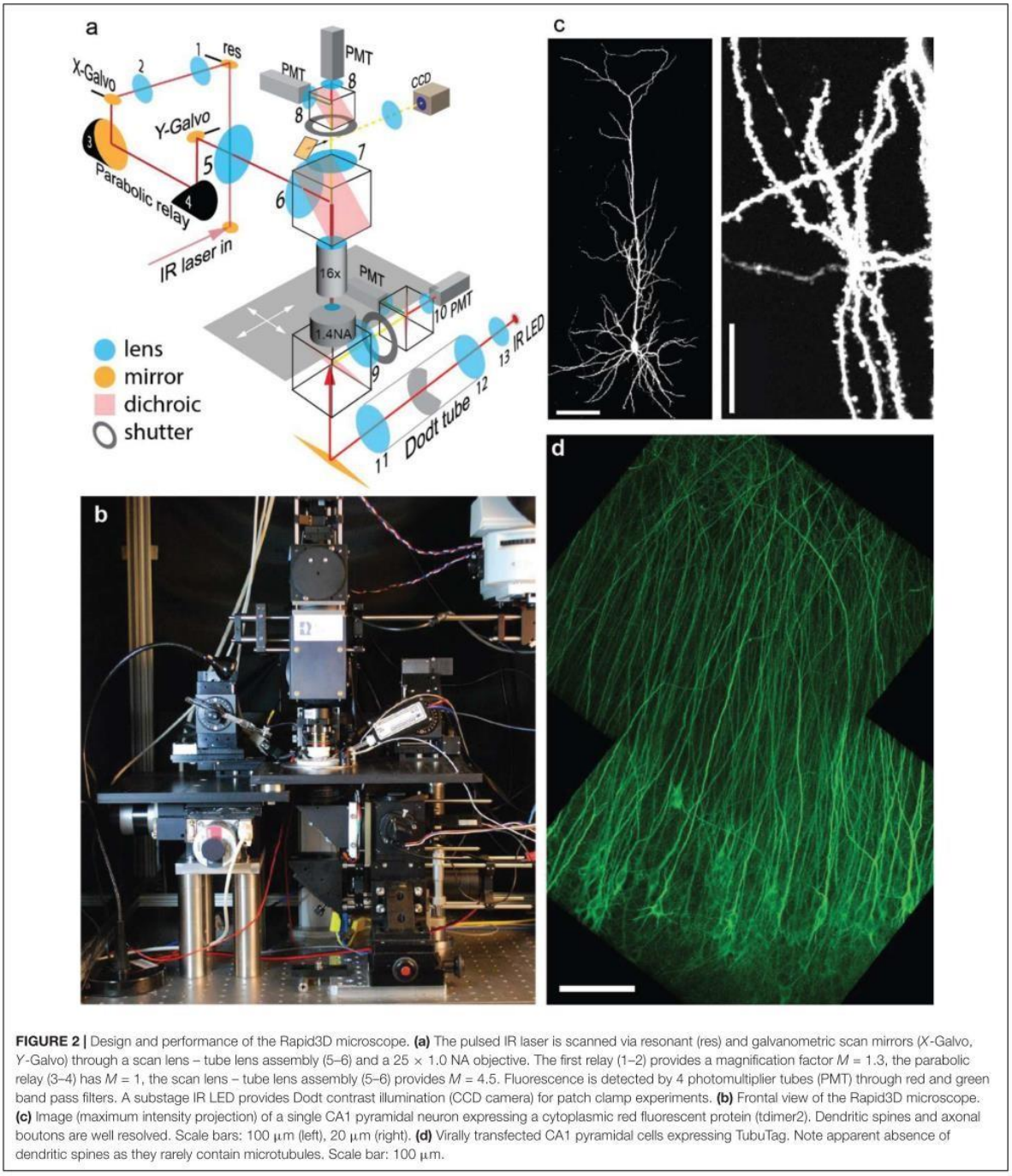

FIGURE 2 | Design and performance of the Rapid3D microscope. **(a)** The pulsed IR laser is scanned via resonant (res) and galvanometric scan mirrors (*X*-Galvo, *Y*-Galvo) through a scan lens – tube lens assembly (5–6) and a 25 × 1.0 NA objective. The first relay (1–2) provides a magnification factor $M = 1.3$, the parabolic relay (3–4) has $M = 1$, the scan lens – tube lens assembly (5–6) provides $M = 4.5$. Fluorescence is detected by 4 photomultiplier tubes (PMT) through red and green band pass filters. A substage IR LED provides Dodt contrast illumination (CCD camera) for patch clamp experiments. **(b)** Frontal view of the Rapid3D microscope. **(c)** Image (maximum intensity projection) of a single CA1 pyramidal neuron expressing a cytoplasmic red fluorescent protein (tdimer2). Dendritic spines and axonal boutons are well resolved. Scale bars: 100 μm (left), 20 μm (right). **(d)** Virally transfected CA1 pyramidal cells expressing TubuTag. Note apparent absence of dendritic spines as they rarely contain microtubules. Scale bar: 100 μm.

CA1 region (**Figures 4a,b**). After fixation, we used the primary anti-CaMPARI-red antibody and a far-red secondary antibody (AF648) to selectively enhance the photoconverted signal. Anti-CaMPARI-red highlighted the same neurons we previously identified as converted, indicating excellent specificity for the photoconverted form of TubuTag (**Figures 4c,d**). At higher magnification, photoconverted dendrites could be identified by their high immunoreactivity (**Figure 4e**).

Figure 2 Design and performance of the Rapid3D microscope

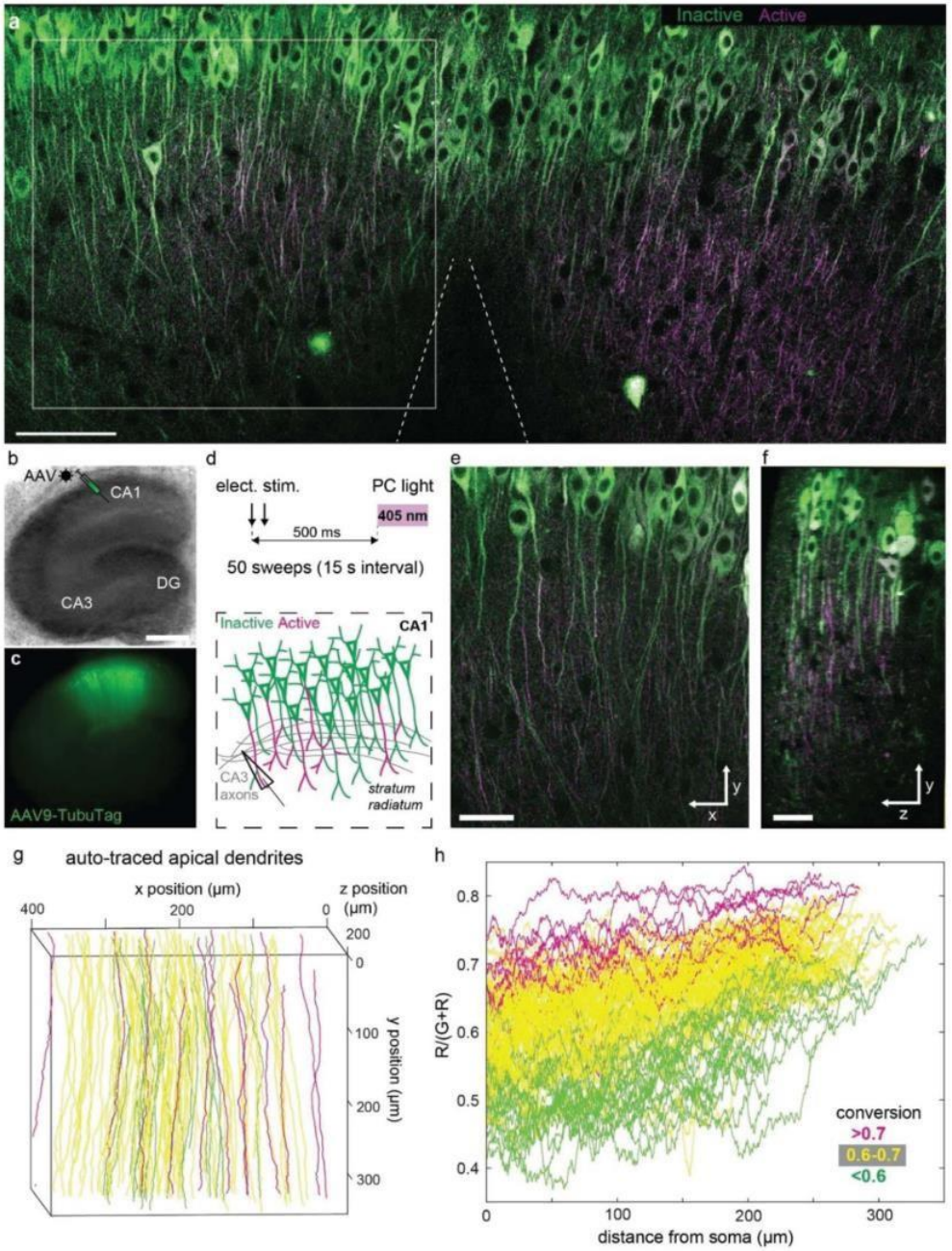

FIGURE 3 | Photoconversion of TubuTag by extracellular stimulation paired with violet light. **(a)** Two-photon image (single plane) of CA1 after pairing extracellular stimulation with violet light. Scale bar: 100 µm. **(b)** Rat hippocampal slice culture microinjected with AAV9-syn-TubuTag in the CA1 region. Scale bar: 500 µm. **(c)** Epifluorescence image of the transduced culture. **(d)** To account for the slow conformational change of TubuTag upon Ca^{2+} binding, photoconversion light (405 nm, 11 mW/mm^2, 200 ms duration) was delayed relative to the electrical stimulation of Schaffer collateral axons. This stimulation was repeated 50 times. **(e)** Detail of **(a)** showing strong differences in photoconversion between neighboring dendrites. Scale bar: 50 µm. **(f)** Side view of the volume shown in **(e)**. Scale bar: 30 µm. Note that photoconversion is not restricted to superficial dendrites (left), but independent of depth. **(g)** Automatic tracing of apical dendrites, color coded according to their average conversion [R/(G + R)]. Traced region corresponds to gray square in **(a)**, but extends further in depth. **(h)** Photoconversion profiles of the individual dendrites shown in **(f)**, color coded according to their average conversion. Note trend to stronger photoconversion toward the distal tips (right).

Figure 3 Photoconversion of TubuTag by extracellular stimulation paired with violet light

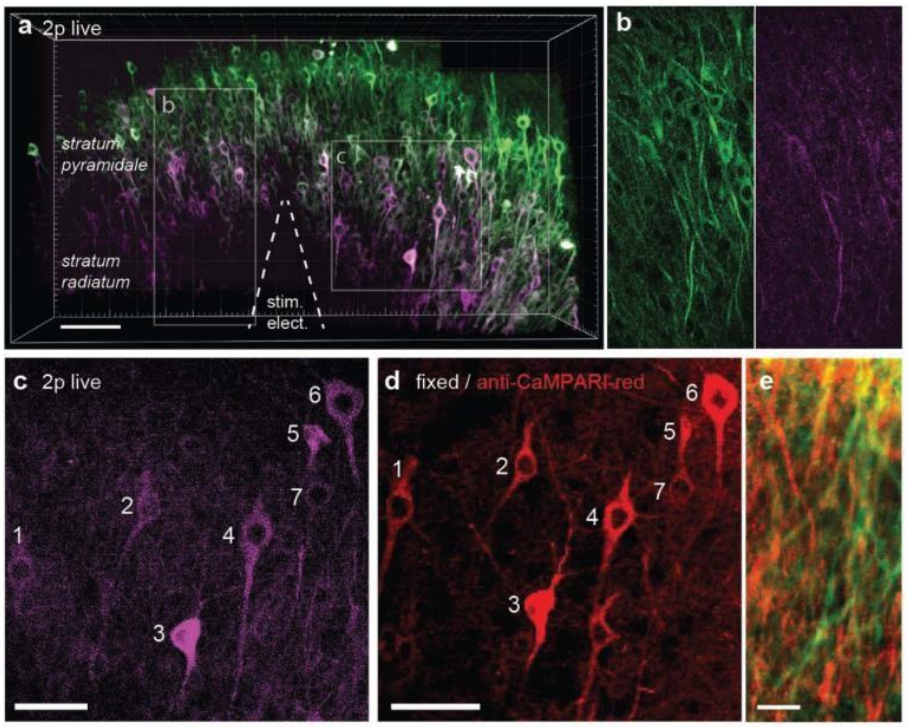

FIGURE 4 | TubuTag immunodetection. **(a)** Three-dimensional display of CA1 area of hippocampal slice virally transfected with TubuTag after photoconversion (smoothed with Gaussian filter). Electrical stimulation at 37°C followed by long violet light illumination (405 nm, 11 mW/mm^2, 500 ms duration, 1 s delay, 50 pair repeats at 0.1 Hz). Scale bar: 100 μm. **(b)** Detail (single optical plane, raw image) of green and red channel, showing photoconverted dendrites. **(c)** Detail of somatic layer (maximum intensity projection), showing photoconverted neurons (magenta). Scale bar: 50 μm. **(d)** Confocal image of same region as in **(b)** after fixation and staining against red (i.e., photoconverted) TubuTag. The far-red secondary antibody is displayed in red. Scale bar: 50 μm. **(e)** Detail of dendrites in stratum radiatum, overlay of endogenous green fluorescence and antibody-enhanced red fluorescence. Scale bar: 10 μm.

DISCUSSION

Calcium signals provide a unique window into neuronal physiology. From the release of neurotransmitter, induction of synaptic plasticity, complex spike bursts, to immediate early gene expression: all significant events in the life of a neuron are accompanied by calcium transients. Two-photon microscopy is a powerful tool to monitor such intracellular calcium signals at high resolution in intact brain tissue. Since fluorescence is sampled point-by-point, however, imaging of large and densely labeled volumes at the speed necessary to catch physiological calcium signals in subcellular detail is challenging. The calcium integrator CaMPARI irreversibly labels active neurons in a time window defined by violet illumination (Fosque et al., 2015; Moeyaert et al., 2018). This was a revolutionary concept, since it completely dissociated the labeling event from the optical recording of the results. Obviously, the speed of the microscope becomes much less important once the functional signal is frozen in time. Since CaMPARI is free to diffuse inside a neuron, subcellular gradients in photoconversion rapidly dissipate and the location of active inputs is lost. By fusing CaMPARI2 to tubulin, we immobilized the calcium reporter, providing a lasting record of high [Ca^{2+}] areas across the dendritic arbor. To be able to interpret differential TubuTag photoconversion as [Ca^{2+}] differences, it is important to ensure homogenous intensity of the photoconversion light across the brain region of interest.

For the previously published synaptically localized calcium integrator SynTagMA (Perez-Alvarez et al., 2020), we acquired separate image stacks to collect green and red fluorescence, exciting at 980 and 1040 nm, respectively. Green images had very little autofluorescence and were used to mask out non-synaptic fluorescence in the red channel. Due to chromatic aberration and imperfect alignment of the two laser lines, however, image registration was required before SynTagMA analysis. For TubuTag, we used a single wavelength (1,040 nm) used to excite both green and red species simultaneously. This simplified the analysis, as there was no need to register green and red images prior to analysis.

A topic of considerable interest is the possibility that synapses with synchronous activity are able to stabilize each other when situated close together, leading over time to a clustered input

organization (Kleindienst et al., 2011; Iacaruso et al., 2017). In principle, an activity tag exclusively located at excitatory synapses like postSynTagMA (Perez-Alvarez et al., 2020) could be used to investigate the input organization of individual neurons, but photoconversion of a group of spines could also result from a local dendritic calcium event. Combining SynTagMA and TubuTag might be a way to resolve this ambivalence: red spines on a green section of dendrite would be incontrovertible evidence for synchronous synaptic activity. If the postsynaptic neuron spikes at high frequency, however, not only input sites, but also other parts of the dendrite would become photoconverted. For precise localization of active inputs, it may thus be useful to co-express TubuTag with a light-gated potassium or chloride channel (Wietek et al., 2015; Beck et al., 2018) to prevent action potential generation during the photoconversion period.

The most important feature of TubuTag is the hour-long preservation of subcellular [Ca^{2+}] gradients in live tissue. Here we report the gradient along the long apical dendrite of CA1 pyramidal cells, but it would also be very interesting to investigate dendritic calcium events in interneurons, which are known to have a much higher calcium buffering capacity (Francavilla et al., 2019; Topolnik and Camiré, 2019). We envision that a head-mounted violet LED could be used to trigger photoconversion in intact animals, a situation where high-resolution imaging is very challenging. As we show, the signal-to-noise ratio in fixed tissue can be considerably improved by an antibody that recognizes only the red form of TubuTag. Compared to acute two-photon calcium imaging *in vivo*, which usually requires head fixation, TubuTag may provide a way to map cortical activity in freely moving animals.

MATERIALS AND METHODS

Plasmid Construction

TubuTag is CaMPARI2 (Moeyaert et al., 2018) fused to human α-tubulin, high affinity TubuTag contains 2 point mutations in the CaMPARI2 domain, F391W and L398V. To generate high affinity TubuTag, we replaced mCherry from pcDNA3.1 mCherry-human-alpha-tubulin (a gift from Marina Mikhaylova) with the CaMPARI moiety from preSynTagMA (Perez-Alvarez et al., 2020; Addgene ID 119738) using *Hin*dIII and *Bsp*1407I restriction sites. To insert the CaMPARI-tubulin fusion construct into a pAAV backbone, we first replaced in the C-terminus the restriction site *Xho*I by *Hin*dIII using PCR. Subsequently, we used *Nhe*I and *Hin*dII to insert it into the pAAV backbone of pAAV-syn-ChR2ETTC (Berndt et al., 2011; Addgene ID 101361). To create TubuTag, we mutated residues W391 and V398 by overlap extension PCR to obtain a W391F_V398L variant (CaMPARI2). Briefly, we designed primers to amplify two DNA segments containing both the point mutations, namely between *Nhe*I and V398L, W391F and *Box*I. The resulting amplified segments with sizes 1304 bp and 728 bp were overlaid, resulting in a 1968 bp segment size that was inserted to replace the segment in TubuTag using restriction sites *Nhe*I and *Box*I. TubuTag (Addgene ID 164184) and high affinity TubuTag (Addgene ID 164193) are available at Addgene.org.

Organotypic Hippocampal Slice Cultures

Hippocampal slice cultures from Wistar rats of either sex were prepared at postnatal day 4–7 as described (Gee et al., 2017). Briefly, rats were anesthetized with 80% CO_2 20% O_2 and decapitated. Hippocampi were dissected in cold slice culture dissection medium containing (in mM): 248 sucrose, 26 $NaHCO_3$, 10 glucose, 4 KCl, 5 $MgCl_2$, 1 $CaCl_2$, 2 kynurenic acid, and 0.001% phenol red. pH was 7.4, osmolarity 310–320 mOsm kg^{-1}, and solution was saturated with 95% O_2, 5% CO_2. Tissue was cut into 400 μM thick sections on a tissue chopper and cultured at the medium/air interface on membranes (Millipore PICMORG50) at 37°C in 5% CO_2. No antibiotics were added to the slice culture medium which was partially exchanged (60–70%) twice per week and contained (for 500 ml): 394 ml Minimal Essential Medium (Sigma, United States), 100 ml heat inactivated donor horse serum (Sigma, United States), 1 mM L-glutamine (Gibco, United States), 0.01 mg ml^{-1} insulin (Sigma, United States), 1.45 ml 5 M NaCl (Sigma, United States), 2 mM $MgSO_4$ (Fluka, United States), 1.44 mM $CaCl_2$ (Fluka, United States), 0.00125% ascorbic acid (Fluka, United States), 13 mM D-glucose (Fluka). Wistar rats were housed and bred at the University Medical Center Hamburg-Eppendorf. All procedures were performed in compliance with German law and according to the guidelines of Directive 2010/63/EU. Protocols were approved by the Behörde für Justiz und Verbraucherschutz (BJV) – Lebensmittelsicherheit und Veterinärwesen, of the City of Hamburg.

Neuronal Transduction

CA1 neurons in rat organotypic hippocampal slice culture (DIV 17–21) were transfected by single-cell electroporation (Wiegert et al., 2017a). Thin-walled pipettes (~10 MΩ) were filled with intracellular K-gluconate based solution into which plasmid DNA was diluted to 20 ng μl^{-1}. Pipettes were positioned against neurons and DNA was ejected using an Axoporator 800A (Molecular Devices) with 50 hyperpolarizing pulses (−12 V, 0.5 ms) at 50 Hz. Experiments were conducted 3–5 days after electroporation.

For viral transduction of hippocampal slices, AAV2/9 viral vectors containing TubuTag variants under the control of the synapsin promoter was prepared at the UKE vector facility. Working in a laminar air flow hood, organotypic hippocampal slices were microinjected at DIV 7–11 (Wiegert et al., 2017b). A pulled glass pipette was backfilled with 1 μl of the viral vector and the tip inserted in the hippocampal CA1 area. A picospritzer (Parker, United States) coupled to the pipette was used to deliver 3–4 short (50 ms) low pressure puffs of viral vector into the tissue. Injected slices were taken back to the incubator and imaged in the two-photon microscope 15–21 days later.

Two-Photon Imaging and Photoconversion

For fast two-photon imaging, we used a customized version of the Rapid3Dscope (Rapp OptoElectronic GmbH, Germany),

a large field of view two-photon microscope equipped with relayed resonant-galvo-galvo scanners (RGG). The microscope is controlled by the open access software ScanImage 2017b (Vidrio, United States; Pologruto et al., 2003). To simultaneously excite both the green and red species of TubuTag, we used a Ti:Sapphire laser (Chameleon Ultra II, Coherent, United States) tuned to 1040 nm, controlled by a Pockels cell (Conoptics, United States) and an electronic shutter (Uniblitz, United States). Red and green fluorescence was detected through upper and lower detection path with one pair of photomultiplier tubes (PMTs, H7422P-40SEL, Hamamatsu, Japan) on each side. The upper detection is placed above the objective (CFI75 LWD, 16x, 0.8 NA, Nikon, Japan), using a short-pass dichroic mirror (Chroma ZT775sp-2p) and a secondary red/green splitter (Chroma T565lpxr, United States) with red and green band path emission filters (Chroma ET525/70m-2p, Chroma ET605/70m-2p, United States). The lower detection uses an oil immersion condenser (1.4 NA, Olympus, Japan) and equivalent red/green detection optics. With the 16 × 0.8 NA Nikon objective, axial resolution was 4.0 μm in the center of the image, 5.5 μm at a lateral distance of 212 μm and 7.1 μm at a lateral distance of 425 μm (FWHM of Gaussian fits to the axial intensity profile of 175 nm green fluorescent beads in agarose, excited at 980 nm).

For extracellular synaptic stimulation, a glass monopolar electrode filled with extracellular solution was placed in *stratum radiatum*. Paired 0.2 ms pulses (40 ms inter stimulus interval) were delivered using an ISO-Flex stimulator (A.M.P.I., Israel) at 0.1 Hz. Overview images were acquired, covering an area close to the electrode tip. The resonant-galvo-galvo scanner allowed z-stack acquisition covering a brain volume of 435 μm × 435 μm × 100 μm in 2 min at 1024 × 1024 pixel resolution and 1 μm z-steps. Homogenous photoconversion light (405 nm) was provided by coupling an LED light source (CoolLED pE4000, United Kingdom) via liquid light guide (3 mm dia.) into the microscope. The end of the liquid light guide, which homogenizes the Lambertian emission profile of the LED, was projected into the specimen plane of the microscope (critical illumination).

Electrical stimulation and 405 nm illumination were controlled by the open source software WaveSurfer[1]. Electronic shutters (NS45B, Uniblitz, United States) protected PMTs during photoconversion. Series of 2–3 images acquired to cover a mm-long brain area were registered using the pairwise stitching plugin from ImageJ (Preibisch et al., 2009). For suprathreshold stimulation and photoconversion, three 0.2 ms pulses at 100 Hz were applied with a glass monopolar electrode followed 1 s later by 500 ms violet light (14 mW/mm^2). This pairing was repeated ten times at 0.033 Hz.

For calcium sensitivity calibration, CA1 neurons expressing TubuTag or CaMPARI variants or 3–5 days after electroporation were patched and brought into whole-cell configuration. Back-propagating action potentials (bAPs) were induced by injecting 1 nA pulses of 1 ms duration in current clamp. Fluorescence in the main apical dendrite was acquired at 500 Hz and changes from basal values were reported as $\Delta F/F$ ($F\text{-}F_0/F_0$). To depict photoconversion, red and green channels were merged.

[1]https://wavesurfer.janelia.org/

Automated Tracing of Apical Dendrites

We used the Fiji plugin ParticleTracker 2D (MOSAIC suite, Germany) to trace cross-sections of apical dendrites ("particles") from the soma to their distal tips. Red and green fluorescence was added prior to particle detection to avoid bias for (or against) strongly converted dendrites. At bifurcations, the algorithm followed the brighter branch. Only long trajectories (>450 points) were considered for analysis. The coordinates of the tracked dendrites were exported to Matlab to extract red and green fluorescence intensities from the original stacks. Single-voxel values were smoothed along the dendritic track (41-point Gaussian kernel) to reduce the impact of shot noise. We then calculated $R/(G + R)$ to normalize results between 0 (no conversion) and 1 (full conversion); actual values ranged from 0.4 to 0.8. We defined strongly converted dendrites as having a mean conversion ratio >0.7.

Fluorescence Recovery After Photobleaching (FRAP)

To estimate the diffusion of TubuTag molecules, we took *z*-stacks of dendrites in *stratum radiatum* from neurons electroporated with TubuTag and we bleached central parts of dendrites, subsequently following the recovery of fluorescence over time. After obtaining a baseline of 1–2 images, we zoomed (4X) onto the dendrite and performed 10 *z*-stacks at twice the laser power to achieve ∼50% bleaching without signs of tissue damage. Images were subsequently taken at the original settings and magnification at different intervals for 180 min. For analysis of each dendrite, we used a macro written in Fiji (Schindelin et al., 2012) to quantify fluorescence changes over time (Moeyaert et al., 2018) in the bleached area and two immediately adjacent non-bleached areas. Kinetics of recovery after bleaching was fit using non-linear regression in Prism 8 (GraphPad, United States).

Immunohistochemistry

After imaging and photoconversion in the 2p microscope, slices were fixed in a PBS solution containing 4% PFA for 30 min at room temperature (RT), washed and kept overnight in PBS at 4°C. Slices were then incubated in blocking buffer (1x PBS, 0.3% TritonX, 5% goat serum) for 2 h at RT. Next, sections were placed in the primary antibody (1:1,000, mouse Anti-CaMPARI-Red 4F6-1 clone, a gift from Eric Schreiter) carrier solution (PBS, 0.3% TritonX, 1% goat serum, 1% BSA) and incubated overnight at 4°C. After 3x washing with 1xPBS for 5 min, the sections were incubated for 2 h at RT in the secondary antibody (1:1,000, goat anti mouse Alexa Fluor 647, Life Technologies, United States) carrier solution (1x PBS, 0.3% TritonX, 5% goat serum). Sections were washed 3 × 10 min in 1x PBS, mounted on coverslips using Immu-Mount (Shandon, United States), and imaged with a confocal microscope (Olympus FV 1000) using a 20x oil immersion objective (UPLSAPO 20X NA 0.85).

Two-channel images were obtained at 1024 × 1024 pixel resolution. Excitation/emission spectra and filters were selected using the automatic dye selection function of the Olympus FluoView software (Alexa 488 and Alexa 647).

DATA AVAILABILITY STATEMENT

The raw data supporting the conclusions of this article will be made available by the authors, without undue reservation.

ETHICS STATEMENT

The animal study was reviewed and approved by the Behörde für Justiz und Verbraucherschutz (BJV) – Lebensmittelsicherheit und Veterinärwesen, of the City of Hamburg. All procedures were performed in compliance with German law and according to the guidelines of Directive 2010/63/EU.

AUTHOR CONTRIBUTIONS

AP-A, PJL-M, and AF conducted the experiments and analyzed the data. FH, AP-A, and CDD designed and built the microscope. TGO and AP-A conceived the experiments. AP-A wrote the first draft of the manuscript. All authors contributed to the final version.

FUNDING

This project was supported by the German Federal Ministry of Education and Research (BMBF) through the grant "Rapid3D" (FKZ: 13N14537) in the initiative "KMU-innovativ: Photonik und Quantentechnologien," and by the German Research Foundation (DFG) through grants SPP 1665 220176618, SFB 936 178316478, and FOR 2419 278170285.

ACKNOWLEDGMENTS

We thank Iris Ohmert, Sabine Graf, and Jan Schröder for excellent technical assistance. Subcloning of constructs was performed by Iris Ohmert, AAV vectors were produced by Ingke Braren of the UKE Vector Facility. Anti-red CaMPARI was a gift from Eric Schreiter, mCherry-α-tubulin was a gift from Marina Mikhaylova.

REFERENCES

Antic, S. D., Zhou, W. L., Moore, A. R., Short, S. M., and Ikonomu, K. D. (2010). The decade of the dendritic NMDA spike. *J. Neurosci. Res.* 88, 2991–3001. doi: 10.1002/jnr.22444

Beck, S., Yu-Strzelczyk, J., Pauls, D., Constantin, O. M., Gee, C. E., Ehmann, N., et al. (2018). Synthetic light-activated ion channels for optogenetic activation and inhibition. *Front. Neurosci.* 12:643. doi: 10.3389/fnins.2018.00643

Berndt, A., Schoenenberger, P., Mattis, J., Tye, K. M., Deisseroth, K., Hegemann, P., et al. (2011). High-efficiency channelrhodopsins for fast neuronal stimulation at low light levels. *Proc. Natl. Acad. Sci. U.S.A.* 108, 7595–7600.

Bouchard, M. B., Voleti, V., Mendes, C. S., Lacefield, C., Grueber, W. B., Mann, R. S., et al. (2015). Swept confocally-aligned planar excitation (SCAPE) microscopy for high-speed volumetric imaging of behaving organisms. *Nat. Photonics* 9, 113–119. doi: 10.1038/nphoton.2014.323

Fosque, B. F., Sun, Y., Dana, H., Yang, C. T., Ohyama, T., Tadross, M. R., et al. (2015). Labeling of active neural circuits in vivo with designed calcium integrators. *Science* 347, 755–760. doi: 10.1126/science.1260922

Francavilla, R., Villette, V., Martel, O., and Topolnik, L. (2019). Calcium dynamics in dendrites of hippocampal CA1 interneurons in awake mice. *Front. Cell. Neurosci.* 13:98. doi: 10.3389/fncel.2019.00098

Gee, C. E., Ohmert, I., Wiegert, J. S., and Oertner, T. G. (2017). Preparation of slice cultures from rodent hippocampus. *Cold Spring Harb. Protoc.* 2017, 126–130. doi: 10.1101/pdb.prot094888

Helmchen, F., Svoboda, K., Denk, W., and Tank, D. W. (1999). In vivo dendritic calcium dynamics in deep-layer cortical pyramidal neurons. *Nat. Neurosci.* 2, 989–996. doi: 10.1038/14788

Iacaruso, M. F., Gasler, I. T., and Hofer, S. B. (2017). Synaptic organization of visual space in primary visual cortex. *Nature* 547, 449–452. doi: 10.1038/nature23019

Kahn, O. I., Schätzle, P., Van De Willige, D., Tas, R. P., Lindhout, F. W., Portegies, S., et al. (2018). APC2 controls dendrite development by promoting microtubule dynamics. *Nat. Commun.* 9:2773. doi: 10.1038/s41467-018-05124-5

Kleindienst, T., Winnubst, J., Roth-Alpermann, C., Bonhoeffer, T., and Lohmann, C. (2011). Activity-dependent clustering of functional synaptic inputs on developing hippocampal dendrites. *Neuron* 72, 1012–1024. doi: 10.1016/j.neuron.2011.10.015

Lecoq, J., Orlova, N., and Grewe, B. F. (2019). Wide. fast. deep: recent advances in multiphoton microscopy of in vivo neuronal activity. *J. Neurosci.* 39, 9042–9052.

Losonczy, A., and Magee, J. C. (2006). Integrative properties of radial oblique dendrites in hippocampal CA1 pyramidal neurons. *Neuron* 50, 291–307. doi: 10.1016/j.neuron.2006.03.016

Major, G., Larkum, M. E., and Schiller, J. (2013). Active properties of neocortical pyramidal neuron dendrites. *Annu. Rev. Neurosci.* 36, 1–24. doi: 10.1146/annurev-neuro-062111-150343

Moeyaert, B., Holt, G., Madangopal, R., Perez-Alvarez, A., Fearey, B. C., Trojanowski, N. F., et al. (2018). Improved methods for marking active neuron populations. *Nat. Commun.* 9:4440. doi: 10.1038/s41467-018-06935-2

Perez-Alvarez, A., Fearey, B. C., O'Toole, R. J., Yang, W., Arganda-Carreras, I., Lamothe-Molina, P. J., et al. (2020). Freeze-frame imaging of synaptic activity using SynTagMA. *Nat. Commun.* 11:2464. doi: 10.1038/s41467-020-16315-4

Pologruto, T. A., Sabatini, B. L., and Svoboda, K. (2003). ScanImage: Flexible software for operating laser scanning microscopes. *Biomed. Eng. Online* 2:13. doi: 10.1186/1475-925X-2-13

Polsky, A., Mel, B. W., and Schiller, J. (2004). Computational subunits in thin dendrites of pyramidal cells. *Nat. Neurosci.* 7, 621–627.

Preibisch, S., Saalfeld, S., and Tomancak, P. (2009). Globally optimal stitching of tiled 3D microscopic image acquisitions. *Bioinformatics* 25, 1463–1465. doi: 10.1093/bioinformatics/btp184

Remy, S., and Spruston, N. (2007). Dendritic spikes induce single-burst long-term potentiation. *Proc. Natl. Acad. Sci. U.S.A.* 104, 17192–17197. doi: 10.1073/pnas.0707919104

Schiller, J., Major, G., Koester, H. J., and Schiller, Y. (2000). NMDA spikes in basal dendrites of cortical pyramidal neurons. *Nature* 404, 285–289.

Schindelin, J., Arganda-Carreras, I., Frise, E., Kaynig, V., Longair, M., Pietzsch, T., et al. (2012). Fiji: an open-source platform for biological-image analysis. *Nat. Methods* 9, 676–682. doi: 10.1038/nmeth.2019

Schmidt, E., and Oheim, M. (2020). Infrared excitation induces heating and calcium microdomain hyperactivity in cortical astrocytes. *Biophys. J.* 119, 2153–2165. doi: 10.1016/j.bpj.2020.10.027

Szalay, G., Judák, L., Katona, G., Ócsai, K., Juhász, G., Veress, M., et al. (2016). Fast 3D imaging of spine, dendritic, and neuronal assemblies in behaving animals. *Neuron* 92, 723–738. doi: 10.1016/j.neuron.2016.10.002

Takahashi, N., Ebner, C., Sigl-Glöckner, J., Moberg, S., Nierwetberg, S., and Larkum, M. E. (2020). Active dendritic currents gate descending cortical outputs in perception. *Nat. Neurosci.* 23, 1277–1285. doi: 10.1038/s41593-020-0677-8

Takahashi, N., Oertner, T. G., Hegemann, P., and Larkum, M. E. (2016). Active cortical dendrites modulate perception. *Science* 354, 1587–1590. doi: 10.1126/science.aah6066

Topolnik, L., and Camiré, O. (2019). Non-linear calcium signalling and synaptic plasticity in interneurons. *Curr. Opin. Neurobiol.* 54, 98–103. doi: 10.1016/j.conb.2018.09.006

Wiedenmann, J., Ivanchenko, S., Oswald, F., Schmitt, F., Röcker, C., Salih, A., et al. (2004). EosFP, a fluorescent marker protein with UV-inducible green-to-red fluorescence conversion. *Proc. Natl. Acad. Sci. U.S.A.* 101, 15905–15910. doi: 10.1073/pnas.0403668101

Wiegert, J. S., Gee, C. E., and Oertner, T. G. (2017a). Single-cell electroporation of neurons. *Cold Spring Harb. Protoc.* 2017, 135–138. doi: 10.1101/pdb.prot094904

Wiegert, J. S., Gee, C. E., and Oertner, T. G. (2017b). Viral vector-based transduction of slice cultures. *Cold Spring Harb. Protoc.* 2017, 131–134. doi: 10.1101/pdb.prot094896

Wietek, J., Beltramo, R., Scanziani, M., Hegemann, P., Oertner, T. G., and Wiegert, J. S. (2015). An improved chloride-conducting channelrhodopsin for light-induced inhibition of neuronal activity in vivo. *Sci. Rep.* 5:14807. doi: 10.1038/srep14807

Yang, W., and Yuste, R. (2017). In vivo imaging of neural activity. *Nat. Methods* 14, 349–359. doi: 10.1038/nmeth.4230

Conflict of Interest: FH is an employee of Rapp OptoElectronic GmbH, the company which designed and manufactured the prototype microscope. AP-A and CDD received support from Rapp OptoElectronic GmbH.

The remaining authors declare that the research was conducted in the absence of any commercial or financial relationships that could be construed as a potential conflict of interest.

Acknowledgements

Diese Dissertation wäre ohne die gemeinsame Hilfe vieler Personen nicht möglich gewesen. Mein besonderer Dank gilt Prof. Dr. Thomas Oertner, der mir die Möglichkeit gegeben hat, an einer Vielzahl von wissenschaftlichen Projekten mitzuarbeiten. Im Rahmen dieser Dissertation konnte ich von Deiner Expertise lernen. Außerdem hatte ich die Möglichkeit, wichtigste wissenschaftliche Fähigkeiten zu erlernen. Ich bedanke mich für die Unterstützung meiner wissenschaftlichen Laufbahn durch die Finanzierung der Teilnahme an wissenschaftlichen Fortbildungen und Konferenzen.

Besonders bedanken möchte ich mich bei Dr. Paul J. Lamothe. Paul, deine geduldige Betreuung, dein kreativer Blick und deine Freundschaft waren mir eine Stütze und Inspiration. Ebenso gilt mein Dank Dr. Christine Gee für die inspirierenden Diskussionen über wissenschaftliche Konzepte und das Design von Experimenten sowie das geduldige Korrigieren meiner Doktorarbeit. Vielen Dank auch an Dr. Laura Laprell für ihre Freundschaft, das Teilen ihrer Expertise und ihre Unterstützung beim Erlernen neuer Techniken. Ein großes Dankeschön geht an Iris Ohmert für ihre jahrelange unermüdliche technische Unterstützung und ihre entspannter Optimismus. Für weitere technische Unterstützung danke ich Jan Schröder sowie Sabine und Ingke Braren. Ich danke Dr. Fabio Morellini für seinen wissenschaftlichen Input und seine Hilfe bei den Verhaltensexperimenten. Mein Dank geht auch an Dr. Christian Schulz für seine Unterstützung und Beratung in verschiedenen Bereichen meines Projekts. Vielen Dank an Dr. Simon Wiegert für den wissenschaftlichen Austausch.

Ein besonderer Dank geht an Kristina für die abwechslungsreichen Mittagspausen während des Endspurts meines PhDs. Ein großes Dankeschön geht an all meine Freunde und Arbeitskollegen: Brenna, Oana, Marie, Rui, Alberto, Carolina, Charlotte, Kelsey, Mauro, Della, Celine und Tim, für ihre Freundschaft, Zusammenarbeit und viele erfreuliche Momente im Labor. Des Weiteren bedanke ich mich bei meinen Freunden Friedrich, Wiebke, Leo, Leonie, Drenize, Laura, Tobi, Philip, Anton und Marius, die immer an meiner Seite waren.

Der größte Dank gilt meiner Familie für die jahrelange Unterstützung, Ermutigung und Liebe während meiner gesamten akademischen Laufbahn. Diese Reise wäre ohne euch alle nicht möglich gewesen.

Ihr alle habt auf unterschiedliche Art und Weise zu meinem Erfolg beigetragen, und dafür bin ich euch von ganzem Herzen dankbar.

Eidelstattliche Versicherung

Hiermit erkläre ich, Andreas Franzelin, an Eides statt, dass ich die vorliegende Dissertationsschrift selbst verfasst und keine anderen als die angegebenen Quellen und Hilfsmittel benutzt habe.

I hereby declare, on oath, that I, Andreas Franzelin, have written the present dissertation by my own and have not used other than the acknowledged resources and aids.

Hamburg, den 21.02.24 Unterschrift